DNA nanotubes: An elastic mechanical perspective



Hemani Chhabra

Magdalen College

University of Oxford

A thesis submitted for the degree of

Doctor of Philosophy

Trinity 2021-22

Acknowledgements

The first note of thanks is for Jon! Thank you for all the quick chats at all times during the day and night which were rarely short but certainly crisp. It would have been impossible to see this day without your constant help and support. Thanks for replying to all mails that did deserve a reply and ignoring the ones that should have never been drafted in hindsight. Most importantly, thank you for keeping my interest in research alive throughout the DPhil. and beyond.

To all the professors who taught me during my MSc., I am grateful to have received such a wonderful training from the TMCS team that helped me get through my DPhil. smoothly. Prof. David Logan, Prof. Mark Wilson, Prof. William Barford, Prof. Stuart Mackenzie and Magdalen College deserve a special thanks for helping me fund my research though the EPSRC grant and Perkin research scholarship. I am thankful to the department for giving me a special friend - Leema.

The present(Ian, Marco, Mike, Hannah, Wilber) and past(Dan, Domen, Max, Navo) members of the Doye and Ard Louis lab have been a great company throughout my MSc. and DPhil. journey.

Suvajit, Viveka, Natasha, Aditi, Aditya, Mayur, Shivohum, Varnika, Mohita, Samarth, Nitin, Sudipto and Henal deserve a special note of appreciation for keeping me sane for the past 5 years and especially during COVID. I am glad you decided not to deceive me unlike the imposter in Among us - a role you all played exceedingly well. I sincerely appreciate your consent in being the test subjects to my culinary experiments. Also, a standing ovation to the few who did agree to sit in my car; even though you prayed for your life while I occasionally steered to and away from accidents. The rest made a very wise decision to avoid me showcasing my driving skills. Mayur deserves a special note as he made sure we kept connected to our roots by including us in all cultural festivities. Any words for Suvajit will not be sufficient to thank him for his presence in my life but I will still try to pen down a few lines. Suvajit, thank you for dealing with me through thick and thin with your infinite calmness. Importantly, thank you for hearing me rant about life and people.

The people who deserve the most appreciation are my parents and my sister. My mum has been the constant cheerleader in my life. Coincidentally, I am writing this on mother's day and I think I can never thank her enough for her constant support and love; not just during the DPhil. but since forever. Lastly but most importantly, the creator who continues to enlighten me.

Abstract

DNA nanotubes are a versatile nanoscale structural element that have seen an increasingly wide range of uses, such as appendages to facilitate the propulsion of magnetic beads and as potential drug carriers that can help us achieve targeted drug delivery especially in the case of cancer. To enable their use for such applications, it is vital to understand the elastic properties and mechanical limits of such nanotubes.

Simulations and modelling have the potential to play a particularly important role in this regard, because detailed mechanical characterization of such nanoscale structures is hard to obtain experimentally. To study the elastic properties of rod-like DNA nanostructures (with and without defects) we perform long simulations of these structures using the oxDNA coarse-grained model. By analysing the thermal fluctuations in these trajectories we obtain estimates of the bend and twist persistence lengths, and the underlying bend and twist elastic moduli and couplings between them. That the bending persistence lengths we obtain are generally somewhat higher than in experiment probably reflects both that the simulated origami have no assembly defects and that the oxDNA extensional modulus for double-stranded DNA is too large. We also study some DNA nanotubes under torsional stress providing both an alternative means to obtain twist moduli and the first insights into the nature of torsional buckling in DNA nanostructures. The structures of these plectonemes show significant differences as compared to DNA duplexes because they are in a different mechanical regime with respect to their basic mechanical properties.

Finally, we simulate the properties of a recently developed nanomechanical device to help interpret the experiments on this system. In particular, we show that a proper accounting of the elastic mechanical response of the origami component of this force clamp is essential if the forces that the device can exert are to be correctly estimated.

Contents

List of Figures **vii**

List of Tables **xviii**

List of Abbreviations **xx**

1 Introduction **1**
- 1.1 The discovery of genetic material . . . 1
- 1.2 Components of DNA . . . 3
- 1.3 Structure of DNA . . . 4
- 1.4 DNA nanotechnology . . . 8
- 1.5 Theoretical approach to understanding DNA . . . 10
- 1.6 Nucleotide-level coarse graining . . . 13

2 Methods **17**
- 2.1 oxDNA1 . . . 17
- 2.2 oxDNA2 . . . 18
- 2.3 Molecular Dynamics . . . 20
- 2.4 Simulation overview . . . 21

3 Computing the Elastic Mechanical Properties of Rodlike DNA Nanostructures **23**
- 3.1 Introduction . . . 23
- 3.2 Methods . . . 26
  - 3.2.1 DNA nanotubes . . . 26
  - 3.2.2 Simulations . . . 28
  - 3.2.3 Elastic model . . . 30
  - 3.2.4 Persistence lengths and elastic moduli . . . 33
  - 3.2.5 Triad definitions . . . 35
  - 3.2.6 Extracting limiting values . . . 40
- 3.3 Results . . . 44
- 3.4 Conclusions . . . 55

4 Twisting DNA nanotubes **58**
4.1 Introduction . . . 58
4.2 Methods . . . 61
4.2.1 Simulation . . . 61
4.3 Results and Discussion . . . 66
4.3.1 Geometry of a plectoneme in helix bundles . . . 66
4.3.2 The physics of plectoneme formation in helix bundles . . . 70
4.3.3 Calculation of elastic parameters . . . 76
4.4 Conclusion . . . 77

5 Understanding mechanics of gapped rods **79**
5.1 Introduction . . . 79
5.2 Methods . . . 81
5.3 Persistence lengths . . . 83
5.3.1 l_b and l_t for 10HB gapped origamis . . . 83
5.3.2 l_b and l_t for 4HB gapped origamis . . . 86
5.4 Structural effects of the gaps . . . 91
5.5 4HB with graduated gap size . . . 92
5.6 Conclusion . . . 96

6 Theoretical study of DNA force clamp - a reality check **97**
6.1 Experimental setup . . . 98
6.2 System setup . . . 100
6.3 Simulation details . . . 100
6.4 Results . . . 103
6.5 Measurement of forces . . . 105
6.6 Conclusion . . . 107

7 Conclusions and Future Work **109**

Appendices

A SI 1 **115**
A.1 Further Equilibration and Simulation details . . . 115
A.2 Further details of mechanical properties calculations . . . 118
A.2.1 Angular deformations distributions . . . 118
A.2.2 Further effects of α . . . 118
A.2.3 Triad definitions . . . 120
A.2.4 Limiting values . . . 123
A.3 Further results . . . 126
A.3.1 Nanotube radii . . . 126

A.3.2 Persistence lengths 127
A.3.3 DNA extensional modulus 129
A.3.4 Elastic moduli 132
A.3.5 SST nanotube cross-sections 134

B SI 2 **135**
B.1 Trajectory overview for 6HB-SST 135
B.2 Trajectory overview for 4HB-SST 140

C SI 3 **142**
C.1 Simulation details 142
C.2 Calculation of persistence lengths for 10HB origamis 143
C.3 Calculation of persistence lengths for 4HB-1 nt 145
C.4 Calculation of persistence lengths for 4HB-3 nt 147
C.5 Calculation of persistence lengths for 4HB-5 nt 149

Bibliography **152**

List of Figures

1.1 Diagrammatic representation of Hersey and Chase's experiment. The absence of radioactive sulphur and the presence of radioactive phosphorous in bacteria confirmed that DNA was indeed the information carrier and contained phosphorous in some form. Picture adapted from Ref. [4]. 2

1.2 Structure prediction of DNA by Levene. He deemed the structure of DNA to be too chemically simple to store the genetic information. Structure derived from Ref. [7]. 4

1.3 (a) The double helix structure consists of the sugar phosphate backbone and the base pairing that leads to major and minor grooves. (b) Representation of the anti-polar nature of the 2 strands along with base-pairing. (c) shows the hydrogen bonds that A forms with T and G forms with C. Figure reproduced from Ref. [12]. 5

1.4 Hoogsteen base-pairing is observed in a G-quadruplex. In such base pairs G–C rather than forming 3 hydrogen bonds is linked via only 2 hydrogen bonds. If this base pairing is to predominantly exist in DNA, the stable structure ought to be very different to what Watson-Crick postulated. Figure reproduced from Ref. [13] with appropriate permissions. 6

1.5 The figures from left to right show A-DNA, B-DNA and Z-DNA, respectively, and and their projections on a plane perpendicular to the helical axis. Picture reproduced from Ref. [14]. 7

1.6 (A) Depicts Rothemund's scaffold - staple method of creating 2-D origamis. (B) Example of 2-D DNA origami systems studied by Rothemund [28]. (Ca) DNA honeycomb-lattice [29], (Cb) DNA nano-structure with complex curvature [30] and (Cc) a wire-frame structure with arbitrary shape [31]. (D) DNA structure assembled using multiple DNA origamis [32]. (E) Is a ssDNA/RNA origami where the rainbow gradient represents the folding route starting from the $5'$ and $3'$ ends (red) to the middle of the strand (purple) [33]. (F) and (G) are examples of dynamic DNA origami nanostructures [34]. Picture adapted with permission from [35]. 9

2.1 (a) oxDNA is a 1BPN CG model. The nucleotide is represented by a backbone(red) and a base(cyan). (b) Shows a 12-bp DNA duplex with major and minor grooves as depicted by oxDNA2. Inset figure shows the various interactions that have been used to parameterize oxDNA. Figure adapted from Ref. [121]. 19

3.1 Snapshots of two of the DNA nanostructures (a) 4HB-SST; (b) 6HB-S, including close-ups from the ends and the side. 28
3.2 Snapshots of the 4HB-MT and 6HB-MT origami. The second image of the 4HB-MT origami shows an exceptionally bent configuration. The blocks at each end of the origamis are to facilitate attachment to the beads in magnetic tweezer experiments. 29
3.3 Snapshots of the 6HB-SST and 8HB-SST nanotubes. The end views clearly show the alternating distances of the helices from the centres of the tubes. 29
3.4 Snapshots of the 10HB origami. The two side views are roughly perpendicular to their thick and thin dimensions. Note this is not perfectly maintained because of the slight right-handed twist of the origami. 29
3.5 (a) An oxDNA nucleotide along with the "base" and "normal" vectors used to define its orientation. (b) An oxDNA base pair illustrating the directions of $\widehat{\mathbf{e}}_1$ and $\widehat{\mathbf{e}}_2$. (c) Schematics of the cross-sections of the different types of DNA nanostructures considered showing $\widehat{\mathbf{e}}_1$ and $\widehat{\mathbf{e}}_2$. In (b) and (c) $\widehat{\mathbf{e}}_3$ is directed out of the plane of the paper. . . . 31
3.6 $l_b(m)$ for (a) dsDNA and (d) the 6HB-S origami at different values of α, as labelled. (b) $\langle\Theta_2\rangle$ for dsDNA as a function of α. (c) Helicity measure for the dsDNA centerline as a function of inverse wavelength at $\alpha = 0$ and 0.06. The peak in the $\alpha = 0$ curve occurs at the inverse of the DNA pitch length, i.e. $1/(10.5 \times 0.34\,\mathrm{nm})$. 38
3.7 Elastic moduli for 6HB-SST using singular value decomposition. $\alpha = 0.06$. 39
3.8 $\log\langle\cos\theta(m)\rangle$ versus m for (a) duplex and (b) 6HB-SST along with fit lines to the exponential tail. 41
3.9 The effect of averaging on A_1 for different n_{avg} for the 6HB-SST nanotube. 42
3.10 (a) Radius as a function of position, (b) m-dependent persistence lengths and (c) elastic moduli (using $n_{\mathrm{avg}} = 0$) for the 6HB-S origami. 47
3.11 (a) m-dependent persistence lengths and (b) elastic moduli (using $n_{\mathrm{avg}} = 0$) for the 10HB origami. 48

3.12 (a) m-dependent elastic moduli (using $n_{\text{avg}} = 0$) and (b) radii for equivalent helices as a function of position for the 4HB-SST nanotube. 49

3.13 The variation of the bend and twist persistence lengths with n_{helix} for all systems including dsDNA. Lines have been added for the SST series of nanotubes. There are also two additional lines (with no data points) that represent the predictions of Eq. 23 for the SST nanotubes using both the actual radius of dsDNA or an effective radius that is chosen to fit the observed data. 51

4.1 (a) shows two representative configurations of the 6HB-SST nanotube under bending stress. The left snapshot shows the presence of a kink which is centrally located when the end-to-end distance between the ends is 130 nm. In the right configuration, where the ends are just 13 nm apart, it is more favourable to relieve the stress through the formation of 2 kinks. (b) is a schematic showing Kauert *et al.*'s interpretation of their magnetic tweezers results on the 6HB-MT or 4HB-MT systems in terms of the expected plectonemic loop formation [144]. (c), (d) End-to-end distance as a function of applied twist for (c) 6HB-MT and (d) 4HB-MT systems subject to a pulling force of 0.6 pN. It is noticeable that buckling occurs significantly earlier for the 4HB-MT nanotube, whereas it requires more than 20 applied turns for the 6HB system. Note that the systems studied by Kauert *et al.* contain bulky DNA blocks at each end of the nanotube that connect to the magnetic tweezer beads; their effect on the propagation of twist stress to the main part of the nanotube is not clear. (a) is adapted from Ref. [179], whilst (b), (c) and (d) adapted from Ref. [144] with permission. 60

4.2 The nanotube is aligned along the z-direction. (a) and (b) show configurations of a 6HB-SST before and after a small force of 4 pN was applied to the central 64 slices in the $-y$ direction to create a structure where bending is focussed in the centre, thus facilitating plectoneme nucleation in centre of the nanotube. (c) The geometry of a 4HB-SST nanotube as seen from one end of the nanotube after introducing a 4 pN bending force at 2 turns. The coupling of the twist and bend to create a proto-curl configuration is clear from this viewpoint. 63

4.3 (a) A representative configuration of a 4HB-SST plectoneme held under an external force of 2 pN. The presence of kink defects at the tips of plectonemes is a universal feature of plectonemes in helix bundle systems, regardless of the magnitude of the tension that is applied to the system. Plectonemes are also observed to form at an acute angle to the unwrithed segment of the helix bundle. It is also noticeable that in the plectoneme stem one of the filaments is relatively straight with the other wrapping around it in a helical fashion. (b) This figure shows a generic representation of plectonemic loop and tail in systems such as DNA duplexes which contrasts with the slanted plectonemic loop we observe in origamis. F_{ext} is the pulling force, M_{ext} is the twisting force which applies a $2n\pi$ twist, Δz is the end-to-end distance, α is the superhelical angle and R is defined as the superhelical radius. (b) is adapted from Ref. [200] with permission. 66

4.4 Snapshots of a 6HB-SST nanotube being twisted at a rate of $2\pi \times 10^{-7}$ per simulation step at (a) 3, (b) 5, (c) 6, (d) 7, (e) 8, (f) 9 and (g) 11 imposed turns. These are non-relaxed configurations from simulations where the nanotube was still being twisted. The applied tension is 2 pN. The increasing number of turns leads to a typical plectoneme structure that is slanted at an acute angle to the unwrithed segment of the nanotube. In the plectoneme stems often one filament is relative straight with the other wrapping around it. As the plectoneme nucleated slightly off-centre, once 11 turns have been applied further growth is only possible by nucleation of a new plectoneme loop in the longer unwrithed arm near to the base of the original plectoneme. 67

4.5 Snapshots of a 4HB-SST nanotube at (a) 3, (b) 8 and (c) 10 imposed turns. (d), (e) and (f) correspond to the same number of turns as in (a), (b) and (c), respectively, but while untwisting the 4HB-SST nanotube. The applied tension is 2 pN. Both the rates of twisting and untwisting were fixed at $2\pi \times 10^{-7}$ per simulation time step. The untwisting simulations started from a configuration with 16 imposed turns. The contrasting accumulation of loops in the untwisting process as compared to the twisting trajectory indicates the non-reversible pathway of plectonemes in origami systems. Another observable difference is the greater build-up of twist stress in the unwrithed arms during twisting runs (visible by the bowing out of the helices between junctions) because the unwrithed sections are able to more quickly respond to the changes in twist than the plectoneme. Also, as motion of the kink at the base of the plectoneme is relatively slow, during untwisting the length of the plectoneme does not change much, but instead the pitch of the braided section increases. 68

4.6 (a) End-to-end extension and (b) post-buckling torque plots for a 4HB-SST nanotube. (c) End-to-end extension and (d) post-buckling torque plots for a 6HB-SST nanotube. Error bars represent the standard error of the mean. In the case of the 4HB-SST nanotube the mean is obtained from simulations started from configurations generated in both the twisting and untwisting trajectories. Edge effects become apparent when the number of imposed turns is large. Plectonemes are pinned by the kink defect at their tips. If these plectonemes are formed near the edge of the helix bundle, then their continuous lengthening will be prevented as the number of imposed turns increases, leading to the formation of secondary plectonemes which results in a deviation from the expected trends in the end-to-end extension and torque plots. 72

4.7 (a) A 6HB-SST nanotube under a tension of 10 pN when 11 turns have been applied to the system. Tensions beyond 4 pN increasingly undo the effect of the bending force, and hence kinks and bends near to the ends of the origami that are prone to offer seeding points to plectoneme nucleation because of their proximity to the site of twist application. If the growth of the plectoneme begins close to the end of the nanotube, the growth is inhibited as in this case. After a couple of turns, there is little stem left on one side to enable further growth. (b) As a consequence further twisting (12 turns have been applied to the illustrated configuration) leads to the nucleation of a second plectoneme near to the other end of the nanotube. 73

4.8 Variation of the number of intact base pairs with the number of imposed turns in (a) 4HB-SST, and (b) 6HB-SST. A base pair is considered denatured if the binding energy falls below 10% of its maximum possible value. In 4HB-SST, approximately 5 base pairs are broken per turn whereas in 6HB-SST, this number goes up to approximately 10 base pairs per turn. 74
4.9 (a) Variation of torque with N_{turns} for 6HB-SST at a tension of 7pN. There is a linear increase in torque until 1.6 turns indicating that the nanotube has still not encountered bucking. Note that the graph does not go through the origin because N_{turns} is measured with respect to an untwisted geometry, whereas the relaxed structure of this nanotube is slightly right-twisted (Table 3.1). (b) Variation of the end-to-end distance versus applied twist in the pre-buckling regime. There are minimal changes in this quantity indicating the absence of any plectonemic loop formation. 75

5.1 Short sections of the cadnano designs (a) show the presence of multiple crossovers between non-adjacent helices at the same slice index in the 10HB of Ref. [171] that we studied in Chapter 3, while (b) the 10HB [146] that we study in this chapter shows a much less regular pattern of junctions with scaffold as well as staple crossovers and has some short 2-nt domains which together give rise to a somewhat more flexible origami. In the 33-slice section in (b) there are 9 sites at which staple ends meet. These are the sites at which gaps are introduced. 83
5.2 (a) A 10HB origami without any gaps is relatively straight and rigid as compared to the (b) 10HB-5 nt with 100% gap density in which a significant left handed twist is observed, along with higher bending flexibility. (c) A gap site in the 4HB-5 nt nanotube with 100% gap density. The gap reduces the mechanical connectivity between the double helices on either side of the gap. Note in this example the non-helical path of the yellow strand through the gap. The gap also affects the duplex structure near to gap. The end base pairs are more likely to fray and even when base-paired the distance between the relevant nucleotides increases somewhat because of the changes to the interactions at the gap site that contribute to the normal duplex structure. 84
5.3 $\log\langle\cos\theta(m)\rangle$ versus m for all 10HB systems. 85
5.4 The variation of (a) l_b and (b) $l_t/2$ in the 10HB-5 nt system with increasing gap density. 86

5.5 Cadnano sections of (a) 4HB-MT nanotube that was studied experimentally using magnetic tweezers [144]. The crosses indicate base-pair deletions. This origami also has bulky DNA blocks at the end to allow it to be attached to the magnetic tweezer beads (not shown in this section). (b) 4HB-no gap origami studied in this chapter. (c) 4HB-SST which has single cross-overs between adjacent helices every 21 slices and is relatively rigid. The systems in (a) and (c) were studied in Chapter 3. 88

5.6 The variation of (a) l_b in 4HB-1 nt, 4HB-3 nt and 4HB-5 nt with increasing gap density and (b) $l_t/2$ 4HB-1 nt, 4HB-3 nt and 4HB-5 nt with increasing gap density. 89

5.7 (a) $\log\langle\cos\theta(m)\rangle$ versus m and (b) exponential decay of the correlation function used to calculate $l_t/2$ for 4HB-no gap origami. 92

5.8 Variation of the radius of the graduated 4HB nanotube with slice index shows a gradual widening of the tube due to greater splaying as the gap size increases. The "no-gap" and the 5-nt-gap sections appear smaller due to the removal of the 60 terminal slices from each end for the analysis. The repeating motif in the graphs reflects the patterns of junctions and gaps with helices being closest together at junctions. 93

5.9 Although there is an increase in angular fluctuations along the tube, $\langle\Omega_1\rangle$ and $\langle\Omega_2\rangle$ are still centered at zero. By contrast, $\langle\Omega_3\rangle$ becomes more negative along the tube, consistent with the fact that the gaps lead the tube to being more left-twisted. 94

5.10 (a) The splay of centre lines of all 2371 configurations from the rigid end and (b) a wider splay of centre lines from the softer end in y-z axis shows the asymmetry in the nanotube. In case of a symmetrical nanotube , both ends would produce equal dispersion. The y- and z-axis in this plot are in oxDNA simulation units. 95

6.1 (a) Schematic of the DNA Origami-Polymer force clamp, particularly showing the layout of the DNA single strands on the origami and the polymer sphere that allow binding of the origami to the polymer sphere both directly via the linker duplexes and via the target hairpins. The sequences a and a* and b and b* are complementary. This example, denoted L_{110nm}, has the three hairpins bound at the end of the DNA origami rod. (b)(i) is a representation of L_{110nm} at low (left) and high (right) temperatures. The plots on the right show temperature-dependent fluorescence measurements of DNA hairpins (red curve) compared to mechanical unfolding of the same hairpin using OPFC (blue curve). (b)(ii) is a representation of L_{110nm} at low (left) and high (right) temperatures but without the hairpin stem and loop and shows no fluorescence enhancement at 45°C (yellow curve). (b)(iii) shows the mechanical changes in Δ32 at low (left) and high (right) temperatures. Since the origami has a 32 slice ssDNA section in the middle, the origami is relatively compliant and leads to dampening of the mechanical unfolding signal in experiments (green curve). (b)(iv) shows the different mechanical stresses exerted on the hairpins when they are positioned at the centre of the origami; hence L_{10nm} shows minimal signal enhancement compared to L_{110nm} suggesting any tensile stresses applied to these hairpins is below the threshold required to cause unfolding. The plot on the right in panels (b)(i)-(b)(iv) highlights the behaviour in the 30 to 60°C range. Error bars in each curve show standard deviation of n = 3 experiments. The fluorescence intensity was acquired at 575 nm from temperature-dependent fluorescence spectra. 99

6.2 Schematic to show how the parameters for modelling the polymer sphere in the oxDNA simulations are chosen (for clarity only two of the three hairpins are shown). The relative sizes of the objects are not to scale. 101

6.3 The average force acting on all hairpins for each system at low and high temperature. Results of the force experienced by hairpins on Δ32 are plotted using triangles. The dashed black line represents the $\mathbf{F}_{\frac{1}{2}}$ of the hairpin. 106

A.1 The fluctuation of the "end-to-end" distance during the molecular dynamics trajectories for (a) 4HB-MT, (b) 6HB-S, (c) 6HB-SST and (d) 10HB. The different colours represent separate trajectories. Each configuration is separated by 6.06 μs. In order for the measure to capture the fluctuations of the molecular contour in the bulk of the tube, the distance is measured between slices that are 100 slices in from each end. 116

A.2 Probability distributions for (i) $a\Omega_{1,\mathrm{cum}}(m)/\sqrt{m}$, (ii) $a\Omega_{2,\mathrm{cum}}(m)/\sqrt{m}$, and (iii) $a\Omega_{3,\mathrm{cum}}(m)/\sqrt{m}$ for the 4HB-MT origami at different values of m: (a) $m = 1$, (b) $m = 3$, (c) $m = 11$ and (d) $m = 41$. The solid lines are Gaussian fits to the distributions. 119
A.3 Probability distributions for (i) $a\Omega_{1,\mathrm{cum}}(m)/\sqrt{m}$, (ii) $a\Omega_{2,\mathrm{cum}}(m)/\sqrt{m}$, and (iii) $a\Omega_{3,\mathrm{cum}}(m)/\sqrt{m}$ for the 6HB-MT origami at different values of m: (a) $m = 1$, (b) $m = 3$, (c) $m = 11$ and (d) $m = 41$. The solid lines are Gaussian fits to the distributions. 120
A.4 Probability distributions for (i) $a\Omega_{1,\mathrm{cum}}(m)/\sqrt{m}$, (ii) $a\Omega_{2,\mathrm{cum}}(m)/\sqrt{m}$, and (iii) $a\Omega_{3,\mathrm{cum}}(m)/\sqrt{m}$ for the 6HB-SST nanotube at different values of m: (a) $m = 1$, (b) $m = 3$, (c) $m = 11$ and (d) $m = 41$. The solid lines are Gaussian fits to the distributions. 121
A.5 Elastic moduli for (a) 6HB-S and (b) 6HB-SST at $\alpha = 0.0$. The origami exhibits an oscillation on the pitch length of double-stranded DNA, whereas the elastic moduli increase smoothly for the SST nanotube. 121
A.6 Double-stranded DNA elastic constants A_1, A_2, C, G as a function of α. 122
A.7 The effect of the orthogonalization scheme to obtain the triad $\{\hat{\mathbf{e}}_1, \hat{\mathbf{e}}_2, \hat{\mathbf{e}}_3\}$ on the elastic moduli for the 6HB-SST nanotube. In (a) $\hat{\mathbf{y}}$ is orthogonalized to $\hat{\mathbf{e}}_3$, whereas in (b) $\hat{\mathbf{x}}$ is orthogonalized to $\hat{\mathbf{e}}_3$. . . . 123
A.8 The exponential decay of the correlation function used to calculate the twist persistence length for the 6HB-SST nanotube. 124
A.9 A comparison of elastic constants calculated using Equations 3.7 (solid lines) and 3.20 (dashed lines) for the 6HB-SST nanotube. . . 125
A.10 The effect of averaging on (a) A_2, (b) C, (c) l_b and (d) l_t for different n_{avg} for the 6HB-SST nanotube. 125
A.11 Twist per slice as a function of the designed twist in turns (i.e. 2×LH is -2, 1×RH is +1) for the series of twisted 6HB origamis. 126
A.12 Radii as a function of position in the nanotube for (a) 4HB-MT and (b) 6HB-MT. 127
A.13 Radiii as a function of position in the nanotube for (a) 4HB-SST, (b) 6HB-SST and (c) 8HB-SST. 127
A.14 Radii as a function of position in the nanotube for (a) 6HB-2×LH, (b) 6HB-1×LH, (c) 6HB-S and (d) 6HB-1×RH. 128
A.15 m-dependent persistence lengths for (a) 4HB-MT and (b) 6HB-MT. 129
A.16 m-dependent persistence lengths for (a) 4HB-SST, (b) 6HB-SST and (c) 8HB-SST. 129
A.17 m-dependent persistence lengths for (a) 6HB-2×LH, (b) 6HB-1×LH, (c) 6HB-S and (d) 6HB-1×RH. 130

A.18 m-dependent persistence lengths for the 10HB origami. 130
A.19 Force-extension curve for a 150-bp duplex, neglecting the 10 base pairs at each end. The data points are from simulations and the solid line a fit to the curve using the extensible worm-like chain formula (Eq. A.10). 131
A.20 Elastic moduli for (a) 4HB-MT and (b) 6HB-MT. 131
A.21 Elastic moduli for (a) 4HB-SST, (b) 6HB-SST and (c) 8HB-SST. . 132
A.22 Elastic moduli for (a) 6HB-2×LH, (b) 6HB-1×LH, (c) 6HB-S and (d) 6HB-1×RH. 133
A.23 Elastic moduli for the 10HB origami at $\alpha = 0.06$. 133
A.24 Radii for equivalent helices in 6HB-SST and 8HB-SST. 134

B.1 Relaxed configurations of the 6HB-SST nanotube at (a) 3 turns (b) 4 turns, (c) 5 turns, (d) 6 turns, (e) 8 turns, (f) 10 turns and (g) 12 turns under a tensile force of 2 pN. The relaxation of the tubes at each turn shows the formation of plectonemic loops even at lower numbers of turns. 137
B.2 Snapshots of 6HB-SST being twisted at a rate of $2\pi \times 10^{-7}$ at (a) 6 turns, (b) 7 turns, (c) 8 turns, (d) 9 turns, (e) 10 turns, (f) 11 turns and (g) 12 turns. These are non-relaxed configurations snapped while the rod was still being twisted and had incurred the required number of turns at a string force of 10pN. 138
B.3 Relaxed configurations of 6HB-SST at (a) 4 turns, (b) 6 turns, (c) 8 turns, (d) 9 turns, (e) 10 turns and (f) 12 turns which belongs to the data set used for measuring torque and other measurable quantities at 10pN string force. 139
B.4 Snapshots of 4HB-SST being twisted at a rate of $2\pi \times 10^{-7}$ at (a) 13 turns, (b) 14 turns, (c) 15 turns and (d) 16 turns . These are non-relaxed configurations at a string force of 7pN. The regular ssDNA overhangs at such high tension are observed throughout the nanotube. The 4HB-SST origami was a troublesome system to simulate to get 'well' formed plectonemes. 141

C.1 $\log\langle\cos\theta(m)\rangle$ versus m for (a) 10HB-no gap, (b) 10HB-5 nt-20% gap density, (c) 10HB-5 nt-40% gap density, (d) 10HB-5 nt-60% gap density, (e) 10HB-5 nt-80% gap density and (f) 10HB-5 nt-100% gap density. 144
C.2 The exponential decay of the correlation function used to calculate the twist persistence length for (a) 10HB -no gap, (b) 10HB-5 nt-20% gap density, (c) 10HB-5 nt-40% gap density, (d) 10HB-5 nt-60% gap density, (e) 10HB-5 nt-80% gap density and (f) 10HB-5 nt-100% gap density. 145

C.3 $\log\langle\cos\theta(m)\rangle$ versus m for (a) 4HB-1 nt-25% gap density, (b) 4HB-1 nt-50% gap density, (c) 4HB-1 nt-75% gap density and (d) 4HB-1 nt-100% gap density. 146
C.4 The exponential decay of the correlation function used to calculate the twist persistence length for (a) 4HB-1 nt-25% gap density, (b) 4HB-1 nt-50% gap density, (c) 4HB-1 nt-75% gap density and (d) 4HB-1 nt-100% gap density. 147
C.5 $\log\langle\cos\theta(m)\rangle$ versus m for (a) 4HB-3 nt-25% gap density, (b) 4HB-3 nt-50% gap density, (c) 4HB-3 nt-75% gap density and (d) 4HB-3 nt-100% gap density. 148
C.6 The exponential decay of the correlation function used to calculate the twist persistence length for (a) 4HB-3 nt-25% gap density, (b) 4HB-3 nt-50% gap density, (c) 4HB-3 nt-75% gap density and (d) 4HB-3 nt-100% gap density. 149
C.7 $\log\langle\cos\theta(m)\rangle$ versus m for (a) 4HB-5 nt-25% gap density, (b) 4HB-5 nt-50% gap density, (c) 4HB-5 nt-75% gap density and (d) 4HB-5 nt-100% gap density. 150
C.8 The exponential decay of the correlation function used to calculate the twist persistence length for (a) 4HB-5 nt-25% gap density, (b) 4HB-5 nt-50% gap density, (c) 4HB-5 nt-75% gap density and (d) 4HB-5 nt-100% gap density. 150

List of Tables

3.1 Structural and mechanical properties of all the systems studied. All angles are given in degrees and elastic moduli and persistence lengths in nanometres. The n_{avg} and m_{limit} values used to extract the bulk values of the elastic constants are given in Table A.1. The errors in $\langle\Theta_3\rangle$ are standard errors in the mean. The values of the persistence lengths (and elastic moduli) are given to the nearest 10 nm as the errors associated with the fits to the relevant correlation functions for l_b and l_t were at most 10 nm with the exception of l_b for the 10HB origami which we report to the nearest 100 nm. Imperfect sampling and deviations from worm-like chain behaviour may also contribute additional sources of uncertainty. 45

5.1 Gap size and density (0 indicates the system with no defects). Gap size of 1 nt , 3 nt and 5 nt denote that 1 nucleotide , 3 nucleotides and 5 nucleotides respectively have been removed from the available sites. Similarly, gap density refers to the percentage of available sites that have gaps. A gap density of 100% means that all available sites have gaps and a 25% gap density implies that only 25% of the total available sites incorporate gaps. 87

6.1 Snapshots of L_{10nm}-L_{110nm} and Δ32 at low and high temperatures. At high temperature, a strong bend is visible in all systems from L_{10nm} to L_{110nm} while Δ32 is kinked. 104

6.2 Average force along hairpins at low and high temperatures. A graphical representation of this data is given in fig. 6.3. 105

A.1 Details of the simulations and the parameters used when calculating elastic properties. t_{sim} is the total simulation time of the trajectories. N_{config} is the number of configurations in the ensemble used to calculate the elastic properties of each system. N_{ends} is the number of slices at each end that are ignored in these calculations. $2n^X_{\text{avg}} + 1$ is the number of slices over which averaging is performed in Eq. (3.21) for the elastic constant X. m_{limit} is the value of m used when taking the limiting values of the elastic constants. 117

A.2 Structural and mechanical properties of double-stranded DNA before and after applying the correction to remove the helicity of the centreline. The elastic constants obtained from those at $\alpha = 0$ by applying the transformation from a helical to a straight coordinate system outlined in Ref. [175] are also given. The results are for $[Na^+]$=0.5 M and a temperature of 23°C. $a = 0.3462$ nm. 122

C.1 Details of the simulations and the parameters used when calculating persistence lengths. t_{sim} is the total simulation time of the trajectories. N_{config} is the number of configurations in the ensemble used to calculate the persistence length of each system. N_{ends} is the number of slices at each end that are ignored in these calculations. 143

List of Abbreviations

DNA . . . . . Deoxyribonucleic acid.

RNA . . . . . Ribonucleic acid.

mRNA . . . . Messenger Ribonucleic acid.

HB . . . . . Helix bundle.

2-D . . . . . 2-dimensional.

3-D . . . . . 3-dimensional.

dsDNA . . . . Double-stranded DNA.

ssDNA . . . . Single-stranded DNA.

CHARMM . . Chemistry at HARvard Macromolecular Mechanics.

AMBER . . . Assisted Model Building with Energy Refinement .

MC . . . . . Monte Carlo

CG . . . . . Coarse-grained

BPN . . . . . Bead-per-nucleotide

SST . . . . . Single-stranded tile.

MT . . . . . Magnetic tweezers.

MD . . . . . Molecular Dynamics.

nt . . . . . nucleotide.

SAXS . . . . . Small-angle X-ray scattering.

OPFC . . . . . Origami polymer force clamp.

FRET . . . . . Fluorescence resonance energy transfer.

QM . . . . . Quantum Mechanics.

WLC . . . . . Worm-like chain.

DNA is like a computer program but far, far more advanced than any software ever created.

— Bill Gates

1 Introduction

1.1 The discovery of genetic material

DNA's acceptance as the hereditary material by the scientific fraternity was not an easy journey. Mendel's work on studying the genotype and phenotype of pea plants in the late 1800s inculcated the concept of something passing on from one generation to the next, i.e. inheritance [1]. Though his work did not answer what was being inherited, it did lay the groundwork for understanding dominance and numerous Mendelian disorders like color-blindness, sickle-cell anemia, etc. Mendel's pea plant definitely left behind seeds of curiosity and inquisition about human existence.

Meischer's work (1869) during the same period to Mendel, complemented Mendel's findings and provided more clarity. Meischer was successful in isolating 'nuclein' from the nucleus of white blood cells, and discovered that the nuclein was made up of hydrogen, oxygen, nitrogen and phosphorus. He observed that there was a unique ratio of phosphorus to nitrogen [2].

Despite the breakthrough discoveries of Mendel and Meischer that there exists

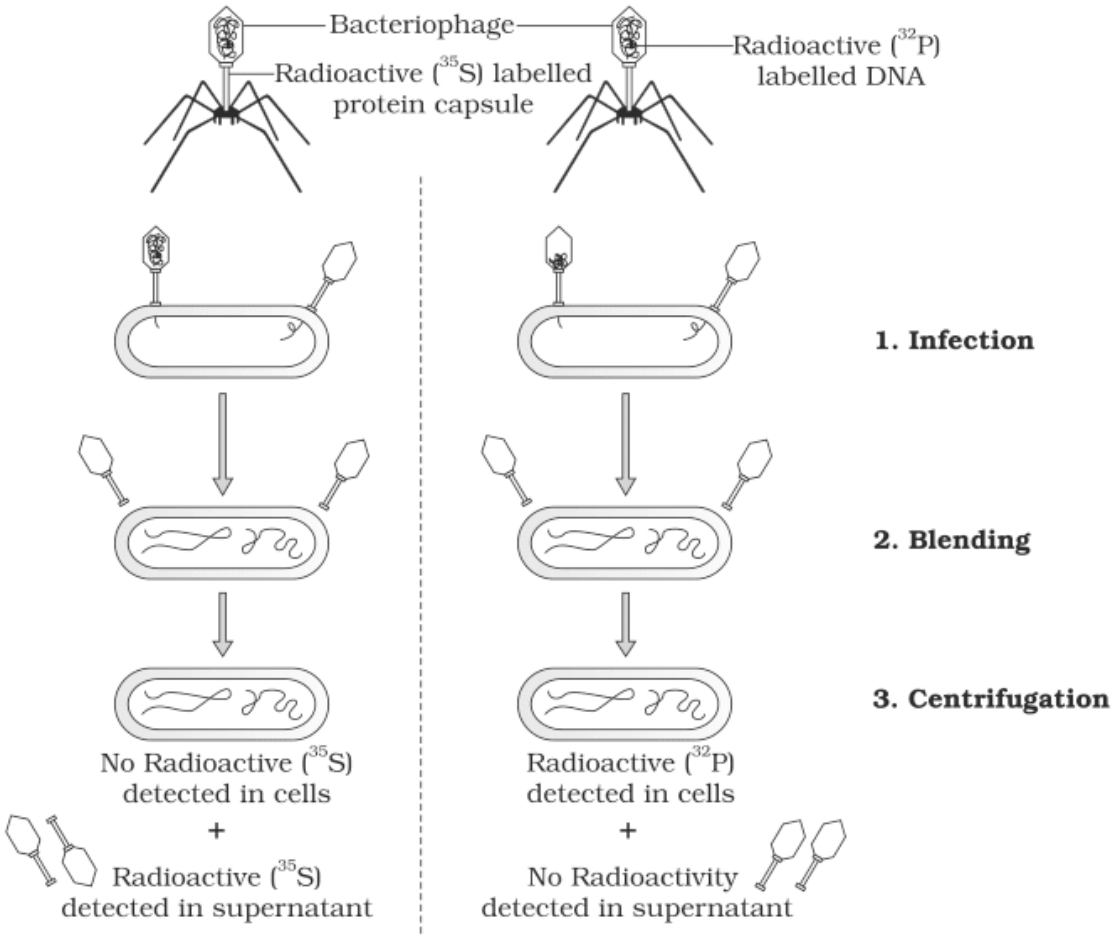


Figure 1.1: Diagrammatic representation of Hersey and Chase's experiment. The absence of radioactive sulphur and the presence of radioactive phosphorous in bacteria confirmed that DNA was indeed the information carrier and contained phosphorous in some form. Picture adapted from Ref. [4].

a genetic material inside the nucleus it took years for DNA to be discovered and proved as the genetic material. Prior to the work of Oswald Avery, Colin MacLeod and Maclyn McCarty (1933-44), the genetic material was thought to be made of protein [3]. Avery *et al.* discovered that protein-digesting enzymes (proteases) and RNA-digesting enzymes (RNases) did not affect inheritance in bacteria. But DNase (DNA digesting enzymes) did inhibit transformation. This indicated that DNA is the hereditary material. However, this did not seem to convince the scientific world about DNA's role as the genetic material.

The work that did seal the fate of DNA came from Alfred Hershey and Martha Chase in 1952 [5]. They worked with bacteriophages (viruses that infect

bacteria) —it attaches to the bacteria and its genetic material then enters the bacterial cell. The bacterial cell hosts the viral genetic material as its own and subsequently replicates more viral particles. They grew some viruses on a medium containing radioactive phosphorus and some others on radioactive sulphur medium. Viruses grown on radioactive phosphorus contained radioactive DNA but not radioactive protein because DNA contains phosphorus but proteins do not. Similarly, viruses grown on radioactive sulphur contained radioactive protein, as sulphur is present in proteins but absent in DNA. Bacteria infected with bacteriophages containing radioactive phosphorus were radioactive while the bacteria infected with bacteriophages containing radioactive sulphur did not show any trace of radioactivity. Fig. 1.1 is a diagrammatic overview of the experiment carried out by Hershey and Chase. This was a convincing result for the scientific community to accept DNA as the genetic material.

1.2 Components of DNA

Finally, in 1953 James Watson and Francis Crick, using the X-ray diffraction data produced by Maurice Wilkins and Rosalind Franklin, proposed the famous double-helix model for the structure of DNA [6]. Their work was commendable and went to win the Nobel prize in 1962 but many biochemists played an indirect role in that discovery.

One such work worth mentioning was by the American biochemist Phoebus Levene. In 1909, Levene and Walter Jacobs recognised the D-ribose (component of RNA) as a natural product and an essential component of nucleic acids [8, 9]. He also discovered deoxyribose in 1929 and identified the linkage in DNA to be of the order phosphate-sugar-base to form units which he called nucleotides [10]. His further deductions about the structure were the major flaws in his predictions. He stated that the DNA molecule consisted of a string of nucleotide units linked via the phosphate groups, which are the 'backbone' of the molecule and the DNA consists

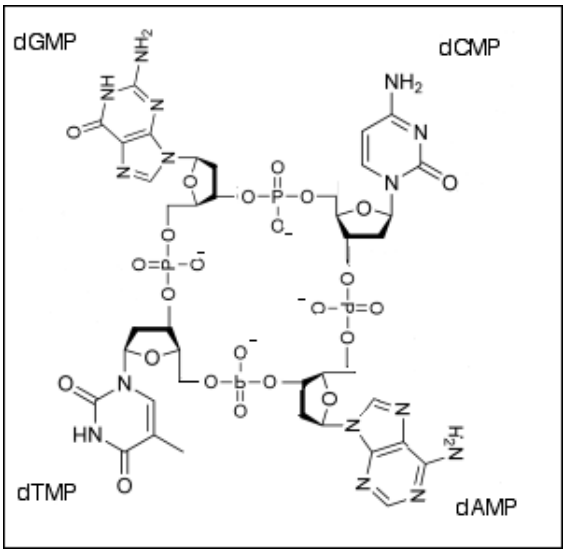


Figure 1.2: Structure prediction of DNA by Levene. He deemed the structure of DNA to be too chemically simple to store the genetic information. Structure derived from Ref. [7].

of equal amount of all 4 bases: adenine (A), guanine (G), cytosine (C) and thymine (T). Fig. 1.2 outlines the structural bonding of DNA as predicted by Levene.

The final and most important discovery by Chargaff [11] in 1950 completed the missing pieces of the puzzle that was finally put together by Watson and Crick in the 1953 Nobel-winning paper. Chargaff via his experiments proved that in natural DNA the number of G units equals the number of C units and the number of A units equals the number of T units which was contradictory to Levene's work where he assumed equal proportions of all bases.

1.3 Structure of DNA

The features of DNA structure that were put forward by Watson and Crick are as follows:

- DNA is made of two poly-nucleotide chains (with anti-parallel polarity) where the backbone is constituted by a sugar-phosphate (a correction to Levene's work where he stated a phosphate only interaction between nucleosides), and the bases project inside.

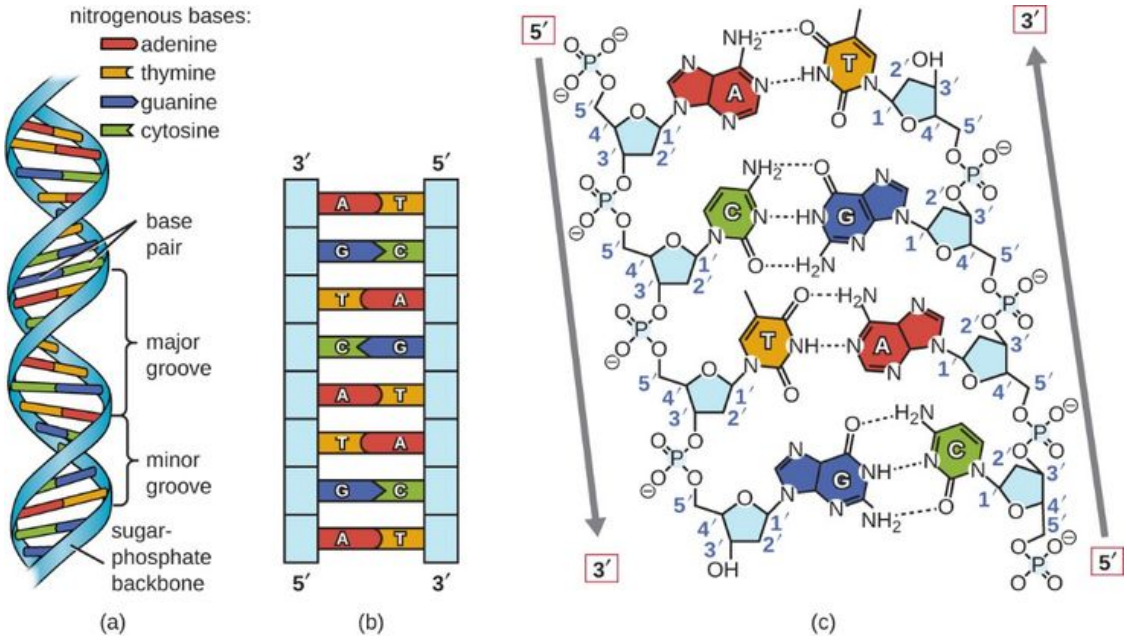


Figure 1.3: (a) The double helix structure consists of the sugar phosphate backbone and the base pairing that leads to major and minor grooves. (b) Representation of the anti-polar nature of the 2 strands along with base-pairing. (c) shows the hydrogen bonds that A forms with T and G forms with C. Figure reproduced from Ref. [12].

- The bases in two strands are paired via hydrogen bonds, thus forming base pairs (bp). A forms two hydrogen bonds with T from the opposite strand and vice-versa. Similarly, G is bonded to C via three hydrogen bonds. Thus, H-bonding ensures an approximately uniform distance between the two strands of the helix. Fig. 1.3 (a) and (b) show the major-minor grooving and anti-parallel polarity of the 2 chains respectively, while Fig. 1.3 (c) highlights the hydrogen bonding between the complementary bases.

- Another important feature they highlighted was the right handedness of DNA helix with a pitch of 3.4 nm.

- Another contributing factor that they observed added to the stability of the double helix was the stacking of the plane of one base-pair over the other.

The year this work won the Nobel prize, Hoogsteen [15] pointed out alternative hydrogen-bonding (Fig. 1.4) patterns in DNA bases which in fact would alter the

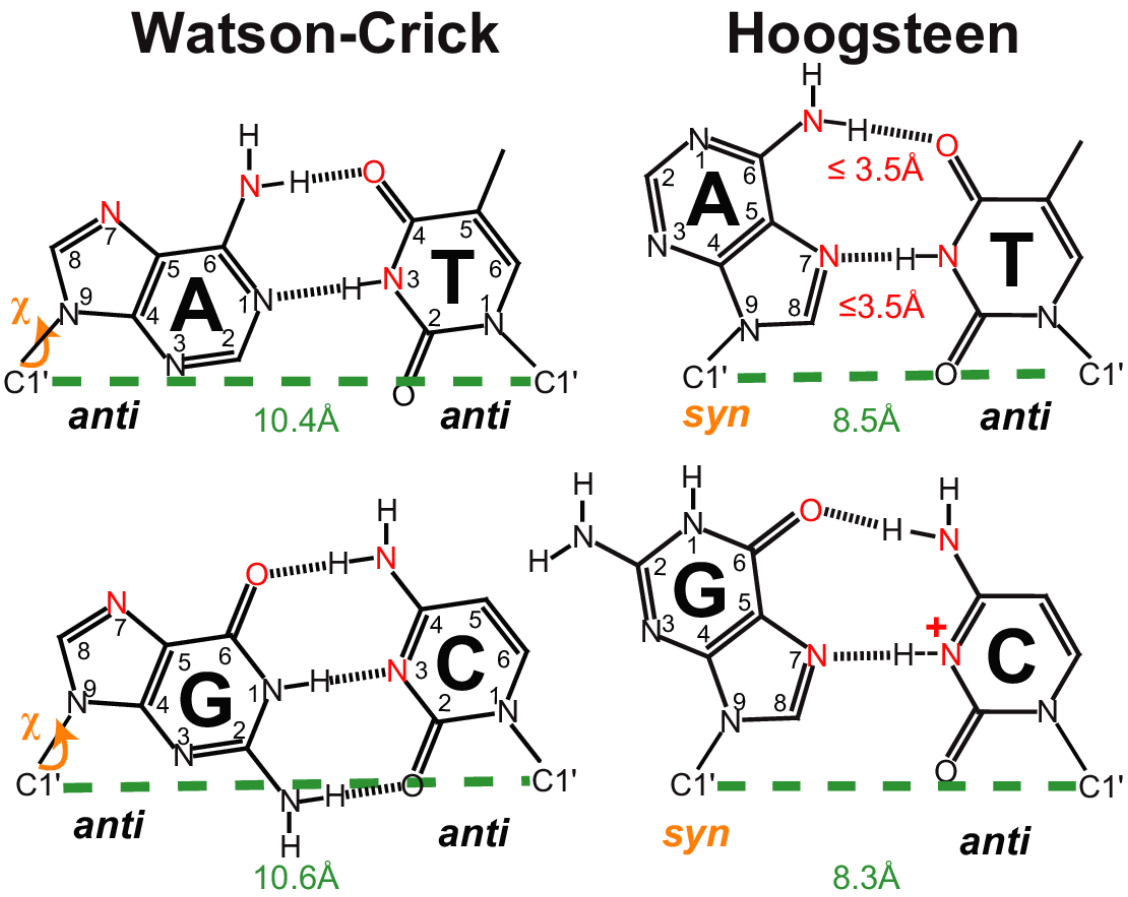


Figure 1.4: Hoogsteen base-pairing is observed in a G-quadruplex. In such base pairs G–C rather than forming 3 hydrogen bonds is linked via only 2 hydrogen bonds. If this base pairing is to predominantly exist in DNA, the stable structure ought to be very different to what Watson-Crick postulated. Figure reproduced from Ref. [13] with appropriate permissions.

shape of the double helix. There are examples of Hoogsteen base-pairing observed in DNA [16] as well as RNA [17].

Though we generally study the B-DNA as it is the most common form found in living organisms, there are 2 other alternate DNA conformations called A-DNA and Z-DNA which have been reported in a few organisms [18]. The RNA helix is an example of an A-Helix. The naming of both A and B forms and the discovery of A-DNA was done by Franklin [19]. In terms of structure, A-DNA has 11 bp per turn while B-DNA has 10 bp per turn. The increase in bp/turn leads to a smaller twist angle and a smaller rise per base pair thus, making the pitch of A-DNA smaller than B-DNA (Fig. 1.5). While A- and B-forms are right handed helices, the Z-conformer is a left-handed helix [20].

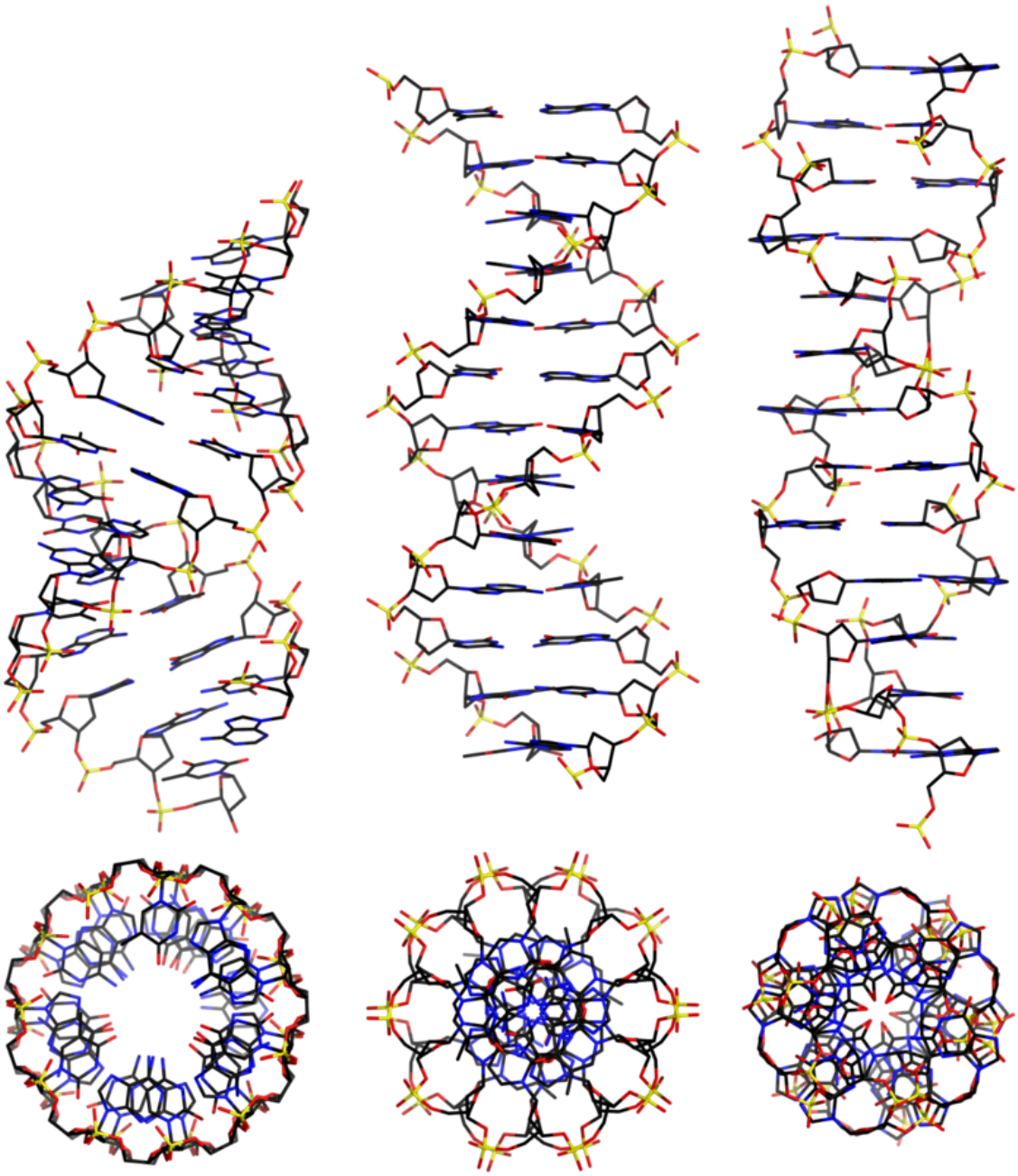


Figure 1.5: The figures from left to right show A-DNA, B-DNA and Z-DNA, respectively, and and their projections on a plane perpendicular to the helical axis. Picture reproduced from Ref. [14].

1.4 DNA nanotechnology

With the knowledge of DNA structure and bonding, the science fraternity became interested in finding uses of DNA outside the genetic world. The foundation of DNA nanotechnology was laid by Nadrian Seeman in the early 1980s. In his pioneering works he showed how base-pairs can be used to create immobile junctions [21]. Realising this potential of DNA to fold and bend gave him the inspiration to create 3-D structures made out of DNA, the first one being a DNA 'cube' [22]. Another breakthrough contribution he added to the field was the concept of the DNA double crossover [23]. It would have been impossible to think about the existence of DNA origamis without Seeman's revolutionary ideas.

Seeman's work inspired the study of self assembly of various 3-D DNA structures including DNA cages [24], a ssDNA built octahedron [25], a DNA bipyramid [26], polyhedra [27] and many other 2-D and 3-D DNA nanostructures.

Another major contribution was by Rothemund in 2006 [28] when he presented the idea of creating DNA origamis using numerous small ssDNA strands (called 'staples') that act as connecting units between domains of the main DNA strand which is called the 'scaffold'. Fig. 1.6 depicts a few DNA 3-D nanostructures that have been successfully assembled and studied.

These nano-engineered DNA structures have facilitated the detection of mRNA in living organisms [36] and helped in advancing medicinal research [37]. They have also found potential use in molecular and cellular biophysics [38]. Starting from DNA walkers [39, 40] to the present research that incorporates a working device within a self-assembled DNA crystal [41], creating DNA nanodevices [35, 42, 43] for photonics or drug delivery to the recent advances that involve creating rotary ratchet motors using 10HB [44] we can safely assume that DNA nanotechnology has multiple uses yet to be explored.

More recently there has been an increasing interest in characterizing their mechanical properties. One reason is the advent of "DNA mechanotechnology", that is the use of DNA nanodevices to generate, transmit and sense nanoscale forces [45]. These include examples where DNA nanostructures are used as the "hardware

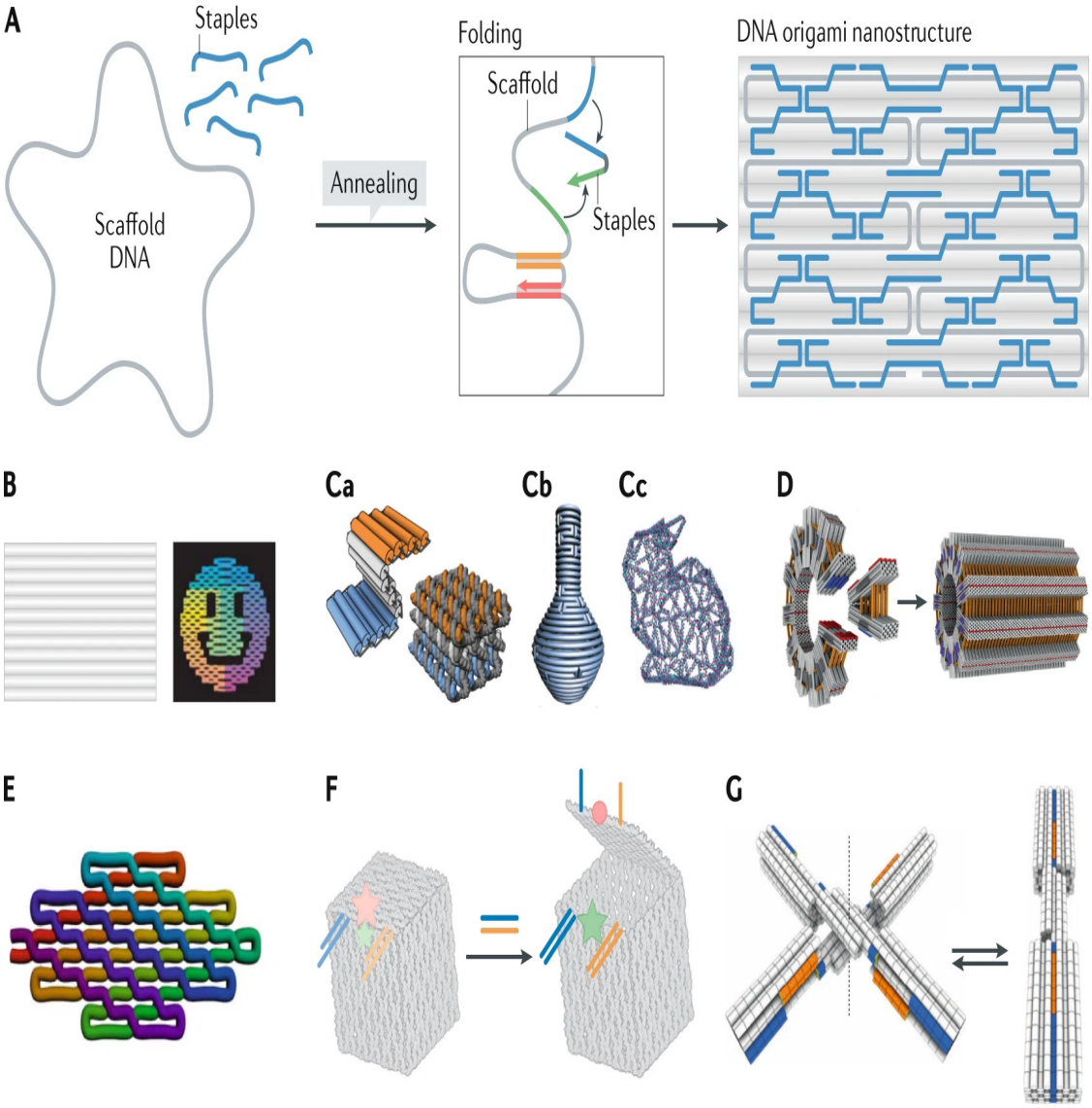


Figure 1.6: (A) Depicts Rothemund's scaffold - staple method of creating 2-D origamis. (B) Example of 2-D DNA origami systems studied by Rothemund [28]. (Ca) DNA honeycomb-lattice [29], (Cb) DNA nano-structure with complex curvature [30] and (Cc) a wire-frame structure with arbitrary shape [31]. (D) DNA structure assembled using multiple DNA origamis [32]. (E) Is a ssDNA/RNA origami where the rainbow gradient represents the folding route starting from the 5′ and 3′ ends (red) to the middle of the strand (purple) [33]. (F) and (G) are examples of dynamic DNA origami nanostructures [34]. Picture adapted with permission from [35].

for single-molecule investigations" [46]. For example, in force spectroscopy, rod-like origami have been used as stiff handles for force application with molecular tweezers [47, 48], and small origami have been used to create multivalent force sensors [49]. Origami with inbuilt tension in components have been used to apply forces to unravel protein-DNA complexes [50, 51] and to study the force-dependent binding of proteins to DNA motifs [52, 53]. Protein-protein interactions have also been measured by the shape changes they induce in an origami to which they are attached [54]. Similarly, origami sensors have been designed that produce a change in FRET signal when interactions are sufficiently strong to induce a shape change [55].

For the above applications, it is important to have a good understanding of the mechanical properties of the DNA origami; for example, knowing the stiffness of the origami handles, knowing the compliance of the origamis with respect to the internal forces that they are seeking to apply, being able to accurately calibrate the magnitude of the forces that are being applied, knowing the limits of the forces that can be applied whilst maintaining the structural integrity of the origami.

1.5 Theoretical approach to understanding DNA

With the increased use of such nanostructures in biophysics, it became important to understand the physical dynamics of such nanostructures. Since quantum mechanics [56] was being used to calculate energies and stability's of chemical systems by the time DNA nanotechnology made its mark in the scientific world, it was the first go-to approach used for DNA as well. A few quantum mechanical calculations on basic DNA systems [57–60] showed that despite the detail that QM calculations provide with respect to DNA studies, the computational demand limits the QM simulations to nearest-neighbour base pairs. If studying basic structures was so cumbersome with QM, it surely could not be the most effective way forward if we ever want to study huge DNA assemblies that contain million of atoms.

The only way the computational requirement could be narrowed down was by compromising on the detail of calculations. Hence, biomolecular software like

AMBER [61] and CHARMM [62] which offered atomistic detail of calculation using force fields became a popular choice. The atomistic approach to DNA calculations has allowed the study of larger systems including DNA-protein complexes [63, 64] which would have been impossible to simulate using a QM approach.

Due to recent developments in computing over the past 20 years, atomistic calculations have offered better insights about DNA mechanics. How stretching [65], twisting [66], supercoiling [67] and cytosine methylation [68] of DNA affects its mechanical properties and the changes it encounters have been well studied for small DNA duplexes using atomistic MD simulations. Success has also been achieved in studying the dynamics of DNA origamis [69–71]. Very short sections of such DNA nanotubes have been studied by all-atom molecular dynamics with estimates of the stretch moduli being obtained from rapid pulling simulations and persistence lengths from bend angle distributions [72–74]. Although atomistic simulations offer numerous pros, the limitations associated with the imperfections of present atomic force fields, inadequate sampling and size constraints cannot be ignored [75].

An alternative approach where DNA is treated as a semi-flexible polymer using theoretical descriptions like the worm-like chain [76] and freely-jointed chain [77] have helped understand the large-scale behaviour of DNA in terms of twisting [78], stretching [79] and folding [80]. The macroscopic view of these models comes at the expense of missing out the basic microscopic dynamics like duplex formation.

A possible middle ground between the different levels of description can be achieved via coarse-grained DNA models. These models rather than using the atom as the monomer of the DNA biopolymer, group together multiple atoms into larger units which altogether experience effective inter-unit interactions. This approach also helps overcome the computing restraint that atomistic MD simulations entail but it comes with a bittersweet option of "selectivity". What I mean by selectivity is that the number of atoms that one selects to group together to coarse-grain determines the effective use of the model. By the sole virtue of coarse-graining, it becomes impossible to study all microscopic dynamics and details of DNA. Hence, to be

done effectively coarse-graining ought to balance computation time with resolution bearing in mind the specific problem one seeks to study using the model [81].

Some notable CG models have been successful in replicating the properties of DNA origami, for example, CanDo [82, 83]. CanDo depicts each DNA helix in an origami as an elastic rod, single-stranded regions are represented as springs, and connections between DNA helices are represented as rigid crossovers while major–minor grooves of DNA are ignored. This model works well to predict structural features of DNA origami, such as their bending and twisting due to internal stresses, but clearly cannot capture the microscopic self-assembly mechanisms.

Another example is where coarse-graining is carried out at the domain level [84]. A domain can either be a small single-stranded section of a staple or scaffold which implies the main purpose is to study assembly. Another such setup may involve defining 'binding domains' where a lattice representation of sub-units helps increase computational efficiency by reducing configuration space. Since all sub-units are a part of the same helix, MC simulations will facilitate the formation of the most stable assembly [85].

Since origamis are an accumulation of many staple strands, each staple strand alongside its complementary bases in the scaffold can be used as a monomeric unit to study self-assembly. Reshetnikov *et al.* [86] rather proposed 7-bp sections as the monomeric unit of the CG model. Generic models for DNA at the base-pair level [87] are able to reproduce persistence lengths of DNA origamis in good agreement with experiments [88].

The major issue with coarse-graining at the base-pair level is that it makes it difficult to study the thermodynamic stability of nanostructures. The fact that one of the primary effects of increasing the temperature, lowering the salt concentration or applying external forces can be to break base pairs, any coarse graining above the single nucleotide level will only allow the study of the mechanics of known stable structures. But if the motive is also to study the thermodynamics of nanostructures, then the maximum level of coarse-graining we can achieve is at the level of nucleotide.

1.6 Nucleotide-level coarse graining

Coarse-graining can either be a 'bottom-up' approach where the statistical behaviour of a more detailed atomistic model is mapped onto a coarse-grained description [89] or a 'top-down' approach that seeks to use measured experimental properties to fit the parameters of a model [90–94]. One of the models that is based on the 'bottom-up' approach was presented by Savelyev and Papoian [95]. This model, which has 1-bead-per-nucleotide (1BPN) and explicit ions, was parameterised on the basis of coarse graining of a high-resolution all-atom (AA) force field (AMBER force field derived for nucleic acids). The model was successful in studying the dependence of DNA persistence length on ionic strength [95, 96]. Since this model was fit to an elastic network model of dsDNA, its use was limited to dsDNA.

The 2-bead-per-nucleotide (2BPN) model proposed by Maffeo *et al.* [75] where the 2 beads represent the centers of mass of the backbone and sugar/base groups was mapped to bonded potentials optimized to reproduce the solution structure of DNA observed in atomistic molecular dynamics simulations. Though the model fails to describe sequence dependence, hybridization and disassembly it has been successfully used to study the translocation of dsDNA through nanopores [97]. Morriss-Andrews *et al.* [98] proposed a 3-beads-per-nucleotide (3BPN) CG model that is parametrized from all-atom simulations and represents solvent ions implicitly. The model mimics DNA dynamics well but fails to replicate persistence lengths well.

The 5-bead-per-nucleotide model by Korolev *et al.* [99] calculates the force field potentials for their CG DNA model using inverse Monte Carlo. It fails to capture the properties of ssDNA and, consequently, hybridization. The Martini-force-field-based model [92] which uses 6 or 7 beads per nucleotide (depending on the base) model involves a mixture of bottom-up and top-down parameterizations. Limitations of this model include its inaccuracy in reproducing experimental persistence lengths and DNA structures.

The Nucleic Acid United Residue 2-Point (NARES-2P) model [100] uses 6-8 beads-per-nucleotide (BPN). The model's poor agreement with experimental thermodynamic data limits its usage. The 6-8 BPN SIRAH model [91, 101]

has not been optimized to reproduce the mechanical behaviour of ssDNA and dsDNA. High-Resolution DNA (HiReDNA) model [102] incorporates 3- and 4-body interaction terms but is computationally inefficient and cannot be used to simulate large nanostructures effectively.

The 'top-down' approach seems to be gaining more popularity as it must be noted that the CG models are bound to inherit the errors of parameterization of the atomic model on which they have been mapped. One such example of a 'top-down' 1-bead-per-nucleotide CG model is the new coarse-grained molecular dynamics double-stranded DNA model (nCG-dsDNA model) developed by Yagyu *et al.* [103]. The model has been mapped to structural DNA data but lacks a thermodynamic mapping.

oxDNA [104–106] is an example of a 1BPN CG model that has been parameterized to experimental thermodynamics and efficiently captures the self-assembly of DNA chains [107] as well DNA origami sub-units [108]. It has been used to characterize in detail some of the fundamental structural features of 2-D and 3-D DNA origamis [109]. Some examples of 3BPN models include the TIS (Three Interaction Site) model [110] which has been parameterized using DNA crystal structures and melting data. Linak's *et al.* [111] top-down approach is capable of studying structures that are stabilized by Hoogsteen bonds. The Knotts *et al.* [112] model overestimates the stiffness of ssDNA as it was originally parameterized only for duplex DNA.

oxDNA, TIS-DNA and Knott's CG parameterization offer good mechanical descriptions of ssDNA and dsDNA and have been mapped to experimental data. This thesis uses oxDNA to model DNA nanotubes as it is the most extensively used model to study DNA nanostructures [113–116] and these applications have confirmed its reliability in reproducing and helping to interpret experimental data. oxDNA's widespread usage has led to it being incorporated into the widely-used LAMMPS MD code [117].

Thesis outline

The structure of the thesis is as follows:

- Chapter 2: This chapter provides a detailed description of oxDNA, the improvements that have been made to overcome a few of its original limitations and some of its success stories that illustrate why oxDNA is a suitable model to be used for determining the elastic properties and limits of DNA nanotubes.

- Chapter 3: We use oxDNA to understand and calculate the elastic mechanical properties of defect-free DNA nanotubes by characterizing the thermal fluctuations in long simulations. This chapter outlines a mathematical framework that can be used to compute persistence lengths and elastic moduli of DNA rods using modelling.

- Chapter 4: Having achieved a thorough understanding of the elastic regime of DNA nanotubes, we move on to try to understand the response of these stiff rod-like objects to extreme twisting. This chapter focuses on plectoneme formation in 4HB-SST and 6HB-SST nanotubes and compares their plectoneme behaviour to that of DNA duplexes.

- Chapter 5: This chapter focuses on extending the mathematical model developed in Chapter 3 to calculate the mechanical properties of origami systems that have defects, namely "gaps", systematically introduced to modulate their properties. Based on long oxDNA simulations we have calculated the persistence lengths of various gapped 4HB and 10HB systems. The systems have been studied experimentally and provide good validation of our theoretical findings.

- Chapter 6: This was a collaborative study with the Salaita group, Emory, U.S.A, where we use oxDNA to model a force-clamp sensor in which a 16HB DNA origami as a substrate is attached to a thermo-responsive polymer sphere via the molecules whose force response are to be probed, in this case DNA

hairpins. Our simulations probe the force response of these hairpins under different temperature conditions with respect to the shrinkage of the polymer sphere. We also study how both the attachment position of the hairpins to the origami and the introduction of a staple-free region in the 16HB origami alters the behaviour of the force clamp.

- Chapter 7: This chapter provides a short summary of the results that we have obtained in this thesis and of possible future research directions that extend and build on the present work.

I hear and I forget. I see and I remember. I do and I understand.

— Confucius

2 Methods

2.1 oxDNA1

oxDNA [118] is a nucleotide-level coarse-grained model of DNA [104–106], where each nucleotide is a rigid body that has sites representing the backbone and base. The model is based on three interaction sites and six inter-nucleotide interactions. The three interaction sites that lie in a straight line on each nucleotide are namely the backbone site, stacking site and hydrogen-bonding site.

oxDNA interactions can be represented by the following equation;

$$V_{oxDNA1} = \sum_{\langle ij \rangle} \left[V_{\text{backbone}} + V_{\text{stack}} + V_{\text{exc}}^{'} \right] + \sum_{i,j \notin \langle ij \rangle} \left[V_{\text{HB}} + V_{\text{cr.st}} + V_{\text{cx.st}} + V_{\text{exc}} \right]$$

$\langle ij \rangle$ sums over nearest neighbour pairs(adjacent nucleotides on a DNA strand) and $i, j \notin \langle ij \rangle$ sums over all other nucleotide pairs. The various interaction terms are as follows:

- $V_{backbone}$ represents the covalent bonds which hold the nucleotides in a strand

together and has the form of a finitely extensible non-linear elastic spring (termed a FENE potential).

- V_{stack} represents the tendency of the bases to form co-planar stacks. It is a smoothly cut-off Morse potential between base-stacking sites.

- $V_{exc}^{'}$ and V_{exc} represent the excluded volume of the nucleotides, thus preventing the crossing of chains and provides stiffness to unstacked single strands. This interaction uses a cut-and-shifted Lennard-Jones potential to create a soft repulsion.

- V_{HB} represents the hydrogen bonds which are responsible for base pairing. It is a smoothly cut-off Morse potential between hydrogen-bonding sites.

- $V_{cr.st}$ represents cross-stacking interactions between a base in a base pair and nearest-neighbour bases on the opposite strand.

- $V_{cx.st}$ captures the tendency of stacking across nicked backbones. Both $V_{cross-stack}$ and $V_{coaxial-stack}$ are represented via harmonic potentials.

Fig. 2.1 (a) shows the close-up view of a single nucleotide in oxDNA. Fig. 2.1 (b) shows the interactions that have been parameterized to reproduce DNA structure, the thermodynamics of hybridization and the mechanical properties of double- and single-stranded DNA. This oxDNA1 model was used to calculate the detailed free-energy landscape of DNA-tweezers [119] and effect of topology on DNA kissing complexes [120]. oxDNA1 despite a few limitations was able to replicate results for small DNA structures which were in good agreement with experimental data.

2.2 oxDNA2

oxDNA1 had neglected some features which were incorporated in oxDNA2 [106].

- The model did not account for explicit electrostatic interactions. The model was fit to experimental data at $[Na^{+}] = 0.5\,\mathrm{M}$ where electrostatic properties

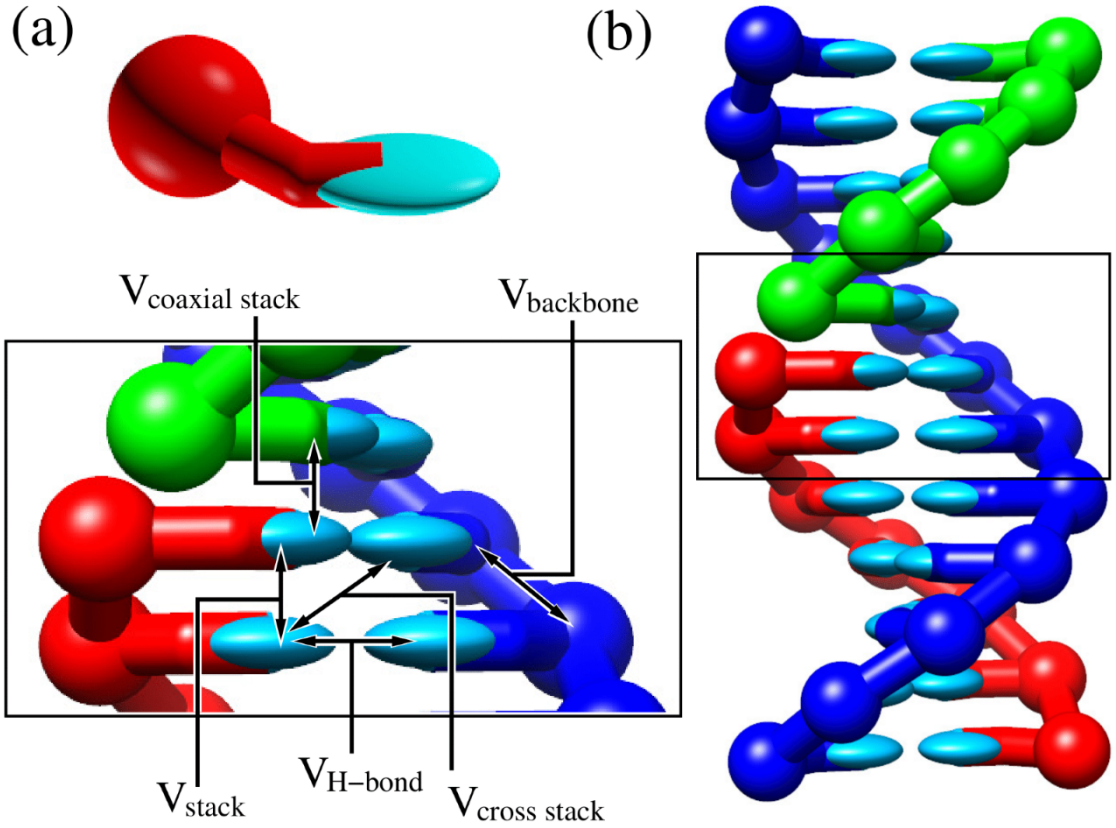


Figure 2.1: (a) oxDNA is a 1BPN CG model. The nucleotide is represented by a backbone(red) and a base(cyan). (b) Shows a 12-bp DNA duplex with major and minor grooves as depicted by oxDNA2. Inset figure shows the various interactions that have been used to parameterize oxDNA. Figure adapted from Ref. [121].

are strongly screened. This limited the use of oxDNA1 to high-salt stable structures only.

- oxDNA1 over-simplified the DNA geometry by adopting a symmetric helix rather than one with major-minor grooving. This is an important feature of DNA that helps with protein binding and origami designs. The lack of this feature made it necessary to bring oxDNA2.

All the above mentioned problems were addressed in oxDNA2 [106] by incorporating major-minor grooving and introducing a Debye-Hückel electrostatic term(V_{DH}^n). The pitch of oxDNA2 is fitted to 10.55 bp/turn which in fact is slightly larger than the experimentally known value of 10.5 bp/turn. Also, the Debye-Hückel electrostatic potential is a monovalent Na^+ effect which works well for salt

concentrations of 0.2M and beyond but fails below 0.2M as the approximations are no longer valid due to increased electrostatic repulsion.

$$V_{oxDNA2} = \sum_{\langle ij \rangle} \left[V^*_{\text{backbone}} + V^*_{\text{stack}} + V^{'}_{\text{exc}} \right] + \sum_{i,j \notin \langle ij \rangle} [V^*_{\text{HB}} + V_{\text{cr.st}} + V^*_{\text{cx.st}} + V_{\text{exc}} + V^n_{\text{DH}}]$$

where V^*_x indicates that the term is either modified for oxDNA2, or, in the case of V^n_{DH} is a new addition in oxDNA2.

The resolution offered by oxDNA2 extended its use to study assembly of small DNA origamis [107, 114] and large nanoprisms [116]. oxDNA helped determine the thermodynamic stability and assembly pathways in DNA-brick self-assembly [122]. Numerous DNA origamis and their assembly systems have been studied using oxDNA [123, 124] making it an apt choice for the work of this thesis.

Also, to lay groundwork for the next chapter, we include a brief summary about the positions and orientations of each nucleotide in the oxDNA simulation code. The positions and orientations of each nucleotide are defined by $\mathbf{r}$ the notional centre of mass of the nucleotide (this is collinear with the hydrogen-bonding and stacking sites), $\widehat{\mathbf{b}}$ the "base" vector (this points from centre of mass towards the base interaction sites), and $\widehat{\mathbf{n}}$ the base normal vector that is perpendicular to the notional plane of the base (Fig. 3.5(a)). These vectors will be used to define the local bend and twist angles for both a DNA duplex and the DNA nanotubes.

2.3 Molecular Dynamics

This N-body simulation technique is used to compute the equilibrium and transport properties of a classical many-body system [125, 126]. It involves numerically solving Newton's equations for each particle, a nucleotide in the case of oxDNA, by integrating them forward in time to generate a trajectory for a model system with N particles. Here, this is typically done until the properties of the system no

longer change with time which technically means to equilibrate the system. Once the system has reached an equilibrium, the required measurements can be made.

To perform a Molecular Dynamics simulation the initial positions $r^N(t=0)$ and momenta $p^N(t=0)$ are assigned to the system. Once the initial system is decided, the forces of interaction between the particles are computed using the derivative of V_{oxDNA2}. oxDNA uses the velocity Verlet algorithm [127] to integrate the equations of motion. The Verlet scheme updates the position as follows:

$$r_i(t+\delta t) = 2r_i(t) - r_i(t-\delta t) + \frac{F_i(t)}{m_i}\delta t^2 + \mathcal{O}(\delta t^4) \tag{2.1}$$

where m_i is the mass of particle, F_i is the instantaneous force experienced by the particle at time t and δt is the MD simulation time-step which should neither be too large (which can lead to instabilities) nor too small (which can lead to excessive compute times).

2.4 Simulation overview

The MD simulations in this thesis have been carried out using the NVT canonical ensemble where the system and a heat bath are coupled using an Andersen-like thermostat [128, 129]. All simulations in chapters 3, 4 and 5 of this thesis have been carried out between 293 K–300 K. As we are interested in the generic properties of DNA nanotubes, we use the sequence-averaged version of the model, where the interaction strengths of the stacking and hydrogen-bond interactions do not depend on the identity of the base. The salt concentration used for all simulations is either 0.5 M or 1 M. At lower salt, dsDNA (and oxDNA [106]) is known to become stiffer. Rarely are experiments on DNA nanostructures performed under low salt as the effects of the increased electrostatic repulsion may alter the stability of DNA origami [74, 130]. The exact temperature and salt conditions will be mentioned in the simulation sections of each chapter.

oxDNA is compatible with CPUs as well as GPUs. GPUs offer a speed-up for systems larger than a few hundred nucleotides [131]. Most of the MD simulations

of large DNA origami nanostructures in this thesis were run on GPUs, with a few exceptions where long waiting times for the GPU resources forced us to take the non-conventional approach of using CPUs for such large systems.

If you think life is bad, you are an optimist. It's gonna get worse.

— Nadrian C Seeman

3

Computing the Elastic Mechanical Properties of Rodlike DNA Nanostructures

3.1 Introduction

DNA nanotechnology exploits the programmability of DNA and its ability to self assemble to make nanoscale structures and devices. This is perhaps most famously achieved through the DNA origami approach, where a long single-stranded scaffold can be folded up into almost any arbitrary shape made up of arrays of double helices by the addition of the appropriate short staple strands [28]. Similar scaffold-free approaches where the size of the object is not constrained by the scaffold length are also available [132–134]. Although a huge variety of structures have been produced by these techniques [135, 136], one of the most common classes of structures have been DNA rods or filaments [137]; these are the subject of this chapter.

Understandably, much of the characterization of DNA origami and other large DNA nano-assemblies initially focused on their structure. Cryo-electron

Reprint(adapted) with permission from [159]. *Copyright ©2020 , American Chemical Society.*

microscopy, for example, has revealed the detailed structure of DNA origami in exquisite detail [138].

Understanding the mechanical properties of DNA origami is also of fundamental interest. How does the coupling of the DNA double-helical elements lead to the net mechanical behaviour of the origami? How can it be tuned or controlled? The answers to these questions build on our fundamental understanding of the mechanics of double-stranded and single-stranded DNA, which has been revealed in detail through single-molecule experiments, for example using optical and magnetic tweezers to pull and twist DNA [139], and further analysed theoretically [140] and in simulations [141, 142].

The most basic mechanical properties of DNA nanostructures that we might wish to understand are their elastic moduli. The quantity that has been most commonly probed in experiments is the bending persistence length of elongated origami, particularly of DNA nanotubes. This has been done for origami that are four-, six-, eight- and ten-helix bundles [47, 143–146], single-stranded-tile nanotubes with from five to ten helices [147] and nanotubes made from double-crossover [148, 149] or other [150] larger tiles, as well as more open wireframe origami [151, 152].

The experimental approaches used include analyses of their molecular contours when adsorbed on surfaces (either through their end-to-end distances [47, 145, 146, 149, 150] or from an analysis of their tangent-tangent correlation function [143, 147]), their cyclization rates [148] and their force response in magnetic tweezers [144]. For example, the values of the persistence length obtained are in the ranges 740 nm–1 μm, 1–3 μm and 3–8.2 μm for four- [144, 146], six- [47, 143–147, 150] and eight-helix [47, 147] bundles, respectively. These values are much larger than those for double-stranded DNA ($\sim$50 nm), and show how the coupling of double-helical elements in a DNA assembly can lead to new mechanical behaviours. Persistence lengths have also been measured for origami connected by linkers of varying stiffness [153]. The magnetic tweezer study was also able to measure the twist modulus of DNA origami, finding values of 390 nm and 530 nm for four- and six-helix bundles,

Reprint(adapted) with permission from [159]. *Copyright ©2020 , American Chemical Society.*

respectively [144]. The moduli associated with radial compression of rod-like origamis have also been probed by atomic-force microscopy [154].

Most explorations of the mechanical limits of DNA origami have focused on the effects of tension typically applied by optical tweezers or an atomic-force microscope [155–158]. These studies have revealed saw-tooth force-extension profiles, where the origamis yield through multiple unravelling events. The buckling of DNA nanotubes under extreme twisting has also been briefly studied [144].

Modelling has the potential to play an important role in better understanding the mechanics of DNA nanostructures.

- Firstly, the experimental measurement of mechanical properties can be challenging, so if modelling can provide a means to accurately estimate such properties, this could be extremely useful—particularly as a means to pre-screen a design for the required mechanical properties, and to explore how those properties can be modulated.

- Secondly, it can enhance our fundamental understanding, particularly as it allows the mechanical and structural responses to stress to be directly related and the relative roles of different factors to be identified. Modelling also allows theories that predict the mechanical properties of DNA nanostructures from duplex properties to be consistently tested.

In this chapter, the focus is on computing the elastic mechanical properties of DNA nanotubes. To do this, one has to decide at what level of description it is most appropriate to model the DNA. Apart from the atomistic approach that we have mentioned in detail previously, the other limit are models that consider DNA helices as simple mechanical elements. Such models have been very successful at providing rapid structural predictions of DNA origami structure, including the effects of internal stresses on structure [82, 93, 160], but their application to study mechanical properties has been more limited [161].

As mentioned before, coarse-grained models at the nucleotide level have a number of attractive features when considering origami mechanics. Here, we use the oxDNA

model as it provides a good description of the elastic properties of double-stranded DNA (dsDNA), including not only the persistence length and torsional modulus [106], but also non-trivial features such as twist-bend coupling [162, 163]. It also captures well the yielding of dsDNA under tension [141] and twist [164].

oxDNA has also been shown to provide a very good structural description of DNA origami [106, 108, 109, 115, 165–167] and other large DNA nanostructures [116, 168, 169]. It has been used to probe the mechanisms of origami failure under tension [158], and even to explain the origins of phase chirality of cholesteric phases of twisted DNA origami rods in terms of the net chirality of their thermal fluctuations [170].

The systems that we consider here focus on those for which there are experimental measurements. As such rod-like origamis are often termed helix bundles we label each system as nHB, where n is the number of helices. Firstly, we consider the 4HB and 6HB origami of Ref. [144] whose mechanical properties were probed by magnetic tweezers (MT). Secondly, we consider the set of four 6HB origamis whose liquid-crystalline properties were experimentally studied in Ref. [171] and analysed by simulation and theory in Ref. [170]. These are labelled by their designed global axial twist (2×LH,1×LH,1×RH) or lack thereof (S: straight, i.e. untwisted). The persistence length of 6HB-S was measured in Ref. [47]. We also consider a 10HB that was also studied in Ref. [171]. Finally, we consider 6HB and 8HB systems made from single-stranded tiles (SST) whose mechanical properties were studied in Ref. [147], plus an additional equivalent 4HB example.

3.2 Methods

3.2.1 DNA nanotubes

We study the mechanical properties of ten different elongated DNA nanostructures that have been studied experimentally in three separate papers [144, 147, 171], focussing mainly on systems where some mechanical properties have been experimentally estimated. Seven of these are DNA origamis. The scaffold strands in origami typically derive from the genome of an M13 virus, which is just over

Reprint(adapted) with permission from [159]. *Copyright ©2020 , American Chemical Society.*

7000 nucleotides long. The remaining three DNA nanostructures are structurally very similar, but are made up of just a small number of short DNA strands (or single-stranded tiles [132]) with a repeating motif along the length of the tube.

All the structures are helix bundles, i.e. they are made up of parallel arrays of double helices. The points at which strands pass between helices are termed crossovers or junctions. In the DNA origamis these are typically "double" crossovers where two strands pass between the helices at the junctions, and the ends of the staple strands occur between junctions. By contrast, in the SST nanotubes, the junctions are all "single" crossovers as the ends of the strands are located at the junctions (Fig. 3.1(a)).

Non-planar DNA origami designs are typically based on either a hexagonal or square lattice of DNA helices, where crossovers occur between adjacent helices of the lattice, and the spacings between junctions are chosen to best match the pitch of DNA (e.g. the junctions are separated by seven base pairs in the hexagonal lattice giving an angle of exactly $4\pi/3$ between consecutive junctions if the pitch of DNA is 10.5 base pairs per turn). The six-helix bundles origamis are based on the hexagonal lattice, and the four-helix bundles on the square lattice.

For the SST nanotubes, junctions are alternatively spaced 10 and then 11 base pairs apart. For a flat sheet with this design, one might expect that they would be flat and untwisted, as the average crossover spacing matches the DNA pitch. However, as adjacent crossovers involve opposing strands, the groove structure of DNA origami also needs to be considered, and it has been suggested that this leads to a natural curvature [132]. Even with this curvature, rolling up the sheets into tubes will likely introduce stress into the tubes, as the interhelix angles will no longer match their relaxed angles. We choose to study the tube isomer consistent with the presumed natural curvature, where the major groove is on the outside of the tube at the junctions.

The 10HB origami is the only system considered that is not a tube. Instead, it has a double hexagon cross-section (Fig. 3.5(c)). The anisotropy of the cross-section is expected to lead to substantial differences in the two bending moduli. The

Reprint(adapted) with permission from [159]. *Copyright ©2020 , American Chemical Society.*

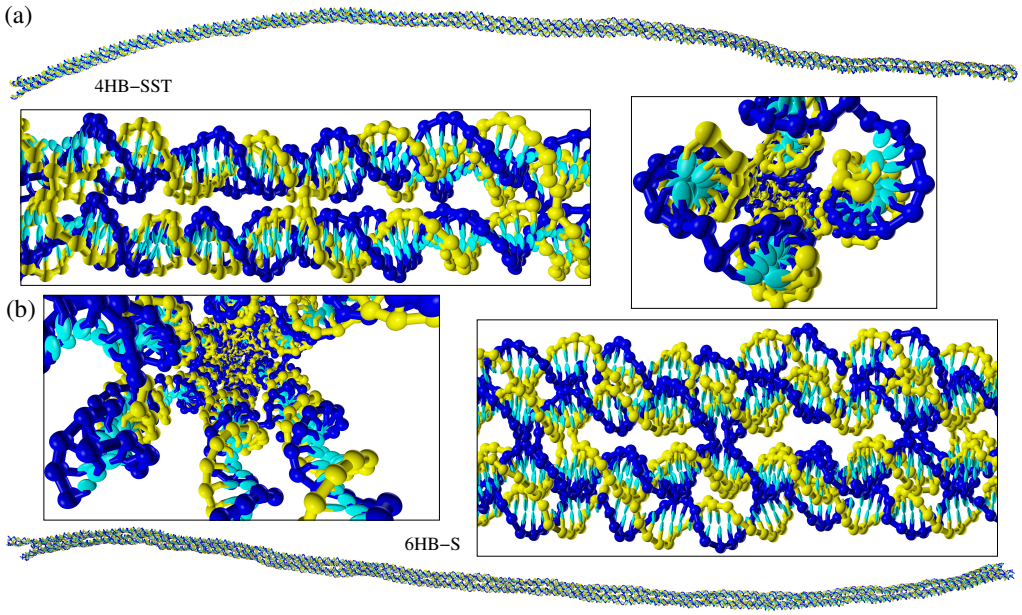


Figure 3.1: Snapshots of two of the DNA nanostructures (a) 4HB-SST; (b) 6HB-S, including close-ups from the ends and the side.

4HB-MT and 6HB-MT origami are also slightly different from the rest in that they have wider blocks at each end of the origami (Fig. 3.2) to facilitate attachment to the beads in the magnetic tweezer experiments that were performed on them.

Snapshots of example origami and SST nanotubes are given in Fig. 3.1. These illustrate the typical scale of the bending fluctuations in these systems. The differences in the nature of the junctions for these two types of system should also be evident from the close ups. The snapshots of some of the remaining systems are given in Figs. 3.2–3.4. Some snapshots of the twisted origami nanotubes can also be found in Ref. [170]. The snapshots give an impression of the scale of typical bending fluctuations. Apparent from the end views of 6HB-SST and 8HB-SST is the departure of their cross-sections from a regular hexagonal and octagonal form, respectively, due to the alternating inter-helix angles in these systems, an effect noted for 4HB-SST in chapter 3.

3.2.2 Simulations

Simulations for origamis studied in this chapter were run at a temperature of 20 or 23°C at $[Na^+]$=0.5 M, which in oxDNA gives similar behaviour to the high-

Reprint(adapted) with permission from [159]. *Copyright ©2020 , American Chemical Society.*

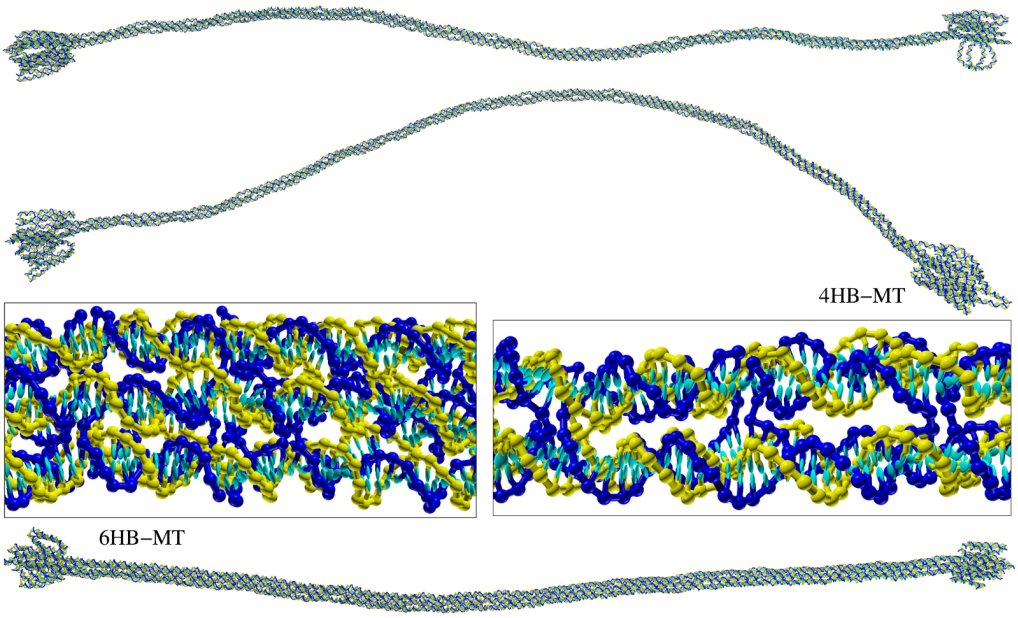


Figure 3.2: Snapshots of the 4HB-MT and 6HB-MT origami. The second image of the 4HB-MT origami shows an exceptionally bent configuration. The blocks at each end of the origamis are to facilitate attachment to the beads in magnetic tweezer experiments.

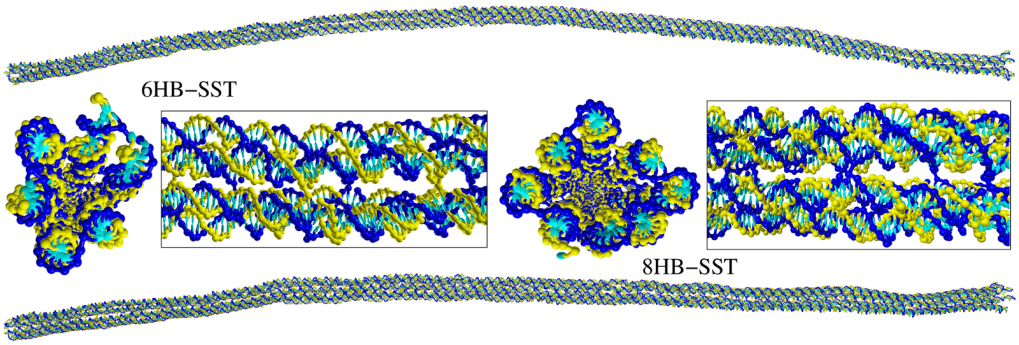


Figure 3.3: Snapshots of the 6HB-SST and 8HB-SST nanotubes. The end views clearly show the alternating distances of the helices from the centres of the tubes.

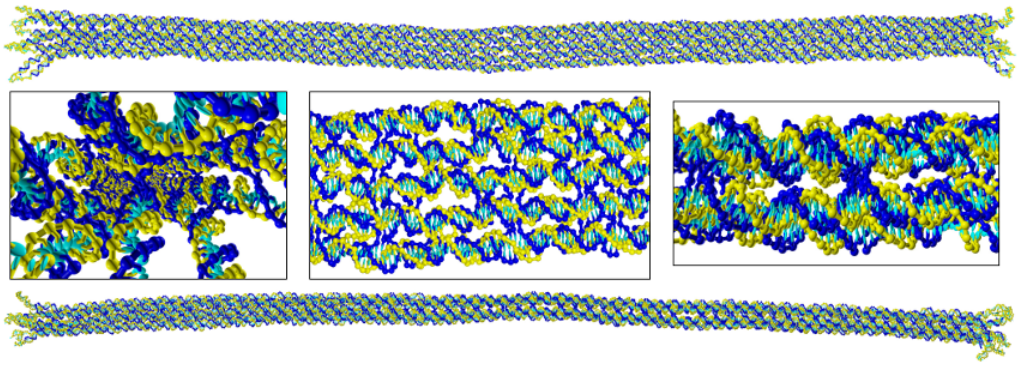


Figure 3.4: Snapshots of the 10HB origami. The two side views are roughly perpendicular to their thick and thin dimensions. Note this is not perfectly maintained because of the slight right-handed twist of the origami.

magnesium conditions typically used in origami assembly. As the Debye-screening length is very short-ranged at this concentration we do not expect the mechanical properties of the DNA nanotubes to be particularly sensitive to the salt concentration in this regime. To generate an equilibrium ensemble that samples the large length-scale bending fluctuations well requires very long simulations (the total length of the simulations for each system are between 3 and 18 ms (Table A.1)). We monitor the sampling by following the distance between points near the opposite ends of the nanotubes as a function of time (see Fig. A.1 for examples).

The fastest equilibration occurs for the SST nanotubes. The reason for the somewhat slower dynamics for the origamis is not obvious. The main structural difference in the origamis is that the junctions involve mainly double rather than single crossovers, and so there may be some coupling of bending to different internal geometric states of these junctions that leads to the slower dynamics of the bending fluctuations. The slowest dynamics are for the 4HB-MT and 6HB-MT origamis where the blocks at the end of the origami perhaps slow down the diffusive dynamics of the long length-scale fluctuations. Consequently, these two systems have the worst statistics, which in turn impacts the precision of the computed elastic properties. Further details of the simulations are given in the appendix (Section A.1). It should be noted that 1 time step in oxDNA corresponds to 3.03 ps, hence very long simulations in oxDNA correspond to very small time scales for real systems.

3.2.3 Elastic model

The conformation of a stiff polymer can be described by an orthonormal reference frame $\{\widehat{\mathbf{e}}_1(s), \widehat{\mathbf{e}}_2(s), \widehat{\mathbf{e}}_3(s)\}$ as a function of the arc length s along the molecular contour, where $\widehat{\mathbf{e}}_3(s)$ is tangential to the contour. Fig. 3.5 (b) shows the orthonormal reference frame for a basepair in duplex DNA while Fig. 3.5(c) is a diagrammatic representation of $\widehat{\mathbf{e}}_1(s)$ and $\widehat{\mathbf{e}}_2(s)$ for 4HB, 6HB, 8HB and 10HB. For a DNA duplex or nanotube it is natural to discretize a configuration into steps along the contour. For the duplex a natural step is between consecutive base pairs. Similarly, the nanotubes considered here can be divided up into well-defined "slices" transverse

Reprint(adapted) with permission from [159]. *Copyright ©2020 , American Chemical Society.*

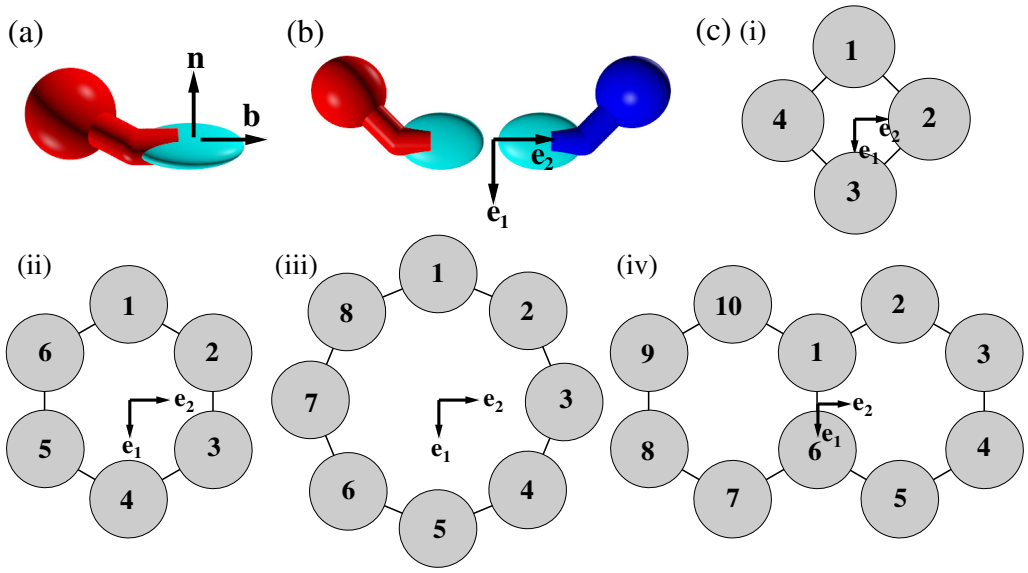


Figure 3.5: (a) An oxDNA nucleotide along with the "base" and "normal" vectors used to define its orientation. (b) An oxDNA base pair illustrating the directions of $\hat{\mathbf{e}}_1$ and $\hat{\mathbf{e}}_2$. (c) Schematics of the cross-sections of the different types of DNA nanostructures considered showing $\hat{\mathbf{e}}_1$ and $\hat{\mathbf{e}}_2$. In (b) and (c) $\hat{\mathbf{e}}_3$ is directed out of the plane of the paper.

to the contour, where each helix of the bundle has a base pair in each slice, and a step corresponds to moving one base pair along each helix. The junctions that interconnect the helices maintain the registry between the base pairs in each slice. Note that, unlike for the duplex, the slices are not all strictly equivalent because of their different positions relative to the junctions.

A rotation vector $\boldsymbol{\Theta}^{(n)}$ can be defined that represents the rotation of the triad $\{\hat{\mathbf{e}}_1(n), \hat{\mathbf{e}}_2(n), \hat{\mathbf{e}}_3(n)\}$ onto the adjacent triad $\{\hat{\mathbf{e}}_1(n+1), \hat{\mathbf{e}}_2(n+1), \hat{\mathbf{e}}_3(n+1)\}$ [163]. The components Θ_1 and Θ_2 represent local bending, whereas Θ_3 is a twist angle about the system axis. If the system is on average straight then one would expect $\langle\Theta_1\rangle = \langle\Theta_2\rangle = 0$. If we define $\Omega_i = (\Theta_i - \langle\Theta_i\rangle)/a$, where a is the average separation of successive steps, then the harmonic form of the energy due to angular deformations is

$$\beta E = \frac{a}{2} \sum_{n=1}^{N} \sum_{\mu,\nu=1}^{3} \Omega_\mu^{(n)} M_{\mu\nu} \Omega_\nu^{(n)}. \tag{3.1}$$

These are the dominant terms at small angular deviations, but higher-order terms may be relevant for larger deformations. Note this form also neglects the potential coupling of angular deformations to other deformation modes, such as

stretch and shear.

If there are no couplings between the different angular degrees of freedom, then

$$\mathbf{M} = \begin{pmatrix} A_1 & 0 & 0 \\ 0 & A_2 & 0 \\ 0 & 0 & C \end{pmatrix}, \tag{3.2}$$

as would be the case if Ω_1 and $-\Omega_1$, and Ω_2 and $-\Omega_2$ were equivalent by symmetry. However, in the general case

$$\mathbf{M} = \begin{pmatrix} A_1 & A_{12} & G_1 \\ A_{12} & A_2 & G_2 \\ G_1 & G_2 & C \end{pmatrix}. \tag{3.3}$$

For duplex DNA, if Ω_2 describes bending deformations into the grooves of the helix, there is a symmetry with respect to the bending deformation Ω_1 that implies $A_{12} = G_1 = 0$, and G_2, the twist-bend coupling constant, is the only non-zero off-diagonal element of $\mathbf{M}$ [162, 172].

For all the origamis we consider, the designs are based either on a hexagonal lattice (6HB) or square lattice (4HB). For a perfectly regular pattern of junctions and staple ends the highest possible C_n axis for these two lattices would be C_3 or C_2, respectively. However, if the helix bundles were infinite in length, and ignoring strand ends (the scaffold runs antiparallel in adjacent helices), the tubes could also possess six-fold and four-fold screw axes, respectively. Therefore, the 4HB and 6HB systems have approximate four-fold and six-fold symmetry. The presence of 2-fold axial symmetry implies that $A_{12} = G_1 = G_2 = 0$, and 3-fold or higher rotational symmetry also implies that $A_1 = A_2$. That the elastic constants do not fully obey the above is likely due to the breaking of the symmetry due to the irregular placement of junctions and strand ends.

By contrast, adjacent helices in the SST nanotubes are not equivalent, because the alternating 10 and 11-base-pair spacing between junctions breaks the potential screw symmetry that applies to the origamis. The 4HB-, 6HB- and 8HB-SST

nanotubes thus have 2-fold, 3-fold and 4-fold symmetry, respectively. (Note that, unlike the origamis, these systems have a perfectly regular pattern of junctions.) The alternating junction spacing also causes the inter-helix angles to alternate [132], and so the cross-sections of the tubes are not expected to be on average regular polygons. Therefore, A_1 and A_2 are expected to be different for the 4HB system, but identical for the larger tubes, whereas one would expect $A_{12} = G_1 = G_2 = 0$ for all SST systems.

3.2.4 Persistence lengths and elastic moduli

If a system behaves like an ideal worm-like chain, one expects

$$\langle \widehat{\mathbf{e}}_3(n) \cdot \widehat{\mathbf{e}}_3(n+m) \rangle = \langle \cos\theta(m) \rangle = e^{-ma/l_b}, \tag{3.4}$$

where l_b is the bending persistence length, a is the contour length associated with a step and the averaging is performed over both different origins n and different configurations. Rearranging allows an m-dependent persistence length to be defined:

$$l_b(m) = -\frac{ma}{\log\langle \cos\theta(m) \rangle}. \tag{3.5}$$

Note that, as the number of possible origins is fewer for larger m, and the longest length scale fluctuations will be least well sampled in the simulations, the statistical errors are expected to increase with m. Similarly, one can define a twist persistence length in terms of the decay of the cumulative twist angle deviation

$$l_t(m) = -\frac{ma}{\log\langle \cos\left(\sum_{k=n}^{n+m-1} a\Omega_3^{(k)}\right) \rangle}. \tag{3.6}$$

To compute the elastic constant matrix $\mathbf{M}$ we use the same approach as was used for DNA duplexes in Ref. [163]. Namely, we first calculate the correlation matrix $\boldsymbol{\Xi}$ which is defined below

$$\Xi_{\mu\nu}(m) = \left\langle \left[\sum_{k=n}^{n+m-1} \Omega_\mu^{(k)} \right] \left[\sum_{l=n}^{n+m-1} \Omega_\nu^{(l)} \right] \right\rangle. \tag{3.7}$$

Reprint(adapted) with permission from [159]. *Copyright ©2020 , American Chemical Society.*

Inversion of $\boldsymbol{\Xi}$ leads to the elastic constant matrix:

$$\mathbf{M}(m) = \frac{m}{a} \left[\boldsymbol{\Xi}(m)\right]^{-1}. \tag{3.8}$$

The use of cumulative angular deformations in Eq. 3.7 is discussed further in Ref. [173].

Note that the local form of the elastic energy in Eq. 3.1 would imply that the persistence lengths and elastic moduli are independent of m. In practice, however, there are longer-range effective couplings that lead to a variation with m, where convergence to a constant value only emerges at larger m, as has previously been observed for the DNA duplex [163]. Here, we are most interested in this asymptotic behaviour, as it describes the long length-scale bending and twisting fluctuations.

Another implication of Eq. 3.1 is that the probability distributions for Ω_i would be expected to be Gaussian. These distributions are illustrated in Figs. A.2(a)-A.4(a) for the 4HB-MT, 6HB-MT and 6HB-SST systems. For the 6HB-SST nanotube, the Ω_i distributions show some deviations from Gaussianity with large angular deformations being somewhat more likely than would be expected. By contrast, the two origami have much more significant deviations in the tails of these distributions, with the 6HB-MT origami showing clear sub-peaks in the distributions for the bending deformations. It might be that these more extreme local fluctuations are related to the slower dynamics of the origamis which were previously noted in Section 3.2.2. Figs. A.2-A.4 also show the distributions for the cumulative angular deformations used in Eq. 3.7 for different values of m. As expected [174], these distributions converge to a Gaussian form as m increases, with this convergence occurring more rapidly for the 6HB-SST nanotube. Thus, although there are deviations from worm-like chain behaviour at the level of a single step, on longer renormalised length scales worm-like chain statistics apply.

When applying the above formulae to a DNA duplex or the DNA nanotubes, we choose to not include a certain number of base pairs or tube slices at either end, as the ends will typically be somewhat more flexible. In the nanotubes, this general

effect is exacerbated by the significant structural differences at the ends. The helices splay out much more at the ends due to the lack of constraining junctions, as is evident from the snapshots in Fig. 3.1. The number of tube slices at each end that are ignored is given in Table A.1 for each system.

3.2.5 Triad definitions

In Ref. [163] a number of different triads were considered when analysing the elastic properties of the DNA duplex. Here, we recap the definitions for their "Triad III", as this approach will be most naturally adapted to the DNA nanotubes. In this triad, the positions of the centres of mass of the base pairs are used to define the vector $\widehat{\mathbf{e}}_3$. Namely,

$$\widehat{\mathbf{e}}_3(i) = \frac{\mathbf{R}_{\text{duplex}}(i+1) - \mathbf{R}_{\text{duplex}}(i-1)}{||\mathbf{R}_{\text{duplex}}(i+1) - \mathbf{R}_{\text{duplex}}(i-1)||} \tag{3.9}$$

where $\mathbf{R}_{\text{duplex}}$ is given by:

$$\mathbf{R}_{\text{duplex}} = \frac{\mathbf{r}_{\text{nuc1}} + \mathbf{r}_{\text{nuc2}}}{2}. \tag{3.10}$$

The vector between the centres of mass of the nucleotides in the base pair is used to define $\widehat{\mathbf{y}}$

$$\widehat{\mathbf{y}} = \frac{\mathbf{r}_{\text{nuc1}} - \mathbf{r}_{\text{nuc2}}}{||\mathbf{r}_{\text{nuc1}} - \mathbf{r}_{\text{nuc2}}||} \tag{3.11}$$

whose orthonormalization with respect to $\widehat{\mathbf{e}}_3$ leads to $\widehat{\mathbf{e}}_2$:

$$\widehat{\mathbf{e}}_2 = \frac{\widehat{\mathbf{y}} - (\widehat{\mathbf{y}} \cdot \widehat{\mathbf{e}}_3)\,\widehat{\mathbf{e}}_3}{||\widehat{\mathbf{y}} - (\widehat{\mathbf{y}} \cdot \widehat{\mathbf{e}}_3)\,\widehat{\mathbf{e}}_3||} \tag{3.12}$$

Finally, $\widehat{\mathbf{e}}_1$ follows from the cross product:

$$\widehat{\mathbf{e}}_1 = \widehat{\mathbf{e}}_2 \times \widehat{\mathbf{e}}_3. \tag{3.13}$$

Reprint(adapted) with permission from [159]. *Copyright ©2020 , American Chemical Society.*

The results for $l_b(m)$ using this triad show an oscillation on the length scale of the pitch length of DNA that dies away at large m (Fig. 3.6(a)). Also, $\langle\Theta_2\rangle$ was found to have a non-zero value (Fig. 3.6(b)) [163]. The reason is that $\mathbf{R}_{\text{duplex}}$ does not exactly lie at the centre of the DNA double helix, but is slightly displaced towards the minor groove. Thus, the line of base-pair centres will be helical, and the correlations in $\widehat{\mathbf{e}}_3$ will be strongest for an integer multiple of the pitch length. Similarly, the helicity measure introduced in Ref. [170] when applied to the contour defined by $\mathbf{R}_{\text{duplex}}$ shows a sharp peak at the reciprocal of the pitch length (Fig. 3.6(c)). (Note, the helicity measure has magnitude one for a perfect helix, and positive/negative values correspond to right-handed/left-handed helicity, respectively.)

Although the above oscillation is not problematic for computing l_b for duplex DNA as the oscillation dies away and the bulk limit is reached on reasonable length scales, when performing a similar analysis for the DNA nanotubes, the issue is much more troublesome. If we define, the centre of the DNA nanotube as the average over the centres of mass of the duplexes in a given slice:

$$\mathbf{R}_{\text{tube}} = \frac{1}{N_{\text{helix}}} \sum_{j=1}^{N_{\text{helix}}} \mathbf{R}_{\text{duplex},j} \tag{3.14}$$

and $\widehat{\mathbf{e}}_3(i)$ in an analogous manner to the duplex

$$\widehat{\mathbf{e}}_3(i) = \widehat{\mathbf{z}}(i) = \frac{\mathbf{R}_{\text{tube}}(i+1) - \mathbf{R}_{\text{tube}}(i-1)}{||\mathbf{R}_{\text{tube}}(i+1) - \mathbf{R}_{\text{tube}}(i-1)||} \tag{3.15}$$

the persistence length can be calculated using Eq. 3.5, as illustrated for one of the origami six-helix bundles in Fig. 3.6(d). The magnitude of the oscillation on the pitch length is much stronger and persists over the whole range of m that can be sampled. This is for two reasons.

- Firstly, the helices in the nanotubes are held in registry by the four-way junctions present in the origamis, and so the helical paths of the centrelines of the individual helices in the nanotubes add up coherently.

- Secondly, the helix bundles are much stiffer than a DNA duplex and so the variations in the tangent-tangent correlation function due to the helicity of the centerline both make a much more significant contribution and do not significantly die away because the persistence length of the tubes is much longer than the contour length of the nanotubes.

Unlike for duplex DNA, a similar oscillation is also seen in the bending elastic constants calculated using Eq. 3.8 (Fig. A.5). Interestingly, for the SST nanotubes no pitch-length oscillation is observed, presumably because the single-crossover junctions place fewer constraints on the relative orientations of adjacent helices, leading to a loss of coherence between the twist of the individual helices (Fig. A.5(b)).

In Ref. [175], an approach to correct for the helicity of the duplex contour was introduced that involved transforming from the helical frame of reference to a non-helical one; this transformation led to a small correction to the elastic moduli. Here, we explore an alternative approach that will be more convenient for the DNA nanotubes and instead uses a new definition of the duplex centre $\mathbf{R}_{\text{duplex}}$ that attempts to remove the helicity by adding a small offset in the direction of the major groove. Namely,

$$\mathbf{R}_{\text{duplex}}(\alpha) = \frac{\mathbf{r}_{\text{nuc1}} + \mathbf{r}_{\text{nuc2}}}{2} + \frac{\alpha}{2}\left(\widehat{\mathbf{b}}_{\text{nuc1}} \times \widehat{\mathbf{n}}_{\text{nuc1}} + \widehat{\mathbf{b}}_{\text{nuc2}} \times \widehat{\mathbf{n}}_{\text{nuc2}}\right) \tag{3.16}$$

where for $\alpha = 0$ the original definition of Eq. 3.10 is recovered.

Using this new definition of $\mathbf{R}_{\text{duplex}}(\alpha)$ in Eq. 3.9, the oscillation in $l_b(m)$ is reduced as α is increased until the oscillation disappears at $\alpha = 0.06$ (Fig. 3.6(a)). α has units of length (simulation units), where $\alpha = 0.06$ corresponds to 0.051 nm. Similarly, if we examine $\langle\Theta_2(\alpha)\rangle$, it passes through zero at $\alpha = 0.06$ (Fig. 3.6(b)). Furthermore, the peak in the helicity measure at the reciprocal of the pitch length disappears for $\alpha = 0.06$ (Fig. 3.6(c)). Although the value of α does not affect the limiting value of the bending persistence length for the duplex, it does lead to small changes in the elastic constants, as was also found when

Reprint(adapted) with permission from [159]. *Copyright ©2020 , American Chemical Society.*

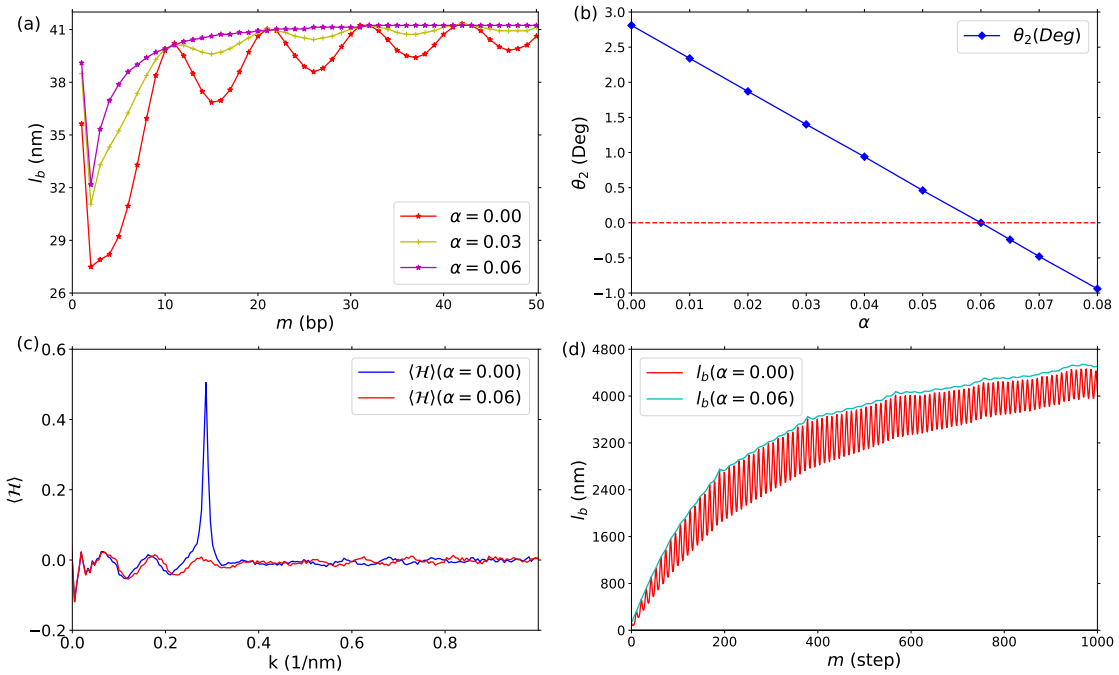


Figure 3.6: $l_b(m)$ for (a) dsDNA and (d) the 6HB-S origami at different values of α, as labelled. (b) $\langle\Theta_2\rangle$ for dsDNA as a function of α. (c) Helicity measure for the dsDNA centerline as a function of inverse wavelength at $\alpha = 0$ and 0.06. The peak in the $\alpha = 0$ curve occurs at the inverse of the DNA pitch length, i.e. $1/(10.5 \times 0.34\,\text{nm})$.

switching to a non-helical frame of reference [175]. The variation of the duplex elastic constants with α is shown in Fig. A.6.

Applying the new definition of the duplex centre with $\alpha = 0.06$ to the origami nanotubes leads to the removal of the oscillations in $l_b(m)$ (Fig. 3.6(d)). Note that the $\alpha = 0.06$ line for $l_b(m)$ is an upper envelope function to the curves for other values of α, because the helicity of the centerline leads to a periodic loss in correlations that is not representative of the true stiffness of the system. For all further results we will use $\alpha = 0.06$.

Now having a non-helical definition of the tube centre, we consider our definitions of $\hat{\mathbf{e}}_1$ and $\hat{\mathbf{e}}_2$. Following the recipe of Triad III for the duplex, we could define $\hat{\mathbf{y}}$ for a six-helix bundle as

$$\hat{\mathbf{y}} = \frac{\mathbf{R}_{\text{duplex},2} + \mathbf{R}_{\text{duplex},3} - \mathbf{R}_{\text{duplex},5} - \mathbf{R}_{\text{duplex},6}}{||\mathbf{R}_{\text{duplex},2} + \mathbf{R}_{\text{duplex},3} - \mathbf{R}_{\text{duplex},5} - \mathbf{R}_{\text{duplex},6}||} \tag{3.17}$$

and then use Equations 3.12 and 3.13 to obtain $\hat{\mathbf{e}}_1$ and $\hat{\mathbf{e}}_2$. However, when we

Reprint(adapted) with permission from [159]. *Copyright ©2020 , American Chemical Society.*

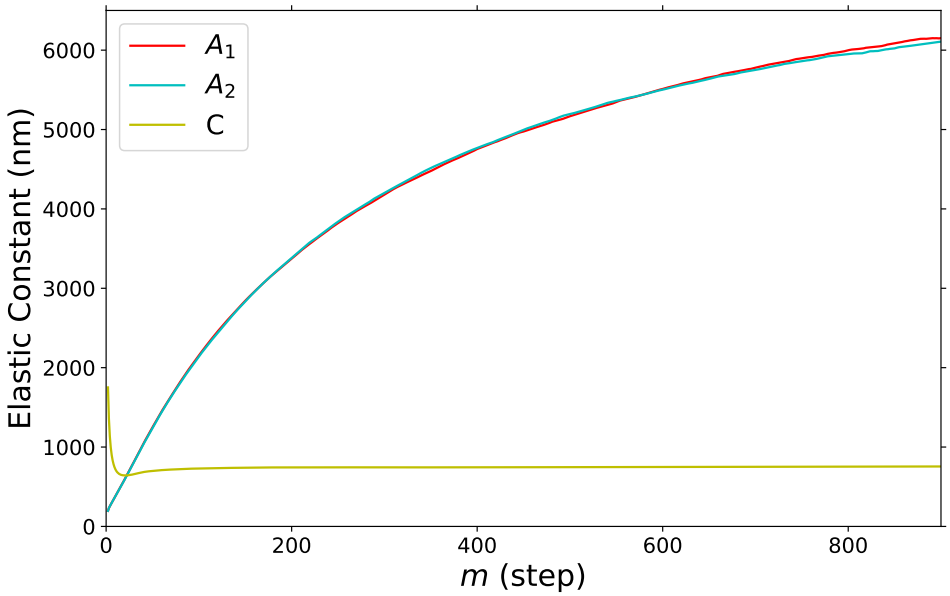


Figure 3.7: Elastic moduli for 6HB-SST using singular value decomposition. $\alpha = 0.06$.

did so for the 6HB-SST system we found that $A_1 > A_2$ (Fig. A.7(a)) in contrast to our expectations based on the symmetry of the system. We suspected this may be because of the "inequitable" treatment of the three directions in the orthogonalization scheme.

As a test we therefore defined

$$\hat{\mathbf{x}} = \frac{\mathbf{R}_{\text{duplex},4} - \mathbf{R}_{\text{duplex},1}}{||\mathbf{R}_{\text{duplex},4} - \mathbf{R}_{\text{duplex},1}||}, \tag{3.18}$$

obtained $\hat{\mathbf{e}}_1$ by orthogonalization of $\hat{\mathbf{x}}$ to $\hat{\mathbf{e}}_3$, and $\hat{\mathbf{e}}_2$ by the vector product of $\hat{\mathbf{e}}_3$ and $\hat{\mathbf{e}}_1$. With this scheme the order of the bending moduli was reversed with $A_2 > A_1$ (Fig. A.7(b)), showing this not to be a property of the tube but a reflection of the order in which we performed the orthogonalization.

Therefore, we instead explored using singular value decomposition to find the orthogonal set $\{\hat{\mathbf{e}}_1, \hat{\mathbf{e}}_2, \hat{\mathbf{e}}_3\}$ that are closest to the set of vectors $\{\hat{\mathbf{x}}, \hat{\mathbf{y}}, \hat{\mathbf{z}}\}$ [176]. As one can see from Fig. 3.7, for the 6HB-SST system, within the statistical errors, there is now essentially no difference between A_1 and A_2, in line with our expectations based on the symmetry of these nanotubes. For the 8HB-SST, this is also true (Fig. A.21(c)). Note that for the origamis, the non-regular pattern of junctions

is one factor that can somewhat break this potential symmetry. For all further results we use the singular value decomposition approach.

The definitions of $\hat{\mathbf{x}}$ and $\hat{\mathbf{y}}$ for the other systems are given in the Supporting Information (Section A.2.3) and illustrated on the tube cross-sections in Fig. 3.5(d). All the definitions that we have introduced are designed for DNA that adopts a base-paired double-helical configuration. However, for structures as large as DNA origamis, there will always be some designed base-pairs that are not intact due to thermal fluctuations. These broken base pairs are most likely to be at nicks and junctions. When such "fraying" occurs, it is likely to lead to anomalous values for the angular deviations Ω_i. However, we do not attempt to treat such cases differently or exclude them from our averaging, because both fraying is a natural part of the dynamics of the systems and the number of broken base pairs is likely to be a very small fraction of the total number of base pairs.

3.2.6 Extracting limiting values

The m-dependent definitions of the persistence lengths (Eqs. 3.5 and 3.6) and elastic moduli (Eq. 3.8) both for the duplexes and the nanotubes show a similar behaviour rising up towards a limiting value at large m (Fig. 3.6(d) and 3.7). However, unlike for the duplex, we cannot simply obtain the bulk values of the bending persistence length and the bend elastic moduli from their values at the largest m value that we sample, because the bending persistence lengths of the nanotubes are much larger than their lengths, and so have not yet converged to their limiting values.

The reason for this strong m-dependence is that the local fluctuations in the angles Θ_1 and Θ_2 are greater than would be expected from the bending of the nanotube contour on long length scales. This effect can be seen in Fig. 3.8, which depicts the tangent-tangent correlation function. The behaviour is not perfectly exponential, as would be the case for an ideal worm-like chain (Eq. 3.4), but shows an initial more rapid decay, which for the duplex is only a few base pairs but for the example nanotube is on the order of twenty-five slices. While for the duplex all base pairs are equivalent, all slices of a nanotube are not equivalent because of

Reprint(adapted) with permission from [159]. *Copyright ©2020 , American Chemical Society.*

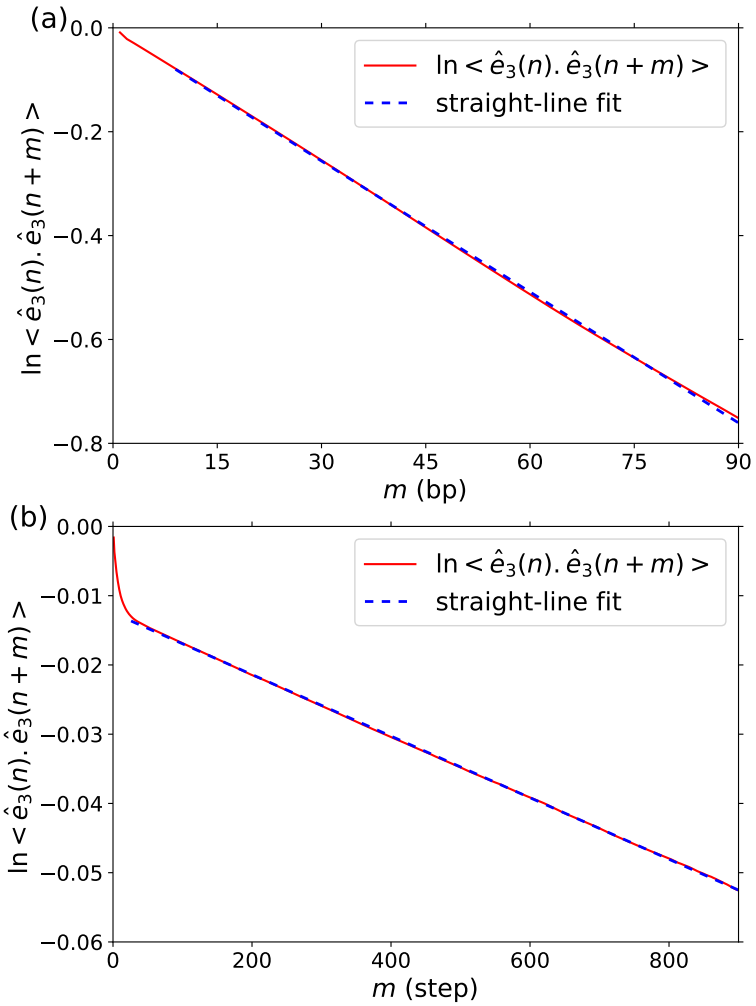


Figure 3.8: $\log\langle\cos\theta(m)\rangle$ versus m for (a) duplex and (b) 6HB-SST along with fit lines to the exponential tail.

their different positions with respect to the junctions. This provides an additional source of heterogeneity that we average over in our analysis. For example, it is well known that the adjacent helices in an origami splay apart slightly as one moves away from the junctions [28, 109, 177] (Fig. 3.1) leading to a local bending of the helices that is not representative of their longer-length-scale behaviour.

Fig. 3.8 suggests a simple way to extract the bulk persistence length. As beyond the transient behaviour at small m the correlation function shows a near perfectly exponential tail, l_b can be extracted from the limiting slope of the graph. The same approach is used to calculate l_t (Fig. A.8).

Extracting bulk bending elastic moduli is more difficult. That the fluctuations of

Θ_1 and Θ_2 are not fully representative of the bending behaviour at long length scales implies that there are correlations beyond a single step. These can be quantified by the following correlation coefficients:

$$\Lambda_{\mu\nu}^{(n)} = \left\langle \Omega_{\mu}^{(i)} \Omega_{\nu}^{(i+n)} \right\rangle . \tag{3.19}$$

In Ref. [173], it has been shown that the matrix $\mathbf{\Xi}(m)$ can be constructed from these correlation coefficients, as follows.

$$\Xi_{\mu\nu}(m) = m\Lambda_{\mu\nu}^{(0)} + \sum_{n=1}^{m-1} (m-n) \left(\Lambda_{\mu\nu}^{(n)} + \Lambda_{\nu\mu}^{(n)} \right) . \tag{3.20}$$

In Fig. A.9 we show that the elastic constants obtained from the above formula reproduce well the elastic constants obtained from Eq. 3.7 for 6HB-SST. However, when we use this approach to extrapolate to larger m, the behaviour becomes less sensible, and so does not provide a method to estimate the bulk elastic constants. The issue is that the weighting of the longer-range (i.e. larger n) correlation coefficients in Eq. 3.20 becomes more significant at large m, and although these coefficients might be expected to converge to zero as n increases, in practice the statistical noise in their values leads to somewhat random behaviour in the predicted elastic constants when extrapolating beyond the length of the nanotubes.

Therefore, we have explored an alternative approach in which we perform averaging over longer length scales to reduce the enhanced local fluctuations that are at the root of the issue, and hence to expedite convergence of the elastic moduli to their bulk limit. This idea is similar to using a renormalized length scale; as we noted in Section 3.2.4 the cumulative angular deformations exhibit behaviour increasingly consistent with worm-like chain statistics as m increases. We do this averaging by defining our local axes at each slice to be an average of the current slice and n_{avg} slices on either side, i.e.

$$\widehat{\mathbf{x}}'(i) = \frac{\sum_{j=i-n_{\text{avg}}}^{j=i+n_{\text{avg}}} \widehat{\mathbf{x}}(j)}{\left|\left| \sum_{j=i-n_{\text{avg}}}^{j=i+n_{\text{avg}}} \widehat{\mathbf{x}}(j) \right|\right|} \tag{3.21}$$

Reprint(adapted) with permission from [159]. *Copyright ©2020 , American Chemical Society.*

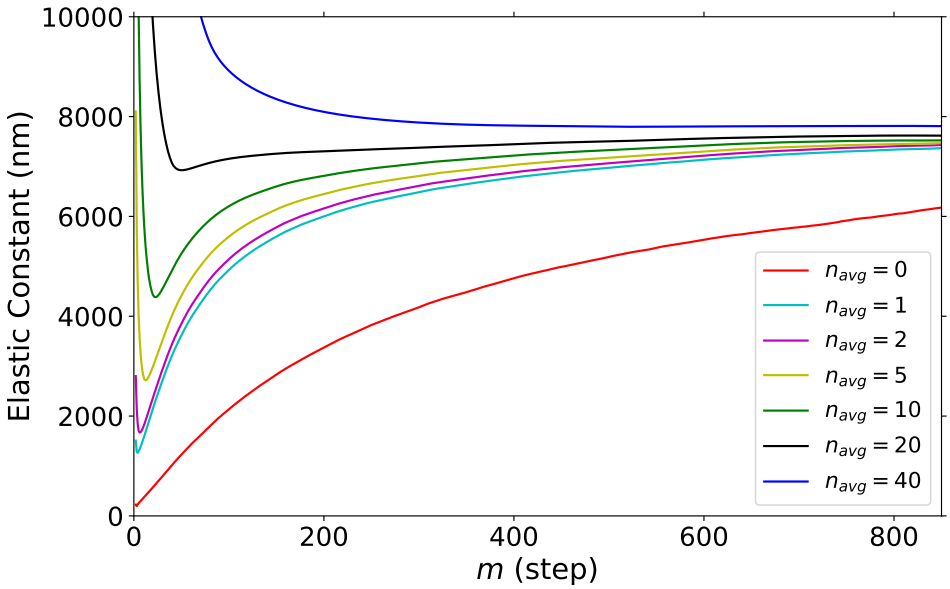


Figure 3.9: The effect of averaging on A_1 for different n_{avg} for the 6HB-SST nanotube.

and equivalently for $\hat{\mathbf{y}}'$ and $\hat{\mathbf{z}}'$. As before we then use singular value decomposition to find the $\hat{\mathbf{e}}_i$ vectors from the triad $\{\hat{\mathbf{x}}', \hat{\mathbf{y}}', \hat{\mathbf{z}}'\}$.

Fig. 3.9 illustrates the behaviour of the elastic constant A_1 for the 6HB-SST system for different values of n_{avg}. As n_{avg} increases, the stiffness at small m increases quickly, as intended. For sufficiently large n_{avg} the m-dependent elastic moduli even become larger than their bulk values and convergence to the limiting value as m increases occurs from above. It is also clear from the figure that the curves for different n_{avg} are converging to the same limiting value. Therefore, we equate the bulk elastic moduli with their value at large m (typically at a m value somewhat lower than the largest we sample because the latter are most affected by statistical noise; the values used are given in Table A.1) when using the value of n_{avg} for which convergence is most rapid. Figures equivalent to Fig. 3.9 but for A_2 and C are given in the Supporting Information (Fig. A.10), along with the effects of this averaging on the persistence length measurements. For example, for the 6HB-SST nanotube we use $n_{\text{avg}} = 20$ to obtain bulk A_1 and A_2 values, and $n_{\text{avg}} = 5$ to obtain C (Table A.1).

Reprint(adapted) with permission from [159]. *Copyright ©2020 , American Chemical Society.*

3.3 Results

A range of structural and mechanical properties of the ten systems that we studied are given in Table 3.1. Firstly, $\langle\Theta_1\rangle$ and $\langle\Theta_2\rangle$ for all systems are zero within statistical error; i.e. all the tubes are on average straight, as expected. The behaviour of $\langle\Theta_3\rangle$ is more interesting. We should first note that the current oxDNA potential has been fine-tuned to reproduce the experiments of Ref. [178] which suggested that origami based on the hexagonal lattice and without any insertions or deletions should be approximately untwisted. Consistent with this, the 6HB-S, 6HB-MT and 10 HB origami are all fairly near to being untwisted, albeit with all showing a slight right-handed twist; as the twist-stress density in these origamis is likely to be similar, that the twist is lowest for the 10HB most likely reflects its significantly larger twist modulus.

The series of twisted six-helix bundles of Ref. [171] show the expected linear variation of the twist (Fig. A.11) across the series, albeit with the nanotube that is designed to be untwisted being slightly right-handed, as noted above. The designed twist in these structures is based on modelling with CanDo [82, 160]. Here, we find that the insertions and deletions (i.e. increasing or decreasing the number of base pairs between these junctions to induce internal twist stress [178]) in these structures have a larger angular effect with 30 sets of insertions or deletions causing a change in twist of just over one and a half turns rather than a single turn.

Interestingly, the single-stranded tiles systems all show significant right-handed twist (equivalent to about 120° degrees per 1000 base pairs). Like for the hexagonal lattice origamis, the average junction spacing in the planar sheets on which they are based matches the presumed pitch length of DNA (10.5 base pairs). Therefore, they might be expected to show a similar twist as those origamis; instead it is over twice as large. This is mostly because the twist angle at a junction with a single-crossover is larger than for one with a double-crossover for the oxDNA model (whether this feature also holds for real DNA is not clear).

	Ref.	n_{helix}	N_{slice}	a	$\langle\Theta_3\rangle$	A_1	A_2	C	l_b	$l_t/2$	l_b^{expt}	C_{expt}
4HB-MT	[144]	4	1354	0.3373	0.035±0.001	2150	2020	330	1040	330	740	390
4HB-SST		4	1029	0.3400	0.143±0.001	3120	1750	370	2030	280		
6HB-2×LH	[171]	6	1259	0.3371	−0.884±0.001	4480	5300	610	4500	620		
6HB-1×LH	[171]	6	1261	0.3376	−0.419±0.001	5520	5980	580	5740	680		
6HB-S	[171]	6	1259	0.3383	0.046±0.001	6400	5780	670	5430	660	2400	
6HB-1×RH	[171]	6	1260	0.3457	0.492±0.001	5590	4860	650	5950	690		
6HB-MT	[144]	6	1085	0.3385	0.071±0.001	6960	5560	800	4140	810	1880	530
6HB-SST	[147]	6	1070	0.3389	0.115±0.001	7560	7630	750	7620	740	3300	
8HB-SST	[147]	8	1050	0.3383	0.111±0.001	16 980	16 880	1290	16620	1270	8200	
10HB	[171]	10	705	0.3379	0.012±0.001	37 600	13 400	2230	19400	1780		

Table 3.1: Structural and mechanical properties of all the systems studied. All angles are given in degrees and elastic moduli and persistence lengths in nanometres. The n_{avg} and m_{limit} values used to extract the bulk values of the elastic constants are given in Table A.1. The errors in $\langle\Theta_3\rangle$ are standard errors in the mean. The values of the persistence lengths (and elastic moduli) are given to the nearest 10 nm as the errors associated with the fits to the relevant correlation functions for l_b and l_t were at most 10 nm with the exception of l_b for the 10HB origami which we report to the nearest 100 nm. Imperfect sampling and deviations from worm-like chain behaviour may also contribute additional sources of uncertainty.

Reprint(adapted) with permission from [159]. *Copyright ©2020 , American Chemical Society.*

Reprint(adapted) with permission from [159]. *Copyright ©2020 , American Chemical Society.*

Another basic structural property that we considered was the radius of the tubes defined as the average distance of the centres of the DNA helices from the tube centre:

$$r = \frac{1}{N_{\text{helix}}} \sum_{j=1}^{N_{\text{helix}}} \left| \mathbf{R}_{\text{duplex},j} - \mathbf{R}_{\text{tube}} \right| . \tag{3.22}$$

Note, to get a measure of the limit of the excluded volume of the tube one should add the radius of the DNA duplex. The dependence of the radius on position along the tube is shown in Fig. 3.10(a) for 6HB-S; equivalent figures for all the other systems are depicted in Figs. A.12–A.14 of the Supporting Information. Typical of all systems, the tube has a significantly larger radius at either end. This is simply a reflection of the significant splaying out of the helices of the origami at the ends that is evident from the snapshots in Fig. 3.1 and is a result of these sections being less constrained by junctions. The radius measurements allows us to decide how many slices from each end to ignore when performing the persistence length and elastic moduli calculations.

The radii are also larger than one would expect from close-packing of the helices. This is a result of the well-documented slight splaying out of helices between junctions [28, 109, 177] that is also visible from the close-ups in Fig. 3.1. Baker *et al.* estimated the inter-helix separation in a 10-helix bundle nanotube to be 2.75 nm from SAXS measurements [177]. This is fairly similar to the 2.4–2.5 nm radius that we find for the six-helix bundles (Figs. 3.10(a), A.12, A.14). The small variations in this radius along the length of the tube are also due to the variations in the interhelix distance caused by this splaying. In the example in Fig. 3.10(a), the relatively irregular placement of these junctions means there seems little clear pattern in this variation, (although if one looks carefully one can spot a pattern that repeats every about 190 base pairs). However, for the origamis of Ref. [144] there is a much clearer repeating pattern as they have a much more regular junction arrangement (Fig. A.12).

The m-dependent persistence lengths and elastic moduli are shown for 6HB-S, 10HB and 4HB-SST in Figs. 3.10, 3.11 and 3.12, respectively; those for the other

Reprint(adapted) with permission from [159]. *Copyright ©2020 , American Chemical Society.*

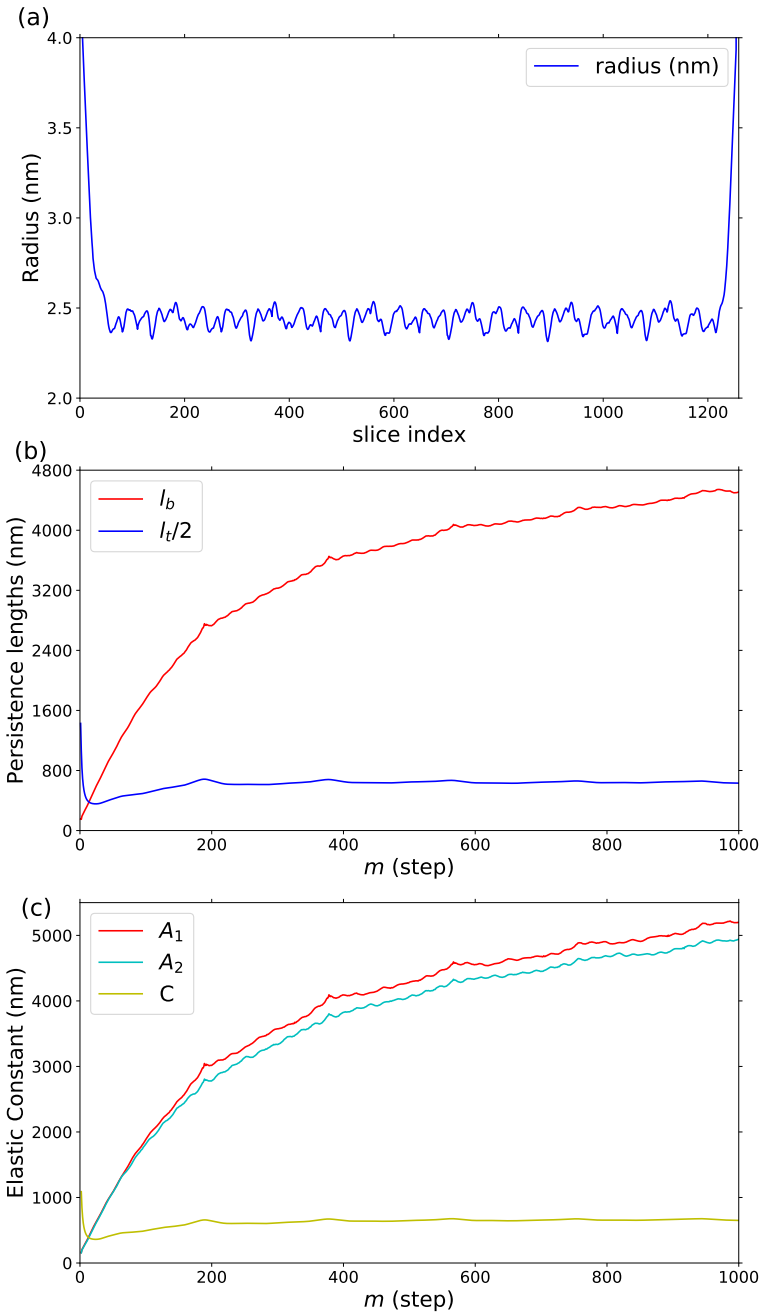


Figure 3.10: (a) Radius as a function of position, (b) m-dependent persistence lengths and (c) elastic moduli (using $n_{\text{avg}} = 0$) for the 6HB-S origami.

systems are shown in Figs. A.15–A.18. The limiting values of these quantities extrapolated by the approaches outlined in Section 3.2.6 are given in Table 3.1 for all systems.

As noted already, the m-dependent bending persistence lengths show a slow convergence to their limiting values due to the enhanced flexibility on short length

Reprint(adapted) with permission from [159]. *Copyright ©2020 , American Chemical Society.*

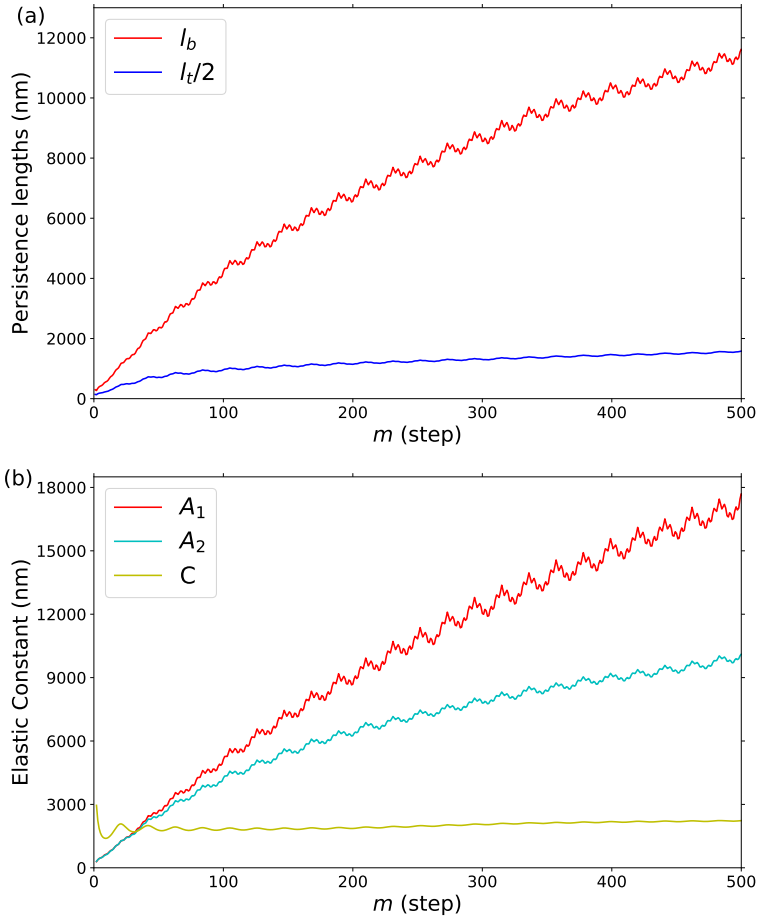


Figure 3.11: (a) m-dependent persistence lengths and (b) elastic moduli (using $n_{\text{avg}} = 0$) for the 10HB origami.

scales. The twist persistence length, partly reflecting its smaller value, converges much more rapidly. All the origamis show some degree of repetitive fine structure in these curves. For example, there is a small peak every about 190 slices for 6HB-S (Fig. 3.10(b)) and a stronger oscillation every 21 slices for 10HB (Fig. 3.11(a)). The enhanced correlations at the peaks are associated with length scales that match a periodicity or approximate periodicity in the pattern of junctions; these periodicities are also evident in the repeating patterns seen in the tube radii. By contrast, the virtual absence of any fine structure, and consequent smoothness of all the data, for the SST nanotubes (e.g. Fig. 3.12(a)) is noteworthy, and reflects the much smaller variations in the tube radii due to the lesser constraints associated with their single-crossover junctions (Fig. 3.12(b)).

In Fig. 3.13 we plot the bulk persistence lengths for bending and twisting versus

Reprint(adapted) with permission from [159]. *Copyright ©2020 , American Chemical Society.*

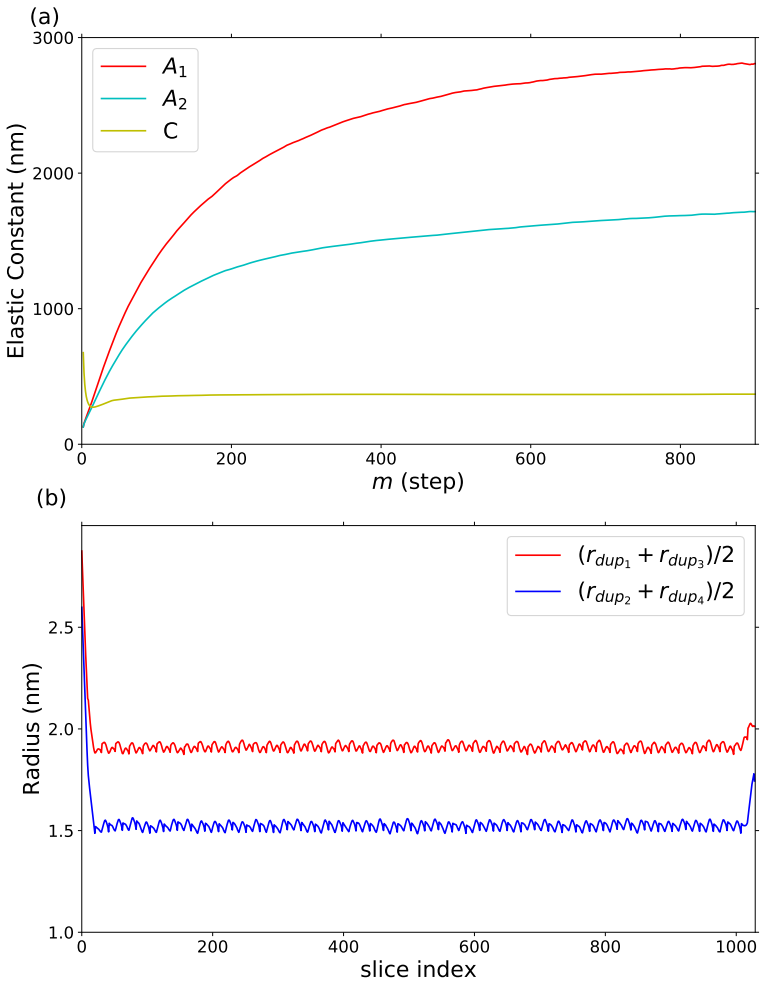


Figure 3.12: (a) m-dependent elastic moduli (using $n_{\text{avg}} = 0$) and (b) radii for equivalent helices as a function of position for the 4HB-SST nanotube.

n_{helix} for all systems, including dsDNA. There is a clear non-linear increase in the bending persistence length with the number of helices, whereas the twist persistence length increases roughly linearly. For example, the bending persistence lengths of the six-helix bundles are 110–190 times that of dsDNA, whereas the twist persistence length increases only by a factor of 6–9. This basic behaviour was previously noted in Refs. [144] and [147]. The variation of the bending persistence length can be described theoretically if one assumes that dsDNA behaves as a uniform elastic cylindrical rod, leading to the expression [150]:

$$l_b^{\text{tube}} = n_{\text{helix}} l_b^{\text{duplex}} \left(1 + 2\left(\frac{R}{r}\right)^2\right). \tag{3.23}$$

Reprint(adapted) with permission from [159]. *Copyright ©2020 , American Chemical Society.*

where r is the radius of dsDNA and R the radius of the nanotube (see Section A.3.2). From this equation it can be seen that the non-linear variation is due to the additional effect of the helices being a distance R from the centreline of the nanotube. One difficulty when applying this to experimental systems is that of measuring R. However, all quantities in this expression can be measured in simulations, allowing the consistency of this expression to be tested. The predicted persistence lengths when applied to the series of three SST nanotubes significantly underestimates the nanotube persistence lengths (Fig. 3.13). A significant factor in the over-prediction likely lies in the assumption that dsDNA can be considered as a uniform elastic rod. Given the structure of DNA—it has a tightly-packed core of stacked and paired bases and, due to the major and minor grooves, a shape more akin to an asymmetric double-threaded screw than a cylindrical rod—it is perhaps not surprising this may not be the best approximation. If we consider r to be a parameter, we can find the value that best fits the SST nanotube data; this fitting gives an effective radius of 0.65 nm, with the resulting form capturing well the dependence on n_{helix}. This compares to 1.15 nm used in the original prediction, which is a measure of the limits of the excluded volume of an oxDNA double helix. As context to this analysis, the combination of the bend persistence length and extensional modulus of dsDNA can be used to estimate the Young's modulus and an effective radius for dsDNA (see Section A.3.2). Using values appropriate for oxDNA gives an effective radius of 0.51 nm. Although this differs somewhat from the value estimated from the nanotube properties, it does add further credence to the idea that viewing dsDNA as a uniform elastic cylinder is a significant approximation.

There is some variation of the persistence lengths for those helix bundles with the same numbers of helices. For example, for the six-helix bundles l_b varies between 4160 and 7650 nm and $l_t/2$ between 620 and 810 nm. Although one in principle expects the persistence lengths to also depend somewhat on the types of junction (single or double crossover), the patterns of nicks and junctions, tube radius (Eq. 3.23) and the degree of internal stress, a significant part of this variation is probably caused by systematic errors arising from imperfect sampling; as mentioned earlier,

Reprint(adapted) with permission from [159]. *Copyright ©2020 , American Chemical Society.*

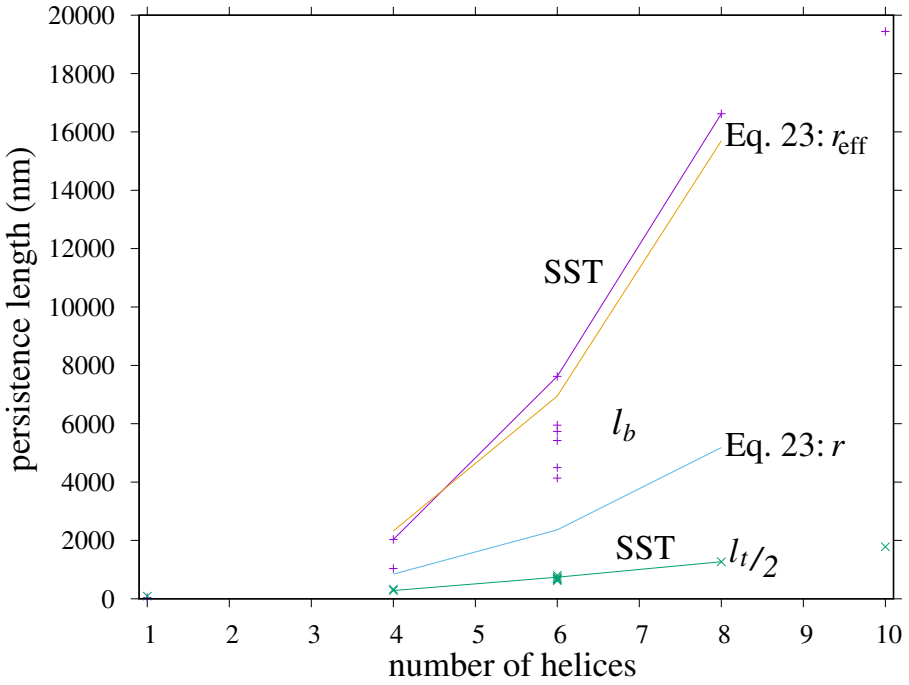


Figure 3.13: The variation of the bend and twist persistence lengths with n_{helix} for all systems including dsDNA. Lines have been added for the SST series of nanotubes. There are also two additional lines (with no data points) that represent the predictions of Eq. 23 for the SST nanotubes using both the actual radius of dsDNA or an effective radius that is chosen to fit the observed data.

the 4HB-MT and 6HB-MT examples suffer particularly in this regard with the tangent-tangent correlations lacking the clear exponential tail that is expected for a worm-like chain. For two of the 6HBs, the persistence length has now also been calculated by an alternative approach in which the end-to-end distribution of the nanotube is computed using umbrella sampling and then fit to a worm-like chain form [179]. For the 6HB-S nanotube the value obtained only differs by 0.1 μm, whereas for the 6HB-SST system it is 1.1 μm smaller. One systematic feature of the current results is that the SST nanotubes have a larger bending persistence. This is perhaps surprising, as one might have expected them to be more flexible given that they have single rather than double crossovers at the junctions. The most likely reason is that the extra freedom associated with the single crossover allows the nucleotides at the junctions to better optimize their stacking interactions, causing the junctions to actually be stiffer. Whether this is just a feature of the oxDNA stacking potential or would also hold for real DNA is not clear.

Reprint(adapted) with permission from [159]. *Copyright ©2020 , American Chemical Society.*

We can also compare our results to the available experimental data for these systems, which are included where available in Table 3.1. Although the persistence length of the 10HB origami design considered here has not been determined experimentally, a value of 5430 nm was obtained for a very similar 10HB design [146]. In all cases the oxDNA values for the bending persistence length are larger. One clear factor is that the simulations have been performed for origamis with the ideal structures, whereas there is likely to be imperfections in the experimental origamis due both to assembly errors, be it a result of missing staples or the incorrect routing of the strands, and to errors in the synthesis of the staples. Quantitative evidence has been obtained for the presence of such assembly errors [32, 180, 181], but estimates of their prevalence have varied significantly. For example, Ref. [181] estimated that on average only 84% of staples were incorporated into a 2-D origami, whereas Ref. [32] obtained folding qualities of 96% or greater for 3-D origamis. The resulting defects could well lead to both local static structural irregularities and enhanced fluctuations, both of which would contribute to lowering the measured persistence lengths. From this viewpoint, the experimentally measured values should be seen as lower bounds to the persistence lengths of ideal structures.

Another factor that we should mention is that in our calculations we choose to ignore the ends of the origami due to their enhanced fluctuations, which would otherwise introduce some degree of non-worm-like chain behaviour and a lowering of the persistence lengths. However, these effects are relatively small. Also, our m-dependent definition of the bending persistence length shows a significant length dependence. However, this is due to enhanced local fluctuations at the shortest length scales, whereas the experimental measurements are unlikely to be sensitive to these effects, both due to the lower resolution of the molecular contour and the analysis methods used. Similarly, these length-dependent effects are dramatically reduced when we use the averaging approach of Section 3.2.6 (Fig. A.10(c)).

The most accurate persistence length measurements are probably those of Ref. [147] because the lengths of the SST nanotubes can be significantly larger than an origami. By visualizing the molecular contours of individual tubes as a function

Reprint(adapted) with permission from [159]. *Copyright ©2020 , American Chemical Society.*

of time they were able to measure the tangent-tangent correlation of individual nanotubes over length scales of up to about 10 μm. One interesting feature of the results was that the variation of the persistence lengths between different examples of the same design was greater than the estimated error in the persistence length for an individual tube. So for the 6HB, the persistence lengths varied between 1.6 and 4.7 μm, and between 5.7 and 10.1 μm for the 8HB. This indicates that the population of nanotubes has a heterogeneous set of mechanical properties. In this case, there is a possible isomerism (associated with whether the strands are in registry or offset as one goes around the circumference of the tube) that may be partly responsible for this heterogeneity, but it is also likely to reflect differences in the assembly quality of individual nanotubes. For this reason, the highest values may provide the best estimates of the persistence lengths of the ideal nanotubes (the average values are reported in Table 3.1).

The difference between the experimental and oxDNA values could also reflect deficiencies in the oxDNA model. One known shortcoming is that although oxDNA reproduces well the bend and twist persistence lengths of dsDNA, it considerably overestimates the stretch modulus. For the original oxDNA model the extensional modulus is about 2100 pN [104], but it has not previously been calculated for the second version of the model used here (sometimes called "oxDNA2"). Fitting the force-extension curve of dsDNA to the extensible worm-like chain form (Fig. A.19) gives an estimate of about 2700 pN for oxDNA2. This compares to experimental estimates of about 1200 pN at high salt conditions [182]. The overestimate of stretch modulus is also a persistent issue with all-atom DNA models. For example, a recent all-atom study that focuses on developing a more accurate force-field called Tumuc1 reports a stretch modulus of about 3000 pN [183] which is roughly 3 times the observed value. The bending of a helix bundle not only involves the bending of the individual helices, but also leads the helices on the inside of the bend to be compressed, and those on the outside to be in tension. Thus, the large value of the oxDNA extensional modulus is likely to contribute to an overestimation of the bending persistence lengths. Note, though, that the tube can also respond to the

Reprint(adapted) with permission from [159]. *Copyright ©2020 , American Chemical Society.*

tension and compression by changing its local structure, e.g. by changing the splay angle of the helices at junctions and hence the interhelix separation.

In Table 1, we report the limiting values of the elastic moduli for all systems. Note that we do not give values for the coupling terms A_{12}, G_1 and G_2 as there is no strong evidence that non-zero values are more than statistical noise. For completeness, we plot their m-dependent values in Figs. A.20–A.23, but it is noteworthy that rather than rising smoothly to their limiting values—as is the case for A_1, A_2 and C, as well as the twist-bend coupling constant for dsDNA [163]—they are generally close to zero for small values of m, where the statistics are best, with any significant deviations from zero occurring at larger m. However, as we estimate the limiting values of A_1, A_2 and C from the large-m behaviour, the non-zero values of the off-diagonal terms are likely to somewhat affect the accuracy of these elastic moduli.

It was expected based on approximate symmetry that for all systems, except for 4HB-SST and the 10HB origami, A_1 and A_2 would be approximately equal. This is generally the case with differences being at most 25%. For the 6HB and 8HB SST nanotubes for which there is an exact symmetry due to the regularity of their junctions, A_1 and A_2 are virtually exactly equal.

The large difference in A_1 and A_2 for the 10HB is expected given its very anisotropic cross-section. The origin of this difference for the 4HB-SST system is more subtle. As a consequence of the alternating pattern of 10 and 11 base-pair spacings between junctions in the SST nanotubes, the interhelix angles alternate on going around the nanotube. This leads to the diamond, rather than square, tube cross-section apparent in Fig. 3.1(a). This effect can be quantified by measuring the distance of equivalent helices in the SST nanotubes from the tube centre. These two distances are shown in Fig. 3.12(b) for the 4HB-SST and in Fig. A.24 for the other SST tubes. The difference in the two distances is roughly 0.4–0.5 nm for the 4HB-SST tube.

If $A_{12} = G_1 = G_2 = 0$ then the bending persistence length should simply be the harmonic mean of the bend elastic constants A_1 and A_2. This generally holds to within 10%, the exceptions being the MT systems for which the sampling issues

affecting the values of l_b have already been noted. Similarly, if the coupling terms are zero then $l_t/2 = C$; this generally holds to within less than 10%, the exceptions being 4HB-SST and 10HB, for which the large differences between A_1 and A_2 make the obtained limiting value of C more sensitive to the behaviour of the coupling terms. For the two experimental systems for which the twist modulus has been measured, the oxDNA values are in reasonable agreement, being a bit smaller for the 4HB-MT origami and about 50% larger for the 6HB-MT origami, which happens to have the largest C of the 6HB systems that we have studied. The potential effect of defects in the experimental structures on C may be relevant to the latter comparison.

3.4 Conclusions

In this chapter we have introduced approaches to compute persistence lengths and elastic moduli associated with bending and twisting for rod-like DNA nanostructures. One feature is that only on length scales beyond those associated with the spacings between the junctions do the bending fluctuations behave like those of a worm-like chain. As our discretization was performed at the level of single base-pair steps along the molecular contour, averaging methods had to be introduced to extract bulk values of the elastic moduli. The approaches, although computationally intensive due to the long simulations required to adequately sample the long length-scale fluctuations, are straightforwardly applicable to other DNA nanostructures. Thus, they could be used as part of a rational design process to produce DNA nanostructures with tailored mechanical properties.

In line with previous experiments [144, 147, 184], we found that the persistence lengths and elastic moduli associated with bending exhibit a strong non-linear dependence on the number of helices, whereas the twist persistence lengths increase approximately linearly. Consequently, the DNA nanotubes are in a very different mechanical regime with respect to angular deformations compared to duplex DNA. For example, for the six-helix bundles the persistence length is on average about

eight times larger than the twist modulus, whereas for dsDNA the twist modulus is over twice as large.

In all cases, the values for the bending persistence lengths that we obtain are larger than those measured experimentally. The main reasons for these differences are firstly that our calculations are performed for ideal structures, whereas the structures in experiments will inevitably have some degree of defects due to both assembly and strand synthesis. Secondly, one of the known deficiencies of the oxDNA model is that it overestimates the stretch modulus of dsDNA, which in turn is likely to lead to the cost of nanotube bending being overestimated as the individual helices will be somewhat compressed on the inside of a bend and stretched on the outside. Note that there are also uncertainties in the accuracy of oxDNA's description of the mechanical properties of junctions and nicks, as there is relatively little experimental information to which to compare. The relative contributions of these two main factors is not fully clear. However, it is interesting to note that oxDNA is able to reproduce well the bending and twisting of the example origamis in Ref. [178] that result from internal stresses induced by insertions and deletions, as the degree of bending and twisting is partly determined by the elastic moduli of the origami [106]. An interesting question one might seek to answer is how local modifications, such as gaps, insertions or deletions affect the elastic moduli of nanotubes. We will attempt to partially address this in Chapter 5 where we have studied a few DNA nanotubes that have been experimentally tailor-made with regular gaps to lower their stiffness.

Here, we have characterized the elastic fluctuations of a set of DNA nanostructures, focussing on their angular deformations. It would also be of interest to probe other types of deformation mode, e.g. stretch or shear, and their potential couplings to twisting and bending, and to go beyond the elastic regime to explore their response to external stresses, in particular how they buckle under extreme twist and bending. For the latter, their generic behaviour could well be quite different from dsDNA, because of the very different ratios of the bend to twist moduli. For example, would they form plectonemes in the same way that dsDNA does under extreme twists, or would the costs of bending the nanotube back on

Reprint(adapted) with permission from [159]. *Copyright ©2020 , American Chemical Society.*

itself at the tip of the plectoneme be prohibitive? Chapter 4 is an effort to try and resolve some of these questions by twisting 4HB-SST and 6HB-SST under different conditions, thus, trying to quantify and contrast plectoneme formation in nanotubes as compared to DNA duplexes.

Once we accept our limits, we go beyond them.

— Albert Einstein

4

Twisting DNA nanotubes

4.1 Introduction

That we have characterized the mechanical behaviour of some DNA nanotubes in the elastic regime [159] evokes our scientific curiosity to seek to understand what happens if we surpass the limits of that regime. Such questions are also of practical relevance to the field of DNA mechanotechnology [45]. If one is seeking to use DNA nanodevices to apply mechanical stresses at the nanoscale [185] and construct mechanoresponsive DNA structures [143], it is important to know the mechanical limits of such devices. The ultra-sensitive response of DNA nanostructures to stress can be useful in studying biochemical processes which involve emergent response [186].

Although one could imagine many scenarios for how such DNA nanostructures might fail under extreme stresses, their complexity means making reliable predictions just based on theoretical considerations would be extremely difficult. Moreover, visualizing such systems whilst under extreme stress is experimentally

very challenging. Therefore, simulations have the potential to play an important role in unravelling the mechanisms of nanodevice failure.

Indeed, oxDNA simulations have recently been used to explore how DNA origamis unravel when subject to sufficient tension applied to the ends of the scaffold strand [187] and how DNA nanotubes buckle when subject to bending stresses [179] (Fig. 4.1(a)). Here, we will consider the behaviour of DNA nanotubes subject to extreme twist stress. Such systems, namely 4HB and 6HB DNA origamis, have been probed experimentally by Kauert *et al.* [144] using magnetic tweezers and our simulations will help to interpret the observed behaviour (Fig. 4.1(b)).

The twist-induced buckling regime of the DNA duplex continues to engross the interest of biologists and biophysicists and provides a useful context for the current chapter. For the former the main motive is to understand how DNA supercoiling affects cellular control in biology [188], while for the latter it is more about understanding the fundamental physical mechanisms of plectoneme formation [164, 189, 190]. DNA duplexes are simpler systems (e.g. they have fewer internal degrees of freedom); hence, they are easier to simulate and theoretically model and have been very extensively studied [191–193]. Simulations of the mechanical properties of DNA nanotubes by contrast are much more computational challenging, as we have observed in the previous chapter, and experimentally very little is known about any complex structures they might form post-buckling.

Worm-like chain models have contributed significantly to the understanding of plectoneme formation in DNA duplexes [194–198]. However, they cannot capture the coupling of the twist response to the internal degrees of freedom of the duplex; for example, at higher forces the DNA duplex responds to negative twist by forming a bubble (a region of broken base pairs) rather than a plectoneme. Interestingly, oxDNA simulations can capture both effects and have revealed novel behaviour in the crossover between these two regimes. In particular, at intermediate forces, the DNA duplex forms a plectoneme with a bubble at its tip, with the bubble both absorbing negative twist and allowing sharper bending at the plectoneme tip [164].

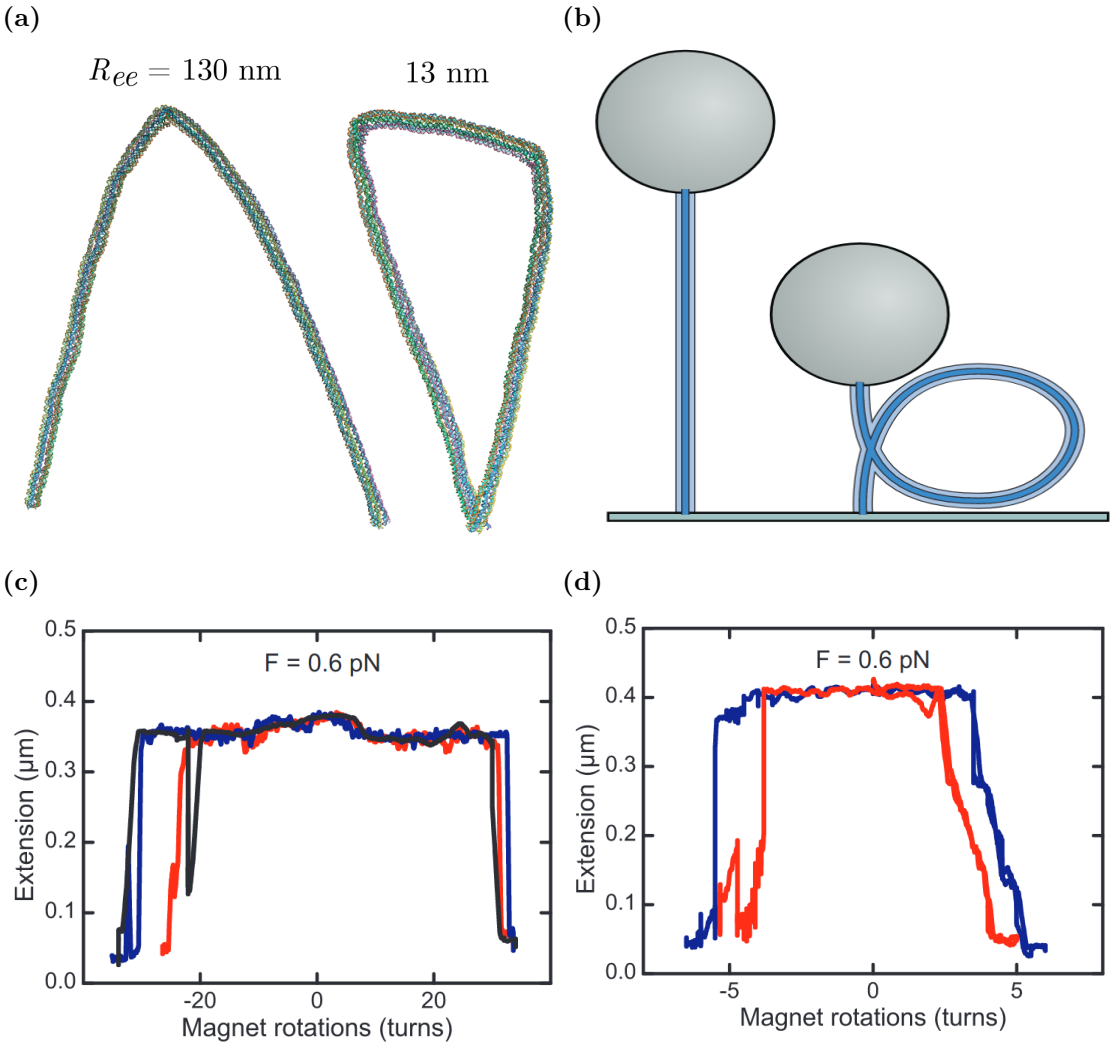


Figure 4.1: (a) shows two representative configurations of the 6HB-SST nanotube under bending stress. The left snapshot shows the presence of a kink which is centrally located when the end-to-end distance between the ends is 130 nm. In the right configuration, where the ends are just 13 nm apart, it is more favourable to relieve the stress through the formation of 2 kinks. (b) is a schematic showing Kauert *et al.*'s interpretation of their magnetic tweezers results on the 6HB-MT or 4HB-MT systems in terms of the expected plectonemic loop formation [144]. (c), (d) End-to-end distance as a function of applied twist for (c) 6HB-MT and (d) 4HB-MT systems subject to a pulling force of 0.6 pN. It is noticeable that buckling occurs significantly earlier for the 4HB-MT nanotube, whereas it requires more than 20 applied turns for the 6HB system. Note that the systems studied by Kauert *et al.* contain bulky DNA blocks at each end of the nanotube that connect to the magnetic tweezer beads; their effect on the propagation of twist stress to the main part of the nanotube is not clear. (a) is adapted from Ref. [179], whilst (b), (c) and (d) adapted from Ref. [144] with permission.

Although, as we have seen in the previous chapter, worm-like chain models can describe the elastic behaviour of DNA nanotubes, they will be much less useful for modelling the effects of extreme twist, because DNA nanotubes occupy a very different l_b/l_c regime (l_c is the contour length). Whereas most experiments on the DNA duplex are in the limit where $l_c \gg l_b$, $l_b \gg l_c$ for DNA origami nanotubes. Essentially, DNA nanotubes are too stiff to form plectoneme-like structures where the bending of the nanotubes is always in the elastic regime. For example, a comparison of the oxDNA results on the extreme bending of a 6HB DNA nanotube with the plectoneme-like structure suggested in Fig. 4.1(b) by Kauert *et al.* [144] quickly allows one to deduce that the latter is physically unrealistic because the curvature in the loop is well beyond where elastic bending behaviour can be expected to still apply. Instead, features like the kinking at the plectoneme tip noted above for duplex DNA are much more likely to be the norm. Note also that $l_b > l_t$ for the DNA nanotubes, whereas $l_t > l_b$ for dsDNA.

4.2 Methods

4.2.1 Simulation

Simulations were run at temperature of 300 K and salt concentration of 1 M [Na^+]. The two systems that are considered are the 4HB-SST and 6HB-SST nanotubes studied in the previous chapter. Note that $l_b/l_c = 7620/291.54 = 26.1$ for the 6HB and $2030/278.46 = 7.3$ for the 4HB system, where l_c is the contour length associated with the portion of the nanotube which is subject to twist stress. Since the simulations were done in many stages to obtain well-formed plectonemes, the different steps are outlined as follows.

- Starting from a configuration generated from the relevant caDNAno file by tacoxDNA [199], standard oxDNA minimization procedures were used to remove any nucleotide overlaps and overly-long bonds that would otherwise

cause the molecular dynamics to fail. We minimized the nanotube for 20 000 steps.

- If the minimized nanotube was allowed to relax freely, it would be difficult to extract a fairly straight nanotube that could then be twisted. Therefore, the traps required to twist the nanotube were put in place at the relaxation stage. Specifically, we fixed the position of 42 slices at each end of the nanotube using rotating harmonic traps that act on the centres of mass of sets of nucleotides (an oxDNA simulation code feature). These traps harmonically constrain the motion in two dimensions (say x, y) whilst allowing free motion in the third dimension (say z). These traps can rotate at a certain rate around an axis, but for the relaxation stage their positions were kept fixed. The stiffness of the traps was fixed to 1.0 simulation units, which corresponds to a force constant of 57.09 pN/nm. The traps were applied in two sets of 21 slices, separated by 21 slices that were free of any external forces. The traps were not placed at the extreme ends but 40 slices into the nanotube, to avoid the zones where the helices are more splayed out. Each trap acted on the centre of mass of a 21-bp section of one of the helices in the origami. Two sets of traps were used to disperse the torque application and to keep the ends of the nanotubes straight. A short relaxation was carried out with the above setup. Note because of the traps, the twist of the nanotube remained unchanged during this relaxation, even though a completely relaxed nanotube has a slight right-hand twist (Table 3.1).

- Two turns of left-handed twist were incorporated into the relaxed nanotubes by the rotation of the above traps. During these simulations, the extreme slice of base pairs was now subjected to a small external pulling force varying from 0.5–7 pN, as in magnetic tweezer experiments. The rate of twisting for the 42 slices at each end was 2π x 10^{-7} turns/simulation time. The nanotube was simulated with a pulling force and a constant twisting rate for 1 x 10^7

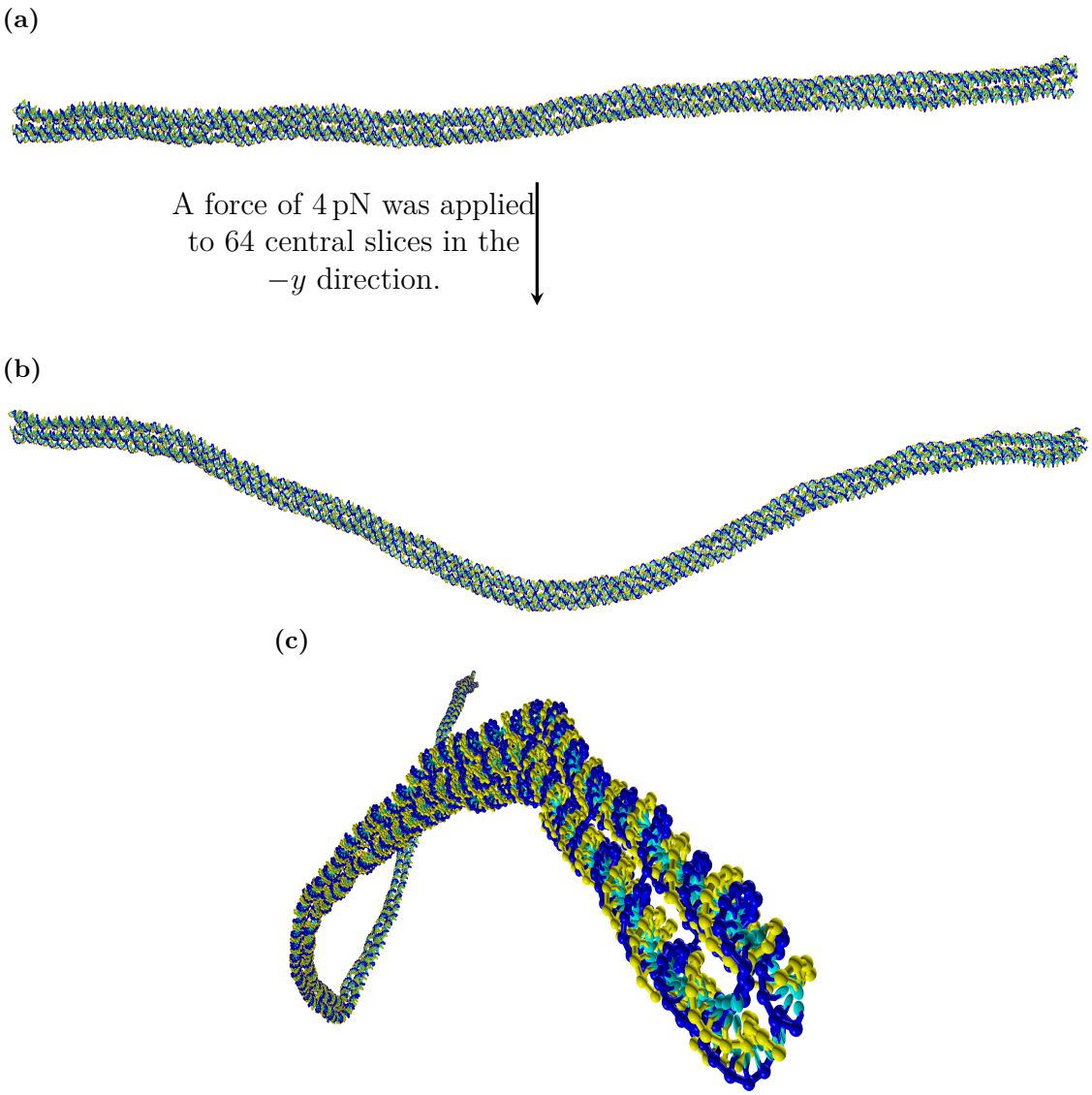


Figure 4.2: The nanotube is aligned along the z-direction. (a) and (b) show configurations of a 6HB-SST before and after a small force of 4 pN was applied to the central 64 slices in the $-y$ direction to create a structure where bending is focussed in the centre, thus facilitating plectoneme nucleation in centre of the nanotube. (c) The geometry of a 4HB-SST nanotube as seen from one end of the nanotube after introducing a 4 pN bending force at 2 turns. The coupling of the twist and bend to create a proto-curl configuration is clear from this viewpoint.

simulation time steps. Fig. 4.2(a) shows a snapshot of 6HB after 2 turns have been incorporated into the system.

- After 2 turns have been applied to the nanotube, the resulting configuration is subjected to a constant soft bending force of 4 pN dispersed over the central 64 slices perpendicular to the length of the tube for 1×10^8 simulation steps(Fig.

4.2(b) shows the final configuration after the bending force has been applied. The objective of this step is to facilitate nucleation of a plectoneme midway along the tube. In the absence of this step plectoneme formation would still occur, but it could occur at any position along the nanotube. The advantage of a centred plectoneme is that it can grow to its fullest extent before reaching the ends of the nanotube, whereas the growth of an off-centre plectoneme will be hindered by reaching one end before the whole nanotube has been incorporated and further twist will lead to the nucleation of additional plectoneme loops. During this step no pulling or further twisting of the ends was carried out. Because of the twist already incorporated into the nanotube, the application of the bending force does not lead to a configuration with a pure bend but a proto-curl configuration that is both twisted and bent (Fig. 4.2(c)).

- The final configuration after the bending simulation was again subjected to twisting with a constant tension until the desired number of turns were applied to the nanotubes.

- The above mentioned steps were repeated multiple times to obtain three sets of "well-formed" plectonemes.

- The final configurations after each complete imposed turn were simulated for at least 1×10^9 to capture as fully as the possible configurations at that applied twist.

The plectoneme is deemed "well-formed" if it is roughly centred and multiple plectoneme loops are absent. For the 4HB-SST we carried out an additional step. The 4HB origami is relatively less rigid than the 6HB-SST and despite multiple attempts, we could not obtain three sets of trajectories where plectonemes were well-formed. Hence, we decided to unwind the 4HB from its most twisted state, hoping to attain configurations where plectonemes are well-formed. This step also showed us that winding and unwinding of an origami does not necessarily follow a reversible pathway in our simulations. We were able to attain better formed

plectoneme configurations in the unwinding process as compared to the twisting process. All 4HB data plots have been plotted using results from both twisting and untwisting "well-formed" plectoneme trajectories. Measurements of post-buckling torque or end to-end distance were made after discarding the first 50% of the total number of time steps taken, which corresponds to at least twice the decay time of the auto-correlation function of the end-to-end distance of the helix bundle.

The end-to-end distance for both 6HB-SST and 4HB-SST is calculated as the distance between two nucleotides, each on an end slice of the nanotube. Since we use pulling forces of up to 10 pN (applied on the last slice on each side), if the origami is unable to retain its structural integrity under such forces, it can easily be identified by inspection of the end-to-end distance plots. For example, for the 4HB-SST nanotube we only report data for a maximum pulling force of 7 pN, even though we did perform simulations at $F = 10$ pN, as at this pulling force we observed an end-to-end distance greater than the contour length of the origami, due to dissociation of strands and consequent breakage of the origami at either the site of force application or at a kink in the origami.

For torque calculations firstly, we defined an origin located roughly at the centre of the nanotube ($\vec{origin}$) with respect to which all our torque measurements are made. We measured the torque experienced by the nucleotides that are subject to the twist traps. Since the traps only constrain the motion of the nanotube in the x and y directions, the value of the torque should average to zero in x and y. Hence, the direction, $\vec{d}$ of the torque measurement is defined as (0,0,1). Now the distance vector $\vec{r}$ is defined as;

$$\vec{r} = (\vec{pos}_{nuc} - \vec{origin}) - [(\vec{pos}_{nuc} - \vec{origin}) \cdot \vec{d}]\vec{d} \tag{4.1}$$

Hence, the torque $\vec{\tau}$ measurement follows as, $\vec{\tau} = \vec{r} \times \vec{F}$ where, $\vec{F}$ is the total external force experienced by the nucleotide and $\vec{pos}_{nuc}$ is the instantaneous position of the nucleotide for which the torque is being calculated. The torque values reported in this chapter have been averaged over all nucleotides used to apply the twist.

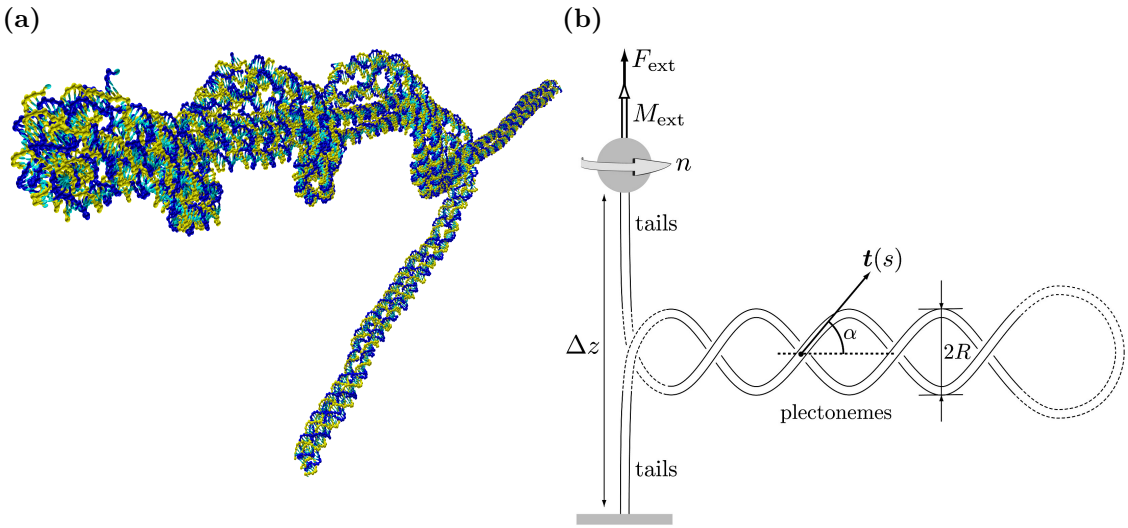


Figure 4.3: (a) A representative configuration of a 4HB-SST plectoneme held under an external force of 2 pN. The presence of kink defects at the tips of plectonemes is a universal feature of plectonemes in helix bundle systems, regardless of the magnitude of the tension that is applied to the system. Plectonemes are also observed to form at an acute angle to the unwrithed segment of the helix bundle. It is also noticeable that in the plectoneme stem one of the filaments is relatively straight with the other wrapping around it in a helical fashion. (b) This figure shows a generic representation of plectonemic loop and tail in systems such as DNA duplexes which contrasts with the slanted plectonemic loop we observe in origamis. F_{ext} is the pulling force, M_{ext} is the twisting force which applies a $2n\pi$ twist, Δz is the end-to-end distance, α is the superhelical angle and R is defined as the superhelical radius. (b) is adapted from Ref. [200] with permission.

4.3 Results and Discussion

4.3.1 Geometry of a plectoneme in helix bundles

Fig. 4.3(a) shows a plectoneme in the 4HB-SST system. These plectonemes are characterised by localised bending at the tip, creating a "kink" defect that contains dozens of broken base pairs and allows the tube to bend sharply back on itself. This is expected because the curvature required at the plectoneme tip is well beyond the nanotube's elastic limit for bending. The plectonemic stem consists of filaments, with a super-helical angle [201] that is generally smaller than 40° for the range of forces that we applied onto the helix bundle system.

The superhelical angle, α is defined as the angle between the tangent $\mathbf{t}(s)$ and the plectoneme axis. The plectoneme radius R and pitch $2\pi p$ were extracted from

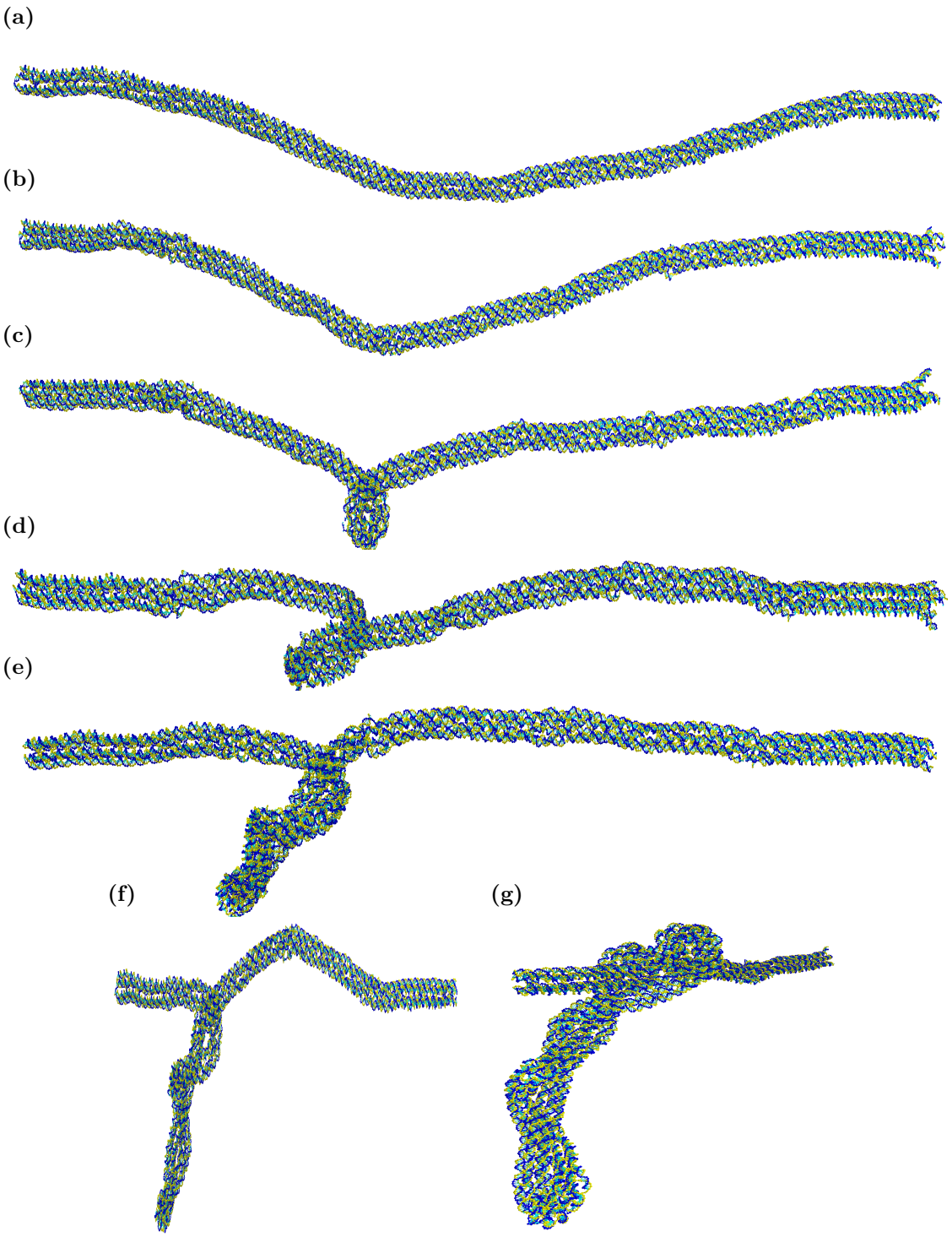


Figure 4.4: Snapshots of a 6HB-SST nanotube being twisted at a rate of $2\pi \times 10^{-7}$ per simulation step at (a) 3, (b) 5, (c) 6, (d) 7, (e) 8, (f) 9 and (g) 11 imposed turns. These are non-relaxed configurations from simulations where the nanotube was still being twisted. The applied tension is 2 pN. The increasing number of turns leads to a typical plectoneme structure that is slanted at an acute angle to the unwrithed segment of the nanotube. In the plectoneme stems often one filament is relative straight with the other wrapping around it. As the plectoneme nucleated slightly off-centre, once 11 turns have been applied further growth is only possible by nucleation of a new plectoneme loop in the longer unwrithed arm near to the base of the original plectoneme.

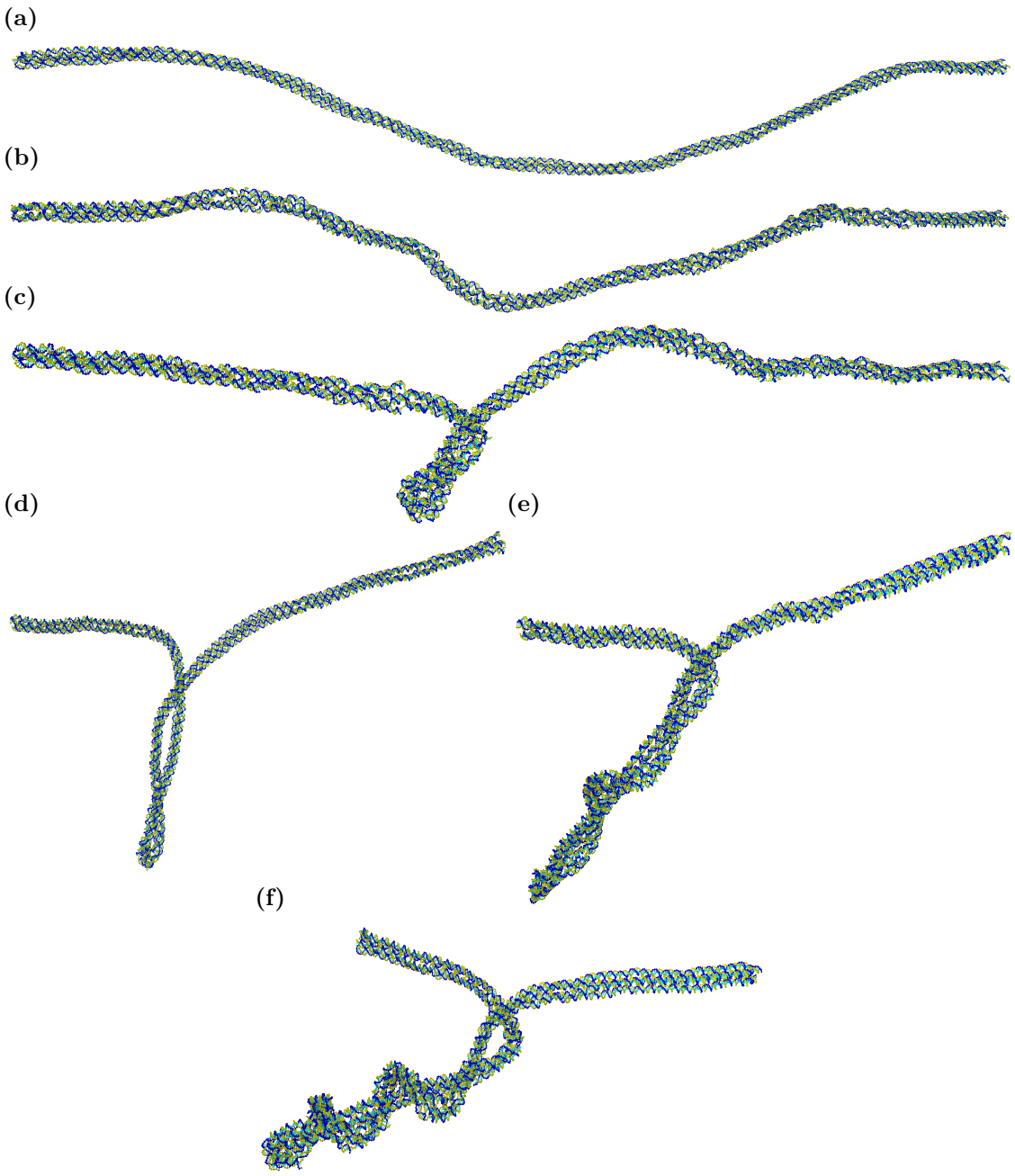


Figure 4.5: Snapshots of a 4HB-SST nanotube at (a) 3, (b) 8 and (c) 10 imposed turns. (d), (e) and (f) correspond to the same number of turns as in (a), (b) and (c), respectively, but while untwisting the 4HB-SST nanotube. The applied tension is 2 pN. Both the rates of twisting and untwisting were fixed at $2\pi \times 10^{-7}$ per simulation time step. The untwisting simulations started from a configuration with 16 imposed turns. The contrasting accumulation of loops in the untwisting process as compared to the twisting trajectory indicates the non-reversible pathway of plectonemes in origami systems. Another observable difference is the greater build-up of twist stress in the unwrithed arms during twisting runs (visible by the bowing out of the helices between junctions) because the unwrithed sections are able to more quickly respond to the changes in twist than the plectoneme. Also, as motion of the kink at the base of the plectoneme is relatively slow, during untwisting the length of the plectoneme does not change much, but instead the pitch of the braided section increases.

a few equilibrated "well-formed" plectoneme configurations at $F = 0.5$ pN and 2.0 pN using oxView [202]. The superhelical angle α as defined in the model by Clauvelin *et al.* [201] is given by:

$$\tan(90^\circ - \alpha) = \frac{p}{R} \tag{4.2}$$

Another unique feature of the plectoneme geometry in helix bundles is the manner by which the plectoneme stem is connected to the straight and unwrithed tails of the nanotube. Rather than being roughly perpendicular as is usually observed for plectonemes, say in a DNA duplex, one of the filaments connects smoothly to a tail with a small geometric curvature while the other is highly bent and kinked at the connecting point irrespective of the number of turns or tension applied. The result is a slanted configuration that is atypical of what we would expect in a worm-like chain, where the filaments, on average, are equally bent at the connecting points. Virtually all the plectonemes produced by our twist simulations adopt the slanted configuration, suggesting that the slanted configuration is free-energetically favoured. Similar to the plectoneme tip, the curvature required favours kink formation. Once a kink is formed, bending the kinked segment further does not increase the free energy cost sufficiently to warrant the nucleation of a kink in the other filament. It is therefore more favourable to create a sharp bend in one of the filaments instead of bending both filaments equally at the plectoneme base.

Another noticeable feature is that when the plectoneme stems have a short pitch length associated with the braiding (this is particularly the case at high applied twists) one of the filaments in the braid tends to be fairly straight whereas the other wraps it around in a helical fashion. This contrasts with the plectonemes in worm-like chains where both filaments would wrap around each other in a double helical fashion. Again this is likely to be because the degree of bending in these short-pitch plectonemes goes beyond the elastic regime and it becomes more favourable to localize the bending in one of the two filaments. Fig. 4.4 shows the growth of plectoneme in 6HB-SST under a tension of 2pN.

4.3.2 The physics of plectoneme formation in helix bundles

End-to-end extension and post-buckling torque

The end-to-end extension curves and post-buckling torque response for the 4HB-SST and 6HB-SST nanotubes are shown in Fig. 4.6. For 4HB-SST systems, the end-to-end extension and torque response are averaged using production runs from both the twisting and untwisting trajectories. The end-to-end extension and torque response for 6HB-SST systems on the other hand are averaged using production runs from the twist trajectories only.

We must apply a strong caveat when interpreting these curves from a theoretical perspective, because although we have tried to adopt simulation strategies that help to generate plectonemes that are 'well-formed' and well sampled, fully equilibrating the plectoneme configurations is beyond current simulation time scales even when using an efficient model such as oxDNA. The issue is not only the system size, but that many of the processes that would help the plectonemes to sample different possible configurations are very slow. For example, the barrier for nucleating a plectoneme is large. Our strategy of applying a bending force to generate a proto-curl configuration certainly helps to reduce that barrier. It is interesting to note that we tend to observe plectoneme formation at lower twists than in the experiments (Fig. 4.1(c)–(d)). In particular, the experiments on the stiffer 6HB origami require very large over-twists and buckling leads the end-to-end extension to jump to almost zero. Together with the differences between individual experiments, it is clear that equilibrium is also very hard to achieve in the experiments.

As well as the slow dynamics of nucleation, the motion of any kinks also tends to be slow. This is why we were particularly concerned to facilitate nucleation in the centre of the plectoneme, because diffusion of the position of plectoneme in these systems is effectively negligible. Kinks at plectoneme tips have been observed to be effective at pinning plectonemes in duplex DNA [164]. This is even more the case in these nanotubes. As kinks (albeit not quite so sharply bent as at the tip) are also present at the base, such pinning will also affect the dynamics of plectoneme

elongation and shrinking. For example, it is noticeable in Fig. 4.5 that the pitch of the braided plectoneme stem is longer for untwisting compared to twisting.

Despite the difference in averaging methods, the end-to-end extension curves and torque response of both helix bundle systems exhibit similar general features. Interestingly, even though much of the bending exhibited by the nanotube plectonemes is beyond the worm-like chain limit, the results show features that are also common to models of buckling in elastic rods or dsDNA [203], because similar physical principle apply, irrespective of the exact nature of the bending. The rate of decrease in end-to-end extension of the helix bundles in the post-buckled state, for instance, varies with the magnitude of the pulling force, namely, the larger the force, the lower the rate of decrease in extension. This observation conforms to what we would expect from classical buckling. Denoting the number of imposed turns as N_{turn}, the length of the plectoneme, or equivalently the number of plectoneme loops, increases as N_{turn} increases. These loops are, on average, similar in size and shape for a particular pulling force, leading to a roughly constant rate of decrease in end-to-end extension as more turns are imposed. Since a larger pulling force means that more work (against the external force) is needed to form a plectonemic loop, each plectonemic loop that is formed to accommodate the additional twist is smaller in size to reduce the amount of work required, leading to a more gradual reduction in the end-to-end extension.

For $N_{turn} \lesssim 7$, the post-buckling torque remains roughly constant as more turns are imposed. This feature has the same origin as in classical buckling models. The torsional energy injected into the system is balanced by the loop's bending energy and work done against the pulling force, both of which are a function of the loop geometry and therefore remains constant throughout the process.

Another feature of the torque response plots that is also seen in worm-like chain models is the variation of the magnitude of the (constant) post-buckling torque with the pulling force. The reduced loop size at a larger applied force is accompanied by an increase in the curvature of the loop that increases its bending energy. The net effect is an increase in post-buckling torque with a larger applied

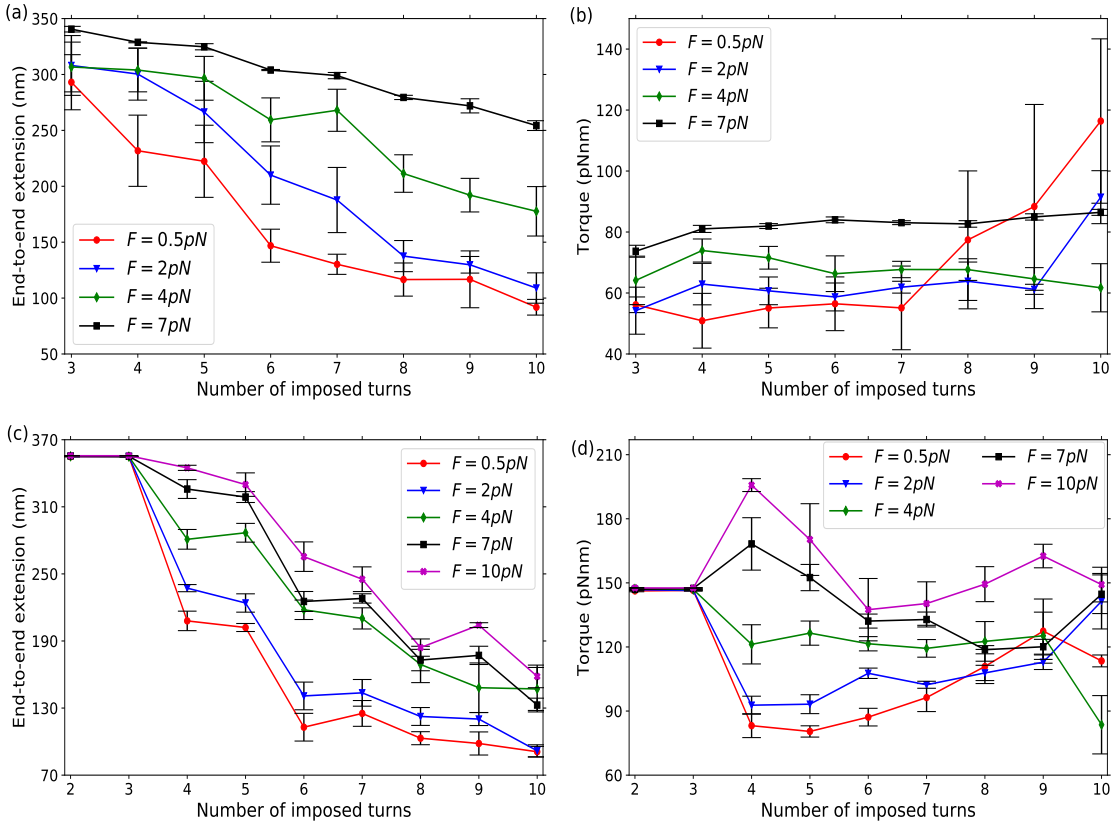


Figure 4.6: (a) End-to-end extension and (b) post-buckling torque plots for a 4HB-SST nanotube. (c) End-to-end extension and (d) post-buckling torque plots for a 6HB-SST nanotube. Error bars represent the standard error of the mean. In the case of the 4HB-SST nanotube the mean is obtained from simulations started from configurations generated in both the twisting and untwisting trajectories. Edge effects become apparent when the number of imposed turns is large. Plectonemes are pinned by the kink defect at their tips. If these plectonemes are formed near the edge of the helix bundle, then their continuous lengthening will be prevented as the number of imposed turns increases, leading to the formation of secondary plectonemes which results in a deviation from the expected trends in the end-to-end extension and torque plots.

force. We can further quantify and verify these observations using the end-to-end extension curves and post-buckling torque plots in Fig. 4.6. The post-buckling slope of the end-to-end extension curves in Fig. 4.6(a) and (c) can be estimated by a linear fit, and its gradient exhibits a clear dependence on the applied force, namely, the larger the force, the smaller the gradient.

Deviation from these general trends can be particularly observed when $N_{turn} > 7$ in both helix-bundle systems. The kink defect at the plectoneme tip pins the helix bundle plectoneme, which, despite the imposition of a bending force, may not

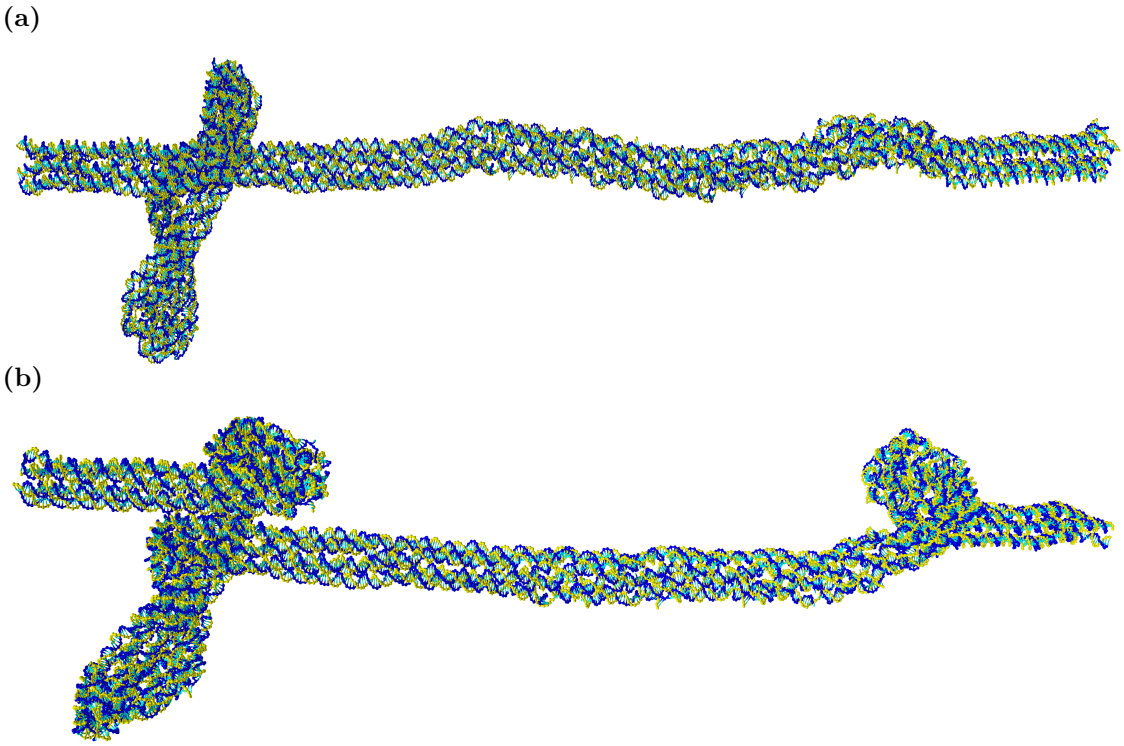


Figure 4.7: (a) A 6HB-SST nanotube under a tension of 10 pN when 11 turns have been applied to the system. Tensions beyond 4 pN increasingly undo the effect of the bending force, and hence kinks and bends near to the ends of the origami that are prone to offer seeding points to plectoneme nucleation because of their proximity to the site of twist application. If the growth of the plectoneme begins close to the end of the nanotube, the growth is inhibited as in this case. After a couple of turns, there is little stem left on one side to enable further growth. (b) As a consequence further twisting (12 turns have been applied to the illustrated configuration) leads to the nucleation of a second plectoneme near to the other end of the nanotube.

always be located at the centre of the nanotube, especially in cases where tension is more than 4 pN (Fig. 4.7). The plectoneme, upon encountering one of the repulsive barriers as it lengthens, is prevented from further growth. This results in a re-buckling transition, or the nucleation of a second plectonemic loop. It is unsurprising that in these instances further features in the torque-response curve might be seen, e.g. a secondary torque overshoot or a further increase in the torque [204, 205]. There is also less space for the plectoneme to grow when N_{turn} is large. The effects of this constraint can perhaps account for the tapering of the decrease in end-to-end extension that we observe and some of the increases in torque at high twist.

Another prominent difference between the helix bundles' end-to-end extension curves and the hat curves of dsDNA is the buckling point's dependence on the

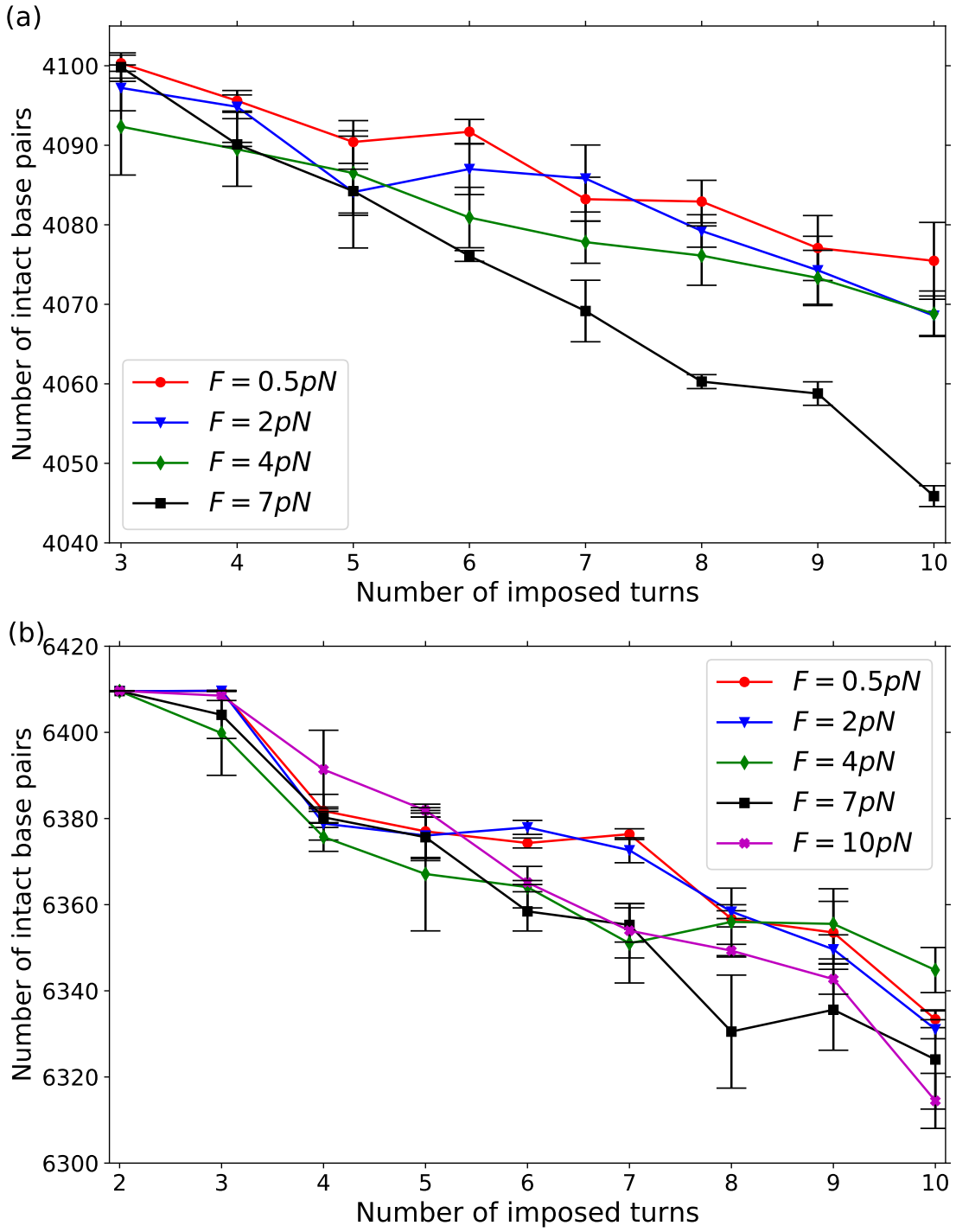


Figure 4.8: Variation of the number of intact base pairs with the number of imposed turns in (a) 4HB-SST, and (b) 6HB-SST. A base pair is considered denatured if the binding energy falls below 10% of its maximum possible value. In 4HB-SST, approximately 5 base pairs are broken per turn whereas in 6HB-SST, this number goes up to approximately 10 base pairs per turn.

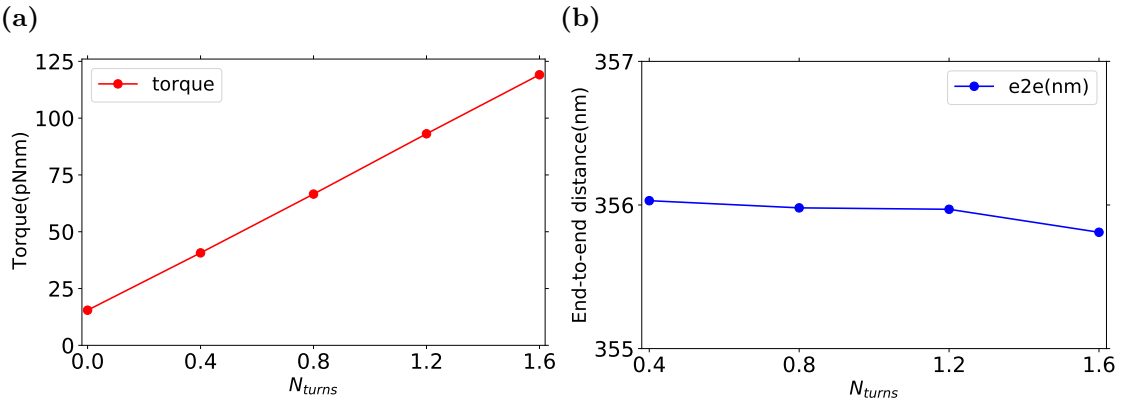


Figure 4.9: (a) Variation of torque with N_{turns} for 6HB-SST at a tension of 7pN. There is a linear increase in torque until 1.6 turns indicating that the nanotube has still not encountered bucking. Note that the graph does not go through the origin because N_{turns} is measured with respect to an untwisted geometry, whereas the relaxed structure of this nanotube is slightly right-twisted (Table 3.1). (b) Variation of the end-to-end distance versus applied twist in the pre-buckling regime. There are minimal changes in this quantity indicating the absence of any plectonemic loop formation.

applied force. In dsDNA, the buckling point shifts with the magnitude of the applied force – the larger the force, the greater the number of turns that is required before buckling occurs. This shift is obscured in helix bundles, especially in 6HB-SST systems at larger applied tensions of 2 pN and more. The absence of a clear-cut shift in buckling point is likely a consequence of a kink-mediated buckling in helix bundles which, to the lowest order, is independent of the applied force. For the 6HB-SST, torque increases linearly until 1.6 turns (Fig. 4.9) and becomes more-or-less stagnant beyond 2 turns, until the second plectonemic bubble forms.

Another interesting feature to note is the decrease in the number of intact base-pairs with each applied turn when in the buckled state. This is a reflection of the strong bending required in the plectonemic state, not just at the tip, but also in the plectoneme stem, and the breaking of base pairs is one mechanism of enhancing flexibility, albeit at a thermodynamic cost. As the 6HB is stiffer than the 4HB nanotube, it is to be expected that the stiffer nanotube suffers a greater breakage of base pairs. The 6HB-SST on average is losing 10 intact base-pairs per applied turn which is about twice that observed in 4HB-SST nanotubes (Fig. 4.8).

4.3.3 Calculation of elastic parameters

Although the focus in this chapter has been on the buckling of the DNA nanotubes, the setup that we have developed can can also be used to measure the elastic behaviour of the nanotubes at low twist. The linear increase in torque with increasing number of turns in the pre-buckling regime enables us to estimate the twist modulus C [206]. Specifically, the effective twist modulus C_{eff} is related to the torque τ by

$$\tau = \frac{2\pi n k_B T C_{\text{eff}}}{l_c}, \tag{4.3}$$

where l_c is the effective length of the rod and n corresponds to the number of imposed turns. The slope of Fig. 4.9(a) can be used to calculate τ/n. The effective length of the 6HB-SST nanotube to which the twist stress is applied is 291.45 nm. This is less than the actual length of the nanotube as 63 slices on each end of the nanotube have been utilised to apply the torque, while the 40 terminating slices on each end have been left unused as they display helix splaying. Thus, we obtain a value of C_{eff} of roughly 731.9 nm. This estimate of the twist modulus is in very good agreement with the value of 750 nm obtained in Chapter 3 (Table 3.1) from the twist fluctuations of these nanotubes. The calculation of C_{eff} from Eq. 4.3 in principle depends on the tension applied. This effect can be described through the Moroz-Nelson formula [207]:

$$C_{\text{eff}} = C\left(1 - \frac{C}{4A}\sqrt{\frac{k_B T}{AF}} + \ldots\right) \tag{4.4}$$

Using the values of C and A (Table 3.1), the above equation predicts that $C_{\text{eff}}/C = 0.9998$ at $F = 7$ pN, i.e. because $l_b \gg l_c$ the effect of writhe fluctuations on the value of C measured is negligible. Similarly, although the end-to-end extension is expected by theory to show a quadratic decrease in the pre-buckling regime as the twist increases due to writhe fluctuations [208], the magnitude of the effect is too small to be visible in Fig. 4.9(b) because the bending persistence length is much greater than the twist persistence length. By contrast such effects are visible for dsDNA.

The calculation of C has only been done for 6HB-SST due to computational limitations, as the nanotube had to be simulated for long times for each value of the imposed twist. The results both provide independent confirmation of the values of the twist modulus calculated in Chapter 3 and a useful check that the setup and computations developed in this chapter are performing correctly.

4.4 Conclusion

In this chapter, I have introduced a simulation approach to apply external torques to a DNA nanotube in a somewhat similar way to how this is done experimentally using magnetic tweezers. I have used this approach to again study the elastic behaviour of a DNA nanotube, obtaining a value of the twist modulus consistent with the value obtained in Chapter 3; the approach also has the potential advantage of not requiring a definition of a local triad. The focus of the chapter, though, has been to study the torsional buckling of DNA nanotubes at large twist stresses.

Like has been previously observed for extreme bending [179], although the torsional stresses that are applied are extreme, the DNA nanotubes generally do not break apart and no strand was observed to dissociate on our simulation time scales, except in the case of the 4HB nanotube at forces greater than 7 pN. Furthermore, the nanotubes are ably to reversibly recover when the stresses are removed.

The nature of the plectonemic buckled state has significant differences compared to systems, such as dsDNA, where worm-like chain behaviour is a reasonable assumption. Because the bending persistence length of the nanotubes is significantly larger than their contour length, the curvatures required to form a plectoneme go beyond the limits of worm-like-chain bending and it becomes favourable to localize bending stresses at strongly-bent kinks. Thus, the plectonemic tips are invariably kinked, a kink often forms at the base of one of the filaments of the plectoneme giving a 'slanted' rather than 'perpendicular' configuration and the bending in the plectoneme stem is often more localized in one of the two filaments.

These features, in addition to the large size the the nanotubes, also make fully equilibrating these systems unfeasible on currently available simulation time scales.

Thus, despite the significant simulation times expended, the analysis can only be semi-quantitative because of the potential systematic errors due to inadequate sampling. This provides an additional reason why it would be interesting to develop mathematical theories of plectoneme formation that can be applied to such rigid systems.

Honorable errors do not count as failures in science,
but as seeds for progress in the quintessential activity
of correction.

— Stephen Jay Gould

5

Understanding mechanics of gapped rods

5.1 Introduction

As we have already stated the importance of studying mechanical properties of defect-free DNA nanostructures in our previous chapters, the study would be incomplete if we did not also study the mechanical effects of defects in such system. In an experimental setting, it is unfeasible to completely prevent defects or errors occurring while assembling these nanotubes; rather they are indeed likely a major contributor to the discrepancy between theoretical and experimental results that we have already noted. In such circumstances it is important to have experimental approaches that can quantify the success of assembly. Methods such as DNA-PAINT super-resolution microscopy where the colour profiling of complementary staples helps quantify the defect sites [181] or the use of fluorescence to probe defects [32] act as useful tools to quantify the success of DNA self-assembly experiments. As a theoretical biophysicist we might be able to quantify how these assembly defects affect properties such as the elastic moduli by extending our existing approaches.

For example, the study of defective DNA nanotubes could also offer insights into the level of discrepancy these assembly defects create between experimental and theoretical data. Now if one can study defective nanotubes, a follow up question would be to ponder if deliberately induced defects could be used to generate a desired trait? The answer to the above question has been a matter of interest for DNA nanotechnology groups around the world.

Dietz et al. [178] demonstrated that twisting and bending limits in rigid nanotubes can be enhanced via strategic insertion and deletion of DNA bases. Mechanical properties of DNA nanotubes can also be altered by introducing "gaps" of various sizes and densities [146]; up to a 70 % reduction in the bending persistence lengths for 4HB origamis was achieved. Incorporating nicks and gaps into origamis also allows a reduction in torsional rigidity [184, 209]. Constraining defects to the centre of the nanotube allows it to act as a hinge, as the origami is softer in the middle; it facilitates extreme bending [210]. Similarly, missing staples have been used to achieve designs with a higher local mechanical compliance [210, 211]. Creating such defects also invokes curiosity to study and characterise what really happens at the defect site and how this leads to the observed change in properties [212].

Tailoring the properties of DNA nanotubes can be achieved not just via removing bases but also by introducing DNA-binding molecules using both intercalation and groove binding modes [213]. Radiation damage has also been shown to facilitate flexibility in a 6HB origami [214]. Tailored introduction of defects either via introducing gaps or using intercalators has also been used to study the chemomechanical instability of DNA rings [215].

Since we have already established oxDNA's competence to study the mechanical properties of defect-free DNA nanotubes [159], it is also appropriate to use oxDNA to model and study nanotubes with defects. Our collaborative [185] work with the Emory group (described in Chapter 6) included the modelling of a variant of a DNA origami force clamp referred to as Δ32, where the 16HB origami had missing staples in the centre. This locally more compliant region in the centre of the nanotube allowed more facile bending of the origami when subject to bending

stress providing a control to better understand the behaviour of the defect-free force clamp. OxDNA simulations confirmed the effectiveness of this approach to modifying the response of the force clamp.

5.2 Methods

Here, we consider a subset of the systems introduced in Ref. [146] where the mechanical properties of a series of nanotubes were modified by the introduction of "gaps" at those sites where two staple ends meet; this was achieved by shortening the lengths of the relevant staples. At the gap sites, the origami will have single-stranded rather than double-stranded DNA. Specifically, we studied the 10HB system with 5 nt gaps and the 4HB system with 1 nt, 3 nt and 5 nt gaps both as a function of the gap density. In Ref. [146] the gap density was given as a percentage where 0% corresponds to no gaps and 100% was the maximum gap density considered and corresponds to gaps being introduced at all available sites. For gap densities less than 100%, the sites were chosen to be as uniformly spread though the nanotube as possible.

OxDNA is particularly well-suited to study such systems, not only because of its ability to accurately model DNA origami that we have already seen in this thesis, but because it provides a physically realistic picture of the single-stranded sections that make up the gaps, unlike many simpler models of DNA. Particularly important to an accurate characterization of single-stranded DNA is the ability of neighbouring bases to stack and unstack. When fully stacked, single-stranded DNA is actually relatively stiff (the persistence length is about 40 nt in oxDNA [104]), but is very flexible when unstacked. Moreover, breaking a stack within an otherwise stacked single strand has a significant effect on the mechanical properties because this site then acts like an almost free hinge. Furthermore, stacked and unstacked single-stranded DNA have different effective contour lengths.

Thus, when the single-stranded DNA is stacked through a gap, the stiffness of the DNA is not lowered that much, but as the gap length increases the probability

of being fully stacked decreases rapidly [216]. Furthermore, in bent configurations the bending is likely to be localized at the gap and facilitated by unstacking.

All simulations were performed at 300 K and 1 M [Na^+]; the latter is representative of the high salt conditions generally used for DNA nanotechnology. The initial structures were generated from the cadnano files for each origami using tacoxDNA [199]. Standard oxDNA relaxation procedures were then used to remove any nucleotide overlaps and overly-long bonds that would otherwise cause the molecular dynamics to fail due to excessively large forces. After sufficiently long equilibration runs to generate representative configurations, five productions runs of 5×10^9 steps were run for the 4HB system, generating at least 11 500 configurations for each system for analysis. For some systems these runs were repeated to improve sampling. The 4HB system used in this study is twice as large compared to either of the 4HB-SST or 4HB-MT [144] that we studied in chapter 3. The 4HB origami due to its size required multiple runs to obtain non-correlated data. The 10HB system is very similar in size as compared to the 10HB [171] studied previously, hence sensible data could be obtained in fewer runs. Table C.1 reports exact details of simulations of each system.

The approach we use to compute the persistence lengths is that developed in Chapter 3. This involves defining an orthogonal triad of vectors at each cross-sectional slice through the nanotube, where each slice is separated by a base-pair step along each of the helices making up the nanotube, and then using these to define local bend and twist angles. We will carry forward the same definitions of $\mathbf{R}_{\text{tube}}$ (Eq. 3.14), $\hat{\mathbf{z}}$ (Eq. 3.15), $\hat{\mathbf{x}}$ (Eqs. A.2 and A.6) and $\hat{\mathbf{y}}$ (Eqs. A.3 and A.7) from Chapter 3 and Appendix A.

Clearly, the definition of $\mathbf{R}_{\text{duplex}}$ (Eq. 3.16) cannot be used where the individual helices have gaps. In these regions we use

$$\mathbf{R}_{\text{gs}} = \mathbf{r}_{\text{nuc1}} + r \times \widehat{\mathbf{b}}_{\text{nuc1}} + \alpha \left(\widehat{\mathbf{b}}_{\text{nuc1}} \times \widehat{\mathbf{n}}_{\text{nuc1}} \right) \tag{5.1}$$

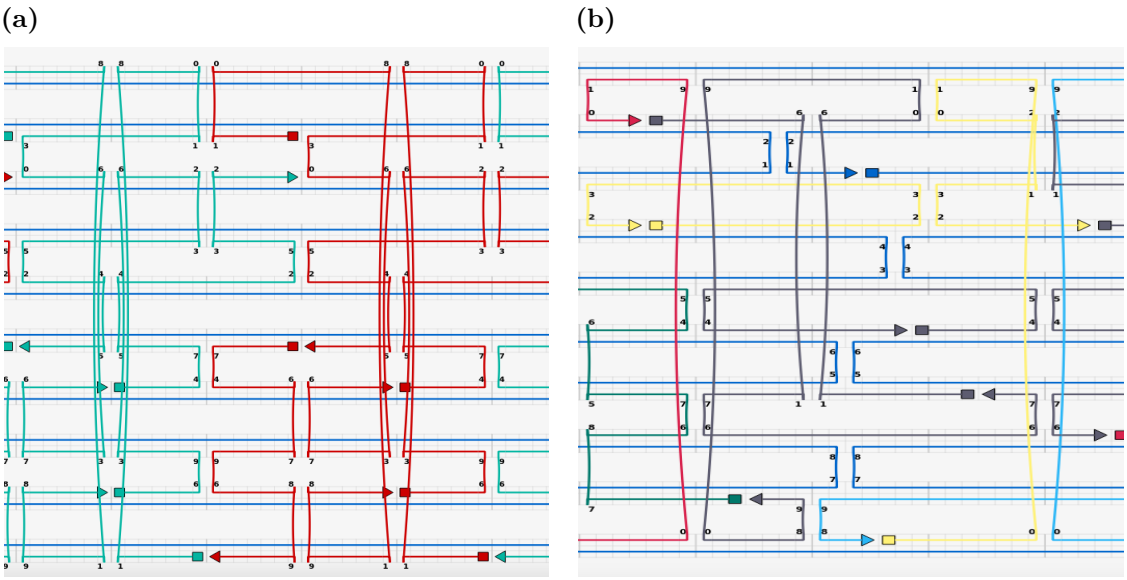


Figure 5.1: Short sections of the cadnano designs (a) show the presence of multiple crossovers between non-adjacent helices at the same slice index in the 10HB of Ref. [171] that we studied in Chapter 3, while (b) the 10HB [146] that we study in this chapter shows a much less regular pattern of junctions with scaffold as well as staple crossovers and has some short 2-nt domains which together give rise to a somewhat more flexible origami. In the 33-slice section in (b) there are 9 sites at which staple ends meet. These are the sites at which gaps are introduced.

where r is half the average separation of base-paired nucleotides in dsDNA, i.e.

$$r = \frac{\langle |\mathbf{r}_{\text{nuc1}} - \mathbf{r}_{\text{nuc2}}| \rangle}{2}$$

The value of r (0.5104 nm) was determined from simulations of a 150-bp duplex at 300 K and $[Na^+]$=1 M ignoring the 5 base pairs nearest to each end.

The calculation of persistence lengths will be carried out following the same principles set out in Chapter 3 (Section 3.2.4). The 60 slices at the end of each nanotube were ignored, the reasons for which have been thoroughly discussed in the previous chapters.

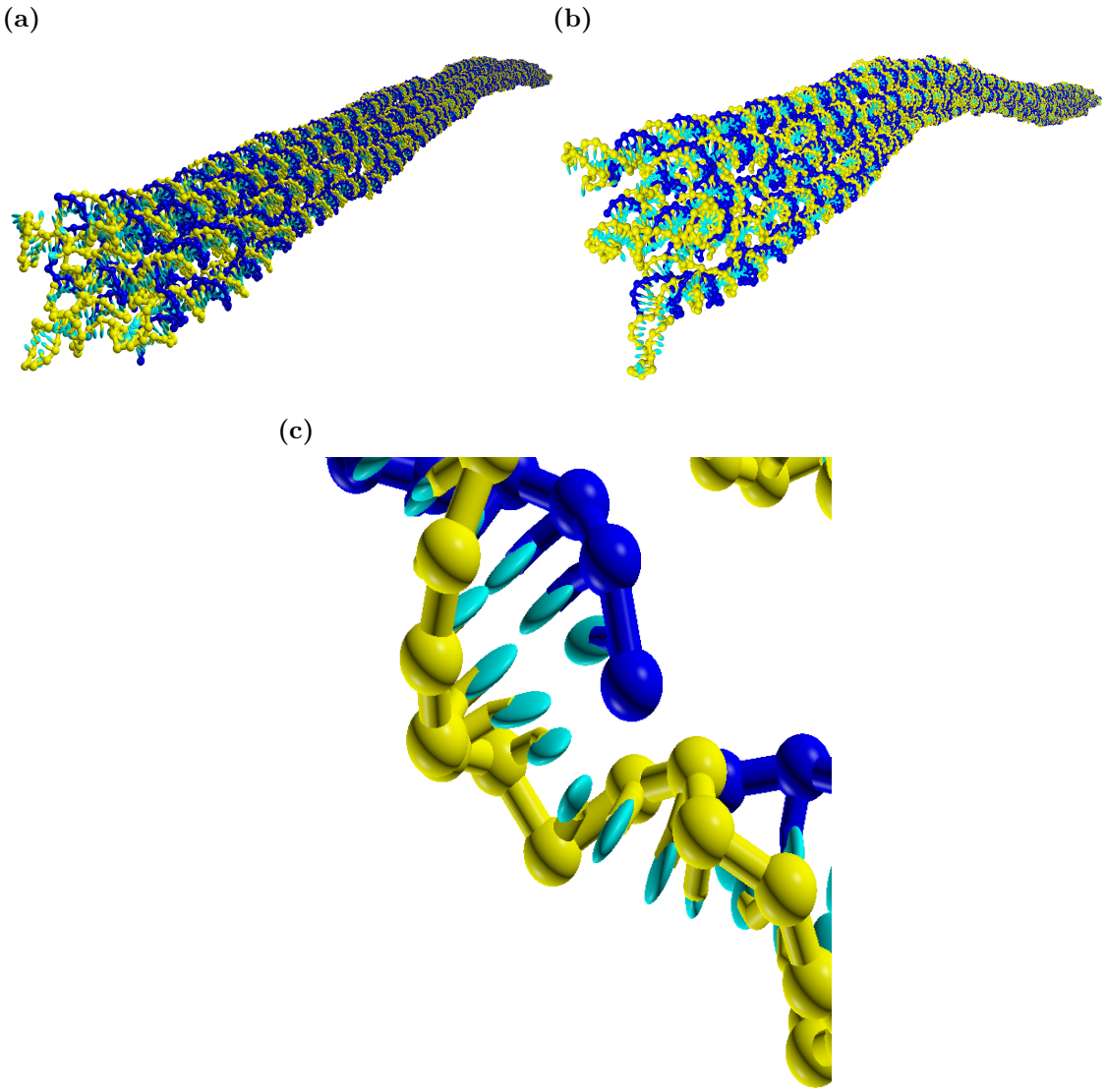


Figure 5.2: (a) A 10HB origami without any gaps is relatively straight and rigid as compared to the (b) 10HB-5 nt with 100% gap density in which a significant left handed twist is observed, along with higher bending flexibility. (c) A gap site in the 4HB-5 nt nanotube with 100% gap density. The gap reduces the mechanical connectivity between the double helices on either side of the gap. Note in this example the non-helical path of the yellow strand through the gap. The gap also affects the duplex structure near to gap. The end base pairs are more likely to fray and even when base-paired the distance between the relevant nucleotides increases somewhat because of the changes to the interactions at the gap site that contribute to the normal duplex structure.

5.3 Persistence lengths

5.3.1 l_b and l_t for 10HB gapped origamis

The 10HB origami that we study in this chapter has the same double hexagon cross-section as the one we considered in Chapter 3, but has differences in the type and placement of junctions. The 10HB origami studied in Chapter 3 has a pattern of junctions that repeats every 21 slices with multiple staple double crossovers occurring at three equally-spaced points in that repeat (Fig. 5.1(a)). The 10HB origami studied in this chapter has a much more irregular pattern of junctions with both staple and scaffold crossovers. It also has a significant number of short 2-nt domains that have the potential to act as weak points in the structure (Fig. 5.1(b)). Consistent with previous results for 6HBs [179] this lowers the rigidity of the system; this 10HB origami has a persistence length that is about 3000 nm less than the 10HB origami [171] studied in Chapter 3.

There are six variations of the gap density that were available for the 10HB, starting with no gaps followed by incremental increases of the gap density by 20% until all available sites incorporate a 5 nt gap (referred to as 100% gap density). The number of gaps at 100% density is 158.

Fig. 5.3 shows the variation of $\log\langle\cos\theta(m)\rangle$ versus m for all 10HB systems. All plots show a clear exponential tail (albeit with a regular fine structure similar to what was observed in Chapter 3 for the 10HB system) that allows the persistence length to be extracted. Fig. 5.4(a) shows the variation of l_b with gap density for the 10HB origami. All values are also reported in Table 5.1.

For the 10HB without any gaps we get an l_b value of 15.5 μm. This is larger than the experimentally obtained value of 5.4 μm, but this is to be expected given the general tendency of oxDNA values to be larger than experiment that we noted in Chapter 3. For 100% gap density with a 5 nt gap size, oxDNA estimates l_b to be around 8.8 μm. Therefore, we observe a decrease of 43% in l_b on going from the defect free 10HB to one with 100% gap density. The experiments [146] report a drop of roughly 60% in l_b for the same system when the gap density is 100%.

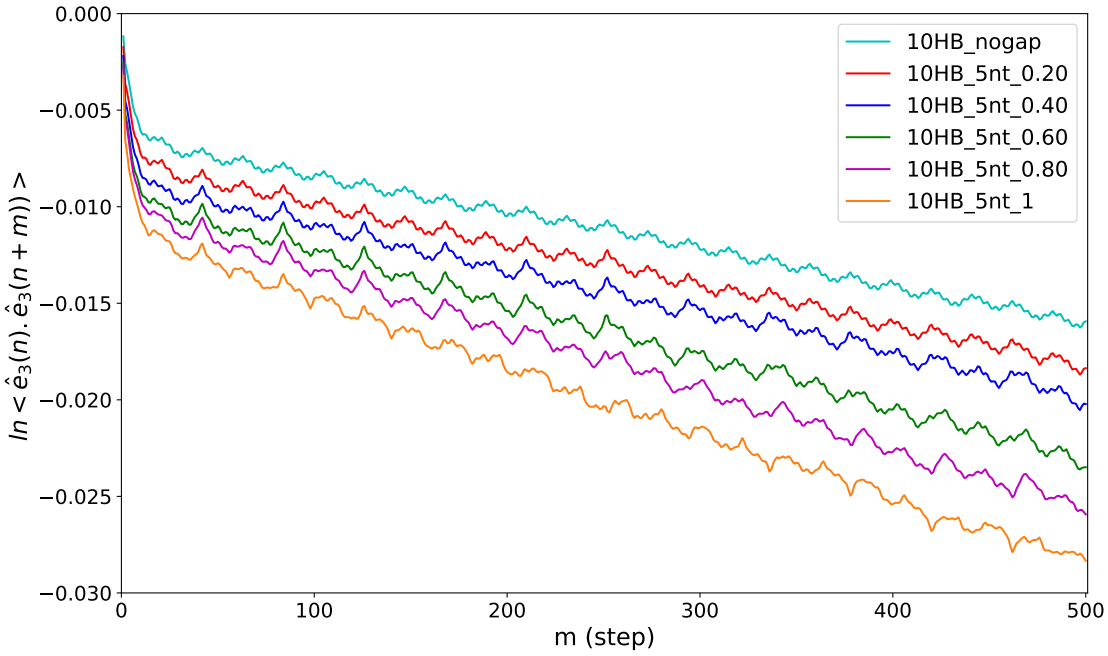


Figure 5.3: $\log\langle\cos\theta(m)\rangle$ versus m for all 10HB systems.

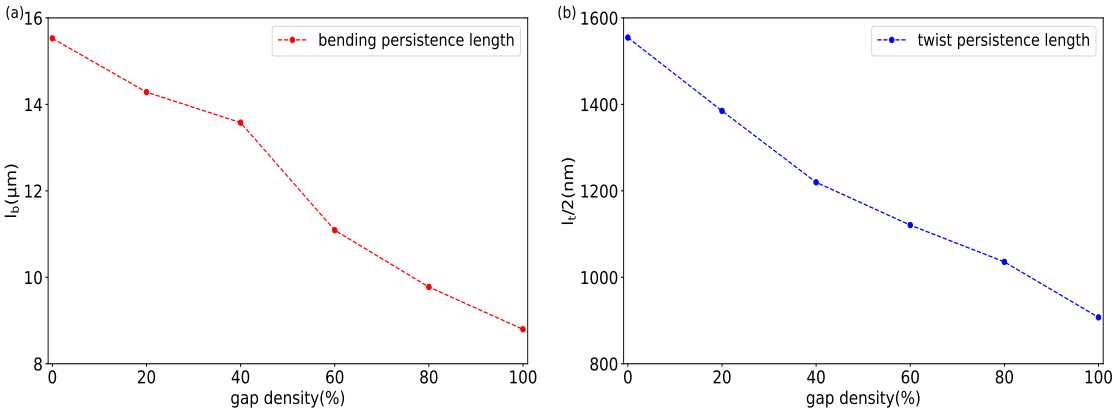


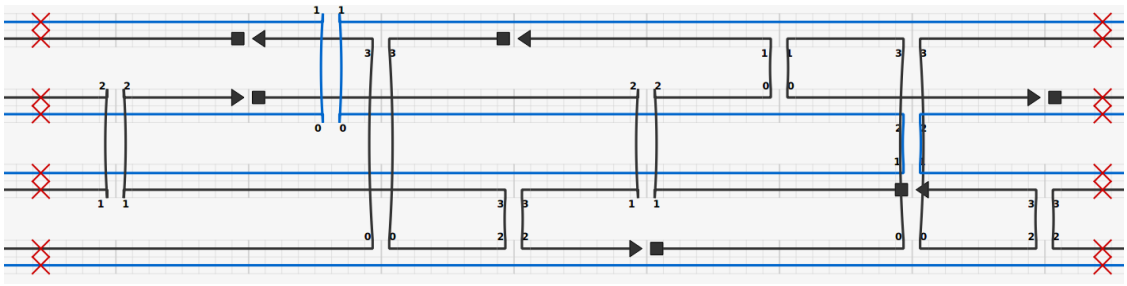
Figure 5.4: The variation of (a) l_b and (b) $l_t/2$ in the 10HB-5 nt system with increasing gap density.

Thus, oxDNA gives us a fair estimate of how gap density affects l_b. An added benefit of the simulations is that we are also able to estimate the twist persistence length. The trend in l_t versus gap density is very similar to that of l_b (Fig. 5.4(b)). Similar to the 10HB in Chapter 3, we find that the twist persistence length is approximately 1/5 of l_b. On going from 0–100% gap density, l_t decreases by 42%; i.e. the gaps have a very similar effect on both l_b and l_t.

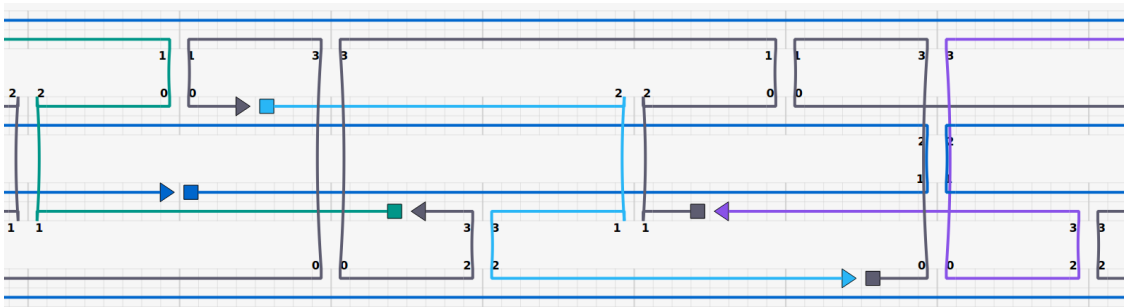
	size	density/%	N_{slice}	a (nm)	$\langle\Theta_3\rangle$ (°)	l_b (nm)	$l_t/2$ (nm)	radius (nm)
4HB	0	0	1784	0.3482	−0.609	1463.06	317.32	1.8799
4HB	1 nt	25	1784	0.3494	−0.695	1292.31	299.06	1.8803
4HB	1 nt	50	1784	0.3509	−0.808	1173.26	265.79	1.8895
4HB	1 nt	75	1784	0.3507	−0.908	1159.68	251.73	1.8994
4HB	1 nt	100	1784	0.3519	−1.007	1105.59	249.29	1.9106
4HB	3 nt	25	1784	0.3514	−0.769	1331.73	263.87	1.8874
4HB	3 nt	50	1784	0.3530	−0.924	958.65	230.49	1.9018
4HB	3 nt	75	1784	0.3538	−1.137	845.05	229.71	1.9200
4HB	3 nt	100	1784	0.3575	−1.354	610.97	181.13	1.9462
4HB	5 nt	25	1784	0.3519	−0.777	1009.08	237.64	1.8891
4HB	5 nt	50	1784	0.3556	−0.946	904.12	196.21	1.9092
4HB	5 nt	75	1784	0.3581	−1.227	627.77	158.58	1.9334
4HB	5 nt	100	1784	0.3620	−1.521	466.59	152.38	1.9695
10HB	0	0	707	0.3474	−0.066	15527.12	1554.53	
10HB	5 nt	20	707	0.3497	−0.107	14283.21	1384.97	
10HB	5 nt	40	707	0.3518	−0.155	13577.02	1219.72	
10HB	5 nt	60	707	0.3536	−0.216	11088.68	1120.76	
10HB	5 nt	80	707	0.3553	−0.315	9775.73	1035.66	
10HB	5 nt	100	707	0.3573	−0.421	8796.82	907.28	

Table 5.1: Gap size and density (0 indicates the system with no defects). Gap size of 1 nt , 3 nt and 5 nt denote that 1 nucleotide , 3 nucleotides and 5 nucleotides respectively have been removed from the available sites. Similarly, gap density refers to the percentage of available sites that have gaps. A gap density of 100% means that all available sites have gaps and a 25% gap density implies that only 25% of the total available sites incorporate gaps.

(a)



(b)



(c)

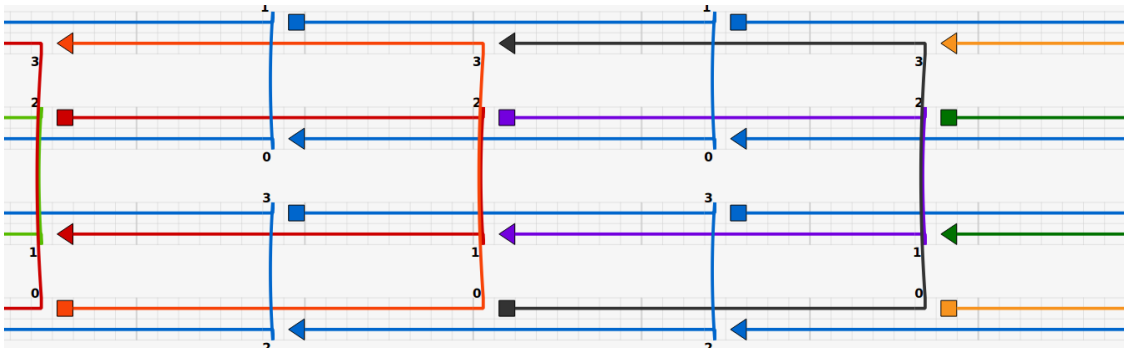


Figure 5.5: Cadnano sections of (a) 4HB-MT nanotube that was studied experimentally using magnetic tweezers [144]. The crosses indicate base-pair deletions. This origami also has bulky DNA blocks at the end to allow it to be attached to the magnetic tweezer beads (not shown in this section). (b) 4HB-no gap origami studied in this chapter. (c) 4HB-SST which has single cross-overs between adjacent helices every 21 slices and is relatively rigid. The systems in (a) and (c) were studied in Chapter 3.

5.3.2 l_b and l_t for 4HB gapped origamis

The 4HB origami that we study here is very similar in design to the 4HB-MT [144], with two major differences. Firstly, the ends of this origami do not contain bulky DNA blocks and secondly, the 4HB-MT system incorporated base-pair deletions to adjust the usual 8-bp junction separation of the square lattice to be compatible with a 63-bp repeat length that helps to reduce twist. The persistence length of the

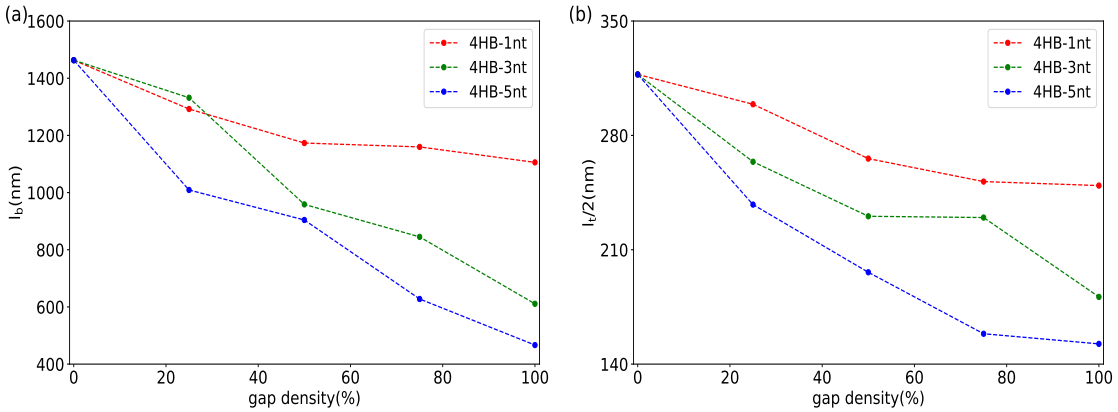


Figure 5.6: The variation of (a) l_b in 4HB-1 nt, 4HB-3 nt and 4HB-5 nt with increasing gap density and (b) $l_t/2$ 4HB-1 nt, 4HB-3 nt and 4HB-5 nt with increasing gap density.

4HB origami that we study in this chapter is larger than 4HB-MT but less than 4HB-SST. For the 4HB origami, we study 13 different variations that include no gap, 1 nucleotide gap, 3 nucleotide gap and 5 nucleotide gap with an incremental increase in gap density from 0 to 100% every 25%. The 4HB system has 1784 slices, making is roughly twice in size as compared to the 4HB-MT or 4HB-SST. This is the major reason of poor sampling in some systems despite running them for sufficiently long time. Fig. 5.5(a), (b) and (c) show the cadnano snapshots of all three 4HB nanotubes that have been studied in this thesis

Fig. 5.7 shows the correlation function plots used to calculate l_b and l_t for the 4HB origami without gaps. Both show clear exponential tails from which the limiting persistence lengths can be obtained. Equivalent plots for all the systems studied are included in Appendix C (See Figs. C.1–C.8).

The trend in l_b and $l_t/2$ is in good accordance with experiments. The experimental persistence length of the 4HB system without gaps is roughly 1000 nm. oxDNA estimates it to be around 1460 nm. Ref. [146] reports that maximum softening is observed for gaps of 5 nt at 100% gap density. oxDNA estimates a 68% drop in persistence length from about 1460 nm to 470 nm when the maximum gap size and density is incorporated into the 4HB nanotubes. Experiments report a 70% drop in l_b, and the persistence length of 4HB-5 nt system at 100% gap density is estimated to be 300 nm. Fig. 5.6(b) shows a similar trend for the variation of

l_t with gap size and density. Table 5.1 reports the l_b and $l_t/2$ for all the 4HB systems that have been studied using oxDNA.

The drop in persistence lengths for the other gapped systems is in good agreement with experiments. For the 4HB-3 nt system, we observe a drop of 58% in l_b with 100% gap density while the experimental drop is roughly 60%. A similar consensus is observed with the 4HB-1 nt system, where we observe a drop of 24% in l_b with 100% gap density, while experiments also suggest a 24% softening in l_b.

Thus, although the values of l_b predicted by oxDNA are generally larger than experiment, as expected from Chapter 3, the relative changes are generally well reproduced with the biggest differences being for the 10HB system. As noted in Chapter 3, sufficient sampling of these types of systems is challenging and so the values we obtain are likely to be subject to significant errors. This can be seen from the lack of smoothness in the variation of l_b with gap density in some of the plots in Figs. 5.4 and 5.6. Furthermore, inspection of the complete set of correlation functions in Figs. C.1–C.8 shows that not all have such clear exponential tails as those presented in Figs. 5.3 and 5.7.

That the persistence lengths decrease with gap density and gap size is physically intuitive. Not only do the gaps make bending easier for the individual helices that make up the origami, they also reduce the cost of stretching or compressing those helices that are on the outside or inside of a bend, respectively.

One might also questions how well worm-like chain models would be expected to apply when the systems have such heterogeneous local properties [217–219]. As noted in Chapter 3, DNA origamis are inherently heterogeneous because of the presence of junctions only at specific slices, but this is further increased with the addition of gaps. However, the correlation functions generally show the exponential tails expected for a worm-like chain and, in our opinion, the deviations that we do observe are more likely to be a result of sampling difficulties. Presumably that the persistence lengths, even at 100% gap density, are still much larger than the length scales associated with the local variations means that the large length scale thermal fluctuations behave similarly to a uniform system but with elastic moduli that are

some kind of average over the local mechanical properties. Whether systematic deviations from worm-like chain behaviour would occur for more extreme bending or twisting (but pre-buckling) is less clear.

5.4 Structural effects of the gaps

The gaps are expected to also affect the local properties of the origamis. For example, the local twist at a gap is not expected to be the same as for the DNA duplex. When fully-stacked, single-stranded DNA in oxDNA actually has a shorter pitch than duplex DNA, however when neighbouring bases are unstacked there is no longer any propensity for twist. The latter effect dominates and so the undertwist of the gapped sections leads to a left-handed torque on an untwisted origami. This effect is analogous to the well-known effects of deletions (missing base pairs) on the twist of origami structures [178]. Thus, for all systems the origamis become increasingly left-twisted (see the $\langle\Theta_3\rangle$ values in Table 5.1) for increasing gap densities with the effects being larger for larger gaps. The effects are also larger for the 4HB systems because they have a lower twist modulus. Hence we observe a left-handed twist of about 1.5° per slice when the gap size and density is maximum for the 4HB origami. Note that the 10HB origami without gaps is approximately untwisted, but that the 4HB system without gaps is already significantly left-handed. As the gaps are roughly uniformly spread through the origamis, $\langle\Theta_1\rangle$ and $\langle\Theta_2\rangle$ are roughly zero for all systems, irrespective of gap size or density; i.e. the origami are on average straight.

Another interesting local feature that we observe in gapped systems is subtle changes to the double-helical structure at gap sites. Fig. 5.2(c) shows us that the absence of nucleotides at gap sites leads to a slight splaying of neighbouring base pairs. The average distance between the base pairs around the gap sites is slightly larger than 0.5104 nm (the value in the centre of a duplex). The absence of bases at gap sites leads to a drop in stacking and cross-stacking interaction at the gap site, as well a removal of some of the constraints of backbone connectivity. As the gap size increases, this splaying of neighbouring base pairs becomes more pronounced.

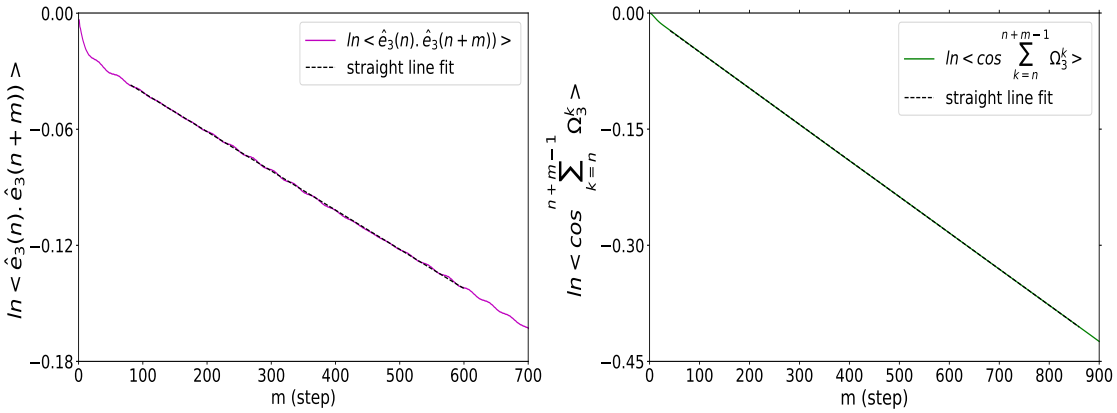


Figure 5.7: (a) $\log\langle\cos\theta(m)\rangle$ versus m and (b) exponential decay of the correlation function used to calculate $l_t/2$ for 4HB-no gap origami.

In DNA origami the helices at the double crossovers are constrained to be roughly anti-parallel. However, this is not the preferred geometry of a four-way junction [220]. One way that the junctions respond to this stress is for the helices to "splay" out at the junctions, leading to the characteristic "weave" patterns of helices that were noted in Rothemund's original origami paper [28]. This splaying increases the inter-helical spacing compared to close-packed straight helices. For the four-helix nanotubes, the radius provides a measure of the inter-helical spacing. From Table 5.1 it can be seen that introducing gaps systematically increases the radius with the effects being larger for larger gaps. The gaps reduce the stiffness of the helical sections allowing the helices more freedom to splay apart and increase their separation.

5.5 4HB with graduated gap size

So far in this chapter we have studied nanotubes with a homogeneous distribution of gaps in nanotubes along their length. Here, we would like to explore to what extent the same approach can be used to tailor the properties further to generate nanotubes with non-uniform mechanical properties. In particular, we investigate how an uniform increase in gap size along the nanotube would lead to a nanostructure with graduated flexibility.

One potential interest in doing this is that this mechanical polarity is likely to lead to an effective shape polarity because of the larger thermal fluctuations

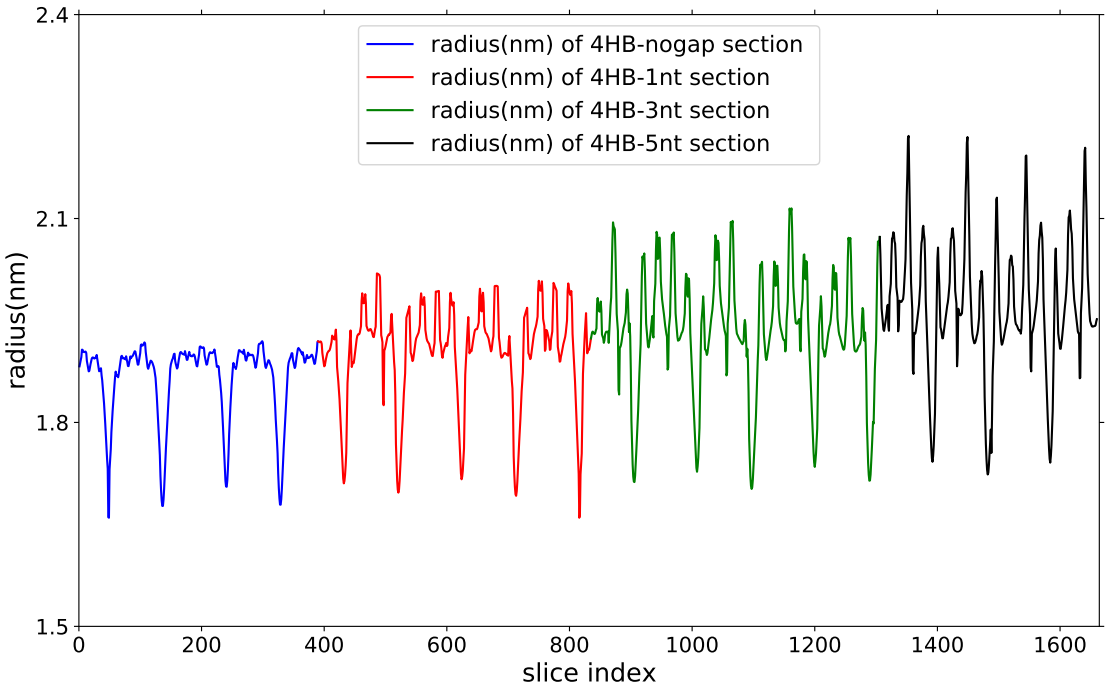


Figure 5.8: Variation of the radius of the graduated 4HB nanotube with slice index shows a gradual widening of the tube due to greater splaying as the gap size increases. The "no-gap" and the 5-nt-gap sections appear smaller due to the removal of the 60 terminal slices from each end for the analysis. The repeating motif in the graphs reflects the patterns of junctions and gaps with helices being closest together at junctions.

of the more flexible end. Previously, the liquid-crystalline behaviour of twisted DNA nanotubes has been studied experimentally [171] and theoretically [170] providing novel insights into how the chirality of the nanotubes and their fluctuations determines the chirality of the resulting cholesteric phase. For tapered rod-like particles, there is a theoretical expectation that they might form novel liquid-crystalline phases, such as splay-bend and twist-bend nematics [221, 222], but no such examples have been experimentally realized. This study might provide a first step towards that goal. We note that differential flexibility between otherwise identical molecules has been shown in simulations of binary mixtures to lead to phase separation into two nematic phases [223, 224].

We could construct the nanotube with graduated gaps in 2 possible ways. Either we could keep the gap size same throughout the tube and increase the gap density along the nanotube or an alternate way would be to keep the gap density constant throughout the tube but keep increasing the gap size from one end of the tube

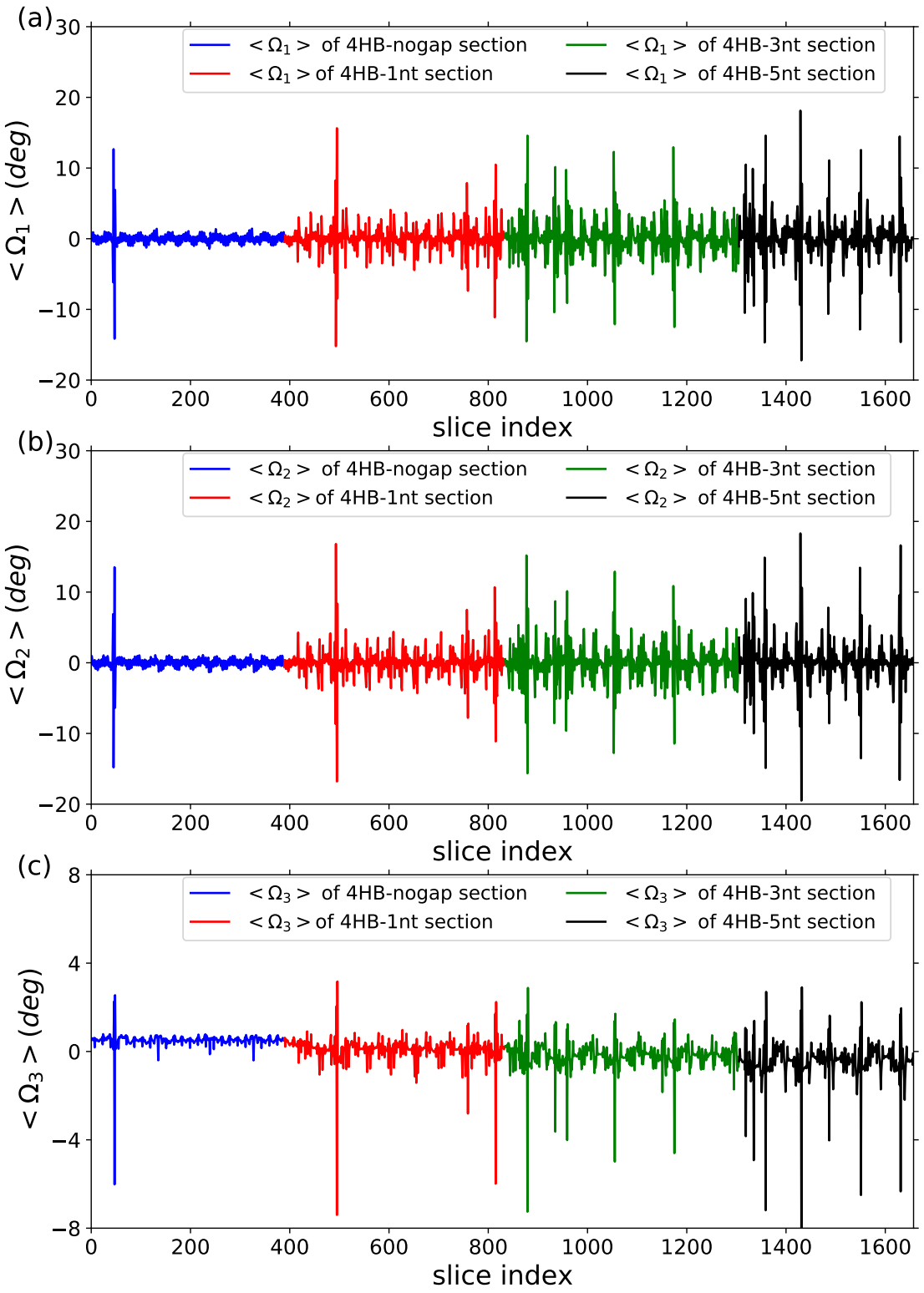


Figure 5.9: Although there is an increase in angular fluctuations along the tube, $\langle\Omega_1\rangle$ and $\langle\Omega_2\rangle$ are still centered at zero. By contrast, $\langle\Omega_3\rangle$ becomes more negative along the tube, consistent with the fact that the gaps lead the tube to being more left-twisted.

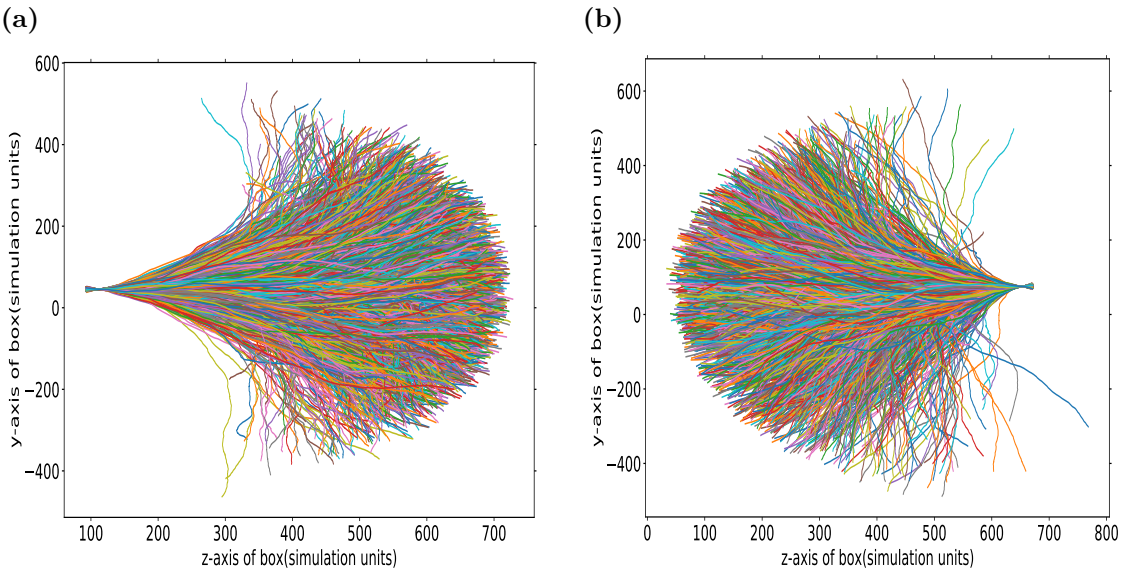


Figure 5.10: (a) The splay of centre lines of all 2371 configurations from the rigid end and (b) a wider splay of centre lines from the softer end in y-z axis shows the asymmetry in the nanotube. In case of a symmetrical nanotube , both ends would produce equal dispersion. The y- and z-axis in this plot are in oxDNA simulation units.

to the other. Since our oxDNA results are most overlapping with experiments at maximum gap density irrespective of the gap size, we decided to follow the latter approach to create the nanotube of interest. Since the 4HB origami has 1784 slices, we increase the gap size roughly every 446 slices; i.e. the first 446 slices have no gaps, followed by the next 446 slices having 1 nt gaps, the next 446 slices have 3 nt gaps and the last set of 446 slices contain 5 nt gaps all with 100 % gap density.

A possible way to measure the effect of increasing gap size along the tube is to calculate the radius (Eq. 3.22) of the nanotube at each slice. As we observed an increase in radius with gap size and gap density, this feature is well reflected in Fig. 5.8 as we see a gradual widening of the tube every 450 slices. There is an effective increase of about 0.1 nm (about 5%) in radius of the tube from the rigid end to the soft end.

Another interesting feature to note is the behaviour of the average values of the Ω's along the graduated tube (Fig. 5.9). There is an increase in the fluctuations of the Ω's suggestive of an increase in the bending and twisting flexibility of the nanotube from one end to the other. This can also be visualised in Fig. 5.2(a) and

(b) where the nanotube with 5 nt gaps displays a strong left-handed twist. Another way to show the anisotropy of the shape fluctuations is to plot the projected centre lines of configurations but where their axes systems have been aligned at either ends of the tube. Since the tube has 2 ends with very contrasting properties, Fig. 5.10(a) shows the dispersion of centre lines in the $y - z$ plane when the axes systems have been aligned along the z-axis at the 50^{th} slice from the rigid end (which has no gaps) while Fig. 5.10(b) shows the dispersion of centre lines in the $y-z$ plane when aligned at the 50^{th} slice from the softer end (which is infused with 5 nt gaps). As one would expect, the centre lines around the rigid end are more constrained and relatively less splayed as compared to the latter plot where the contours are more widely splayed.

5.6 Conclusion

The results reported in this chapter extend those in Chapter 3 and show that oxDNA can accurately capture the effects of defects, in this case gaps, on the mechanical properties of DNA origami and provide a more detailed microscopic picture of the underlying mechanisms. The results illustrate how the presence of assembly defects is likely to reduce the stiffness of DNA origami, consistent with our suggestion that such defects are likely to provide part of the explanation of why oxDNA predicts DNA origamis to be stiffer than inferred from experiment. The results also further show that defect engineering provides a rational design strategy to tailor the mechanical properties of the origamis to that required for a particular application. This is illustrated for the case of a nanotube with graduated flexibility, which may provide the starting point for the discovery of novel liquid-crystalline phases in systems of "tapered" rods.

It is again noteworthy that, within the limits of the simulation sampling, the behaviour of these systems on long length scales is consistent with worm-like chain models, despite being very heterogeneous on the local scales. In future work it would be interesting to see how such gapped DNA nanotubes respond to external

stresses and whether, for more extreme deviations from the equilibrium geometry, the systems can still be described by worm-like chain models.

It doesn't matter how beautiful your theory is, it doesn't matter how smart you are. If it doesn't agree with experiment, it's wrong

— Richard P. Feynman

6

Theoretical study of DNA force clamp - a reality check

Being able to predict the mechanical properties of DNA nanostructures theoretically with precision acts as an added tool for experimentalists. It allows them to choose their origami of interest and design experiments around it as they are aware of the mechanical limits of their substrate. With oxDNA acting as a suitable model to study these elastic mechanical properties [159], as we have shown in the previous chapters, it would be an added bonus if we can use oxDNA to help experimentalists decipher the unknown that may arise due to experimental limitations. oxDNA's ability to capture the effects of tension on small DNA motifs, such as duplexes [141] and hairpins [225, 226] has paved way to extend its use to more complex systems.

OxDNA simulations [187] of the unravelling of the Rothemund origami tile shed light on the effect of the design on the force response of DNA nanostructures. In particular, it revealed the mechanisms of tile unfolding and provided comparisons with other origami systems to which force spectroscopy had been experimentally

Reprint(adapted) with permission from [185]. *Copyright ©2021 , American Chemical Society.*

applied. Similarly, oxDNA has also been used to calibrate the origami force sensor [227] of Nickels *et al.* [52]. Additionally, oxDNA's good description of the thermodynamics of hybridization, hairpin formation [104], the force-extension curves of single-stranded DNA [105] and the persistence length of double-stranded DNA [104, 106] enable its use to model force sensors more generally. This chapter will focus on the theoretical setup and results obtained by modelling a DNA Origami-Polymer force clamp (OPFC) and is adapted from parts of [185] with relevant permission from the journal. This was a joint collaboration with experimentalists in the group of Khalid Salaita, Emory University, Atlanta, GA, USA. This work was done jointly with Navoneel Sen(MSc.), who carried out most simulations. I co-supervised this project and carried out some simulations and was involved in manuscript writing.

6.1 Experimental setup

The system is made up of a DNA origami substrate onto which the target molecules (in this study, DNA hairpins) are attached and a thermo-responsive polymer sphere, which when heated above its lower critical solution temperature (LCST) expels solvent and shrinks. The binding of the origami to the polymer sphere is accomplished using 21-bp long dsDNA strands. One end of each linker is attached to the origami and the other to the polymer sphere. Fig. 6.1(a) details the experimental setup. The shrinkage of the sphere exerts forces on the target molecules the state of which can be monitored using fluorescence techniques. In the experimental setup, each polymer sphere is able to bind to roughly 15 origamis and $\sim 10^{11}$ target molecules can be manipulated in a single experiment. The different systems studied are referred as L_x where x is defined as the minimum distance (in nm) between hairpins placed at opposite ends of the nanotube. Fig. 6.1(b) outlines the experimental results.

Reprint(adapted) with permission from [185]. *Copyright ©2021 , American Chemical Society.*

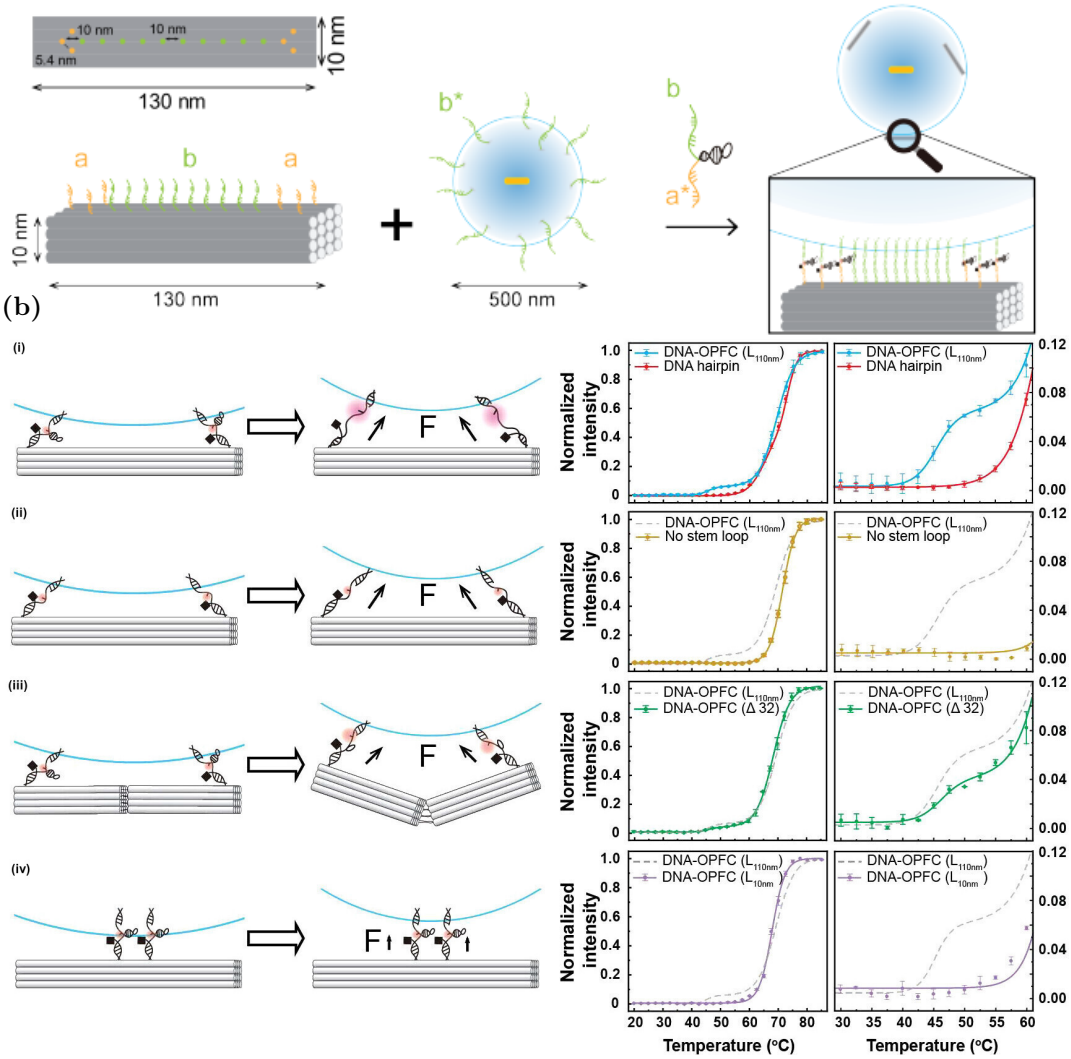


Figure 6.1: (a) Schematic of the DNA Origami-Polymer force clamp, particularly showing the layout of the DNA single strands on the origami and the polymer sphere that allow binding of the origami to the polymer sphere both directly via the linker duplexes and via the target hairpins. The sequences a and a* and b and b* are complementary. This example, denoted L_{110nm}, has the three hairpins bound at the end of the DNA origami rod. (b)(i) is a representation of L_{110nm} at low (left) and high (right) temperatures. The plots on the right show temperature-dependent fluorescence measurements of DNA hairpins (red curve) compared to mechanical unfolding of the same hairpin using OPFC (blue curve). (b)(ii) is a representation of L_{110nm} at low (left) and high (right) temperatures but without the hairpin stem and loop and shows no fluorescence enhancement at 45°C (yellow curve). (b)(iii) shows the mechanical changes in Δ32 at low (left) and high (right) temperatures. Since the origami has a 32 slice ssDNA section in the middle, the origami is relatively compliant and leads to dampening of the mechanical unfolding signal in experiments (green curve). (b)(iv) shows the different mechanical stresses exerted on the hairpins when they are positioned at the centre of the origami; hence L_{10nm} shows minimal signal enhancement compared to L_{110nm} suggesting any tensile stresses applied to these hairpins is below the threshold required to cause unfolding. The plot on the right in panels (b)(i)-(b)(iv) highlights the behaviour in the 30 to 60°C range. Error bars in each curve show standard deviation of n = 3 experiments. The fluorescence intensity was acquired at 575 nm from temperature-dependent fluorescence spectra.

Reprint(adapted) with permission from [185]. *Copyright ©2021 , American Chemical Society.*

6.2 System setup

In oxDNA simulations we do not model the sphere explicitly, but instead model it effectively by a set of harmonic traps that constrain the positions of the end nucleotides that are attached to the polymer sphere. These traps lie on the surface of a sphere with a radius appropriate for the given temperature. Fig. 6.2 illustrates our approach for calculating the positions of the traps at low temperature.

First, we calculate the centres of mass of the origami ($\mathbf{COM_O}$), its top layer ($\mathbf{COM_1}$) and its two top-most layers ($\mathbf{COM_{12}}$). From the centre of the top layer, we then added a vector of magnitude ($\mathbf{d} + \mathbf{r_{sphere}}$) in the direction given by the vector $\mathbf{V_1} = \mathbf{COM_{12}} - \mathbf{COM_O}$ to get the centre of the sphere ($\mathbf{A}$). We assume that the hairpins/linkers are attached to the closest point on the polymer sphere. The details are as follows. For each linker/hairpin, we define their point of attachment ($\mathbf{B_i}$) to the origami based on an equilibrated origami configuration; we then define the vector $\mathbf{V_2} = \mathbf{B_i} - \mathbf{A}$ for each linker/hairpin. In the direction of $\mathbf{V_2}$ we add a vector of magnitude $\mathbf{r_{sphere}}$ to $\mathbf{A}$ to get $\mathbf{C_i}$ the trap centre for that particular linker/hairpin that represents its attachment to the sphere. To calculate the trap positions for the sphere $\mathbf{C_i}$ at high temperature, we assume that the sphere undergoes a uniform contraction, keeping the angle ($\theta_\mathbf{i}$) same but decreasing $\mathbf{r_{sphere}}$ from 280 nm at 313 K to 205 nm at 328 K. After all the trap centres are calculated for the linkers and hairpins, the origami is simulated at 313 K and 328 K until the hairpins have reached the required distance from the centre of the sphere and the forces have equilibrated.

6.3 Simulation details

L_{110nm} is our initial model system, with the six hairpins located at the two extremes of the origami in groups of three. To investigate the effect of the position of the hairpins on the origami on the force exerted by the sphere, we simulated five more systems (L_{90nm}–L_{10nm}) where the hairpins were progressively moved to the centre of the origami. L_{10nm} had all the hairpins concentrated at the centre of the origami. The Δ32 system had the hairpins in the same position as L_{110nm} but lacked multiple

Reprint(adapted) with permission from [185]. *Copyright ©2021 , American Chemical Society.*

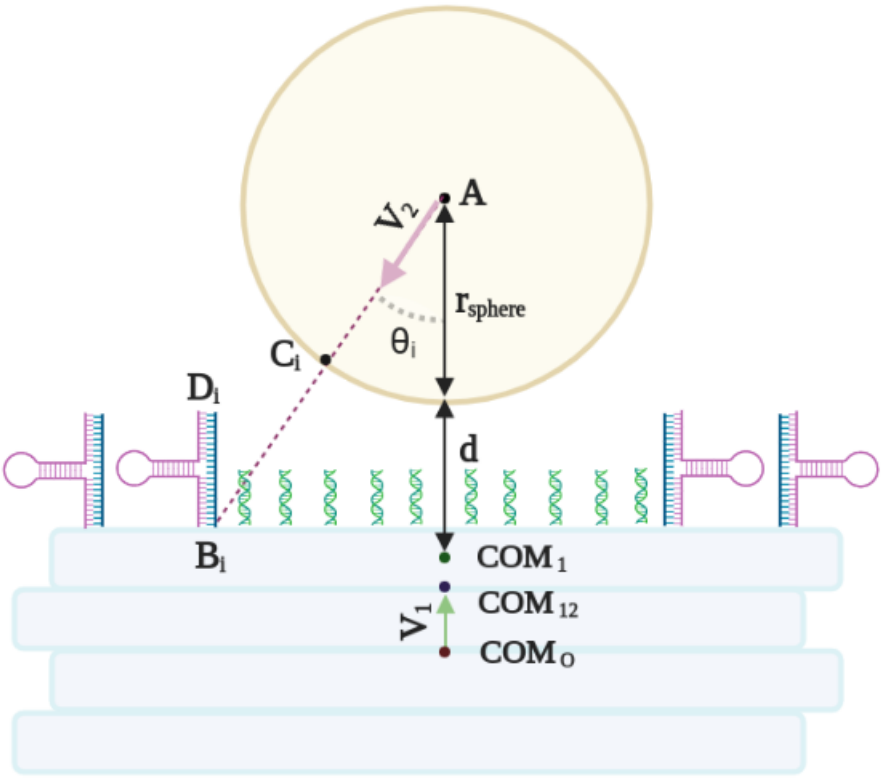


Figure 6.2: Schematic to show how the parameters for modelling the polymer sphere in the oxDNA simulations are chosen (for clarity only two of the three hairpins are shown). The relative sizes of the objects are not to scale.

staple strands at the centre of the origami. The absence of staple strands makes $\Delta 32$ much more flexible than the other origamis.

We assume the sphere to have a radius of 280 nm at 313 K and 205 nm at 328 K. We perform MD simulations to simulate each system at 313 K and 328 K in the canonical NVT ensemble which we will refer to as low and high temperature states. The coupling between the system and a heat bath is emulated by employing an Andersen-like thermostat [129]. We chose harmonic traps with a force constant of 28.545 pN/nm to model the effect of the sphere and run our simulations until the forces have equilibrated.

The only difference between the high and the low temperature states is the radius of the polymer sphere. At low temperature, the trap positions on the sphere are closer to the respective hairpins and linkers, and consequently the force felt is low. At high temperature, the sphere shrinks, and the trap positions all move

towards the centre of the sphere thereby increasing the distance between them and the hairpins and linkers which results in larger forces. The forces felt by the origami at high temperature has a compressive component as well as a lateral bending component because of the sphere shrinkage.

We also perform simulations at high temperature with "mutual traps" between the nucleotides in the hairpin so that the hairpins are prevented from unfolding, thus allowing us to obtain the forces experienced in the absence of any hairpin unravelling.

Assumptions

There are a number of assumptions in the setup of the simulations of which it is important to be aware.

- Firstly, we assume that when the hairpins and linkers attach to the polymer sphere (in the low temperature regime for the sphere size) they attach to the closest point on the polymer spheres, which we assume are perfectly smooth. In practice, although this is a reasonable assumption for the average position of the attachment points across the ensemble of origamis, we expect there to be a distribution of such points across the ensemble of origamis. We do not account for this potential heterogeneity in the population of the OPFCs.

- Secondly, we do not explicitly account for the elastic mechanical properties of the sphere. For example, the spring constant for our harmonic traps is in the "stiff-sphere" limit where the obtained forces do not depend on the spring constant because the origami is more compliant than the traps.

- Thirdly, we assume that all the hairpins and linkers are simultaneously attached to the sphere. The parallel application of the forces through all these linkers and hairpins is the reason for the significant bending of the origami that we will observe. If all linkers/hairpins are not bound, then the total applied force on the origami is likely to be less and the origami less bent, which in turn is likely to lead to higher forces through the hairpins/linkers that are attached.

Reprint(adapted) with permission from [185]. *Copyright ©2021 , American Chemical Society.*

Upon close inspection we note that the 16HB origami has an inherent twist of around -80° between the two ends. Such twist is expected for an origami based on a square lattice of helices without insertions or deletions [228]. However, this twist is too low to affect the geometric assumptions of the design.

6.4 Results

Configurations for each of the origami force clamps is illustrated in Table 6.1 at both low and high temperature. The combined effect of the forces on the hairpins and linkers causes the origami to bend significantly. Although, the force acting through each individual hairpin/linker is not particularly high, the sum of all such forces is substantial. At low temperature, we note that all the hairpins and linkers are roughly oriented radially towards the centre of the sphere, meaning they are co-linear with the radius vector at that point on the sphere. We note from the average forces that as the sphere shrinks, the hairpins and linkers in the centre of the origami tend to be in a state of compression rather than tension because of their proximity to the surface of the sphere.

At high temperature, the origami bends more as a result of the higher average force exerted on the system. The average bending is more for L_{10nm} than L_{110nm} because of the tension in the outer linkers in L_{10nm} whereas in L_{110nm}, the hairpins can also absorb the stress by unfolding. The deletion of 16 staple strands in $\Delta 32$ gives the origami significantly more flexibility and therefore it bends more at high temperature. We observe that the average angle between the two origami blocks on either side of the flexible section is significantly smaller at 328 K (137.5°) compared to at 313 K (167.0°) because the origami has deformed to absorb much of the strain due to the particle collapse, thereby making hairpin unfolding much less likely.

Reprint(adapted) with permission from [185]. *Copyright ©2021 , American Chemical Society.*

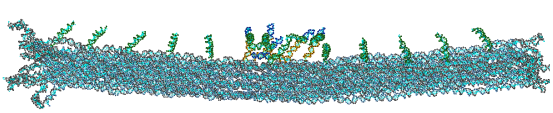
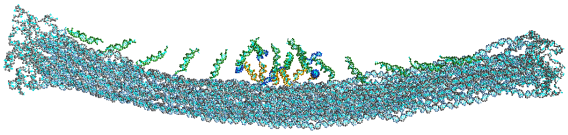
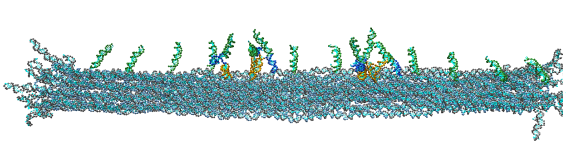
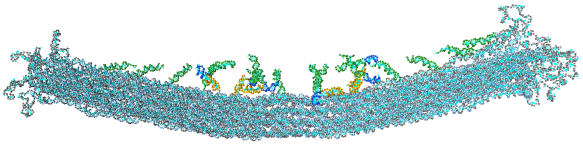
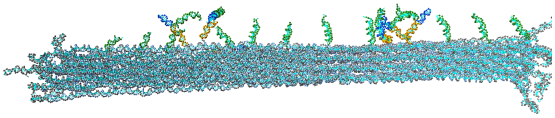
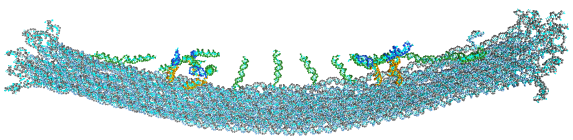
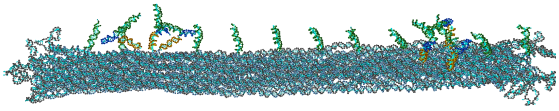
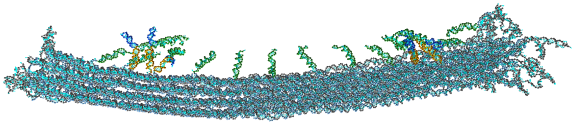
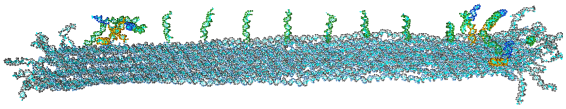
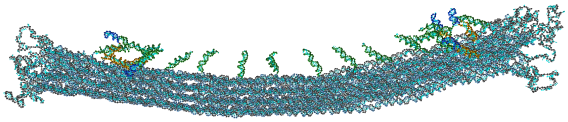
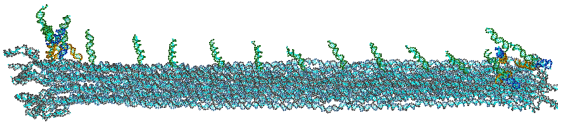
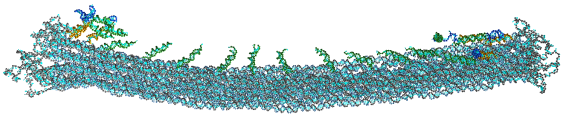
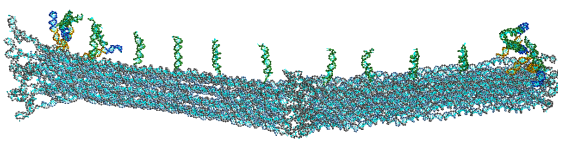
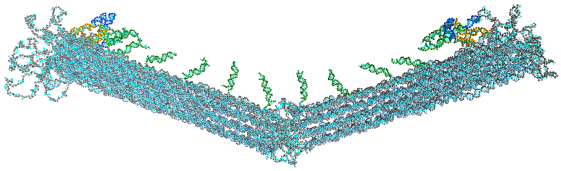
System	Low temperature	High temperature
L_{10nm}		
L_{30nm}		
L_{50nm}		
L_{70nm}		
L_{90nm}		
L_{110nm}		
Δ32		

Table 6.1: Snapshots of L_{10nm}-L_{110nm} and Δ32 at low and high temperatures. At high temperature, a strong bend is visible in all systems from L_{10nm} to L_{110nm} while Δ32 is kinked.

Reprint(adapted) with permission from [185]. *Copyright ©2021 , American Chemical Society.*

Configuration	$\mathbf{F}_{\parallel}^{\text{low}}$ (pN)	$\mathbf{F}_{\parallel}^{\text{high}}$ (pN)
L_{10nm}	-0.18 ± 0.72	-0.63 ± 0.25
L_{30nm}	-0.06 ± 0.83	-0.40 ± 0.42
L_{50nm}	-0.23 ± 0.64	-0.08 ± 0.59
L_{70nm}	-0.13 ± 0.69	0.72 ± 0.81
L_{90nm}	-0.10 ± 0.71	2.61 ± 2.04
L_{110nm}	0.31 ± 0.97	4.46 ± 1.85
$\Delta 32$	-0.25 ± 0.34	1.26 ± 1.04

Table 6.2: Average force along hairpins at low and high temperatures. A graphical representation of this data is given in fig. 6.3.

6.5 Measurement of forces

The forces transmitted through the hairpins and linkers can be measured through the forces exerted by the traps modelling their attachment points to the sphere. These traps are harmonic, and so forces they exert have the form $\mathbf{F} = -\mathbf{k}(\mathbf{r} - \mathbf{r_0})$ where $\mathbf{F}$ is the instantaneous force, k is the spring constant or stiffness, $\mathbf{r}$ is the position of the nucleotide at that instant and $\mathbf{r_0}$ is the equilibrium position of the trap. If $\mathbf{F}$ is the total force acting on a nucleotide at any instance, the force through the hairpin is measured by defining a component of this force $\mathbf{F}_{||}$ which acts along the direction given by the vector $\mathbf{V_3} = \mathbf{B_i} - \mathbf{D_i}$ where $\mathbf{D_i}$ is the position of the top-most nucleotide in that strand (the nucleotide on which the trap force is being applied). So, we have:

$$\mathbf{F}_{\parallel} = \mathbf{F} \cdot \frac{\mathbf{V_3}}{||\mathbf{V_3}||} \tag{6.1}$$

We can say that if $\mathbf{F}_{||} > \mathbf{0}$, the linker/hairpin is under tension and if $\mathbf{F}_{||} < \mathbf{0}$, the linker/hairpin is under compression. $\mathbf{F}$ and $\mathbf{F}_{||}$ were measured at low and high temperatures for each hairpin and were averaged over all configurations and all hairpins in the system (Table 6.2 and graphical representation of the same is shown in Fig. 6.3).

We note that there are fast fluctuations in the instantaneous force due to the trapped nucleotides oscillating around their average position in the trap centre;

Reprint(adapted) with permission from [185]. *Copyright ©2021 , American Chemical Society.*

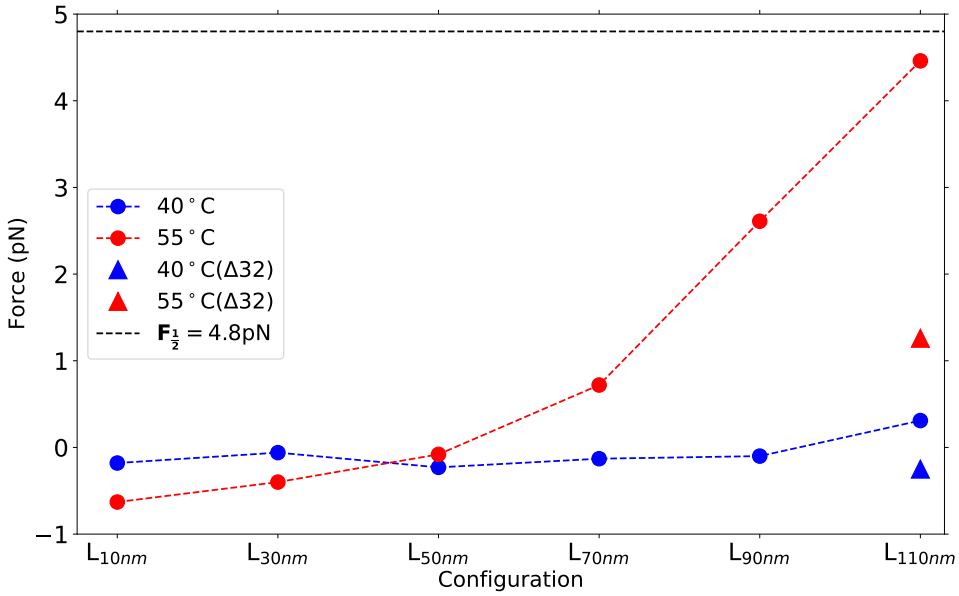


Figure 6.3: The average force acting on all hairpins for each system at low and high temperature. Results of the force experienced by hairpins on Δ32 are plotted using triangles. The dashed black line represents the $\mathbf{F}_{\frac{1}{2}}$ of the hairpin.

thus, the force distribution is quite wide. At low temperature, we do not observe any of the hairpins breaking. Under high temperature conditions, some of the hairpins break which can be attributed to both thermal and mechanical effects. We clearly observe a trend in hairpin unfolding based upon the position of the hairpin on the origami. The hairpins close to the centre of the origami (L_{10nm}) feel the least tension and the ones towards the extremes (L_{110nm}) are the most stressed. Very long simulations are required to average out the forces due to a heterogeneous spread of forces along the origami.

From Table 6.1 it is clear that none of the systems have hairpins under strong tension at 313 K. At 328 K, only the hairpins of L_{110nm} experience tension comparable to their $\mathbf{F}_{\frac{1}{2}}(\sim 4.8pN)$. $\mathbf{F}_{\frac{1}{2}}$ is defined as the force that leads to a 50% probability of unfolding at equilibrium. For this experimental study it was measured at a temperature of 45°C with a salt concentration of 0.01 M Mg^{2+}. This value of $\mathbf{F}_{\frac{1}{2}}$ is obtained via time-dependent fluorescence experiments which is based on "single molecule force-jump" optical tweezer technique introduced by Tinoco and

Reprint(adapted) with permission from [185]. *Copyright ©2021 , American Chemical Society.*

Bustamante [229]. As the experimentalists also observed some hairpin unfolding for the L_{110nm} system, we calculated the force in a system with the hairpins constrained to be unfolded. This leads to a lower tensile force through these strands and the origami is less bent compared to when the hairpins are fully formed, as expected.

Our oxDNA results thus suggest that for a perfectly assembled origami-polymer force clamp the forces passing through the hairpins in the L_{110nm} system are approaching those required to start to unfold the hairpins. Note the experimental signal for mechanical unfolding only suggests that a sub-fraction of the hairpins are open at any one time. Furthermore, it is likely that not all the force clamps are perfectly assembled. For example, in simulations of the L_{110nm} where the linker at either end that is closest to the hairpins was not bound, the force through the intact hairpins increased to 6.1 pN, a value expected to be sufficient to initiate hairpin opening.

6.6 Conclusion

This collaborative study yielded results which were in good correlation with the experiments. The use of oxDNA as a tool provided insight into the mechanical response of the origami when subject to the stresses through its use in this force clamp. Furthermore, being able to directly measure the degree of bending or average twist along the origami would not have been an easy task on the experimental front. Moreover, oxDNA modelling adds a visual sense and deeper understanding of what is really happening on a microscopic level whereas the experiments on their own would have just had to rely on the changes in fluorescence to provide a physical explanation of the behaviour of the force clamp.

For example, without the insights provided by the simulations, it might have been tempting to assume that the origami rods would behave like rigid blocks (we estimate that their persistence length is about 30 μm using the methods of Chapter 3). However, such an assumption would have led to a significant over-estimate of the strain being applied to the hairpins and the effective forces to

Reprint(adapted) with permission from [185]. *Copyright ©2021 , American Chemical Society.*

which the hairpins would have been subject. A proper view of the compliance of the origami is thus key to understanding why only a sub-fraction of the hairpins undergo mechanical unfolding.

People do not like to think. If one thinks, one must reach conclusions. Conclusions are not always pleasant

— Helen Keller

7

Conclusions and Future Work

In this thesis we have used simulations using the oxDNA coarse-grained model to better understand the mechanical properties of DNA nanotubes and rods. This has encompassed both their elastic behaviour and buckling under extreme twist stress, the effects of defects and an example application where an accurate model of the mechanical response of the DNA origami plays a key role in the performance of the nanodevice.

In considering rod-like DNA origami, a natural first model is the worm-like chain. However, there were a number of open questions concerning its potential applicability to these systems. Is the non-uniformity of the origami at a local level (due to junctions, nicks, gaps, insertions, deletions ...) an issue? Does stress localization at weaker points lead to deviation from worm-like chain behaviour as stresses become more extreme? Can the worm-like chain model describe the plectonemic buckling of these systems at extreme twists, as it mostly does for double-stranded DNA?

The first of these questions is directly addressed in Chapter 3, where we adapt the approach of Ref. [163], which was applied to dsDNA, to calculate persistence

lengths and elastic moduli associated with bending and twisting for a set of 10 different rod-like DNA nanostructures ranging from a 4HB on a square lattice to a 10HB with a double-hexagon cross-section. Particular challenges that needed to be overcome were the very long simulation times that were required to sufficiently sample their thermal fluctuations and how best to extract the limiting values of the elastic moduli. The source of the issue for the latter is that although the long-length scale fluctuations are generally well-described by the worm-like chain (e.g. exponential decay of the relevant correlation functions associated with the persistence lengths) the thermal fluctuations on shorter length scales are significantly larger than would be predicted by this worm-like chain description. Such behaviour has also been seen for dsDNA [163, 230], but the added complication here is that, as the bending moduli are much larger than the contour length, a new coarse-graining procedure had to be introduced.

As expected, the most important factor determining the mechanical properties was the number of helices, but on top of that were subtle dependencies on the detailed design, such as the nature of the junctions (e.g. single crossover versus double crossover) and the positioning of the junctions and strand ends. A noteworthy feature was that the values of the bending persistence lengths predicted by oxDNA were larger than those estimated in experiment. Although this is likely to be partly due to inaccuracies in the oxDNA model (e.g. overestimation of dsDNA's stretch modulus), another significant factor is the potential role of defects. The oxDNA values are for perfectly-assembled nanostructures, whereas it is likely that an experimental ensemble of origamis will involve a range of defects, most of which are likely to soften the mechanical properties.

In Chapter 4 we introduced an approach to exert external twist stresses on a DNA nanostructure, applying it to two of the DNA nanotubes studied in Chapter 3. As well as providing an alternative approach to access their twist modulus from the elastic response, this setup allowed us to address questions concerning the nature of the twist buckling in such systems for the first time. Like with dsDNA, the DNA nanotubes formed plectonemes and showed some similar qualitative

features, e.g. the approximately linear decrease in the end-to-end extension and the plateau in the torque as the plectonemes grow with increasing applied twist. However, the plectonemes show significant structural differences from those formed by dsDNA due to the nanotubes' very different positioning in the space of basic mechanical properties. Specifically, as the bending persistence length is much larger than the contour length, the curvatures required to form plectonemes in these systems exceed those where worm-like-chain bending can be expected, not just at the plectoneme tip, but also at the base of the plectoneme and in the plectonemic braid. This leads to sharp kinking at the plectoneme tip and a tendency to localize bending in one of the two sections of the nanotubes that make up the braid. The latter can occur both at the base, thus giving a "slanted" configuration where the orientation of the plectonemic stem is no longer perpendicular to the twist axis, and in the stem, where one of filaments is relatively straight and the other wraps around it in a helical fashion. Detailed quantitative analysis of these systems, however, is hampered by the extreme difficulties of fully equilibrating the simulations, because of the fundamentally slow kinetics associated with such strongly kinked and tightly wrapped plectonemes.

In Chapter 5 we considered the effects of gaps between staple strand ends on the mechanical properties of rod-like DNA origami, both to better understand the mechanical effects of defects and as a potential means to tailor mechanical properties. This was achieved using the methods of Chapter 3 but with the addition of a definition of the helix centre in the gapped regions. The relative mechanical softening as the number of introduced gaps increased overlapped well with experimental results for the bending persistence length [146]. In addition, the simulations were able to show that the defects had a similar effect on the twist persistence length and provided microscopic insights into the structural changes induced by the gaps and the mechanisms of mechanical softening.

Finally, in Chapter 6 we performed simulations to help provide a better understanding of an experimental force clamp that was being developed in the Salaita group. In particular, these highlighted how properly accounting for the bending

compliance of the origami component of the force clamp was vital to any prediction of the forces being exerted on the target molecules. This study also showed both how deliberately induced defects could modulate the properties of this nanodevice and how assembly defects could potentially have a very large effect on device performance.

Experimental collaborations, like the one above, are always a very positive learning experience as we get to know the limitations associated with studying such origami systems experimentally, as well as theoretically. Such collaborations are generally a win-win situation as they not only benefit the experimentalists but also offer an opportunity to us as a theoretical chemist to improve and extend our models and incorporate more experiment-friendly features.

The thesis has convincingly shown that coarse-grained modelling with oxDNA provides a reliable means to estimate mechanical properties of DNA origamis that are hard or even impossible to access experimentally. Furthermore, the simulations also allow fundamental insights into how these properties are connected to structural and design features on the microscopic level. As illustrated by Chapter 6, such simulations have a lot to offer the DNA nanotechnology community, particularly as experimental groups attempt to develop increasingly complex nanomechanical devices.

There are of course limitations to our approaches. Firstly, accurate characterization of these mechanical properties, even with a computationally efficient model like oxDNA, requires very long simulation runs. Notably, when we were considering the twist buckling of DNA nanotubes, we were restricted to at most semi-quantitative insights because full equilibration of the systems was unfeasible. Secondly, the oxDNA model is, unsurprisingly, not perfect. For example, we highlighted the potential effects of oxDNA's overestimate of the dsDNA stretch modulus on the bending persistence length.

The thesis also highlighted the importance of a better understanding of assembly defects for the DNA nanotechnology field. Knowledge of the nature and likelihood of such defects is still relative limited and likewise for their effects. Of course, for some

application such defects might be of little import, but for nanomechanical devices that seeks to apply or measure well-defined forces that is unlikely to be the case.

There are number of natural future research projects that directly build on the work described in this thesis. For example, it would be interesting to quantify how defects, such as the gaps considered here, affect mechanical buckling, both with respect to bending (this has been studied in Ref. [179] for defect-free DNA nanotubes) and twisting, as one would imagine that the defects are likely to facilitate the earlier onset of stress localization. Furthermore, it would be interesting to extend theories of plectoneme formation to better understand how the behaviour evolves as l_b/l_c and l_b/l_t increase away from the values typical of dsDNA. Finally, this thesis has been restricted to "one-dimensional" rod-like objects where the worm-like chain is the natural model. Characterizing the mechanical properties of two-dimensional origami sheets or three-dimensional blocks is likely to provide new challenges and opportunities.

I also hope that the work described in this thesis and the skills I have developed will be the basis for further experimental collaborations. As Sir Ronald Fisher said, "To call in the statistician after the experiment is done may be no more than asking him to perform a post-mortem examination: he may be able to say what the experiment died of." As a theoretical chemist, I always look forward towards developing tools and models that can complement experimental findings and offer accurate diagnostics for improvements.

Appendices

A

SI 1

A.1 Further Equilibration and Simulation details

Figure A.1 shows the end-to-end distance in the molecular dynamics trajectories for four example systems. The 6HB-SST nanotube shows relatively fast fluctuations over the range of end-to-end distances it samples. An origami system with the same number of helices (6HB-S) exhibits both a wider range of end-to-end distances (reflecting its lower bend persistence length) and a slower sampling of those distances. In chapter 3 we have suggested the latter may be due to the more constrained nature of the junctions in origamis and a coupling of bending to changes in junction geometry. It is noticeable that distributions of Ω_1 and Ω_2 for the origamis have a greater degree of non-Gaussianity than for the SST nanotubes (Figs. A.2-A.4). Another possible source of slow dynamics is if there is a coupling of more extreme bending with base-pair breaking (note that all the 6HB origamis have some very short 2 base-pair binding domains).

The plot for the 4HB-MT shows even slower dynamics and parts of the trajectory

Reprint(adapted) with permission from [159]. *Copyright ©2020 , American Chemical Society.*

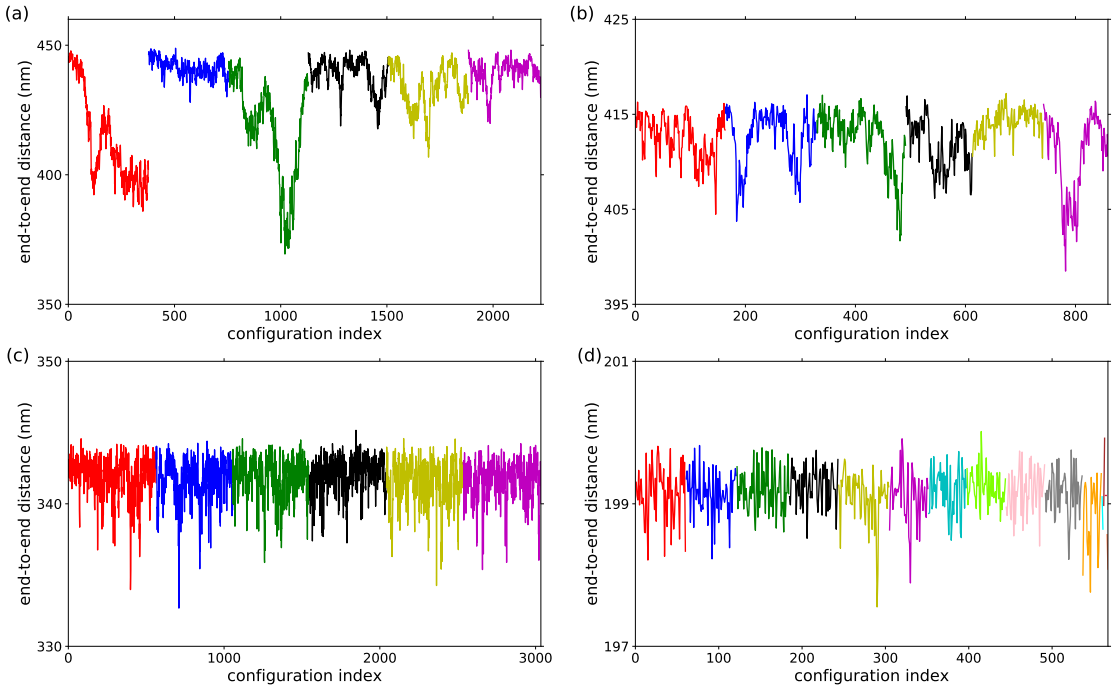


Figure A.1: The fluctuation of the "end-to-end" distance during the molecular dynamics trajectories for (a) 4HB-MT, (b) 6HB-S, (c) 6HB-SST and (d) 10HB. The different colours represent separate trajectories. Each configuration is separated by 6.06 μs. In order for the measure to capture the fluctuations of the molecular contour in the bulk of the tube, the distance is measured between slices that are 100 slices in from each end.

show fluctuation to anomalously bent configurations. The former may be partly due to the effects of the blocks on the ends of these origamis, but the reason for the extremely bent configurations (e.g. the second configuration in Fig. 3.3) is less clear (one unique feature of the 4HB-MT design is that it has some junctions where one helix has a nick on the strand not involved in the crossover). As a result of this, the statistics for this system are probably the worst.

Furthermore, the extreme bending leads to a breakdown of worm-like chain behaviour. For example, the tangent-tangent correlation function lacks a perfectly exponential tail, and that the m-dependent persistence length exhibits a broad maximum (Fig. A.15(a)), rather than smoothly increasing to its limiting value, is a sign that the fluctuations on the longest length scales are greater than one would expect from the (better sampled) shorter length scale fluctuations. That the 6HB-MT origami also exhibits a similar broad maximum (Fig. A.15(a)), in contrast to all the other systems, perhaps suggests that this may not simply be a

	t_{sim}/ms	N_{config}	N_{ends}	$n_{\text{avg}}^{A_1}$	$n_{\text{avg}}^{A_2}$	n_{avg}^{C}	m_{limit}
4HB-MT	13.48	2225	60	20	20	5	600
4HB-SST	6.81	1124	60	15	15	5	600
6HB-2×LH	8.52	1406	60	20	20	5	600
6HB-1×LH	8.05	1328	60	20	20	5	600
6HB-S	5.21	859	60	20	20	5	600
6HB-1×RH	8.34	1376	60	20	20	5	600
6HB-MT	13.33	2199	60	20	20	5	600
6HB-SST	18.38	3034	60	20	20	5	600
8HB-SST	13.91	2295	60	40	40	5	600
10HB	3.44	567	60	40	20	5	400

Table A.1: Details of the simulations and the parameters used when calculating elastic properties. t_{sim} is the total simulation time of the trajectories. N_{config} is the number of configurations in the ensemble used to calculate the elastic properties of each system. N_{ends} is the number of slices at each end that are ignored in these calculations. $2n_{\text{avg}}^{X}+1$ is the number of slices over which averaging is performed in Eq. (3.21) for the elastic constant X. m_{limit} is the value of m used when taking the limiting values of the elastic constants.

case of insufficient sampling, but that the "MT" origami are behaving somewhat differently. The obvious difference from the other origamis is the blocks on the end, but it is hard to see why these might facilitate anomalously large bending fluctuations on long length scales.

We also include data for the 10HB origami in Fig. A.1. This illustrates that as the origami become stiffer the fluctuations become faster and easier to sample.

From the above it is clear that the fluctuations of the SST nanotubes are the most well sampled, and hence the ensembles of configurations are least correlated. It is also noticeable that these systems also have values for the coupling terms that are closest to zero, and in the cases where expected (6HB-SST and 8HB-SST) A_1 and A_2 values that are most similar (Fig. A.21). The greater regularity of their pattern of junctions also likely plays a role.

The total simulation time used to generate the configurations and the consequent size of the configurational ensembles used for each system are given in Table A.1. It also contains details of the parameters used in our calculations of the mechanical properties.

Reprint(adapted) with permission from [159]. *Copyright ©2020 , American Chemical Society.*

A.2 Further details of mechanical properties calculations

A.2.1 Angular deformations distributions

The cumulative angular deformations used in Eq. 3.7 are defined by

$$\Omega^{(k)}_{i,\mathrm{cum}}(m) = \sum_{k=n}^{n+m-1} \Omega^{(k)}_i \tag{A.1}$$

The probability distributions of $a\Omega_{i,\mathrm{cum}}(m)/\sqrt{m}$ for the 4HB-MT and 6HB-MT origamis and the 6HB-SST nanotube for are plotted in Figs. A.2–A.4, respectively. As expected from the central-limit theorem, the distributions become more Gaussian-like as n_{avg} increases, confirming that worm-like chain behaviour holds at longer renormalized length scales. The distributions for the bending deformations become narrower as m increase, consistent with the increase in the m-dependent bending elastic constants with m.

A.2.2 Further effects of α

In Fig. A.5 we show plots of the m-dependent elastic moduli for example origami and SST systems at $\alpha = 0$, i.e. without the correction to remove the helical component of the centreline of double-stranded DNA in oxDNA. Like the plot of the m-dependent persistence length for 6HB-S in chapter 3 (Fig. 3.6(d)) the bending elastic moduli for this system show strong oscillations on the length scale of the DNA pitch. By contrast, the SST systems show a smooth monotonic rise even at $\alpha = 0$. The reason for this is most likely because the single crossovers in these systems place fewer constraints on the relative twist of different helices. The strong correlations between the orientations of the individual helices in the origamis give an additive effect causing the helix-bundle centerlines to have a significant helical character. By contrast, the reduced local orientation correlations in the SST systems cause

Reprint(adapted) with permission from [159]. *Copyright ©2020 , American Chemical Society.*

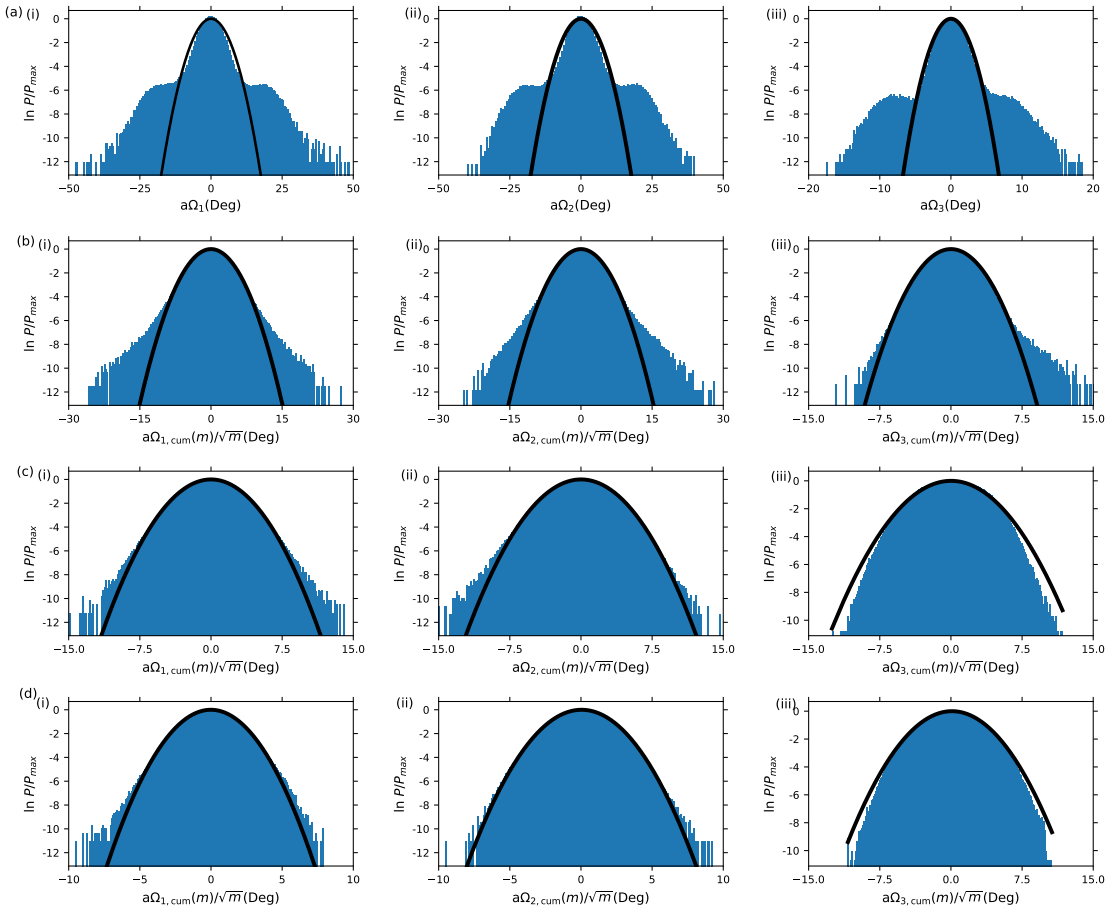


Figure A.2: Probability distributions for (i) $a\Omega_{1,\mathrm{cum}}(m)/\sqrt{m}$, (ii) $a\Omega_{2,\mathrm{cum}}(m)/\sqrt{m}$, and (iii) $a\Omega_{3,\mathrm{cum}}(m)/\sqrt{m}$ for the 4HB-MT origami at different values of m: (a) $m = 1$, (b) $m = 3$, (c) $m = 11$ and (d) $m = 41$. The solid lines are Gaussian fits to the distributions.

the helical character of the centerlines of the individual DNA helices to cancel out giving a smooth nanotube centreline.

The dependence of the elastic constants of double-stranded DNA on α using Triad III of Ref. [163] are depicted in Fig. A.6. The structural and mechanical properties of double-stranded DNA at $\alpha = 0$, i.e. without any correction for the helicity of the centreline, and at $\alpha = 0.06$ (the value that removes the net helicity) are given in Table A.2. Also included in the table are the predicted elastic constants obtained by applying a transformation from a helical to a straight coordinate system, the expressions for which were derived in Ref. [175]. Comparing the two methods for removing the helicity of the centreline, the changes in A_2, C and G are in the same direction, but with some differences in the magnitudes of the changes, and

Reprint(adapted) with permission from [159]. *Copyright ©2020 , American Chemical Society.*

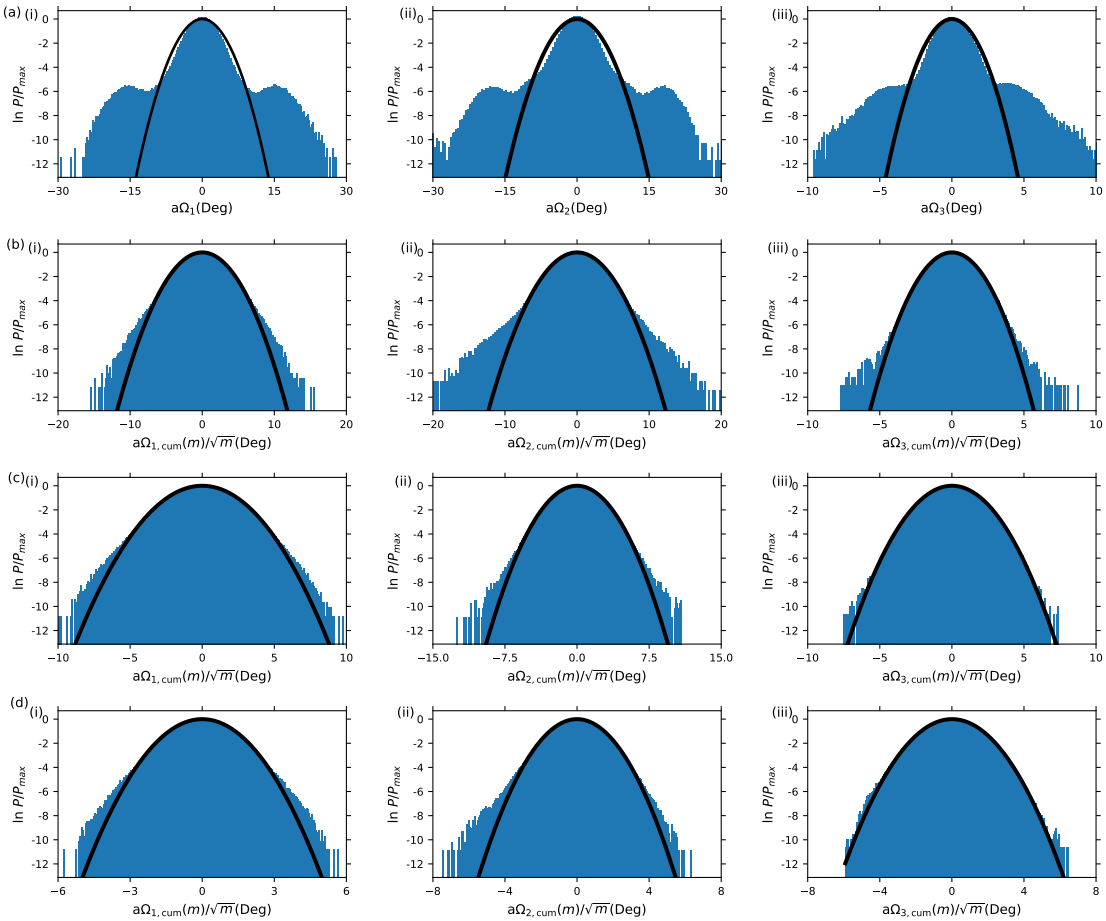


Figure A.3: Probability distributions for (i) $a\Omega_{1,\mathrm{cum}}(m)/\sqrt{m}$, (ii) $a\Omega_{2,\mathrm{cum}}(m)/\sqrt{m}$, and (iii) $a\Omega_{3,\mathrm{cum}}(m)/\sqrt{m}$ for the 6HB-MT origami at different values of m: (a) $m = 1$, (b) $m = 3$, (c) $m = 11$ and (d) $m = 41$. The solid lines are Gaussian fits to the distributions.

although the coordinate transformation approach predicts no change in A_1, we observe a small decrease on going from $\alpha = 0$ to $\alpha = 0.06$.

The removal of the helicity centreline makes little difference to the bending persistence length, but leads to a significant increase in the measured twist persistence length. Note also that compensating for the helicity reduces the measured pitch $(360/\langle\Theta_3\rangle)$ from 10.54 to 10.51 bp.

A.2.3 Triad definitions

The definitions of $\hat{\mathbf{x}}$ and $\hat{\mathbf{y}}$ for the six helix bundles are given in chapter 3, and schematically indicated in Fig. 3.5(c) for the other systems. Here, we give their mathematical definitions, where the numbering of the helices is as in Fig. 3.5(c).

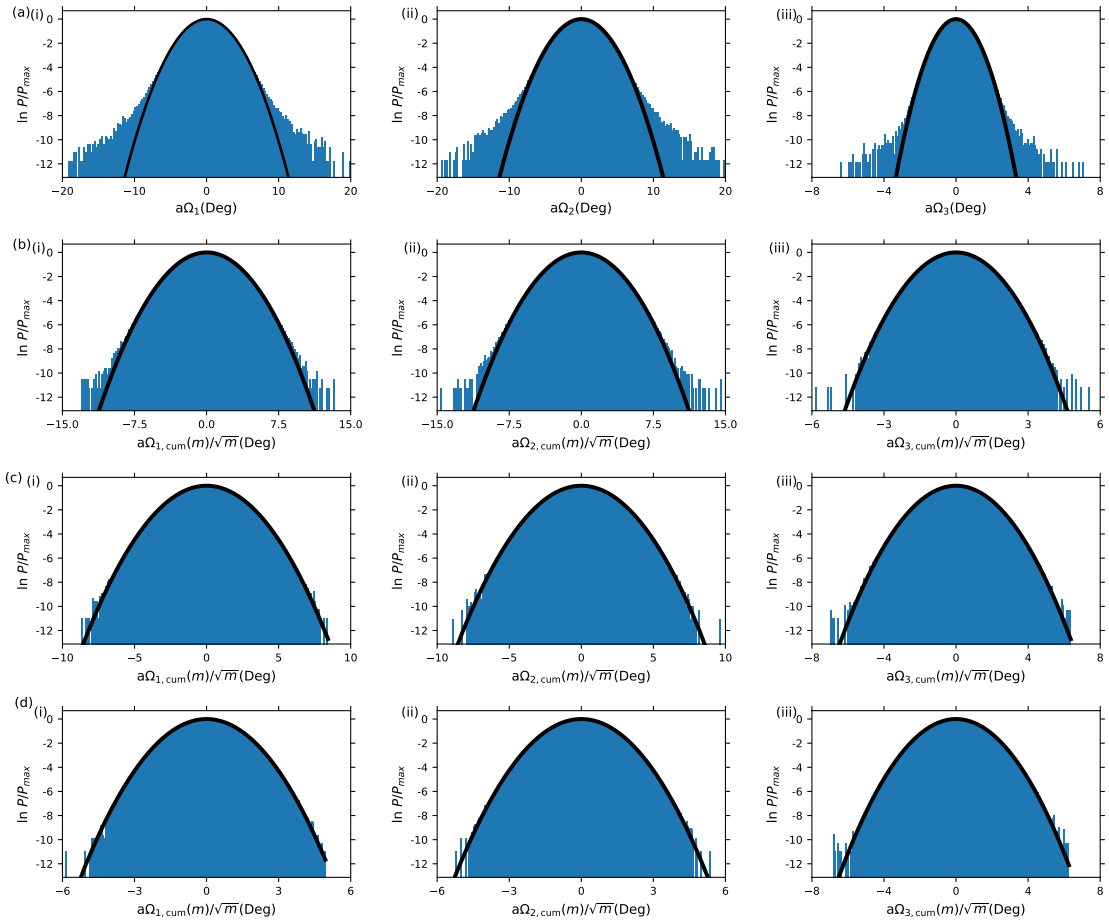


Figure A.4: Probability distributions for (i) $a\Omega_{1,\mathrm{cum}}(m)/\sqrt{m}$, (ii) $a\Omega_{2,\mathrm{cum}}(m)/\sqrt{m}$, and (iii) $a\Omega_{3,\mathrm{cum}}(m)/\sqrt{m}$ for the 6HB-SST nanotube at different values of m: (a) $m = 1$, (b) $m = 3$, (c) $m = 11$ and (d) $m = 41$. The solid lines are Gaussian fits to the distributions.

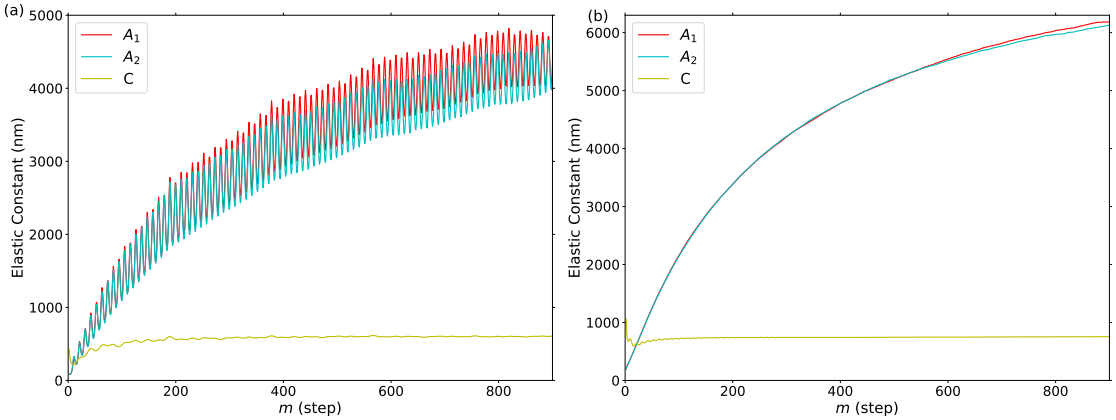


Figure A.5: Elastic moduli for (a) 6HB-S and (b) 6HB-SST at $\alpha = 0.0$. The origami exhibits an oscillation on the pitch length of double-stranded DNA, whereas the elastic moduli increase smoothly for the SST nanotube.

Reprint(adapted) with permission from [159]. *Copyright ©2020 , American Chemical Society.*

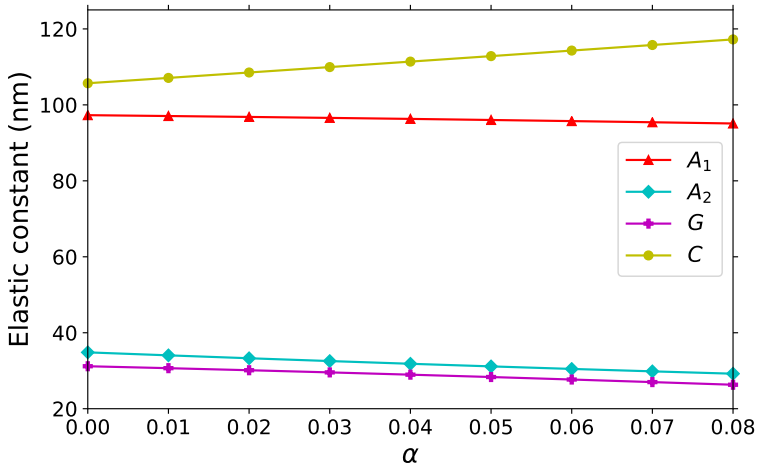


Figure A.6: Double-stranded DNA elastic constants A_1, A_2, C, G as a function of α.

	$\langle\Theta_1\rangle$	$\langle\Theta_2\rangle$	$\langle\Theta_3\rangle$	A_1	A_2	C	G	l_b	$l_t/2$
$\alpha = 0.00$	0.00	2.81	34.16	97.3	34.8	105.7	31.2	40.1	81.1
$\alpha = 0.06$	0.00	0.00	34.26	95.7	30.5	114.3	27.7	41.2	93.2
helically corrected				97.3	30.2	110.3	25.0		

Table A.2: Structural and mechanical properties of double-stranded DNA before and after applying the correction to remove the helicity of the centreline. The elastic constants obtained from those at $\alpha = 0$ by applying the transformation from a helical to a straight coordinate system outlined in Ref. [175] are also given. The results are for $[Na^+]$=0.5 M and a temperature of 23°C. $a = 0.3462$ nm.

For the 4HB systems:

$$\hat{\mathbf{x}} = \frac{\mathbf{R}_{\text{duplex}}(3) - \mathbf{R}_{\text{duplex}}(1)}{||\mathbf{R}_{\text{duplex}}(3) - \mathbf{R}_{\text{duplex}}(1)||} \tag{A.2}$$

and

$$\hat{\mathbf{y}} = \frac{\mathbf{R}_{\text{duplex}}(2) - \mathbf{R}_{\text{duplex}}(4)}{||\mathbf{R}_{\text{duplex}}(2) - \mathbf{R}_{\text{duplex}}(4)||}. \tag{A.3}$$

For the 8HB systems:

$$\hat{\mathbf{x}} = \frac{\mathbf{R}_{\text{duplex}}(5) - \mathbf{R}_{\text{duplex}}(1)}{||\mathbf{R}_{\text{duplex}}(5) - \mathbf{R}_{\text{duplex}}(1)||} \tag{A.4}$$

and

$$\hat{\mathbf{y}} = \frac{\mathbf{R}_{\text{duplex}}(3) - \mathbf{R}_{\text{duplex}}(7)}{||\mathbf{R}_{\text{duplex}}(3) - \mathbf{R}_{\text{duplex}}(7)||}. \tag{A.5}$$

Reprint(adapted) with permission from [159]. *Copyright ©2020 , American Chemical Society.*

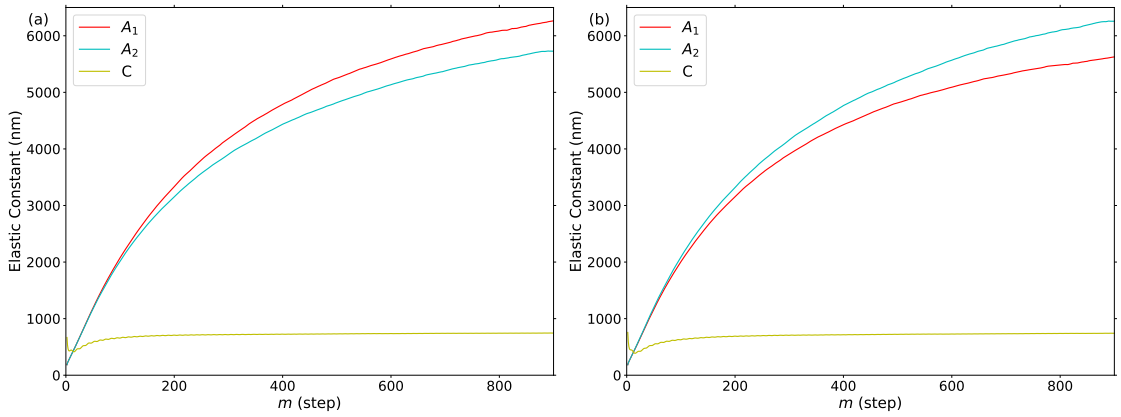


Figure A.7: The effect of the orthogonalization scheme to obtain the triad $\{\hat{\mathbf{e}}_1, \hat{\mathbf{e}}_2, \hat{\mathbf{e}}_3\}$ on the elastic moduli for the 6HB-SST nanotube. In (a) $\hat{\mathbf{y}}$ is orthogonalized to $\hat{\mathbf{e}}_3$, whereas in (b) $\hat{\mathbf{x}}$ is orthogonalized to $\hat{\mathbf{e}}_3$.

For the 10HB system

$$\hat{\mathbf{x}} = \frac{\mathbf{R}_{\text{duplex}}(5) + \mathbf{R}_{\text{duplex}}(7) - \mathbf{R}_{\text{duplex}}(2) - \mathbf{R}_{\text{duplex}}(10)}{||\mathbf{R}_{\text{duplex}}(5) + \mathbf{R}_{\text{duplex}}(7) - \mathbf{R}_{\text{duplex}}(2) - \mathbf{R}_{\text{duplex}}(10)||} \tag{A.6}$$

and

$$\hat{\mathbf{y}} = \frac{\mathbf{R}_{\text{duplex}}(3) + \mathbf{R}_{\text{duplex}}(4) - \mathbf{R}_{\text{duplex}}(8) - \mathbf{R}_{\text{duplex}}(9)}{||\mathbf{R}_{\text{duplex}}(3) + \mathbf{R}_{\text{duplex}}(4) - \mathbf{R}_{\text{duplex}}(8) - \mathbf{R}_{\text{duplex}}(9)||}. \tag{A.7}$$

Figure A.7 shows the effect of the orthogonalization scheme on the elastic moduli. If $\hat{\mathbf{e}}_2$ is obtained by the orthogonalization of $\hat{\mathbf{y}}$ to $\hat{\mathbf{e}}_3$, and $\hat{\mathbf{e}}_1$ from the vector product of $\hat{\mathbf{e}}_2$ and $\hat{\mathbf{e}}_3$ (as in Triad III of Ref. [163]), then $A_1 > A_2$ for the 6HB-SST system. By contrast, if $\hat{\mathbf{e}}_1$ is obtained by the orthogonalization of $\hat{\mathbf{x}}$ to $\hat{\mathbf{e}}_3$, and $\hat{\mathbf{e}}_2$ from the vector product of $\hat{\mathbf{e}}_3$ and $\hat{\mathbf{e}}_1$, then $A_2 > A_1$. These results shows the biases introduced by these orthogonalization schemes. Applying the singular value decomposition technique to find the triad avoids these problems, and results in virtually equal values of A_1 and A_2 (Fig. 3.7), as is expected from the symmetry of this system.

A.2.4 Limiting values

Fig. A.8 illustrates the behaviour of the correlation function used to obtain the twist persistence length (Eq. 3.6) for the 6HB-SST system. It has a clear exponential tail making it straightforward to extract a limiting value of the twist persistence

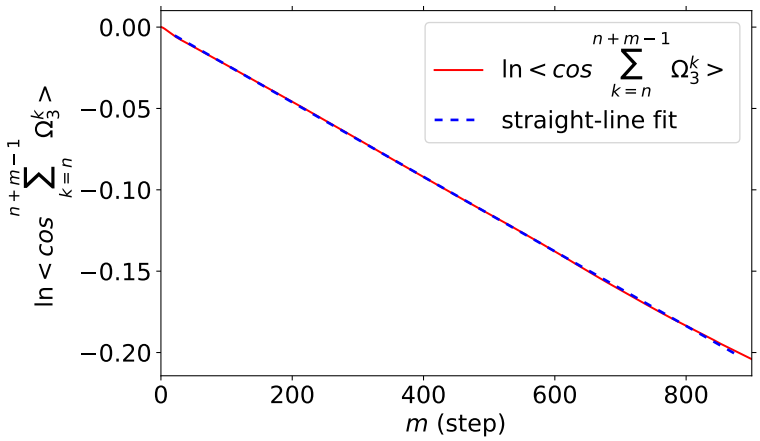


Figure A.8: The exponential decay of the correlation function used to calculate the twist persistence length for the 6HB-SST nanotube.

length. Moreover, unlike for the tangent-tangent correlation function, the deviations from exponential behaviour at small m are barely noticeable. Consequently, the m-dependent twist persistence lengths quickly converge to their limiting values.

The elastic moduli can be calculated from the correlation coefficients describing the correlations between angular deformations separated by n steps (Eq. 3.19) using the expression in Eq. 3.20. The resulting values provide a good description of the elastic moduli over the range of m sampled in simulations (Fig. A.9). However, when one tries to extrapolate the predicted elastic constants to their limiting values, the results become sensitive to the statistical noise in the values of the correlation coefficients.

In Fig. 3.9 of chapter 3, we illustrate the effect of the "averaging" approach we use to obtain the limiting values of the elastic constants for A_1. Equivalent figures for A_2 and C are given in Fig. A.10. The dependence of the behaviour on the parameter n_{avg} for A_2 is, unsurprisingly, very similar to that for A_1, and except for the 10HB origami, which has the largest A_1/A_2 ratio, we always use the same value of n_{avg} when computing the limiting values of these two elastic constants (Table A.1).

Performing this averaging is not so important for the twist elastic constant as it converges reasonably rapidly to its limiting value. This can be accelerated somewhat by using a small value of n_{avg}; we always use $n_{\text{avg}} = 5$. Although we do not use this averaging approach to obtain limiting values of the persistence lengths, Fig.

Reprint(adapted) with permission from [159]. *Copyright ©2020 , American Chemical Society.*

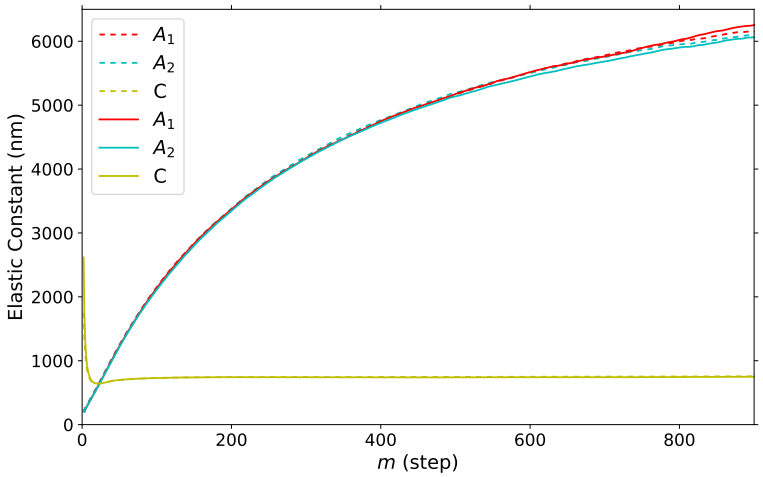


Figure A.9: A comparison of elastic constants calculated using Equations 3.7 (solid lines) and 3.20 (dashed lines) for the 6HB-SST nanotube.

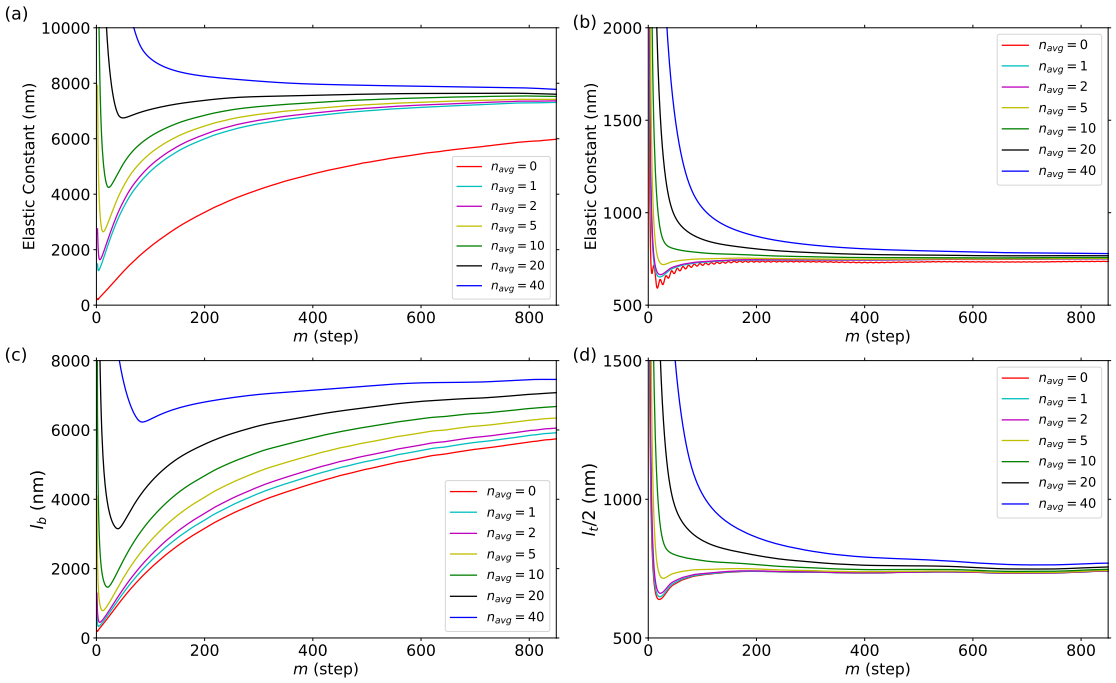


Figure A.10: The effect of averaging on (a) A_2, (b) C, (c) l_b and (d) l_t for different n_{avg} for the 6HB-SST nanotube.

A.10 also illustrates its effects on the m-dependent persistence lengths. Notably, the effect on the convergence of the bend persistence length is less pronounced than it is for the bending moduli.

Reprint(adapted) with permission from [159]. *Copyright ©2020 , American Chemical Society.*

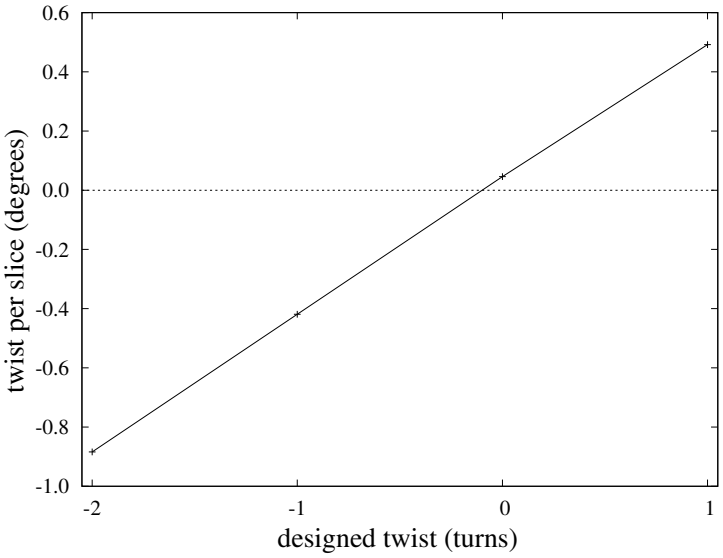


Figure A.11: Twist per slice as a function of the designed twist in turns (i.e. 2×LH is -2, 1×RH is +1) for the series of twisted 6HB origamis.

A.3 Further results

Fig. A.11 depicts the equilibrium twist of the series of twisted origamis versus their designed twist. There is an almost perfect linear relationship, albeit with the origami that is designed to be untwisted having a small right-handed twist. Note that the oxDNA model has been fitted to reproduce the reported zero twist of an origami in Ref. [178]. Interestingly, our slope is larger than would be expected from the designed twist, which is derived from the predictions of the CanDo model[82, 160].

A.3.1 Nanotube radii

The radii of the nanotubes are depicted in Figs. A.12-A.14 as a function of position along the tube. Note that we do not provide any results for 10HB due to its non-tubular cross-section. The periodicity seen in these plots for the main bodies of the nanotubes reflects the periodicity of the pattern of junctions. The SST tubes have a 21-slice repeat and only show very small variation in the radius, probably because their single-crossover junctions do not constrain the helices to come quite so close together as the double-crossover junctions in the origamis. The MT origamis have a clear pattern with a periodicity of 63 slices for 4HB-MT and 42 slices for 6HB-MT.

Reprint(adapted) with permission from [159]. *Copyright ©2020 , American Chemical Society.*

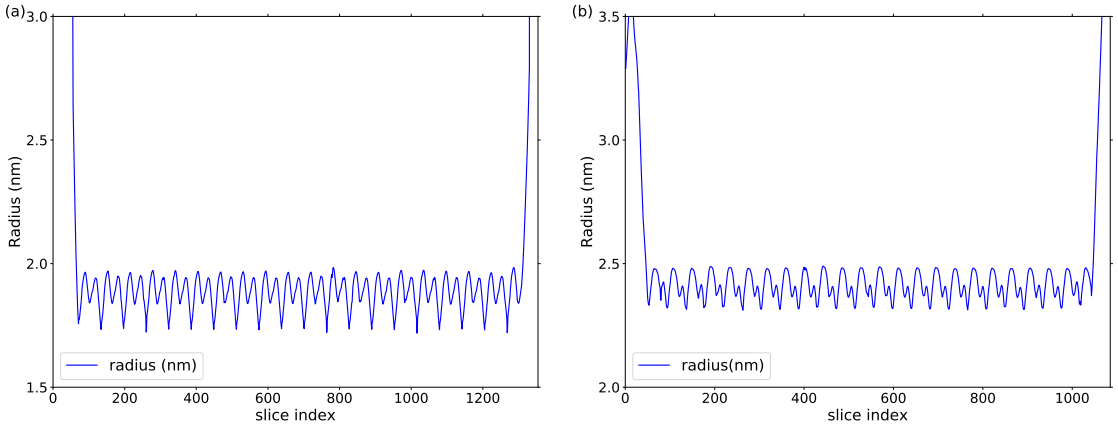


Figure A.12: Radii as a function of position in the nanotube for (a) 4HB-MT and (b) 6HB-MT.

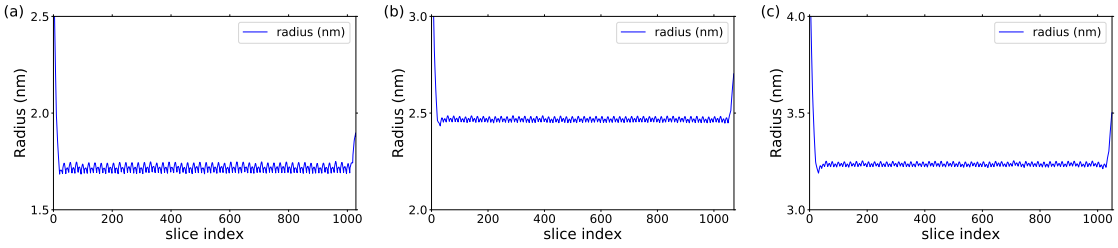


Figure A.13: Radiii as a function of position in the nanotube for (a) 4HB-SST, (b) 6HB-SST and (c) 8HB-SST.

The twisted tubes, by contrast, have a much more irregular pattern of junctions and a more noisy variation in the radius, but there is still a rough repeating pattern on the order of 190 slices (modulated by the insertions and deletions). In the case of the origamis, these periodicities can be related to the small features seen in the m-dependent persistence lengths and elastic moduli at multiples of the repeat.

A.3.2 Persistence lengths

For the SST series of nanotubes, we can compare the persistence lengths to theoretical expectations. A common approach is as follows. For a uniform elastic medium, the persistence length can be related to the Young's modulus through

$$l_b = \frac{YI}{k_B T} \tag{A.8}$$

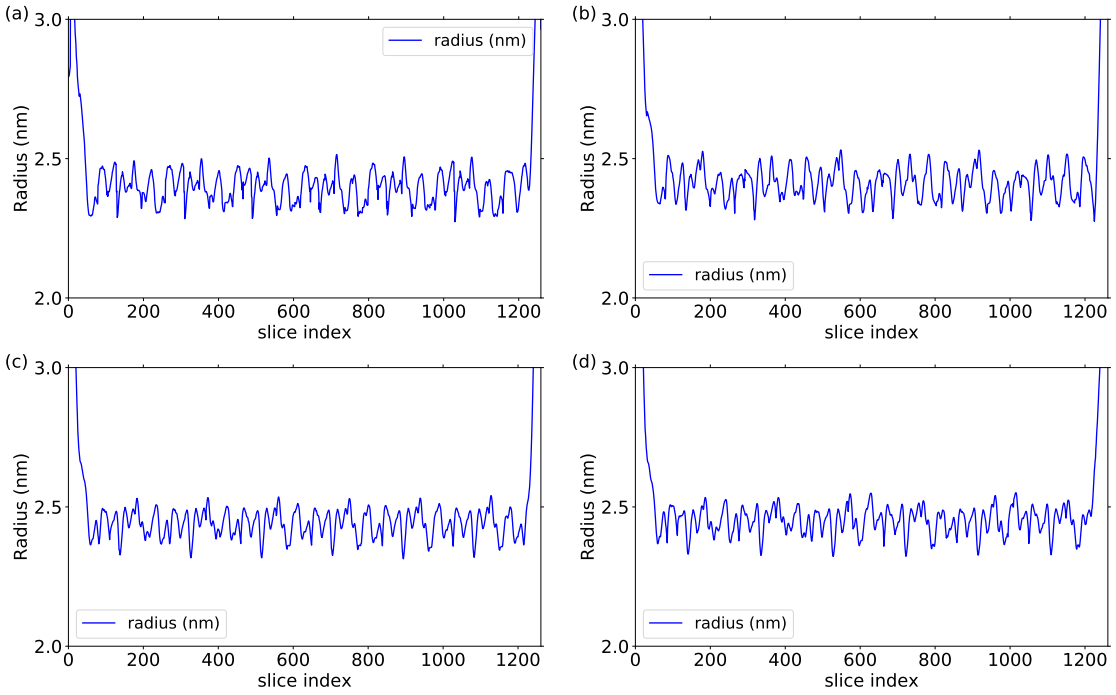


Figure A.14: Radii as a function of position in the nanotube for (a) 6HB-2×LH, (b) 6HB-1×LH, (c) 6HB-S and (d) 6HB-1×RH.

where I is the moment of inertia of the cross-section. Using the parallel-axis theorem to calculate I for a bundle of rods and assuming the Young's modulus for DNA is the same in a duplex and in a helix-bundle, one arrives at the following relationship between the persistence length of a helix bundle and that for duplex DNA:

$$l_b^{\text{tube}} = n l_b^{\text{duplex}} \left(1 + 2\left(\frac{R}{r}\right)^2\right). \tag{A.9}$$

where R is the radius of the bundle and r the radius of duplex DNA[150]. In the experimental papers where this formula has been applied [143, 147, 148, 150] one difficulty is that R cannot be measured directly; therefore, one first approximation has been to assume that the helices are in direct contact [143, 150]. By contrast, for oxDNA we can measure the tube radii (e.g. Fig. A.13). Thus, together with the oxDNA duplex values of $r = 1.15\,\text{nm}$ and $l_b = 41.2\,\text{nm}$ (Table A.2), we can use Eq. A.9 to predict the nanotube persistence lengths. In chapter 3, we use r as an effective parameter to fit the bending persistence lengths of the SST nanotubes. Other potential causes for discrepancies that have been considered in the

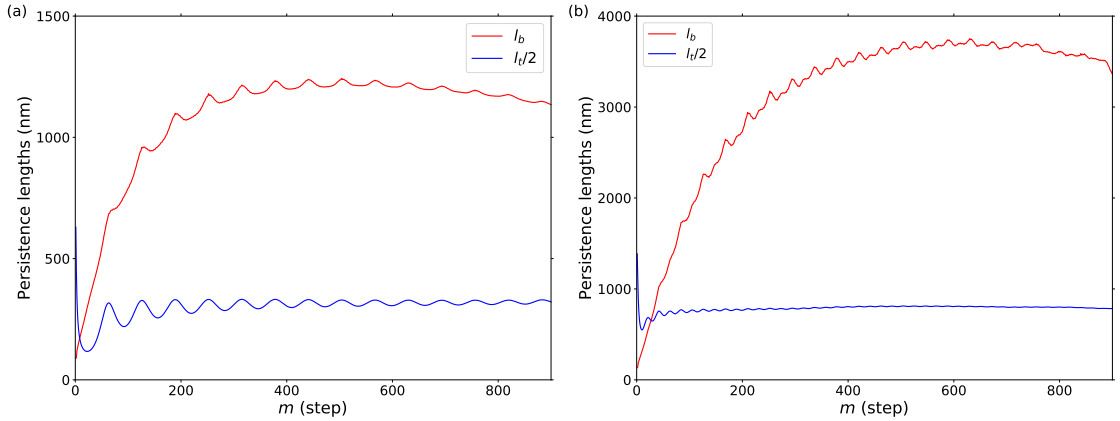


Figure A.15: *m*-dependent persistence lengths for (a) 4HB-MT and (b) 6HB-MT.

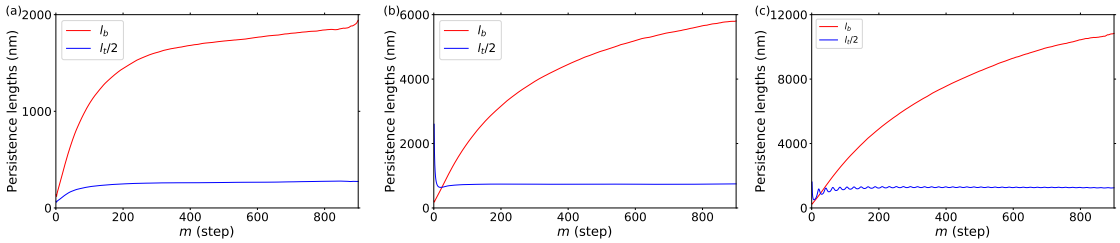


Figure A.16: *m*-dependent persistence lengths for (a) 4HB-SST, (b) 6HB-SST and (c) 8HB-SST.

experimental studies are imperfections in the tubes (not relevant here) and that nicks and junctions reduce the duplex persistence length for the helices in the nanotubes.

The *m*-dependent persistence lengths defined through Eqs. 3.5 and 3.6 are shown in Figs. A.15-A.18.

A.3.3 DNA extensional modulus

We performed simulations to compute the force-extension curve of double-stranded DNA. The strand was 150-bp long and we considered the central 130-bp section. The simulations were at $[Na^+]$=0.5 M. Forces up to 40 pN were considered.

The resulting data (Fig. A.19) was fitted to the extensible worm-like chain expression:

$$x = L_0 \left(1 + \frac{F}{K} - \frac{k_B T}{2 F L_0} \left[1 + y \coth y\right]\right), \tag{A.10}$$

Reprint(adapted) with permission from [159]. *Copyright ©2020 , American Chemical Society.*

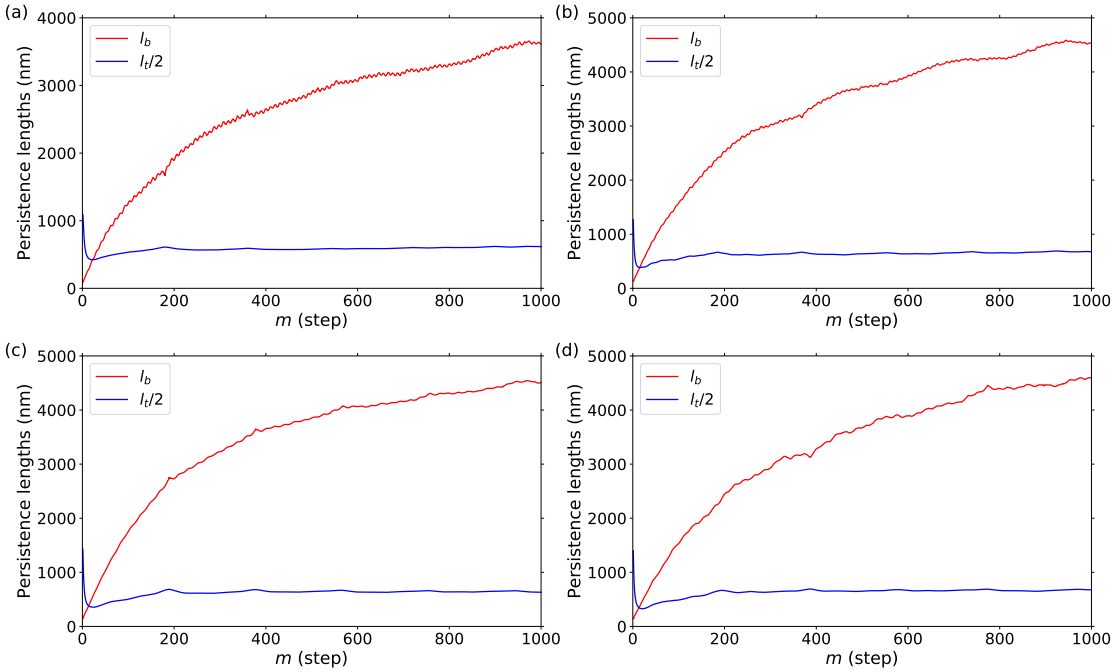


Figure A.17: m-dependent persistence lengths for (a) 6HB-2×LH, (b) 6HB-1×LH, (c) 6HB-S and (d) 6HB-1×RH.

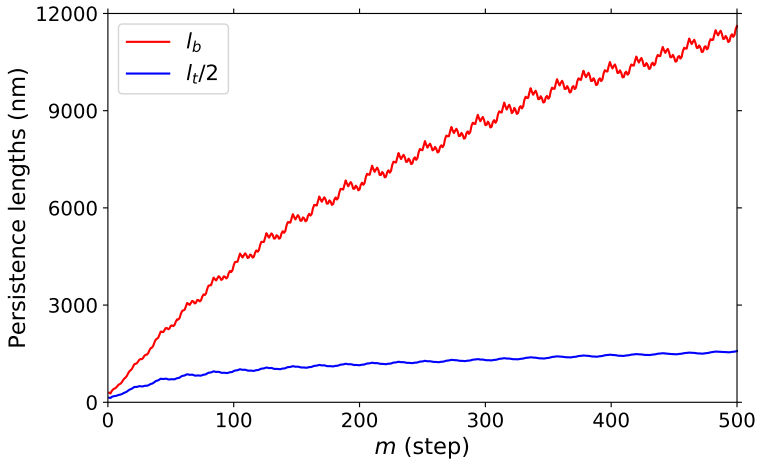


Figure A.18: m-dependent persistence lengths for the 10HB origami.

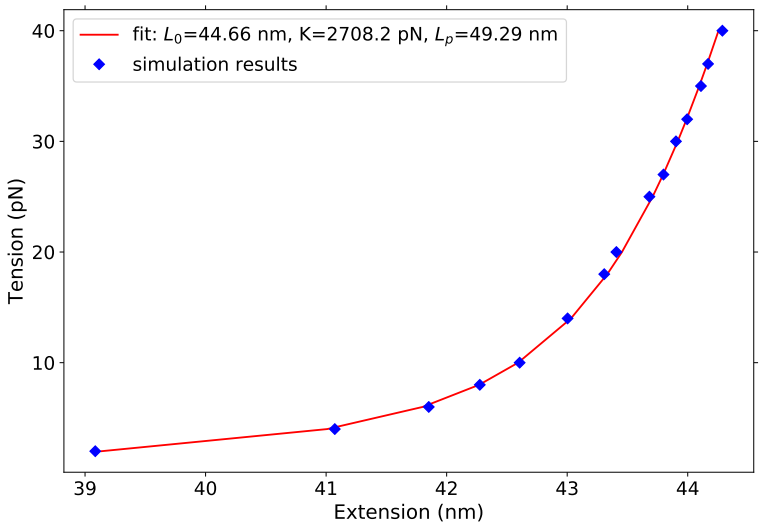


Figure A.19: Force-extension curve for a 150-bp duplex, neglecting the 10 base pairs at each end. The data points are from simulations and the solid line a fit to the curve using the extensible worm-like chain formula (Eq. A.10).

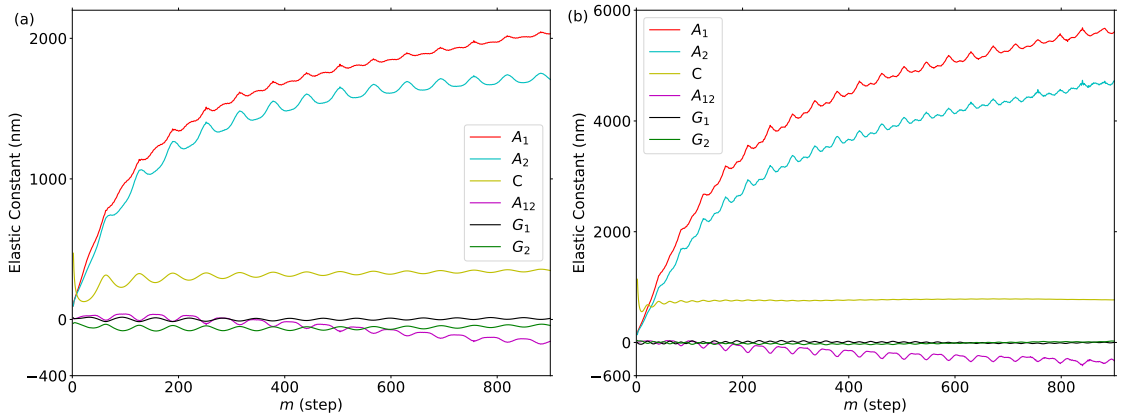


Figure A.20: Elastic moduli for (a) 4HB-MT and (b) 6HB-MT.

where

$$y = \left(\frac{F L_0^2}{l_b k_B T} \right)^{1/2}, \tag{A.11}$$

L_0 is the contour length, x is the extension, F the force and K the extensional modulus. An unconstrained three-parameter fit gave $K = 2708\,\mathrm{pN}$, $L_0 = 44.66\,\mathrm{nm}$ and $l_b = 49.3\,\mathrm{nm}$.

Reprint(adapted) with permission from [159]. *Copyright ©2020 , American Chemical Society.*

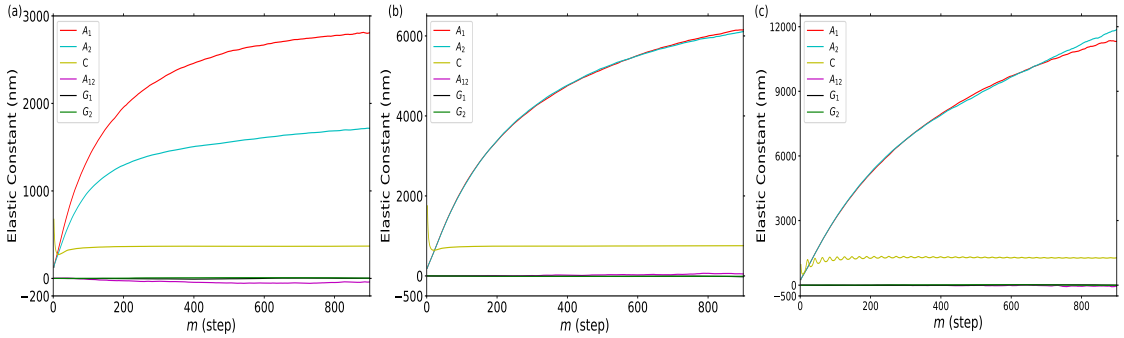


Figure A.21: Elastic moduli for (a) 4HB-SST, (b) 6HB-SST and (c) 8HB-SST.

A.3.4 Elastic moduli

The m-dependent elastic moduli defined through Eqs. 3.7 and 3.8 are given in Figs. A.20–A.23. Unlike in chapter 3 we also illustrate the off-diagonal terms. These off-diagonal terms remain closest to zero for the SST systems, which have both the best statistics and are most symmetric. For the origami systems, although these off-diagonal terms start off close to zero, there is some tendency to increase with m, particularly for A_{12}. We think this behaviour is a result of the worse statistics at longer length scales. If the off-diagonal elastic constants were actually non-zero, we would expect that their dependence on m would be much more similar to that for the diagonal terms, e.g. to display a monotonically decreasing slope with increasing m, as is the case for the twist-bend coupling constant for double-stranded DNA[163]. That A_{12} is typically the largest of the off-diagonal terms is probably due to the greater difficulty of accurately sampling bending compared to twisting, because of the much larger value of the bend persistence lengths. Unfortunately, the non-zero values of the off-diagonal terms at large m are likely to have a consequent effect on the accuracy of the limiting values of the other moduli, and to lead to deviations from the expected relationships between the persistence lengths and elastic moduli that hold when the off-diagonal terms are zero. For example, for most systems the value of C quickly converges to its limiting values and is then approximately constant for larger m. However, for the 10HB origami there is an approximately linear rise in C at large m that seems correlated with the appearance of significant deviations in A_{12} from zero (Fig. A.23).

Reprint(adapted) with permission from [159]. *Copyright ©2020 , American Chemical Society.*

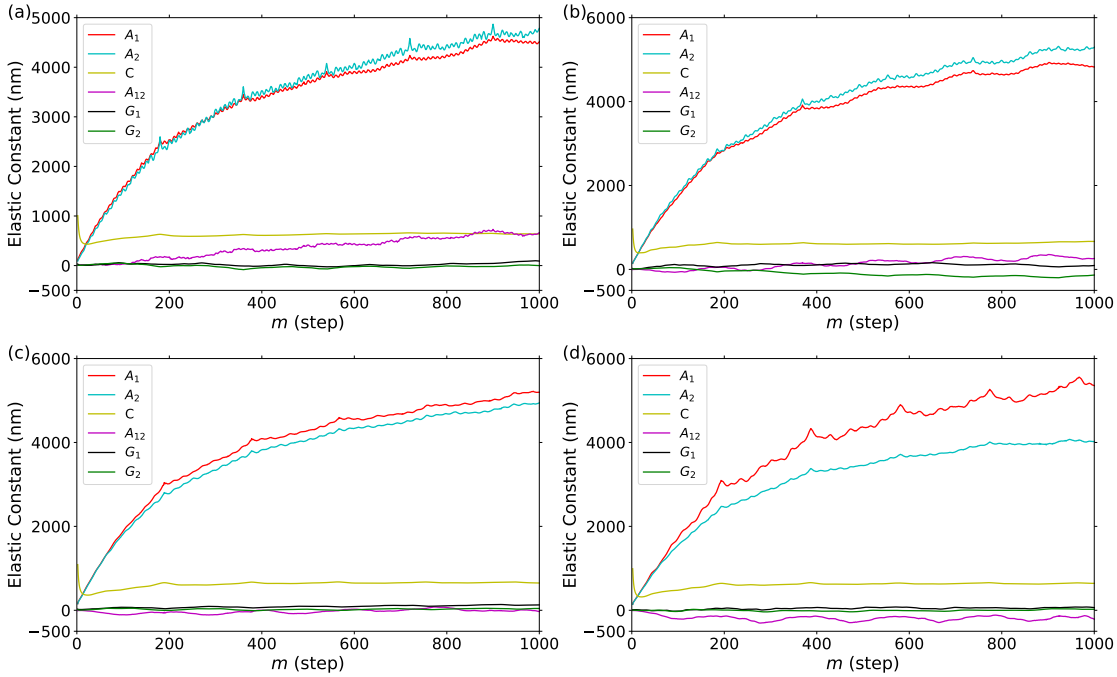


Figure A.22: Elastic moduli for (a) 6HB-2×LH, (b) 6HB-1×LH, (c) 6HB-S and (d) 6HB-1×RH.

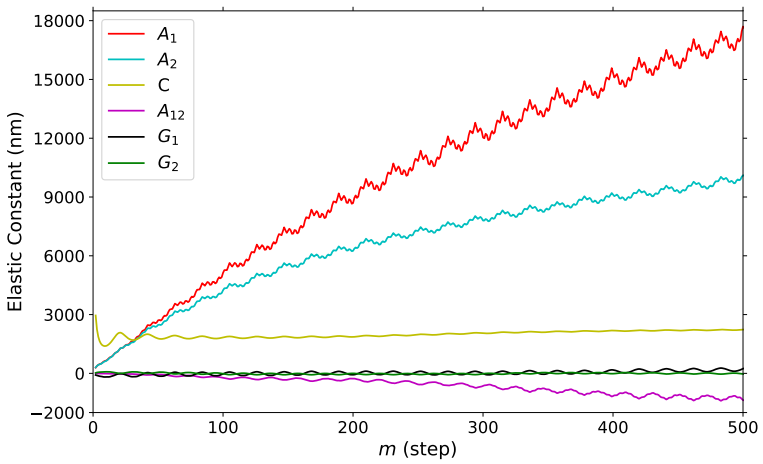


Figure A.23: Elastic moduli for the 10HB origami at $\alpha = 0.06$.

Reprint(adapted) with permission from [159]. *Copyright ©2020 , American Chemical Society.*

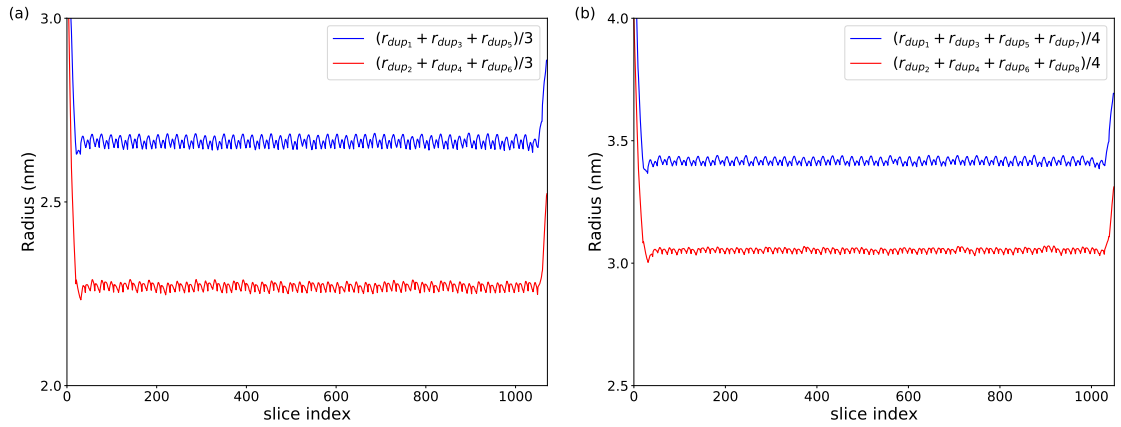


Figure A.24: Radii for equivalent helices in 6HB-SST and 8HB-SST.

A.3.5 SST nanotube cross-sections

In chapter 3 we showed in Fig. 3.12(b) that equivalent helices in the 4HB-SST nanotube had different radii, providing quantitative evidence that the cross-section was diamond-like (Fig. 3.5(c)) rather than square. This is due to the inequivalence of adjacent helices in the SST nanotubes and the alternating inter-helix angle as one goes round the tube. Similar plots are shown in Fig. A.24 for 6HB-SST and 8HB-SST. The snapshots in Fig. 3.3 also confirm the deviations of the cross-section away from a regular polygon.

B

SI 2

B.1 Trajectory overview for 6HB-SST

The formation of plectonemes in nanotubes is very distinct from duplexes. Fig. B.1(a) is indicative of the situation after the bent origami is exposed to tension (2 pN) and twisting. The constant pulling force undoes the effect of bending force to an extent, but if a small kink has been created roughly at the centre, the plectoneme nucleation will more or less be central. Fig. B.1 captures the plectonemic growth in the 6HB-SST system, where configurations at each turn were simulated for long intervals. Generally, the long simulations do lead to the plectoneme being central even if the initial nucleation did not occur in the very centre of the tube. Fig. B.1(c) is such an example where long simulation does help us achieve a desired configuration. More than 7 turns in 6HB-SST leads to deformation of the origami, with kinks and domain dissociation occurring at all bent sites.

For the case of a 10 pN pulling force (Fig. B.3), the origami is strongly stretched, which delays plectoneme growth by 2 turns. Fig. B.2 shows the origami at different

stages of being twisted at 10 pN, while Fig. B.3 records the origami at different stages of being equilibrated with the desired number of turns. The braids in the plectoneme stems appear to have a shorter pitch than for the 2 pN examples, as is expected, in order to offset the greater work against the force needed to grow the plectoneme. Additionally, the large pulling force completely undoes the effect of 4 pN central bending force (B). Despite long equilibration the plectonemes are not well formed as the dynamics associated with plectoneme nucleation, diffusion and growth are even more unfavourable under larger pulling forces.

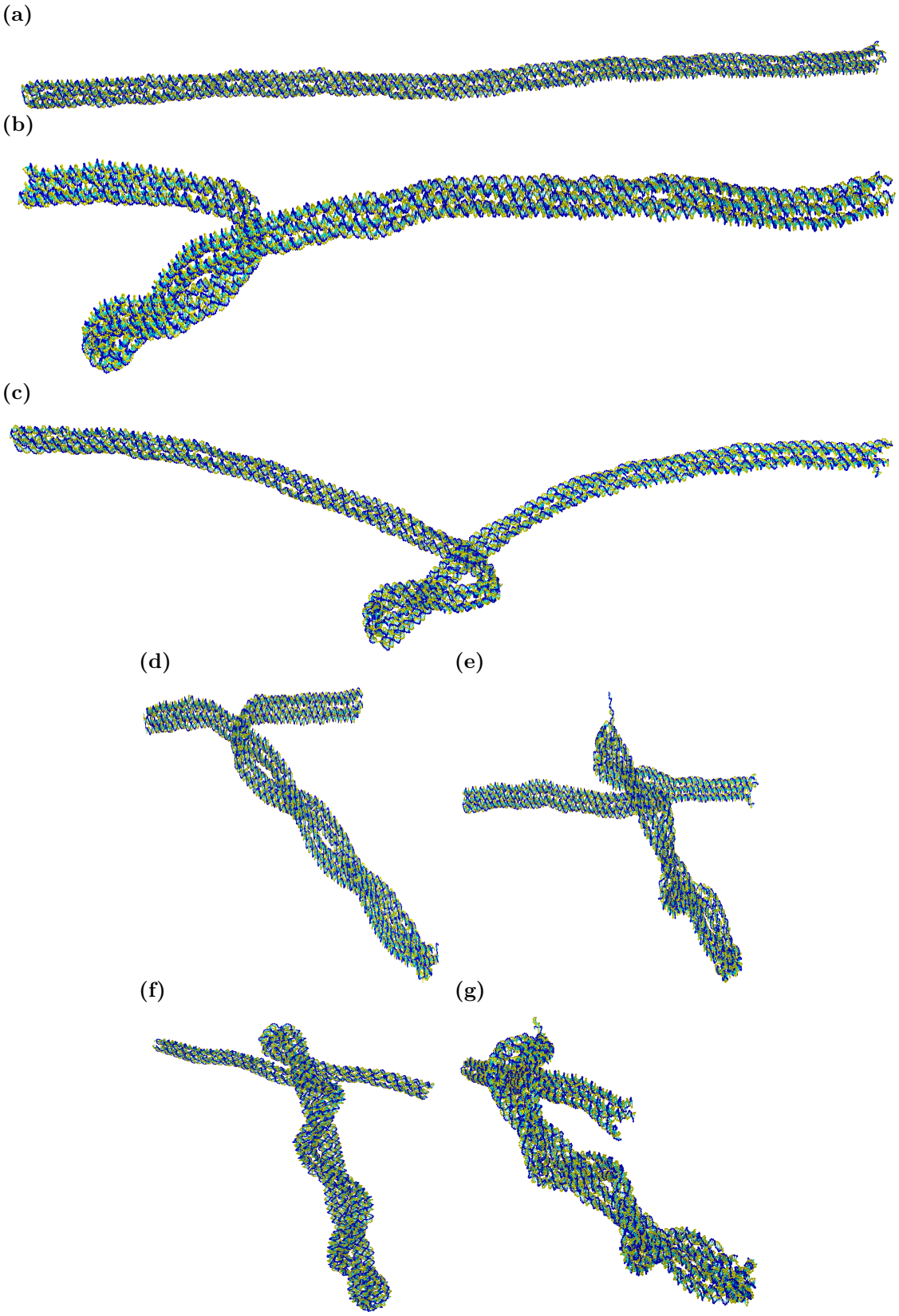


Figure B.1: Relaxed configurations of the 6HB-SST nanotube at (a) 3 turns (b) 4 turns, (c) 5 turns, (d) 6 turns, (e) 8 turns, (f) 10 turns and (g) 12 turns under a tensile force of 2 pN. The relaxation of the tubes at each turn shows the formation of plectonemic loops even at lower numbers of turns.

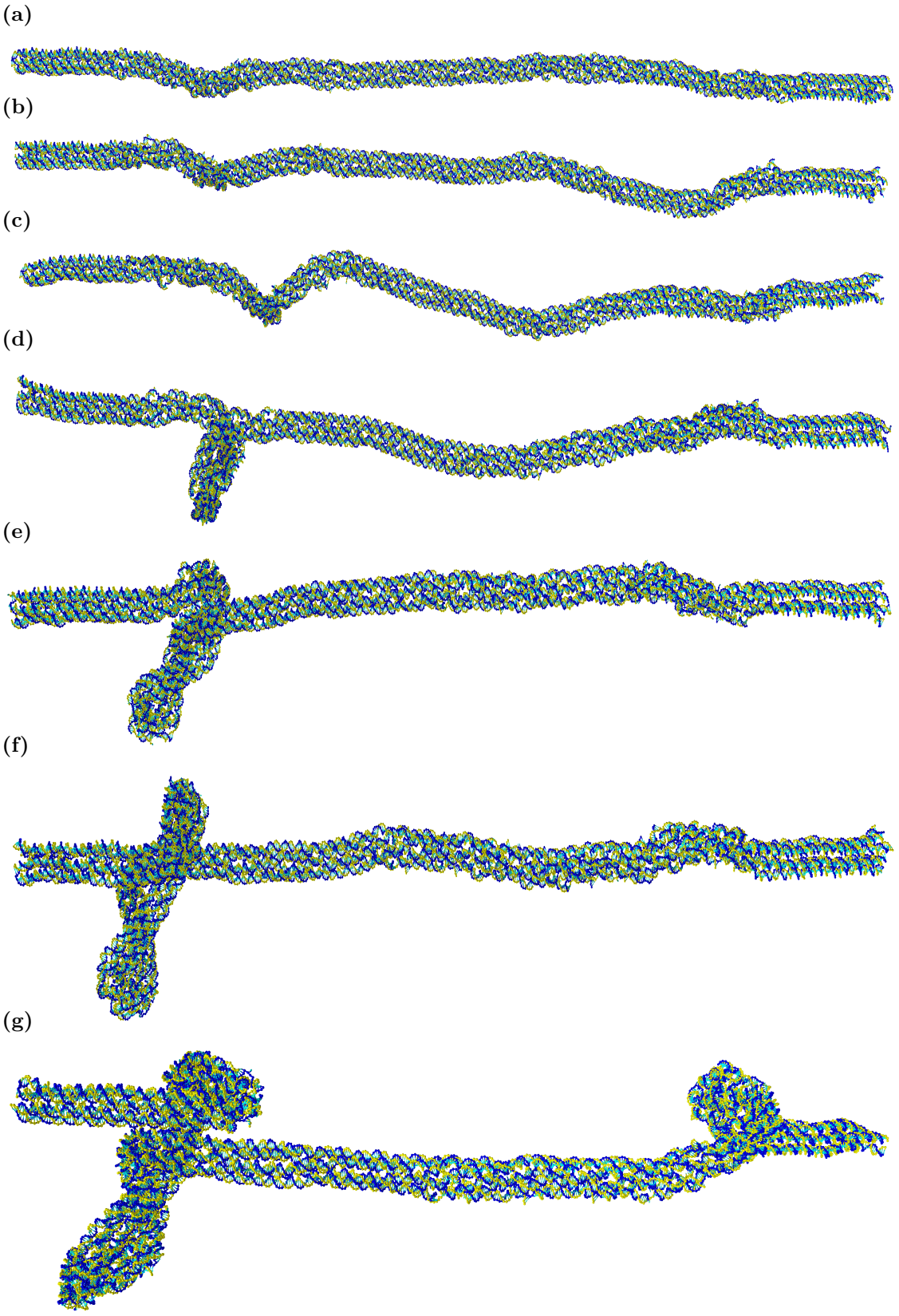


Figure B.2: Snapshots of 6HB-SST being twisted at a rate of $2\pi \times 10^{-7}$ at (a) 6 turns, (b) 7 turns, (c) 8 turns, (d) 9 turns, (e) 10 turns, (f) 11 turns and (g) 12 turns. These are non-relaxed configurations snapped while the rod was still being twisted and had incurred the required number of turns at a string force of 10pN.

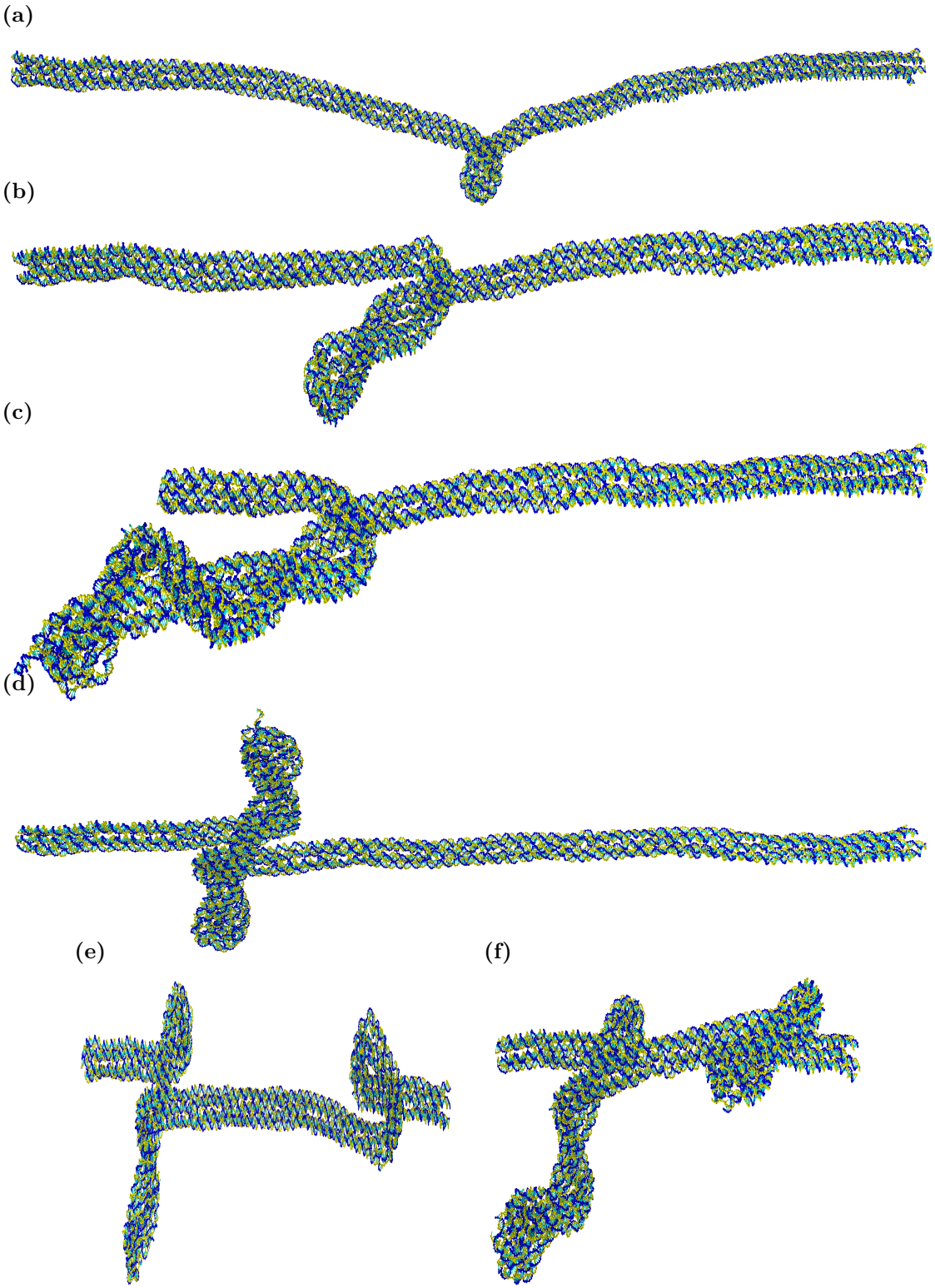


Figure B.3: Relaxed configurations of 6HB-SST at (a) 4 turns, (b) 6 turns, (c) 8 turns, (d) 9 turns, (e) 10 turns and (f) 12 turns which belongs to the data set used for measuring torque and other measurable quantities at 10pN string force.

B.2 Trajectory overview for 4HB-SST

The 4HB-SST shows similar behaviour in terms of the formation of plectonemes. This is despite the 4HB-SST nanotube having lower persistence lengths compared to the 6HB-SST nanotube, which means it is closer to the l_b/l_c regime where more worm-like chain behaviour might be expected. The maximum tension imposed on this system was restricted to 7 pN as the origami showed excessive domain dissociation events at 10 pN and in many cases a split into two was observed due to the high stress and the lower mechanical strength of the system. Even at 7pN, on close observation one can observe fraying and domain dissociation (Fig. B.4(a)). This tension allows multiple kinks, which in turn leads to multiple plectoneme formation at large number of turns (Fig. B.4(c-d)).

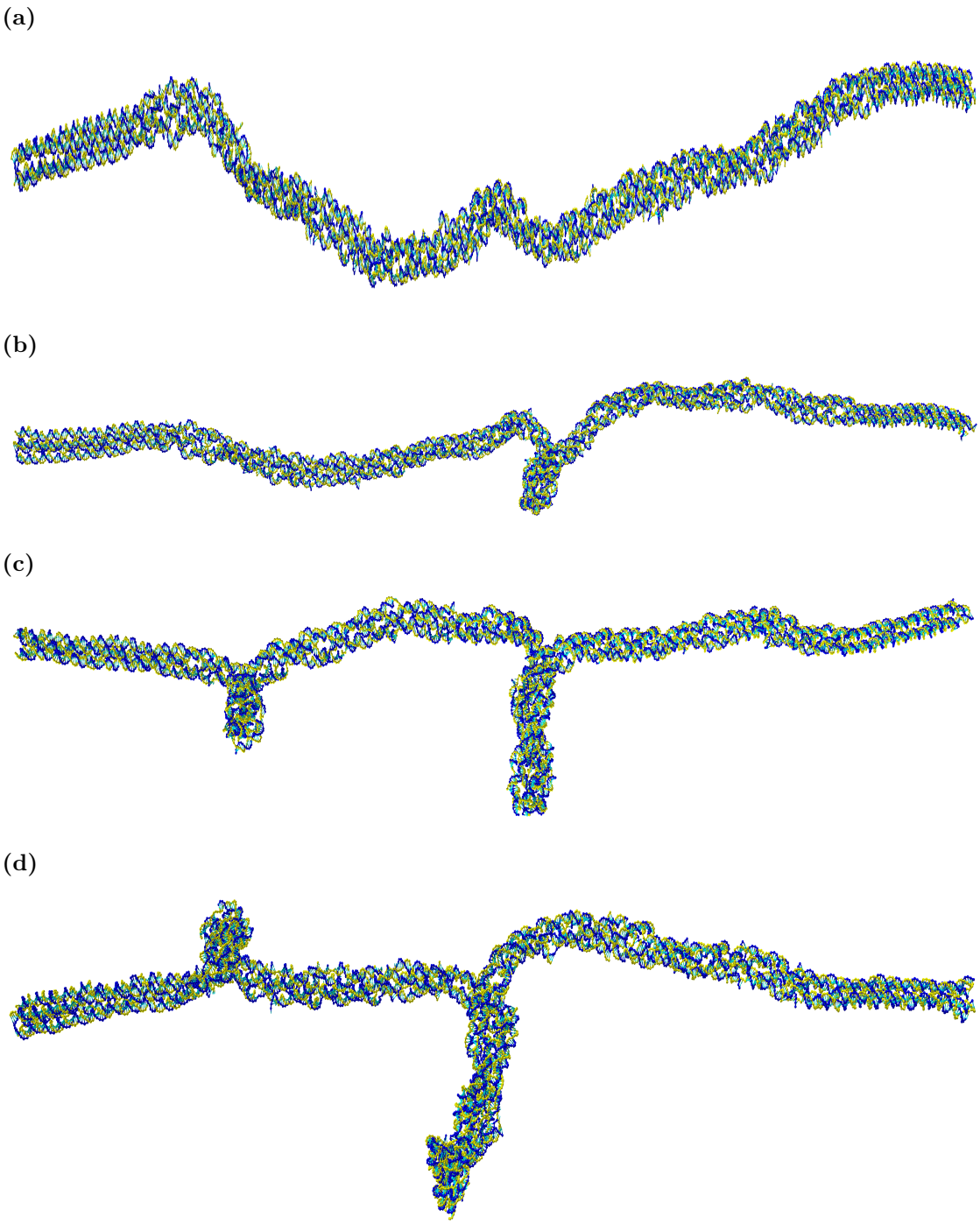


Figure B.4: Snapshots of 4HB-SST being twisted at a rate of $2\pi \times 10^{-7}$ at (a) 13 turns, (b) 14 turns, (c) 15 turns and (d) 16 turns . These are non-relaxed configurations at a string force of 7pN. The regular ssDNA overhangs at such high tension are observed throughout the nanotube. The 4HB-SST origami was a troublesome system to simulate to get 'well' formed plectonemes.

C

SI 3

C.1 Simulation details

The simulation details of all gapped systems are recorded in Table C.1. The simulation time of the 4HB systems is much longer compared to the simulation time for any of the systems studied in Chapter 3. Most 4HB and 10HB systems yielded good straight line fits to the tails of the log plots of the relevant correlation functions after long simulations. For a few plots clear deviations from exponential behaviour are still evident, but it is our expectation that better fits would have been obtained if the simulations were run even longer. Computational limitation may be noted as the likely cause of any sampling issues in this study. Table C.1 records the relevant simulation details for all systems.

	gap size	gap density/%	t_{sim}/ms	N_{config}	N_{ends}
4HB	0	0	80.48	13282	60
4HB	1 nt	25	88.43	14593	60
4HB	1 nt	50	72.13	11904	60
4HB	1 nt	75	73.62	12149	60
4HB	1 nt	100	82.91	13683	60
4HB	3 nt	25	91.28	15063	60
4HB	3 nt	50	100.34	16559	60
4HB	3 nt	75	91.21	15052	60
4HB	3 nt	100	113.99	18811	60
4HB	5 nt	25	103.21	17032	60
4HB	5 nt	50	96.11	15861	60
4HB	5 nt	75	196.62	15944	60
4HB	5 nt	100	111.16	18344	60
10HB	0	0	18.39	3063	60
10HB	5 nt	20	19.47	3214	60
10HB	5 nt	40	18.67	3082	60
10HB	5 nt	60	18.93	3125	60
10HB	5 nt	80	18.58	3067	60
10HB	5 nt	100	18.71	3088	60

Table C.1: Details of the simulations and the parameters used when calculating persistence lengths. t_{sim} is the total simulation time of the trajectories. N_{config} is the number of configurations in the ensemble used to calculate the persistence length of each system. N_{ends} is the number of slices at each end that are ignored in these calculations.

C.2 Calculation of persistence lengths for 10HB origamis

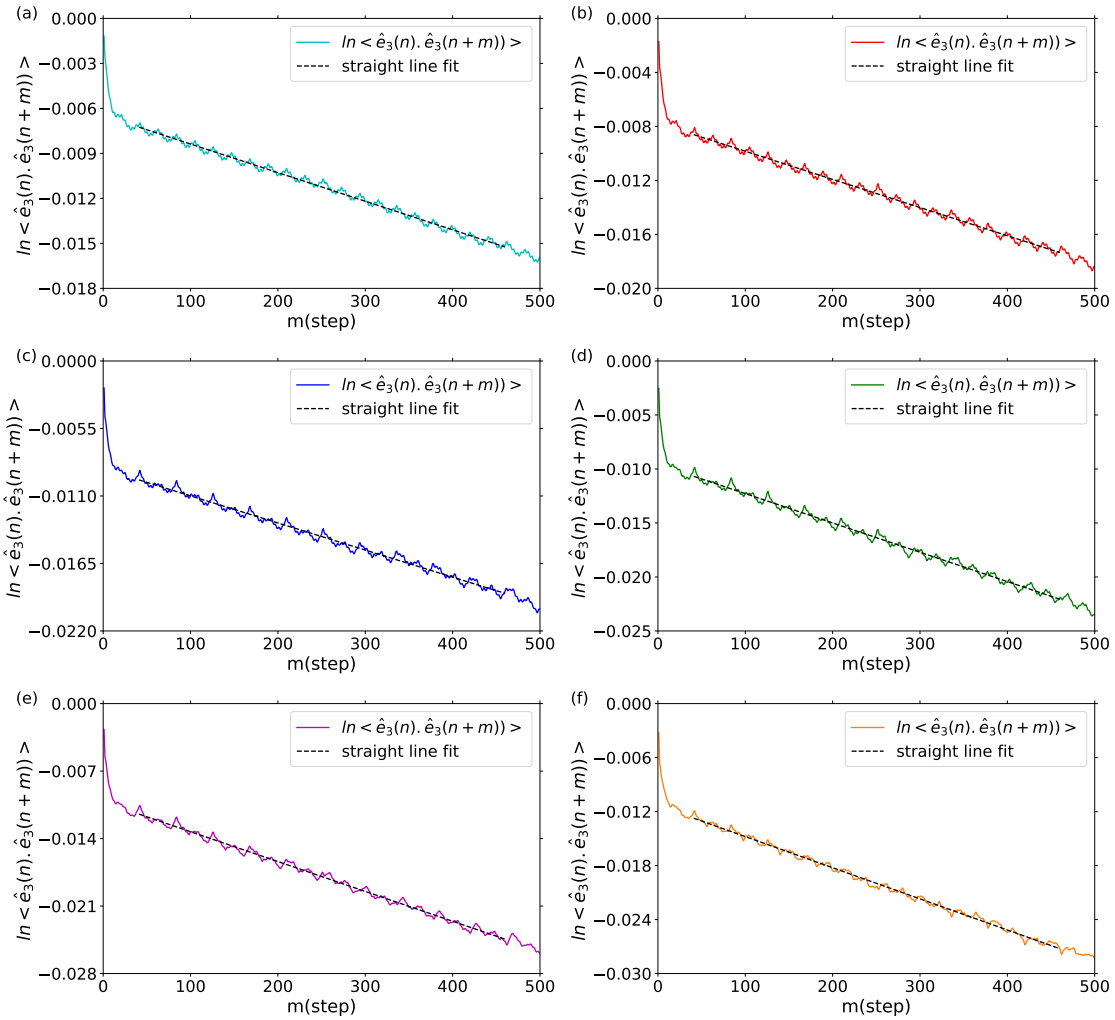


Figure C.1: $\log\langle\cos\theta(m)\rangle$ versus m for (a) 10HB-no gap, (b) 10HB-5 nt-20% gap density, (c) 10HB-5 nt-40% gap density, (d) 10HB-5 nt-60% gap density, (e) 10HB-5 nt-80% gap density and (f) 10HB-5 nt-100% gap density.

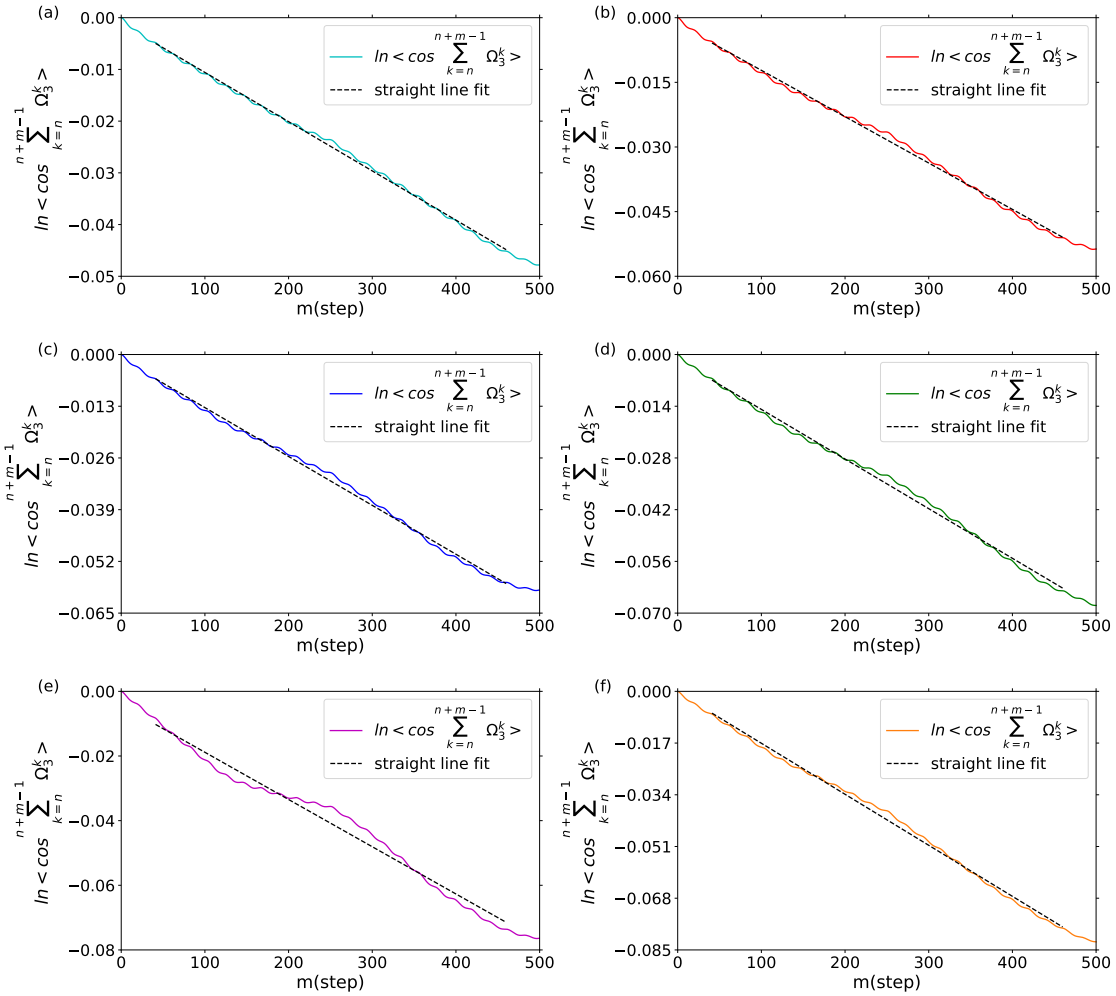


Figure C.2: The exponential decay of the correlation function used to calculate the twist persistence length for (a) 10HB -no gap, (b) 10HB-5 nt-20% gap density, (c) 10HB-5 nt-40% gap density, (d) 10HB-5 nt-60% gap density, (e) 10HB-5 nt-80% gap density and (f) 10HB-5 nt-100% gap density.

C.3 Calculation of persistence lengths for 4HB-1 nt

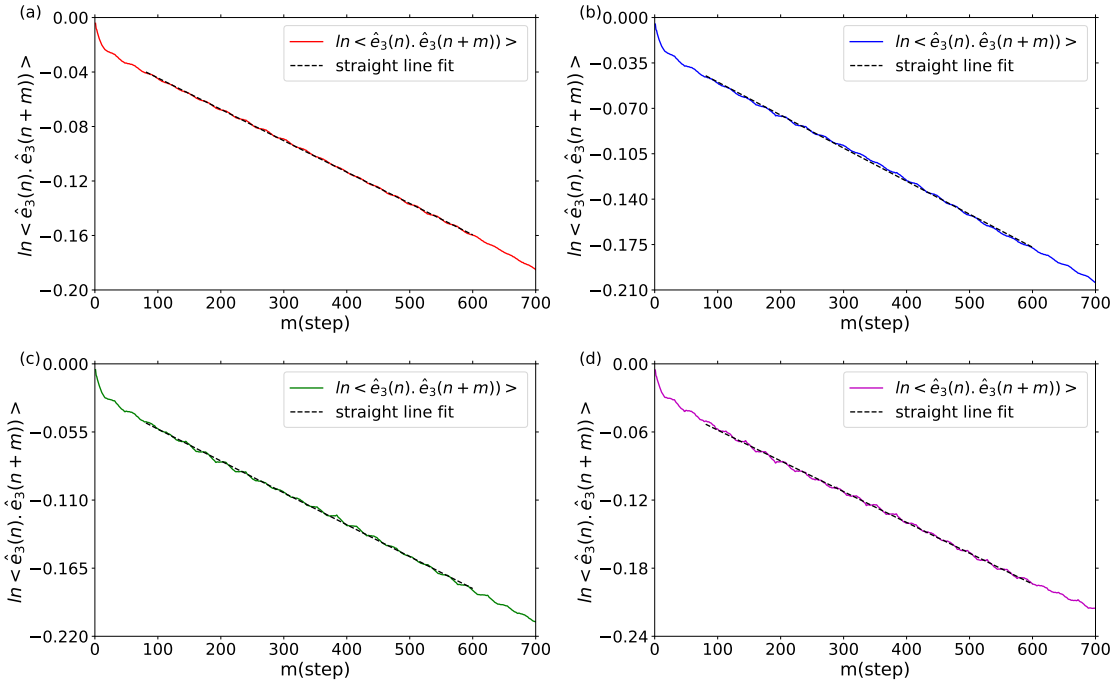


Figure C.3: $\log\langle\cos\theta(m)\rangle$ versus m for (a) 4HB-1 nt-25% gap density, (b) 4HB-1 nt-50% gap density, (c) 4HB-1 nt-75% gap density and (d) 4HB-1 nt-100% gap density.

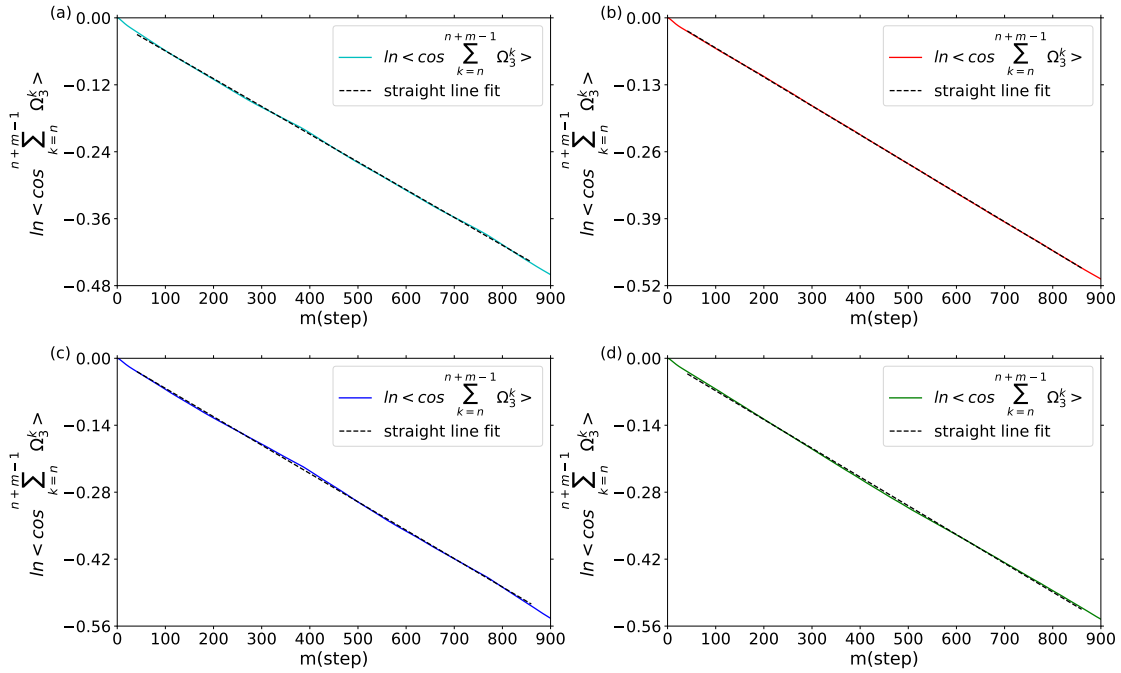


Figure C.4: The exponential decay of the correlation function used to calculate the twist persistence length for (a) 4HB-1 nt-25% gap density, (b) 4HB-1 nt-50% gap density, (c) 4HB-1 nt-75% gap density and (d) 4HB-1 nt-100% gap density.

C.4 Calculation of persistence lengths for 4HB-3 nt

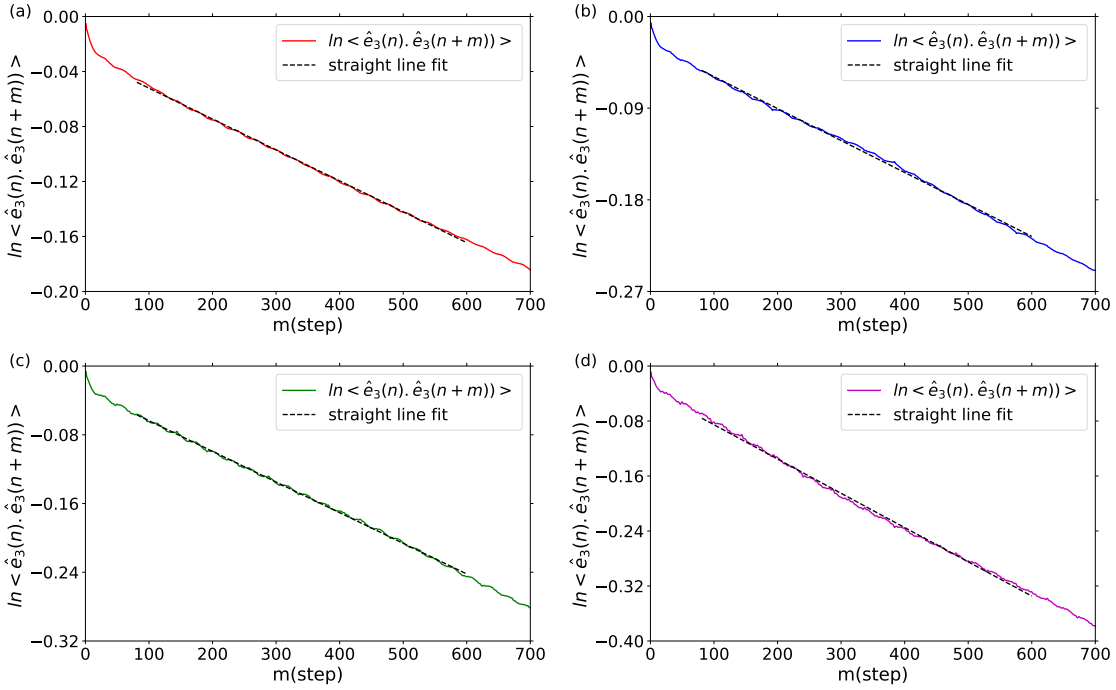


Figure C.5: $\log\langle\cos\theta(m)\rangle$ versus m for (a) 4HB-3 nt-25% gap density, (b) 4HB-3 nt-50% gap density, (c) 4HB-3 nt-75% gap density and (d) 4HB-3 nt-100% gap density.

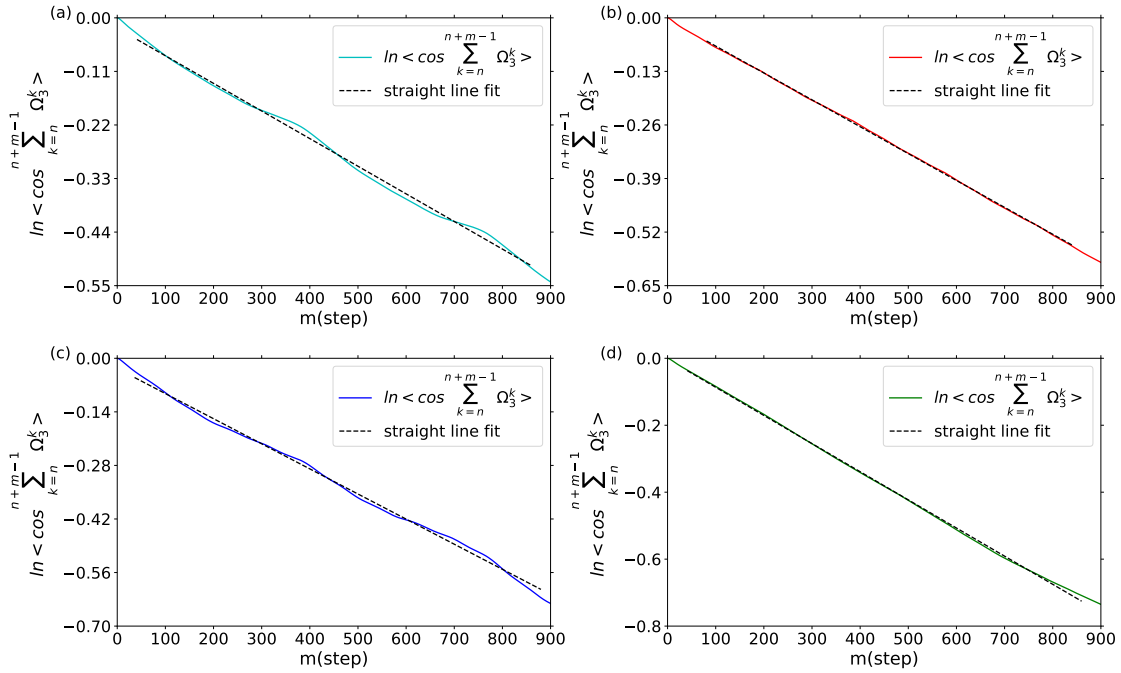


Figure C.6: The exponential decay of the correlation function used to calculate the twist persistence length for (a) 4HB-3 nt-25% gap density, (b) 4HB-3 nt-50% gap density, (c) 4HB-3 nt-75% gap density and (d) 4HB-3 nt-100% gap density.

C.5 Calculation of persistence lengths for 4HB-5 nt

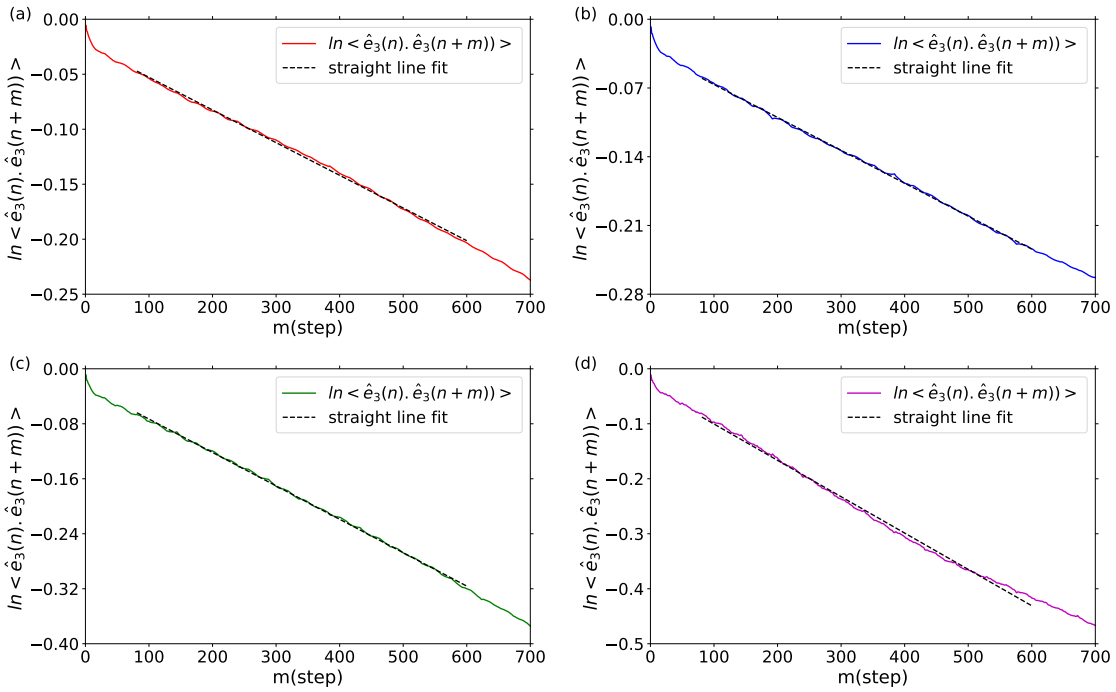


Figure C.7: $\log\langle\cos\theta(m)\rangle$ versus m for (a) 4HB-5 nt-25% gap density, (b) 4HB-5 nt-50% gap density, (c) 4HB-5 nt-75% gap density and (d) 4HB-5 nt-100% gap density.

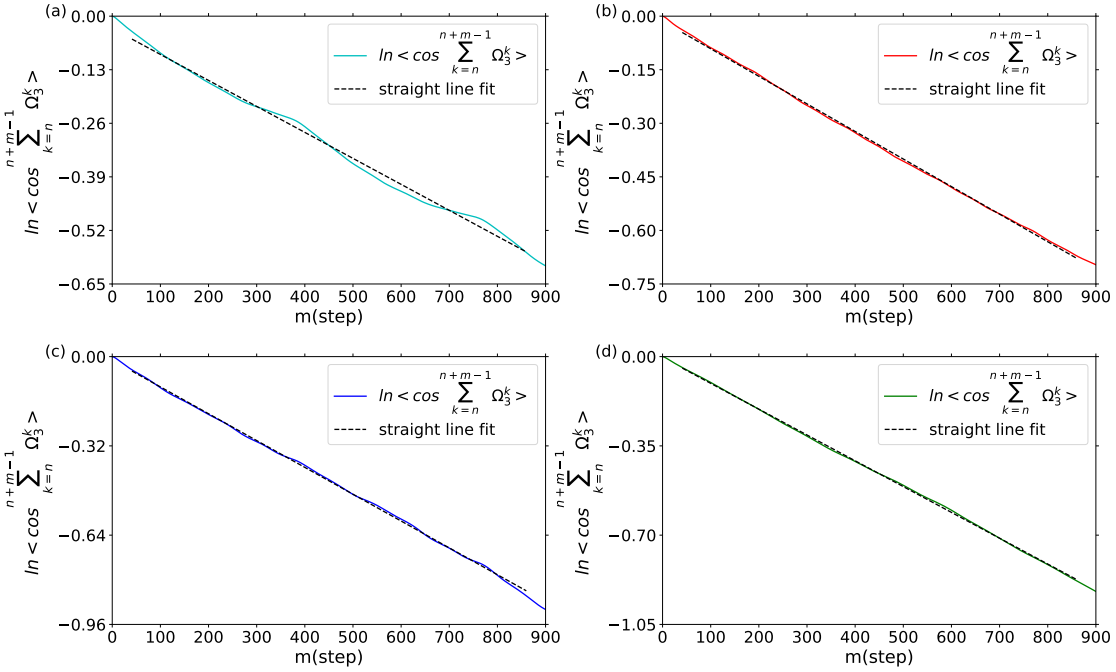
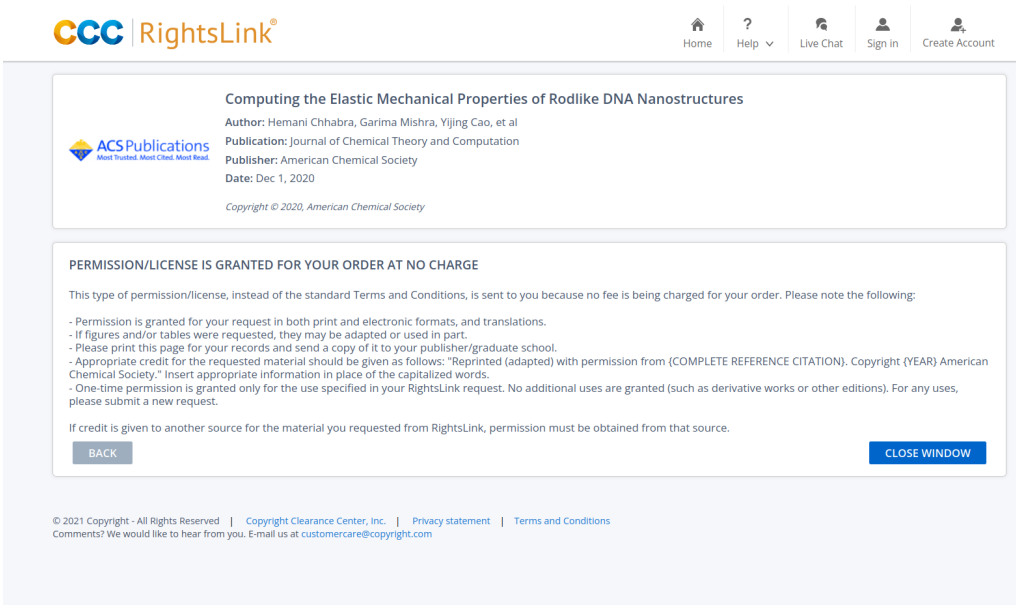


Figure C.8: The exponential decay of the correlation function used to calculate the twist persistence length for (a) 4HB-5 nt-25% gap density, (b) 4HB-5 nt-50% gap density, (c) 4HB-5 nt-75% gap density and (d) 4HB-5 nt-100% gap density.



CCC RightsLink®

Home | Help | Live Chat | Sign in | Create Account

ACS Publications
Most Trusted. Most Cited. Most Read.

Computing the Elastic Mechanical Properties of Rodlike DNA Nanostructures

Author: Hemani Chhabra, Garima Mishra, Yijing Cao, et al
Publication: Journal of Chemical Theory and Computation
Publisher: American Chemical Society
Date: Dec 1, 2020

Copyright © 2020, American Chemical Society

PERMISSION/LICENSE IS GRANTED FOR YOUR ORDER AT NO CHARGE

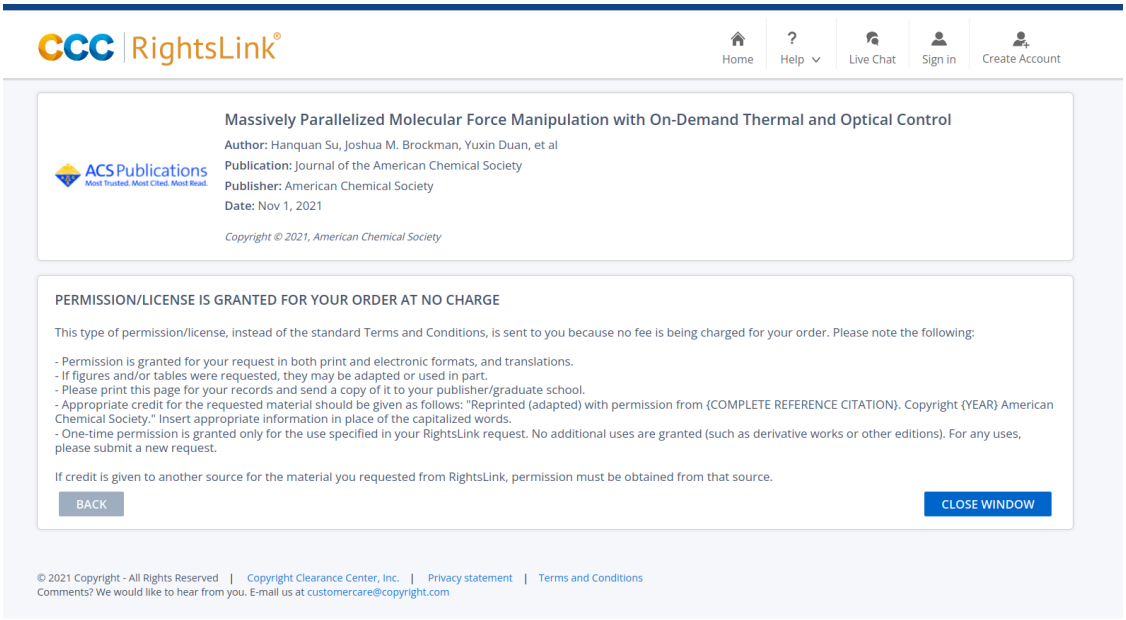
This type of permission/license, instead of the standard Terms and Conditions, is sent to you because no fee is being charged for your order. Please note the following:

- Permission is granted for your request in both print and electronic formats, and translations.
- If figures and/or tables were requested, they may be adapted or used in part.
- Please print this page for your records and send a copy of it to your publisher/graduate school.
- Appropriate credit for the requested material should be given as follows: "Reprinted (adapted) with permission from {COMPLETE REFERENCE CITATION}. Copyright {YEAR} American Chemical Society." Insert appropriate information in place of the capitalized words.
- One-time permission is granted only for the use specified in your RightsLink request. No additional uses are granted (such as derivative works or other editions). For any uses, please submit a new request.

If credit is given to another source for the material you requested from RightsLink, permission must be obtained from that source.

BACK CLOSE WINDOW

© 2021 Copyright - All Rights Reserved | Copyright Clearance Center, Inc. | Privacy statement | Terms and Conditions
Comments? We would like to hear from you. E-mail us at customercare@copyright.com



CCC RightsLink®

Home | Help | Live Chat | Sign in | Create Account

ACS Publications
Most Trusted. Most Cited. Most Read.

Massively Parallelized Molecular Force Manipulation with On-Demand Thermal and Optical Control

Author: Hanquan Su, Joshua M. Brockman, Yuxin Duan, et al
Publication: Journal of the American Chemical Society
Publisher: American Chemical Society
Date: Nov 1, 2021

Copyright © 2021, American Chemical Society

PERMISSION/LICENSE IS GRANTED FOR YOUR ORDER AT NO CHARGE

This type of permission/license, instead of the standard Terms and Conditions, is sent to you because no fee is being charged for your order. Please note the following:

- Permission is granted for your request in both print and electronic formats, and translations.
- If figures and/or tables were requested, they may be adapted or used in part.
- Please print this page for your records and send a copy of it to your publisher/graduate school.
- Appropriate credit for the requested material should be given as follows: "Reprinted (adapted) with permission from {COMPLETE REFERENCE CITATION}. Copyright {YEAR} American Chemical Society." Insert appropriate information in place of the capitalized words.
- One-time permission is granted only for the use specified in your RightsLink request. No additional uses are granted (such as derivative works or other editions). For any uses, please submit a new request.

If credit is given to another source for the material you requested from RightsLink, permission must be obtained from that source.

BACK CLOSE WINDOW

© 2021 Copyright - All Rights Reserved | Copyright Clearance Center, Inc. | Privacy statement | Terms and Conditions
Comments? We would like to hear from you. E-mail us at customercare@copyright.com

Bibliography

[1] R. Wood, A. Robinson in *The Scientists*, *Vol. 1*, Thames & Hudson Ltd, United Kingdom, **2012**, pp. 214–219.

[2] R. Dahm, *Human Genetics* **2008**, *122*, 565–581.

[3] O. T. Avery, C. M. MacLeod, M. McCarty, *Exp. Med.* **1944**, *79*, 137–158.

[4] NCERT, *Biology textbook for class X11.*

[5] A. D. Hershey, M. Chase, *Journal of General Physiology* **1952**, *36*, 39–56.

[6] J. D. Watson, F. H. C. Crick, *Nature* **1953**, *171*, 737–738.

[7] J. Schmidt, English-language Wikipedia, **2006**.

[8] P. A. Levene, W. A. Jacobs, *Berichte der deutschen chemischen Gesellschaft* **1909**, *42*, 1198–1203.

[9] P. A. Levene, W. A. Jacobs, *Berichte der deutschen chemischen Gesellschaft* **1909**, *42*, 3247–3251.

[10] P. A. Levene, *Journal of Biological Chemistry* **1919**, *608*, 415–424.

[11] E. Chargaff, R. Lipshitz, C. Green, *Journal of Biological Chemistry* **1952**, *1*, 155–160.

[12] Lumen, Biology for non majors-1, Module 8: DNA Structure and Replication.

[13] H. Zhou, B. J. Hintze, I. J. Kimsey, et al., *Nucleic Acids Research* **2015**, *43*, 3420–3433.

[14] Wikipedia, A-DNA — Wikipedia, The Free Encyclopedia, **2021**.

[15] K. Hoogsteen, *Acta Crystallographica* **1963**, *16*, 907.

[16] D. Sen, W. Gilbert, *Nature* **1988**, *334*, 364–366.

[17] T. Endoh, A. B. Rode, S. Takahashi, et al., *Analytical Chemistry* **2016**, *88*, 1984–1989.

[18] A. Ghosh, M. Bansal, *Acta Crystallographica Section D Biological Crystallography* **2003**, *59*, 620–626.

[19] R. E. Franklin, R. G. Gosling, *Nature* **1953**, *171*, 740–741.

[20] Y. Mitsui, R. Langridge, B. E. Shortle, et al., *Nature* **1970**, *228*, 1166–1169.

[21] N. C. Seeman, *Journal of Theoretical Biology* **1982**, *99*, 237–247.

[22] J. Chen, N. C. Seeman, *Nature* **1991**, *350*, 631–633.

[23] T. J. Fu, N. C. Seeman, *Biochemistry* **1993**, *32*, 3211–3220.

[24] F. F. Andersen, B. Knudsen, C. L. P. Oliveira, et al., *Nucleic Acids Research* **2008**, *36*, 1113–1119.

[25] W. M. Shih, J. D. Quispe, G. F. Joyce, *Nature* **2004**, *427*, 618–621.

[26] C. M. Erben, R. P. Goodman, A. J. Turberfield, *Journal of the American Chemical Society* **2007**, *129*, 6992–6993.

[27] Y. He, T. Ye, M. Su, et al., *Nature* **2008**, *452*, 198–201.

[28] P. W. K. Rothemund, *Nature* **2006**, *440*, 297–302.

[29] S. M. Douglas, H. Dietz, T. Liedl, et al., *Nature* **2009**, *459*, 414–418.

[30] D. Han, S. Pal, J. Nangreave, et al., *Science* **2011**, *332*, 342–346.

[31] E. Benson, A. Mohammed, J. Gardell, et al., *Nature* **2015**, *523*, 441–444.

[32] K. F. Wagenbauer, C. H. Wachauf, H. Dietz, *Nature Communications* **2014**, *5*, 3691.

[33] D. Han, X. Qi, C. Myhrvold, et al., *Science* **2017**, *358*, eaao2648.

[34] E. S. Andersen, M. Dong, M. M. Nielsen, et al., *Nature* **2009**, *459*, 73–76.

[35] S. Dey, C. Fan, K. V. Gothelf, et al., *Nature Reviews Methods Primers* **2021**, *1*, 13.

[36] C. Y. Tay, L. Yuan, D. T. Leong, *ACS Nano* **2015**, *9*, 5609–5617.

[37] N. C. Seeman, H. F. Sleiman, *Nature Reviews Materials* **2018**, *3*, 17068.

[38] A. V. Pinheiro, D. Han, W. M. Shih, H. Yan, *Nature Nanotechnology* **2011**, *6*, 763–772.

[39] J. Bath, S. J. Green, A. J. Turberfield, *Angewandte Chemie International Edition* **2005**, *44*, 4358–4361.

[40] S. F. J. Wickham, J. Bath, Y. Katsuda, et al., *Nature Nanotechnology* **2012**, *7*, 169–173.

[41] Y. Hao, M. Kristiansen, R. Sha, et al., *Nature Chemistry* **2017**, *9*, 824–827.

[42] M. DeLuca, Z. Shi, C. E. Castro, G. Arya, *Nanoscale Horizons* **2020**, *5*, 182–201.

[43] K. Tapio, I. Bald, *Multifunctional Materials* **2020**, *3*, 032001.

[44] A.-K. Pumm, W. Engelen, E. Kopperger, et al., *Nature* **2022**, *607*, 492–498.

[45] A. T. Blanchard, K. Salaita, *Science* **2019**, *365*, 1080–1081.

[46] C. Gosse, T. R. Strick, D. Kostrz, *Current Opinion in Chemical Biology* **2019**, *53*, 192–203.

[47] E. Pfitzner, C. Wachauf, F. Kilchherr, et al., *Angewandte Chemie International Edition* **2013**, *52*, 7766–7771.

[48] F. Kilchherr, C. Wachauf, B. Pelz, et al., *Science* **2016**, *353*, aaf5508.

[49] P. K. Dutta, Y. Zhang, A. T. Blanchard, et al., *Nano Letters* **2018**, *18*, 4803–4811.

[50] J. J. Funke, P. Ketterer, C. Lieleg, P. Korber, H. Dietz, *Nano Letters* **2016**, *16*, 7891–7898.

[51] J. V. Le, Y. Luo, M. A. Darcy, et al., *ACS Nano* **2016**, *10*, 7073–7084.

[52] P. C. Nickels, B. Wünsch, P. Holzmeister, et al., *Science* **2016**, *354*, 305–307.

[53] K. Kramm, T. Schröder, J. Gouge, et al., *Nature Communications* **2020**, *11*, 2828.

[54] J. J. Funke, P. Ketterer, C. Lieleg, et al., *Science Advances* **2016**, *2*, e160097.

[55] Y. Ke, T. Meyer, W. M. Shih, G. Bellot, *Nature Communications* **2016**, *7*, 10935.

[56] E. Schrödinger, *Annalen der physik* **1926**, *385*, 437–490.

[57] D. Svozil, P. Hobza, J. Šponer, *Journal of Physical Chemistry B* **2009**, *114*, 1191–1203.

[58] A. Mládek, M. Krepl, D. Svozil, et al., *Physical Chemistry Chemical Physics* **2013**, *15*, 7295.

[59] J. Šponer, J. E. Šponer, A. Mládek, et al., *Methods* **2013**, *64*, 3–11.

[60] J. Šponer, J. E. Šponer, A. Mládek, et al., *Biopolymers* **2013**, *99*, 978–988.

[61] W. D. Cornell, P. Cieplak, C. I. Bayly, et al., *Journal of the American Chemical Society* **1995**, *117*, 5179–5197.

[62] B. R. Brooks, C. L. Brooks, A. D. Mackerell, et al., *Journal of Computational Chemistry* **2009**, *30*, 1545–1614.

[63] C. Maffeo, A. Aksimentiev, *Nucleic Acids Research* **2017**, *45*, 12125–12139.

[64] C. A. Laughton, S. A. Harris, *Wiley Interdisciplinary Reviews: Computational Molecular Science* **2011**, *1*, 590–600.

[65] S. A. Harris, Z. A. Sands, C. A. Laughton, *Biophysical Journal* **2005**, *88*, 1684–1691.

[66] G. L. Randall, L. Zechiedrich, B. M. Pettitt, *Nucleic Acids Research* **2009**, *37*, 5568–5577.

[67] J. S. Mitchell, C. A. Laughton, S. A. Harris, *Nucleic Acids Research* **2011**, *39*, 3928–3938.

[68] P. M. D. Severin, X. Zou, H. E. Gaub, K. Schulten, *Nucleic Acids Research* **2011**, *39*, 8740–8751.

[69] J. Yoo, A. Aksimentiev, *Proceedings of the National Academy of Sciences* **2013**, *110*, 20099–20104.

[70] K. Göpfrich, C.-Y. Li, M. Ricci, et al., *ACS Nano* **2016**, *10*, 8207–8214.

[71] S. M. Slone, C.-Y. Li, J. Yoo, A. Aksimentiev, *New Journal of Physics* **2016**, *18*, 055012.

[72] H. Joshi, A. Dwaraknath, P. K. Maiti, *Physical Chemistry Chemical Physics* **2015**, *17*, 1424–1434.

[73] H. Joshi, A. Kaushik, N. C. Seeman, P. K. Maiti, *ACS Nano* **2016**, *10*, 7780–7791.

[74] S. Naskar, M. Gosika, H. Joshi, P. K. Maiti, *Journal of Physical Chemistry C* **2019**, *123*, 9461–9470.

[75] C. Maffeo, J. Yoo, J. Comer, et al., *Journal of Physics: Condensed Matter* **2014**, *26*, 413101.

[76] T. Odijk, *Macromolecules* **1995**, *28*, 7016–7018.

[77] M. Rubinstein, R. H. Colby, *Polymer Physics*, OUP Oxford, **2003**.

[78] S. Neukirch, J. F. Marko, *Physical Review Letters* **2011**, *106*, 138104.

[79] J. F. Marko, *Europhysics Letters (EPL)* **1997**, *38*, 183–188.

[80] K. Neupane, F. Wang, M. T. Woodside, *Proceedings of the National Academy of Sciences* **2017**, *114*, 1329–1334.

[81] A. A. Louis, *Journal of Physics: Condensed Matter* **2002**, *14*, 9187–9206.

[82] C. E. Castro, F. Kilchherr, D.-N. Kim, et al., *Nature Methods* **2011**, *8*, 221–229.

[83] K. Pan, D.-N. Kim, F. Zhang, et al., *Nature Communications* **2014**, *5*, 5578.

[84] F. Dannenberg, K. E. Dunn, J. Bath, et al., *Journal of Chemical Physics* **2015**, *143*, 165102.

[85] A. Cumberworth, A. Reinhardt, D. Frenkel, *Journal of Chemical Physics* **2018**, *149*, 234905.

[86] R. V. Reshetnikov, A. V. Stolyarova, A. O. Zalevsky, et al., *Nucleic Acids Research* **2018**, *46*, 1102–1112.

[87] B. Mergell, M. R. Ejtehadi, R. Everaers, *Physical Review E* **2003**, *68*, 021911.

[88] J. M. Arbona, J.-P. Aimé, J. Elezgaray, *Physical Review E* **2012**, *86*, 051912.

[89] T. Sun, V. Minhas, N. Korolev, et al., *Frontiers in Molecular Biosciences* **2021**, *8*, 159.

[90] D. M. Hinckley, G. S. Freeman, J. K. Whitmer, J. J. de Pablo, *Journal of Chemical Physics* **2013**, *139*, 144903.

[91] P. D. Dans, A. Zeida, M. R. Machado, S. Pantano, *Journal of Chemical Theory and Computation* **2010**, *6*, 1711–1725.

[92] J. J. Uusitalo, H. I. Ingólfsson, P. Akhshi, D. P. Tieleman, S. J. Marrink, *Journal of Chemical Theory and Computation* **2015**, *11*, 3932–3945.

[93] C. Maffeo, A. Aksimentiev, *Nucleic Acids Research* **2020**, *48*, 5135–5146.

[94] T. E. Ouldridge, I. G. Johnston, A. A. Louis, J. P. K. Doye, *Journal of Chemical Physics* **2009**, *130*, 065101.

[95] A. Savelyev, G. A. Papoian, *Proceedings of the National Academy of Sciences* **2010**, *107*, 20340–20345.

[96] A. Savelyev, *Physical Chemistry Chemical Physics* **2012**, *14*, 2250.

[97] S. Pud, S.-H. Chao, M. Belkin, et al., *Nano letters* **2016**, *16*, 8021–8028.

[98] A. Morriss-Andrews, J. Rottler, S. S. Plotkin, *Journal of Chemical Physics* **2010**, *132*, 035105.

[99] N. Korolev, D. Luo, A. Lyubartsev, L. Nordenskiöld, *Polymers* **2014**, *6*, 1655–1675.

[100] Y. He, M. Maciejczyk, S. Ołdziej, H. A. Scheraga, A. Liwo, *Physical Review Letters* **2013**, *110*, 098101.

[101] P. D. Dans, L. Darré, M. R. Machado, et al., *Assessing the Accuracy of the SIRAH Force Field to Model DNA at Coarse Grain Level*, Springer, **2013**, pp. 71–81.

[102] T. Cragnolini, P. Derreumaux, S. Pasquali, *Journal of Physical Chemistry B* **2013**, *117*, 8047–8060.

[103] H. Yagyu, J.-Y. Lee, D.-N. Kim, O. Tabata, *Journal of Physical Chemistry B* **2017**, *121*, 5033–5039.

[104] T. E. Ouldridge, A. A. Louis, J. P. K. Doye, *Journal of Chemical Physics* **2011**, *134*, 085101.

[105] P. Šulc, F. Romano, T. E. Ouldridge, et al., *Journal of Chemical Physics* **2012**, *137*, 135101.

[106] B. E. K. Snodin, F. Randisi, M. Mosayebi, et al., *Journal of Chemical Physics* **2015**, *142*, 234901.

[107] K. G. Young, B. Najafi, W. M. Sant, et al., *Angewandte Chemie International Edition* **2020**, *59*, 15942–15946.

[108] J. F. Berengut, J. C. Berengut, J. P. K. Doye, et al., *Nucleic Acids Research* **2019**, *47*, 11963–11975.

[109] B. E. K. Snodin, J. S. Schreck, F. Romano, A. A. Louis, J. P. K. Doye, *Nucleic Acids Research* **2019**, *47*, 1585–1597.

[110] D. Chakraborty, N. Hori, D. Thirumalai, *Journal of Chemical Theory and Computation* **2018**, *14*, 3763–3779.

[111] M. C. Linak, R. Tourdot, K. D. Dorfman, *Journal of Chemical Physics* **2011**, *135*, 205102.

[112] T. A. Knotts, N. Rathore, D. C. Schwartz, J. J. de Pablo, *Journal of Chemical Physics* **2007**, *126*, 084901.

[113] B. Snodin, PhD thesis, University of Oxford, **2016**.

[114] B. E. K. Snodin, F. Romano, L. Rovigatti, et al., *ACS Nano* **2016**, *10*, 1724–1737.

[115] R. Sharma, J. S. Schreck, F. Romano, A. A. Louis, J. P. K. Doye, *ACS Nano* **2017**, *11*, 12426–12435.

[116] J. S. Schreck, F. Romano, M. H. Zimmer, A. A. Louis, J. P. K. Doye, *ACS Nano* **2016**, *10*, 4236–4247.

[117] O. Henrich, Y. A. G. Fosado, T. Curk, T. E. Ouldridge, *European Physical Journal E* **2018**, *41*, 57.

[118] T. Ouldridge, PhD thesis, Oxford University, UK, **2016**.

[119] T. E. Ouldridge, A. A. Louis, J. P. K. Doye, *Physical Review Letters* **2010**, *104*, 178101.

[120] F. Romano, A. Hudson, J. P. K. Doye, T. E. Ouldridge, A. A. Louis, *Journal of Chemical Physics* **2012**, *136*, 215102.

[121] J. P. K. Doye, H. Fowler, D. Prešern, et al., The oxDNA coarse-grained model as a tool to simulate DNA origami, **2020**.

[122] P. Fonseca, F. Romano, J. S. Schreck, et al., *Journal of Chemical Physics* **2018**, *148*, 134910.

[123] J. P. Doye, A. A. Louis, J. S. Schreck, et al. in *Energy Landscapes of Nanoscale Systems*, (Ed.: D. J. Wales), Frontiers of Nanoscience, Elsevier, **2022**, pp. 195–210.

[124] M. Engel, PhD thesis, University of Oxford, **2018**.

[125] D. Frenkel, B. Smit, *Understanding Molecular Simulation*, 2nd, Academic Press, Inc., USA, **2001**.

[126] M. P. Allen, D. J. Tildesley, *Computer Simulation of Liquids*, *Vol. 1*, Oxford University Press, **2017**.

[127] W. C. Swope, H. C. Andersen, P. H. Berens, K. R. Wilson, *Journal of Chemical Physics* **1982**, *76*, 637–649.

[128] H. C. Andersen, *Journal of Chemical Physics* **1980**, *72*, 2384–2393.

[129] J. Russo, P. Tartaglia, F. Sciortino, *Journal of Chemical Physics* **2009**, *131*, 014504.

[130] T. G. Martin, H. Dietz, *Nature Communications* **2012**, *3*, 1103.

[131] L. Rovigatti, P. Šulc, I. Z. Reguly, F. Romano, *Journal of Computational Chemistry* **2015**, *36*, 1–8.

[132] P. Yin, R. F. Hariadi, S. Sahu, et al., *Science* **2008**, *321*, 824–826.

[133] B. Wei, M. Dai, P. Yin, *Nature* **2012**, *485*, 623–626.

[134] Y. Ke, L. L. Ong, W. M. Shih, P. Yin, *Science* **2012**, *338*, 1177–1183.

[135] F. Hong, F. Zhang, Y. Liu, H. Yan, *Chemical Reviews* **2017**, *117*, 12584–12640.

[136] H. Ramezani, H. Dietz, *Nature Reviews Genetics* **2020**, *21*, 5–26.

[137] W. Pfeifer, B. Saccà, *Biological Chemistry* **2018**, *399*, 773–785.

[138] X.-c. Bai, T. G. Martin, S. H. W. Scheres, H. Dietz, *Proceedings of the National Academy of Sciences* **2012**, *109*, 20012–20017.

[139] C. Bustamante, Z. Bryant, S. B. Smith, *Nature* **2003**, *421*, 423–427.

[140] S. Brahmachari, J. F. Marko, *DNA Mechanics and Topology*, **2018**, pp. 11–39.

[141] F. Romano, D. Chakraborty, J. P. K. Doye, T. E. Ouldridge, A. A. Louis, *Journal of Chemical Physics* **2013**, *138*, 085101.

[142] A. Marin-Gonzalez, J. G. Vilhena, R. Perez, F. Moreno-Herrero, *Proceedings of the National Academy of Sciences* **2017**, *114*, 7049–7054.

[143] T. Liedl, B. Högberg, J. Tytell, D. E. Ingber, W. M. Shih, *Nature Nanotechnology* **2010**, *5*, 520–524.

[144] D. J. Kauert, T. Kurth, T. Liedl, R. Seidel, *Nano Letters* **2011**, *11*, 5558–5563.

[145] C. E. Castro, H.-J. Su, A. E. Marras, L. Zhou, J. Johnson, *Nanoscale* **2015**, *7*, 5913–5921.

[146] C. Lee, K. S. Kim, Y.-J. Kim, J. Y. Lee, D.-N. Kim, *ACS Nano* **2019**, *13*, 8329–8336.

[147] D. Schiffels, T. Liedl, D. K. Fygenson, *ACS Nano* **2013**, *7*, 6700–6710.

[148] P. W. K. Rothemund, A. Ekani-Nkodo, N. Papadakis, et al., *Journal of the American Chemical Society* **2004**, *126*, 16344–16352.

[149] P. O'Neill, P. W. K. Rothemund, A. Kumar, D. K. Fygenson, *Nano Letters* **2006**, *6*, 1379–1383.

[150] T. Wang, D. Schiffels, S. M. Cuesta, D. K. Fygenson, N. C. Seeman, *Journal of the American Chemical Society* **2012**, *134*, 1606–1616.

[151] E. Benson, A. Mohammed, D. Rayneau-Kirkhope, et al., *ACS Nano* **2018**, *12*, 9291–9299.

[152] E. Benson, M. Lolaico, Y. Tarasov, A. Gådin, B. Högberg, *ACS Nano* **2019**, *13*, 12591–12598.

[153] W. Pfeifer, P. Lill, C. Gatsogiannis, B. Saccà, *ACS Nano* **2018**, *12*, 44–55.

[154] Z. Ma, K. Kawai, Y. Hirai, T. Tsuchiya, O. Tabata, *Japanese Journal of Applied Physics* **2017**, *56*, 06GJ02.

[155] W. Bae, K. Kim, D. Min, et al., *Nature Communications* **2014**, *5*, 5654.

[156] D. Koirala, P. Shrestha, T. Emura, et al., *Angewandte Chemie International Edition* **2014**, *53*, 8137–8141.

[157] P. Shrestha, T. Emura, D. Koirala, et al., *Nucleic Acids Research* **2016**, *44*, 6574–6582.

[158] M. C. Engel, D. M. Smith, M. A. Jobst, et al., *ACS Nano* **2018**, *12*, 6734–6747.

[159] H. Chhabra, G. Mishra, Y. Cao, et al., *Journal of Chemical Theory and Computation* **2020**, *16*, 7748–7763.

[160] D.-N. Kim, F. Kilchherr, H. Dietz, M. Bathe, *Nucleic Acids Research* **2012**, *40*, 2862–2868.

[161] Y.-J. Kim, D.-N. Kim, *Journal of Nanomaterials* **2016**, *2016*, 1–7.

[162] S. K. Nomidis, F. Kriegel, W. Vanderlinden, J. Lipfert, E. Carlon, *Physical Review Letters* **2017**, *118*, 217801.

[163] E. Skoruppa, M. Laleman, S. K. Nomidis, E. Carlon, *Journal of Chemical Physics* **2017**, *146*, 214902.

[164] C. Matek, T. E. Ouldridge, J. P. K. Doye, A. A. Louis, *Scientific Reports* **2015**, *5*, 7655.

[165] Z. Shi, C. E. Castro, G. Arya, *ACS Nano* **2017**, *11*, 4617–4630.

[166] L. Zhou, A. E. Marras, C.-M. Huang, C. E. Castro, H.-J. Su, *Small* **2018**, *14*, 1802580.

[167] A. Suma, A. Stopar, A. W. Nicholson, M. Castronovo, V. Carnevale, *Nucleic Acids Research* **2020**, *48*, 4672–4680.

[168] F. Hong, S. Jiang, X. Lan, et al., *Journal of the American Chemical Society* **2018**, *140*, 14670–14676.

[169] M. Matthies, N. P. Agarwal, E. Poppleton, et al., *ACS Nano* **2019**, *13*, 1839–1848.

[170] M. M. C. Tortora, G. Mishra, D. Prešern, J. P. K. Doye, *Science Advances* **2020**, *6*, aaw8331.

[171] M. Siavashpouri, C. H. Wachauf, M. J. Zakhary, et al., *Nature Materials* **2017**, *16*, 849–856.

[172] J. F. Marko, E. D. Siggia, *Macromolecules* **1994**, *27*, 981–988.

[173] E. Skoruppa, *DNA Elasticity from Coarse-Grained Simulations: On the Hunt for Twist- Bend Coupling. M.Sc. thesis, KU Leuven*, **2017**.

[174] P. A. Wiggins, P. C. Nelson, *Physical Review E* **2006**, *73*, 031906.

[175] S. K. Nomidis, E. Skoruppa, E. Carlon, J. F. Marko, *Physical Review E* **2019**, *99*, 032414.

[176] G. Strang, *book*.

[177] M. A. B. Baker, A. J. Tuckwell, J. F. Berengut, et al., *ACS Nano* **2018**, *12*, 5791–5799.

[178] H. Dietz, S. M. Douglas, W. M. Shih, *Science* **2009**, *325*, 725–730.

[179] C. K. Wong, C. Tang, J. S. Schreck, J. P. K. Doye, *Nanoscale* **2022**, *14*, 2638–2648.

[180] C. Myhrvold, M. Baym, N. Hanikel, et al., *Nature Communications* **2017**, *8*, 14698.

[181] M. T. Strauss, F. Schueder, D. Haas, P. C. Nickels, R. Jungmann, *Nature Communications* **2018**, *9*, 1600.

[182] M. Wang, H. Yin, R. Landick, J. Gelles, S. Block, *Biophysical Journal* **1997**, *72*, 1335–1346.

[183] K. Liebl, M. Zacharias, *Journal of Chemical Theory and Computation* **2021**, *17*, 7096–7105.

[184] J. Y. Lee, Y. J. Kim, C. Lee, et al., *Nucleic Acids Research* **2019**, *47*, 93–102.

[185] H. Su, J. M. Brockman, Y. Duan, et al., *Journal of the American Chemical Society* **2021**, *143*, 19466–19473.

[186] Y.-J. Kim, J. Park, J. Y. Lee, D.-N. Kim, *Nature Communications* **2021**, *12*, 1–8.

[187] M. C. Engel, D. M. Smith, M. A. Jobst, et al., *ACS Nano* **2018**, *12*, 6734–6747.

[188] J. Dekker, M. A. Marti-Renom, L. A. Mirny, *Nature Reviews Genetics* **2013**, *14*, 390–403.

[189] P. R. Desai, S. Brahmachari, J. F. Marko, S. Das, K. C. Neuman, *Nucleic Acids Research* **2020**, *48*, 10713–10725.

[190] H. Brutzer, N. Luzzietti, D. Klaue, R. Seidel, *Biophysical Journal* **2010**, *98*, 1267–1276.

[191] W. Xindan, L. Paula Montero, Z. R. David, *Nature Reviews Genetics* **2008**, *86*, 3279–3288.

[192] Y. Zhang, A. E. McEwen, D. M. Crothers, S. D. Levene, *PLOS ONE* **2006**, *1*, 1–13.

[193] V. Vijayan, R. Zuzow, E. K. O'Shea, *Proceedings of the National Academy of Sciences* **2009**, *106*, 22564–22568.

[194] J. F. Marko, S. Neukirch, *Physical Review E* **2012**, *85*, 011908.

[195] B. C. Daniels, J. P. Sethna, *Physical Review E* **2011**, *83*, 041924.

[196] M. Emanuel, G. Lanzani, H. Schiessel, *Physical Review E* **2013**, *88*, 022706.

[197] K. V. Klenin, A. V. Vologodskii, V. V. Anshelevich, A. M. Dykhne, M. D. Frank-Kamenetskii, *Journal of Molecular Biology* **1991**, *217*, 413–419.

[198] A. V. Vologodskii, S. D. Levene, K. V. Klenin, M. Frank-Kamenetskii, N. R. Cozzarelli, *Journal of Molecular Biology* **1992**, *227*, 1224–1243.

[199] A. Suma, E. Poppleton, M. Matthies, et al., *Journal of Computational Chemistry* **2019**, *40*, 2586–2595.

[200] N. Clauvelin, B. Audoly, S. Neukirch, *Biophysical Journal* **2009**, *96*, 3716–3723.

[201] N. Clauvelin, B. Audoly, S. Neukirch, *Macromolecules* **2008**, *41*, 4479–4483.

[202] E. Poppleton, J. Bohlin, M. Matthies, et al., *Nucleic acids research* **2020**, *48*, e72–e72.

[203] T. Strick, M. Dessinges, G. Charvin, et al., *Reports on Progress in Physics* **2002**, *66*, 1.

[204] A. Dittmore, S. Brahmachari, Y. Takagi, J. F. Marko, K. C. Neuman, *Physical review letters* **2017**, *119*, 147801.

[205] S. Brahmachari, A. Dittmore, Y. Takagi, K. C. Neuman, J. F. Marko, *Physical Review E* **2018**, *97*, 022416.

[206] T. Strick, J.-F. Allemand, V. Croquette, D. Bensimon, *Progress in Biophysics and Molecular Biology* **2000**, *74*, 115–140.

[207] J. D. Moroz, P. Nelson, *Proceedings of the National Academy of Sciences* **1997**, *94*, 14418–14422.

[208] J. F. Marko in *Les Houches*, *Vol. 82*, Elsevier, **2005**, pp. 211–270.

[209] Y.-J. Kim, C. Lee, J. G. Lee, D.-N. Kim, *ACS Nano* **2019**, *13*, 6348–6355.

[210] C. Lee, J. Y. Lee, D. N. Kim, *Nature Communications* **2017**, *8*, 2067.

[211] V. A. Turek, R. Chikkaraddy, S. Cormier, et al., *Advanced Functional Materials* **2018**, *28*, 1706410.

[212] J. Y. Lee, M. Kim, C. Lee, D.-N. Kim, *ACS Nano* **2021**, *15*, 20430–20441.

[213] C. Lee, Y.-J. Kim, K. S. Kim, J. Y. Lee, D.-N. Kim, *Nucleic Acids Research* **2021**, *49*, 12591–12599.

[214] W. Fang, M. Xie, X. Hou, et al., *Journal of the American Chemical Society* **2020**, *142*, 8782–8789.

[215] Y.-J. Kim, J. Park, J. Y. Lee, D.-N. Kim, *Nature Communications* **2021**, *12*, 5177.

[216] T. D. Craggs, M. Sustarsic, A. Plochowietz, et al., *Nucleic Acids Research* **2019**, *47*, 10788–10800.

[217] C. Rivetti, C. Walker, C. Bustamante, *Journal of Molecular Biology* **1998**, *280*, 41–59.

[218] E. F. Koslover, A. J. Spakowitz, *Macromolecules* **2013**, *46*, 2003–2014.

[219] P. Benetatos, M. Razbin, *Polymers* **2021**, *13*, 2031.

[220] N. R. Kallenbach, R.-I. Ma, N. C. Seeman, *Nature* **1983**, *305*, 829–831.

[221] I. Dozov, *Europhysics Letters (EPL)* **2001**, *56*, 247–253.

[222] A. Jákli, O. D. Lavrentovich, J. V. Selinger, *Reviews of Modern Physics* **2018**, *90*, 045004.

[223] S. A. Egorov, A. Milchev, A. Nikoubashman, K. Binder, *Journal of Physical Chemistry B* **2021**, *125*, 956–969.

[224] A. Milchev, S. A. Egorov, J. Midya, K. Binder, A. Nikoubashman, *ACS Macro Letters* **2020**, *9*, 1779–1784.

[225] M. Mosayebi, F. Romano, T. E. Ouldridge, A. A. Louis, J. P. K. Doye, *Journal of Physical Chemistry B* **2014**, *118*, 14326–14335.

[226] R. L. Bender, H. Ogasawara, A. V. Kellner, A. Velusamy, K. Salaita, *bioRxiv* **2022**, DOI 10.1101/2022.04.04.487040.

[227] M. C. Engel, F. Romano, A. A. Louis, J. P. K. Doye, *Journal of Chemical Theory and Computation* **2020**, *16*, 7764–7775.

[228] M. Kube, F. Kohler, E. Feigl, et al., *Nature Communications* **2020**, *11*, 6229.

[229] P. T. Li, D. Collin, S. B. Smith, C. Bustamante, I. Tinoco, *Biophysical Journal* **2006**, *90*, 250–260.

[230] E. Skoruppa, A. Voorspoels, J. Vreede, E. Carlon, *Physical Review E* **2021**, *103*, 042408.